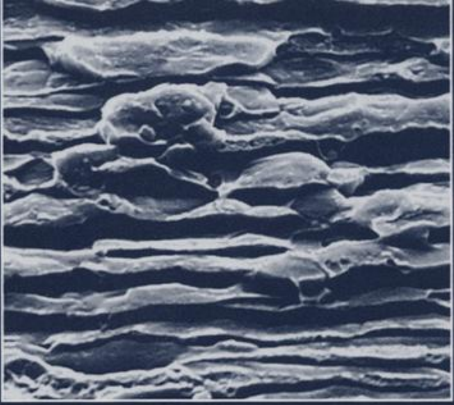

Elevated Temperature Effects on FATIGUE and FRACTURE

Robert S. Piascik
Richard P. Gangloff
Ashok Saxena
EDITORS

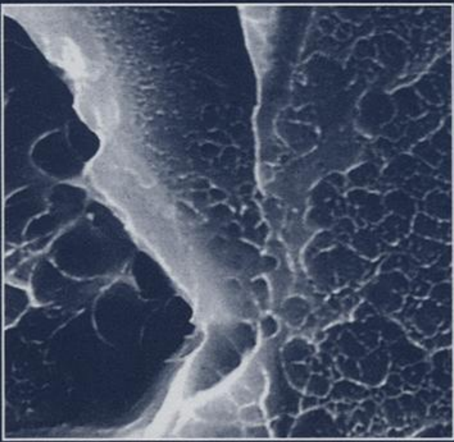

ASTM STP 1297

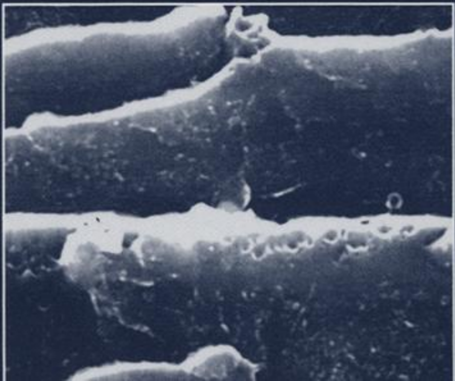

STP 1297

Elevated Temperature Effects on Fatigue and Fracture

Robert S. Piascik, Richard P. Gangloff, and Ashok Saxena, editors

ASTM Publication Code Number (PCN):
04-012970-30

ASTM
100 Barr Harbor Drive
West Conshohocken, PA 19428-2959

Printed in the U.S.A.

Library of Congress Cataloging-in-Publication Data

Elevated temperature effects on fatigue and fracture/Robert S.
Piascik, Richard P. Gangloff, and Ashok Saxena, editors.
(STP: 1297); "ASTM publication code number (PCN): 04-012970-30."
Includes bibliographical references and indexes.
ISBN 0-8031-2413-9
1. Fracture mechanics. 2. Materials—Fatigue—Effect of
temperature on. I. Piascik, Robert S. II. Gangloff, R. P.
III. Saxena, A. (Ashok) IV. Series: ASTM special technical publication:
1297.
TA409.E45 1997 96-52047
620.1'66—dc21 CIP

Photocopy Rights

Authorization to photocopy items for internal, personal, or educational classroom use, or the internal, personal, or educational classroom use of specific clients, is granted by the American Society for Testing and Materials (ASTM) provided that the appropriate fee is paid to the Copyright Clearance Center, 222 Rosewood Drive, Danvers, MA 01923, Tel: 508-750-8400 online: http://www.copyright.com/.

Peer Review Policy

Each paper published in this volume was evaluated by two peer reviewers and at least one of the editors. The authors addressed all of the reviewers' comments to the satisfaction of both the technical editor(s) and the ASTM Committee on Publications.

The quality of the papers in this publication reflects not only the obvious efforts of the authors and the technical editor(s), but also the work of these peer reviewers. The ASTM Committee on Publications acknowledges with appreciation their dedication and contribution to time and effort on behalf of ASTM.

Printed in Philadelphia, PA
February 1997

Foreword

The Twenty-Seventh National Symposium on Fatigue and Fracture Mechanics was held in Williamsburg, Virginia on 26–29 June 1995. The sponsor of the event was ASTM Committee E-8 on Fatigue and Fracture. The symposium chairman was R. S. Piascik, NASA Langley Research Center. Symposium co-chairmen were: J. C. Newman, Jr., NASA Langley Research Center; R. P. Gangloff, University of Virginia; and N. E. Dowling, Virginia Polytechnic Institute and State University. This special technical publication highlights a topical subset of the meeting: research on the critical effect of temperature on the fatigue and fracture of structural materials. The editors of this publication were R. S. Piascik, R. P. Gangloff, and A. Saxena.

Contents

CREEP CRACK GROWTH

FATIGUE

FRACTURE

Overview

The 27th National Symposium on Fatigue and Fracture Mechanics, held in Williamsburg, Virginia in June of 1995, was organized with the goal of providing an international forum for the integration of research on fatigue and fracture mechanics. The intent of this meeting was to reinforce the recent merger of ASTM Committees E09 on Fatigue and E24 on Fracture Mechanics, forming Committee E08 on Fatigue and Fracture. This special technical publication highlights a topical subset of the meeting, that is, research on the critical effect of temperature on the fatigue and fracture of structural materials.

While elevated temperature effects on mechanical behavior have been studied for over 100 years, uncertainties continue to hinder prediction of the long-life performance of flawed aging structures in the aggressive thermal environment, as well as the development of damage-tolerant alloys. The organizing committee aimed to examine the extent to which recent developments in fatigue and fracture mechanics have been exploited to further quantitative understanding of this field. Papers were sought that highlighted:

- Integration of damage evolution, from the distributed form to that focused at a crack tip.
- High-resolution experimental probes of fatigue and fracture processes.
- Measurement and modeling of the important role of time in microstructural degradation, damage evolution, and crack growth.
- Models that provide quantitative predictions and are tested by high-quality experimentation.
- Performance of next-generation structural metals and composites, characterized within a framework useful in component life prediction.

The following is an overview of the Symposium papers included in this topical volume. The selection process adhered to ASTM procedures for peer review by a committee of three experts. The review of each paper was overseen by one of the STP coeditors and a representative of the ASTM Committee on Publications. Authors provided mandatory revisions in response to this process and several papers were not published. This standard of review is equivalent in rigor to that practiced by the archival journals in our field.

The manuscripts are divided according to the topics of creep crack growth, fatigue, and fracture.

Creep Crack Growth

Gao, Chen, Chen, and Wei reported on research conducted to understand the rate controlling process and micromechanisms for environmentally enhanced intergranular creep crack growth in Inconel 718 at elevated temperatures. The effects of environmental oxygen pressure and alloy chemical composition on crack growth rate were elucidated. The role of niobium as an enhancer of creep crack growth rate was identified, providing a basis for alloy development. The approach embodied in this research follows the philosophy but forth by Professor Wei in his J. L. Swedlow lecture that keynoted this conference.

Sester, Mohrmann, and Riedel presented a constitutive model for creep and creep rupture of 12% Cr steel. The aim of this approach was to develop better understanding of the role of microstructure during creep crack growth. The model includes the Hutchinson damage parameter, the Rodin-Parks model for the effect of creep damage on macroscopic constitutive behavior, and an empirical evolutionary equation for estimating microcrack density. Model parameters are adjusted to a set of uniaxial creep data over a wide range of stress. Model predictions compare favorably with creep crack growth test results and are conservative, suggesting further work to refine the constitutive model.

Chell, Kuhlman, Millwater, and Riha considered creep crack growth in terms of C_t. This driving force was estimated for cracks with multiple degrees of freedom, such as an embedded elliptical flaw, using the reference stress to determine C^* and a probabilistic method. It was concluded that the reference stress approach provides a simple and versatile method for evaluating C^*, in addition to including the important effects of self-equilibrated secondary stresses and prior damage in the determination of C_t. The application of a probability analysis, based on fast probability integration techniques, enables decisions regarding inspection schedules for an operating plant and identifies the variables that govern the lifetime of the cracked component.

In a two-part contribution, Hamilton, Hall, Saxena, and McDowell investigated the creep deformation and creep crack growth characteristics of Aluminum Alloy 2519-T87 at 135°C. Experimental work in Part I demonstrated that, characteristic of a creep brittle material, crack growth rate effectively correlates with the applied stress intensity, but not with time-dependent C_t. Subcritical cracking was either distinctly intergranular or transgranular, with the transition between these fracture regions occurring at a critical *K*-level. The incubation time required for crack growth was correlated with *K* and related to an accumulation of a critical amount of damage ahead of the crack tip. In Part II a finite element model of AA2519 creep crack growth was used to gain insight into the relation of crack tip strain field fracture parameters to creep crack growth rate. Numerical results indicate an initial transient period of crack growth, followed by a quasi-steady-state cracking regime in which the crack tip fields change slowly with increasing crack length. Transition of crack growth to the quasi-stead-state regime, where similitude and small-scale creep conditions roughly exist, is given by a transition time (t_s) that depends on crack growth history and material properties. Creep crack growth rate is predicted to correlate with *K* for times in excess of t_s, as observed experimentally.

Fatigue

Ohtani, Kitamura, Tada, and Zhou modeled creep-fatigue damage in 304 stainless steel sheet at elevated temperature. The model predicts the evolution of both surface and internal cracking. For surface cracking, grain boundary facets were generated using an isotropic grain growth model, and cracks were simulated where facets intersect the surface. In the case of internal cracks, grain boundary facets were projected on a plane perpendicular to the stress axis. A random-number description of the intrinsic fracture resistance of each grain facet represented the stochastic nature of crack initiation and propagation. To describe damage evolution, the fracture resistance of each facet was reduced by the magnitude of the driving force after every cycle. Here, the driving force depends on tensile and compressive strain rates, total strain range, and temperature. When the resistance becomes zero, a crack is assumed to initiate. Numerical simulations of surface and internal cracking exhibit similar morphologies compared to creep-fatigue cracking observed in 304 stainless steel sheet. The predicted number of cracks, the distribution of crack length, and the crack propagation rate agree quantitatively with experimental observations.

The effect of a gaseous environment on elevated temperature fatigue crack propagation kinetics was investigated by Sarrazin-Baudoux, Lesterlin, and Petit. Specifically, the crack growth behavior of Ti-6Al-4V and Ti-6Al-3Sn-4Zr-6Mo alloys was studied in purified nitrogen, with controlled additions of small partial pressure quantities of pure oxygen and water vapor. Comparisons with inert vacuum rates suggest that increased *da/dN* in water vapor is due to hydrogen embrittlement at 300°C. Above a critical temperature range (465 to 500°C), a time-dependent damage mechanism operated; fatigue crack growth rate increased as frequency decreased from 35 to 0.1 Hz. Here, oxygen was suspected of being the embrittling specie.

Albertson, Stephens, and Bayha provided data on the fatigue crack growth characteristics of two modern titanium alloys, Timetal-21S and Ti-6Al-2Sn-2Zr-2Mo-2Cr at 25 and 175°C. Differences in constant amplitude fatigue crack growth rate at various stress ratios ($R = 0.1, 0.5$, and -0.4) were rationalized in terms of crack tip closure mechanisms.

The research performed by Yoon, Beak, and Suh is directed towards turbine rotor life prediction. Here, waveform effects on the creep crack growth behavior of 1Cr-1Mo-0.25V rotor steel at 528°C are studied. Large scatter is observed in time-dependent crack growth, $(da/dt)_{avg}$, during hold times when correlated with estimated $(C_t)_{avg}$. A new estimation equation was proposed in which effects of load increasing rate are considered. The effectiveness of the proposed equation was discussed by showing that the scatter of the measured $(da/dt)_{avg}$ data was reduced when the new equation was adopted. The characteristics of the initial transient crack growth behavior are also shown to be dependent on an oxidation-dominated crack growth mechanism.

Fracture

Haynes, Somerday, Lach, and Gangloff predicted the temperature dependence of the initiation fracture toughness for a variety of advanced ingot and powder metallurgy aluminum alloys, utilizing a critical plastic strain-controlled micromechanical model of ductile microvoid fracture. This work showed that toughness is governed by the interplay of the temperature dependencies of the crack tip field and affected by material constitutive behavior and the intrinsic microvoid fracture resistance. A calculated critical distance parameter correlated with the nearest-neighbor spacing of void nucleating particles and with the extent of primary void growth determined fractographically. This work provides a broad confirming test of this crack tip process zone modeling approach and suggests a means to predict absolute values of fracture toughness.

The effect of long-term thermal exposure on the fracture properties of advanced aluminum alloys was studied by Reynolds and Crooks. Both lithium-based and non-lithium-containing alloys were exposed in moist air to temperatures ranging from 93 to 163°C for up to 7000 h, followed by tensile and *J*-integral fracture toughness testing. Detailed fractography revealed a predominantly transgranular microvoid fracture morphology prior to exposure, but both brittle and ductile grain boundary failure after exposure. A reduction in fracture resistance was correlated with boundary precipitation that occurred during long-term elevated temperature exposure. These results are pertinent to the use of light alloys in the next-generation supersonic aircraft.

Yang, Saxena, and Starr investigated the high-temperature (1000°C) fracture behavior of the unidirectional Nicalon fiber-reinforced reaction-bonded silicon nitride (RBSN) composite. Microstructural examinations demonstrated that high porosity and coarse open pores lead to oxidation above 800°C. Severe matrix oxidation leads to substantial expansion of the composite in the transverse direction. Fracture studies of the RBSN composite documented the effect of elevated temperature and oxidation on crack initiation and growth.

We wish to thank those who participated in this meeting and enabled this volume, including the session chairs, authors, reviewers, and ASTM staff. We hope that the collection of manuscripts in ASTM STP 1297 on *Elevated Temperature Effects on Fatigue and Fracture* will contribute to engineering solutions to life prediction problems, stimulate future research on the critical issues represented here, and integrate work on fatigue and fracture mechanics as embodied in the new structure of ASTM Committee E08.

Robert S. Piascik
NASA Langley Research Center
Hampton, VA 23681-0001: symposium chairman and editor.

Richard P. Gangloff
University of Virginia
Charlottesville, VA 22903: symposium co-chairman and editor.

Ashok Saxena
Georgia Institute of Technology
Atlanta, GA 30332: symposium session chairman and editor.

Creep Crack Growth

B. Carter Hamilton,[1] *David E. Hall,*[2] *Ashok Saxena,*[3] *and*
David L. McDowell[4]

Creep Crack Growth Behavior of Aluminum Alloy 2519: Part I—Experimental Analysis

---

REFERENCE: Hamilton, B. C., Hall, D. E., Saxena, A., and McDowell, D. L., "**Creep Crack Growth Behavior of Aluminum Alloy 2519: Part I—Experimental Analysis,**" *Elevated Temperature Effects on Fatigue and Fracture, ASTM STP 1297,* R. S. Piascik, R. P. Gangloff, and A. Saxena, Eds., American Society for Testing and Materials, 1997, pp. 3–18.

ABSTRACT: The discipline of time-dependent fracture mechanics has traditionally focused on the creep crack growth behavior of high-temperature materials that display creep-ductile behavior, such as stainless steels and chromium-molybdenum steels. Elevated temperature aluminum alloys, however, have been developed that exhibit creep-brittle behavior; in this case, the creep crack growth rate correlates with the stress intensity factor, K. The fracture characteristics of aluminum alloy 2519-T87 were studied at 135°C, and the creep and creep crack growth behavior were characterized utilizing experimental and numerical methods.

The strain to failure for creep deformation specimens was limited to only 1.2 to 2.0%. Creep crack growth tests revealed a unique correlation between the creep crack growth rate and K, a result consistent with creep-brittle behavior. No experimental correlation was found between the creep crack growth rate and the C_t parameter. Microscopy of fracture surfaces revealed distinct regions of intergranular and transgranular fracture, and the transition between the fracture regions was found to occur at a critical K-level. Experimental results also appeared to show that initiation of crack growth (incubation) is controlled by the accumulation of a critical amount of damage ahead of the crack tip and that a correlation exists between the incubation time and K. Total time to failure is viewed as a summation of the incubation period and the crack growth period, and the design importance of incubation time is discussed.

KEYWORDS: creep, creep crack growth, creep-brittle, aluminum alloys, crack initiation, incubation

Researchers in time-dependent fracture mechanics (TDFM) have sought to understand the creep crack growth behavior of engineering materials and to establish correlations between the creep crack growth rate and global crack tip parameters. Creep crack growth behavior of metals may be characterized as creep-ductile or creep-brittle. In creep-ductile materials, creep deformation accumulates ahead of the crack tip at a rate much faster than the rate at which the crack propagates, and therefore the crack remains effectively stationary within an expanding creep zone. Under these conditions, time-dependent crack tip parameters that assume a stationary crack, such as C^* [*1*] and C_t [2], characterize crack tip conditions and correlate with the creep

---

[1] Graduate research assistant, School of Materials Science and Engineering, Georgia Institute of Technology, Atlanta, GA 30332.

[2] Assistant professor, Department of Mechanical and Industrial Engineering, Louisiana Tech University, Ruston, LA 71272.

[3] Professor and chair, School of Materials Science and Engineering, Georgia Institute of Technology, Atlanta GA 30332.

[4] Regent's professor, The George W. Woodruff School of Mechanical Engineering, Georgia Institute of Technology, Atlanta, GA 30332.

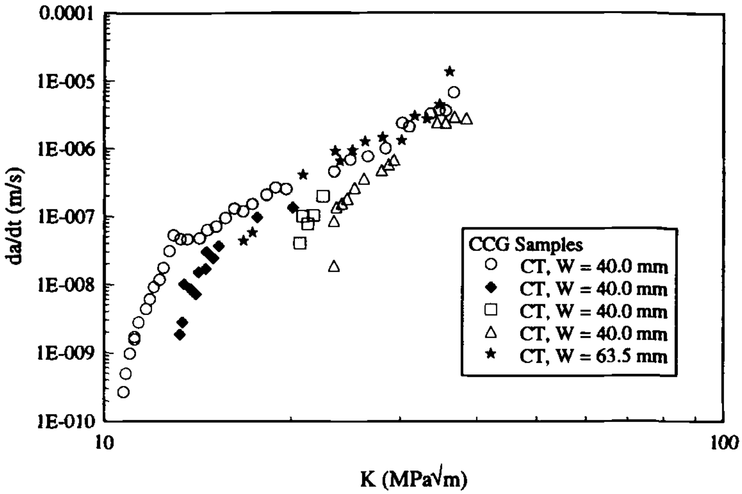

FIG. 1—*Creep crack growth rates versus* K *for aluminum 2219-T851 at 175°C for constant* P *tests* [7,8].

crack growth rate. Many high-temperature structural steels, such as stainless steels and chromium-molybdenum steels, exhibit creep-ductile behavior at elevated temperatures [3,4].

In creep-brittle materials, however, creep strain accumulation at the crack tip and crack extension proceed at comparable rates, and crack growth significantly perturbs the crack tip stress field. Thus, the time-dependent, stationary crack tip parameters no longer characterize the crack tip conditions. Under certain circumstances, time-independent fracture parameters, such as the J-integral [5,6] or K, may correlate with the creep crack growth rate in creep-brittle materials. At elevated temperatures, some aluminum alloys have exhibited such creep-brittle behavior. For example, correlations between the creep crack growth rate and K have been established for aluminum alloy 2219-T851 [7,8] (Fig. 1) and to a limited extent for aluminum alloy 8009 [9]. Similar correlations have also been demonstrated for other creep-brittle materials such as Ti-6242 [10] (Fig. 2). The precise conditions, however, under which K or J characterize the crack growth behavior of creep-brittle materials are not yet well defined.

Aluminum 2519-T87, an aluminum-copper alloy containing 5.3 to 6.4% copper, was developed as an improvement to aluminum 2219-T851 and has displayed superior mechanical properties to 2219 over a wide temperature range [11]. Aluminum 2519 is a precipitation-hardenable alloy, which relates to the enhanced mechanical performance and increased creep resistance imparted to the alloy by second-phase precipitates. The goal of this research is to evaluate the creep and creep crack growth behavior of aluminum 2519 at 135°C.

Experimental Procedure

Creep Deformation Tests

To characterize the creep and creep crack growth behavior of aluminum 2519-T87, several creep deformation and creep crack growth tests were performed at 135°C (275°F). The alloy was manufactured by Alcoa and provided in a heat-treated condition in plate form by the NASA Langley Research Center. For creep deformation testing, twelve tension specimens were ma-

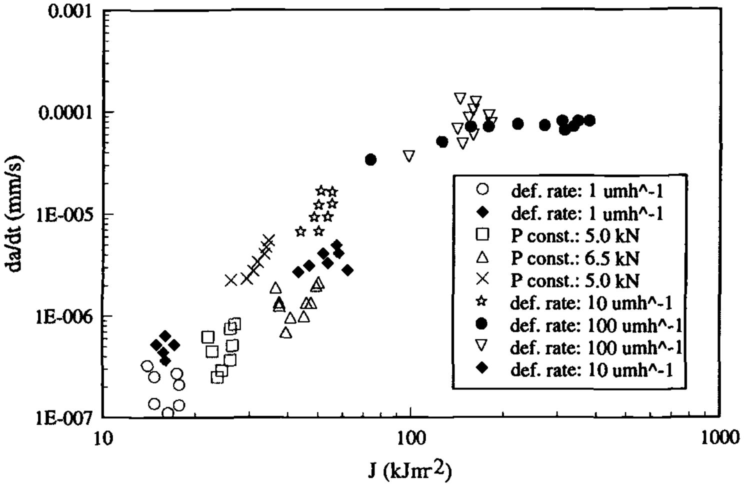

FIG. 2—*Creep crack growth rates as a function of the J-integral for Ti-6242 at 500°C* [10].

chined from the plate material and oriented so that the tensile axis coincided with the rolling direction. The selected geometry and size for these specimens are shown in Fig. 3. Creep deformation tests were performed with dead weight lever-type creep machines under a constant load. In some instances, however, the test loads were too small (approximately less than 4.55 kg) to apply through the lever. For these tests, the constant load was directly applied to the specimen. The test temperature was controlled to within ±1°C, and the creep deflection along the load-line was measured with a direct calibration displacement transducer (DCDT) based extensometer. Following the tests, creep strain versus time and creep strain rate versus time plots were generated and the creep constants calculated. Creep strain rates were determined using the sliding seven-point polynomial fit [*12*]. Because the scatter in the strain versus time data was so low, the authors feel that four creep deformation tests are sufficient to derive consistent and reliable deformation rates.

Creep Crack Growth Tests

For creep crack growth testing, CT-type specimens of two thicknesses were utilized as represented in Fig. 4. Four 22.1-mm-thick and three 6.35-mm-thick specimens were machined from the plate material in the L-T orientation. The specimens were fatigue precracked at room

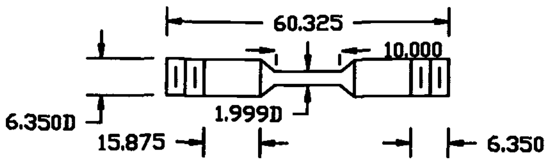

FIG. 3—*Creep deformation specimen geometry and size (unit: mm).*

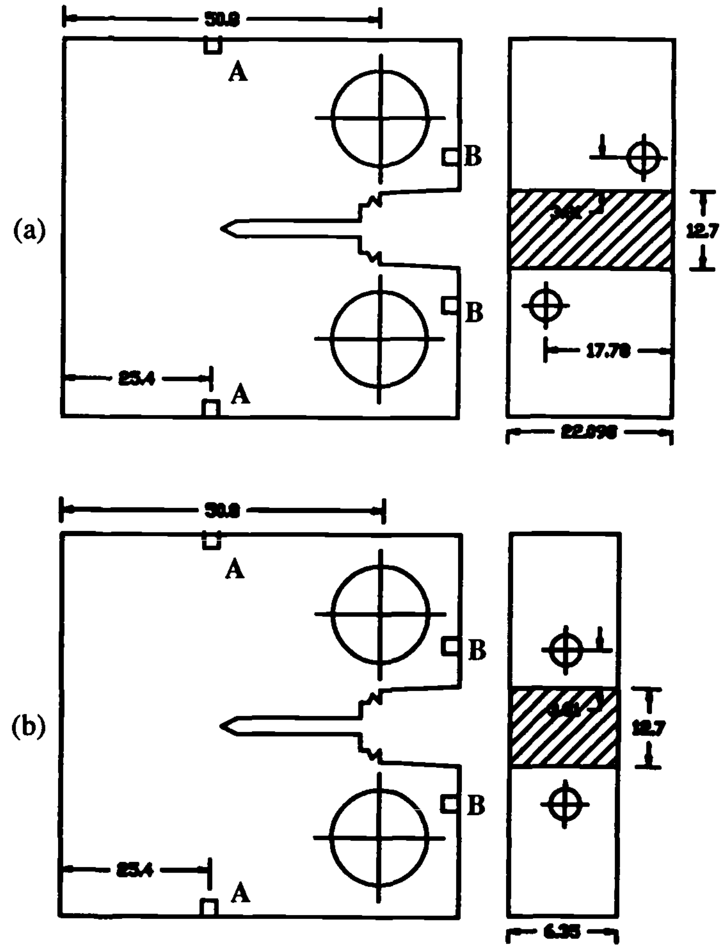

FIG. 4—*Geometry of CT-type specimens used for creep crack growth testing and electrical lead locations (unit: mm).*

temperature using a servohydraulic system to an initial crack length of 21.6 mm. The final 0.635 mm of precrack extension was obtained at a ΔK level of 4.45 MPa$\sqrt{m}$, well below the K-level during creep crack growth testing. Following precracking, the specimens were side grooved 10% of the thickness on each side of the crack plane. The creep crack growth tests were performed using dead-weight lever-type creep machines to apply a constant load, and the test temperature was controlled to within ±1°C. The load-line deflection was continuously monitored with time using a DCDT extensometer attached to knife blades inserted into the notch. Electrical leads were attached to the specimen to monitor the crack length by the d-c potential drop method, as shown in Fig. 4 [*12,13*]. Signals from the extensometer and potential drop were logged on a strip chart recorder throughout the test. Following the tests, crack length versus time and deflection versus time plots were created, and the crack growth rates and deflection rates were determined using the secant (point to point) method [*12*].

TABLE 1—*Summary of creep deformation tests.*

Specimen	Stress Level, MPa	Time, h
CD-4	317	45
CD-5	324	60
CD-6	283	1250
CD-8	296	750

Results and Discussion

Creep Deformation

Four creep deformation tests were performed at different stress levels to evaluate the creep behavior of 2519 at the test temperature. A summary of test results is presented in Table 1. Figures 5 and 6 plot the creep strain behavior of the four specimens as a function of time. The creep strain at fracture in all specimens was less than 2.0%, which is consistent with the creep-brittle characteristics of this material. Steady-state creep dominates the creep response of the material in terms of the fraction of total time to failure, but the primary creep region, which is present for less than 1% of the total failure time, contributes significantly to the overall creep strain.

A useful constitutive equation employed to describe the creep strain rate as a function of stress, σ, and accumulated strain, ε, is given by [*14*]:

$$\dot{\varepsilon}_c = A_1\varepsilon^{-p}\sigma^{n_1(1+p)} + A\sigma^n + A_3\sigma^{n_3}(\varepsilon - A\sigma^n)^{p_3} \tag{1}$$

The first term in the equation represents the contribution to the creep strain rate from primary creep, where A_1, p, and n_1 are material constants. The second term in the equation represents the secondary (or steady-state) creep regime with A and n as constants, and the last term in the equation describes the tertiary creep regime, where A_3 and n_3 are regression constants. These

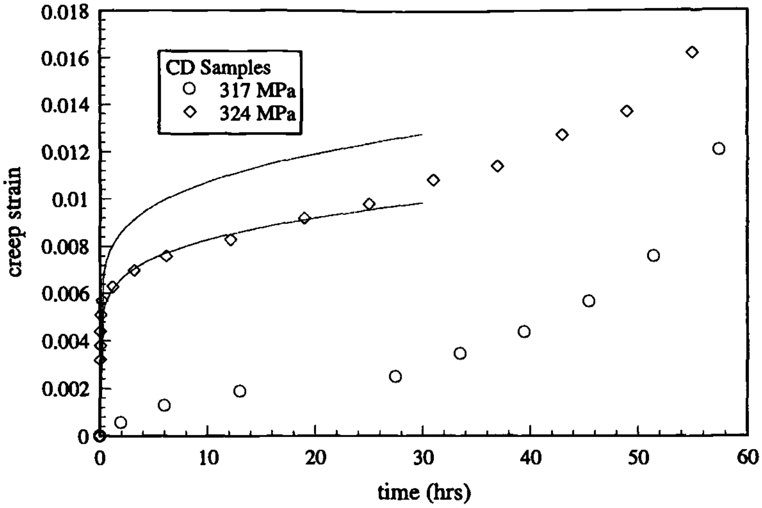

FIG. 5—*Creep strain versus time for creep deformation specimens CD-4 and CD-5·at 135°C with fitted creep data from Eq 3.*

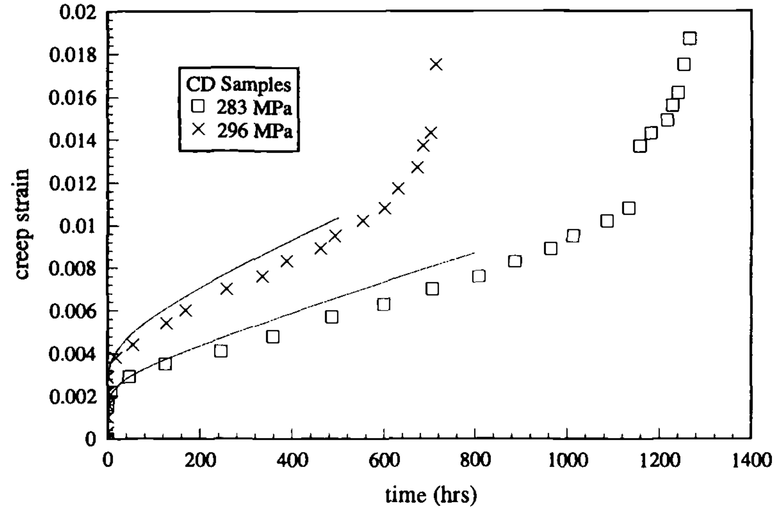

FIG. 6—*Creep strain versus time for creep deformation specimens CD-6 and CD-8 at 135°C with fitted creep data from Eq 3.*

creep constants (except for tertiary creep) are provided in Table 2. In comparison with creep constants for typical creep-ductile materials [*4,15*], aluminum 2519 appears to have an unusually high value for the steady-state creep exponent. These results, however, are consistent with data on other high-temperature, creep-brittle aluminum alloys such as 2219 [*16,17*], for which $n = 24$ and $A = 1.2 \times 10^{-63}$ at 175°C, and aluminum 8009 [*9*].

Though this constitutive equation accurately models the behavior of the secondary region, the equation yields a poor fit to the primary creep regime, especially at the high stress levels. Because the model more reliably describes a gradual accumulation of primary creep strain, the model cannot account for the rapid primary creep strain accumulation in a short time interval (less than 10 h) as observed in this material. To overcome this limitation, the Garafalo equation [*18*], Eq 2, was employed to fit the primary creep data:

$$\varepsilon_c = A_1''\sigma^{n_1'}(1 - e^{-mt}) + A\sigma^n t \qquad (2)$$

where A_1'', n_1', and m are regression constants, and all other terms have their previous meaning as defined in Eq 1. The regression constants for the Garafalo equation are presented in Table

TABLE 2—*Primary and secondary creep constants (SI units) for Eq 1.*

Consant	Value
PRIMARY CREEP CONSTANTS	
n_1	13
p	1.404
A_1	1.98E-86
SECONDARY CREEP CONSTANTS	
n	25
A	1.08E-67

TABLE 3—*Primary and secondary creep constants (SI units) for the Garafalo equation.*

Constant	Value
PRIMARY CREEP CONSTANTS	
n_1'	1.49
m	0.50
A_1''	5.248E-7
SECONDARY CREEP CONSTANTS	
n	25
A	1.08E-67

3. Another approach for modelling creep deformation is to add an additional steady-state term to Eq 1 such that:

$$\dot{\varepsilon}_c = A_1 \varepsilon_{pc}^{-p} \sigma^{n_1(1+p)} + A\sigma^n + A'\sigma^{n'} + A_3\sigma^{n_3}(\varepsilon - A\sigma^n)^{p_3} \tag{3}$$

The values for the creep constants in this model are provided in Table 4. The fitted creep data utilizing Eq 3 are displayed in Figs. 5 and 6 along with the experimental data. On initial inspection, this equation apparently fails to model the entire creep behavior of the deformation test performed at 317 MPa (specimen CD-4). This poor fit, however, is a result of an experimental error rather than a deficiency in the constitutive model itself. During the initial stages of the test, a data-recording error occurred that essentially caused the primary creep regime to be missed. Equation 3, however, accurately models the steady-state creep behavior of this specimen. Of the three models discussed, Eq 3 provides the best fit to the experimental data and was, therefore, selected as the appropriate constitutive equation.

Creep Crack Growth

Five constant load creep crack growth tests were performed at various initial *K*-levels to evaluate the creep crack growth behavior of aluminum 2519. Four specimens had a nominal thickness of 22.1 mm and one had a thickness of 6.35 mm. A summary of test conditions and durations is presented in Table 5. Also presented in this table are the final crack lengths of each

TABLE 4—*Primary and secondary creep constants (SI units) for Eq 3.*

Constant	Value
PRIMARY CREEP CONSTANTS	
n_1	11.82
p	6.95
A_1	7.13E-255
SECONDARY CREEP CONSTANTS	
n	21
A	2.32E-58
n'	5.33
A'	4.77E-19

TABLE 5—*Creep crack growth tests.*

Specimen No.	Thickness, mm	K-Level, MPa$\sqrt{m}$	Failure time, h
BCH-1	6.35	18.67	740-i*
BCH-4	22.1	16.51	354
BCH-5	22.1	18.73	31
BCH-6	22.1	18.73	104
BCH-7	22.1	17.60	144-i*

Specimen No.	Initial Crack Length, mm	Final Length Potential, mm	Final Length Comp., mm
BCH-1	22.20	31.12	30.43
BCH-4	22.53	26.42	31.50
BCH-5	22.56	28.45	32.51
BCH-6	22.50	27.18	27.18
BCH-7	22.58	26.51	29.77

NOTE: *i indicates that test was interrupted before failure.

specimen determined by both the d-c potential drop method and the change in elastic compliance. Because rapid fracture often occurred before the tests could be interrupted to determine the crack extension, visual measurements of the final crack lengths are available only for specimens BCH-1 and BCH-7. These visually measured lengths are 32.1 and 27.0 mm, respectively. Though the d-c potential drop method appears to be theoretically more accurate and reliable compared to the compliance technique, fluctuations in the thermal voltage limit its crack extension resolution for 2519 [*17*]. Due to the high electrical conductivity of the test material, unusually high fluctuations in the thermal voltage were observed. In many instances the fluctuations were comparable in magnitude to the d-c potential changes due to crack extension; therefore, to unambiguously determine the crack length, the thermal voltage had to be measured at all points of crack length calculation. Since the thermal voltage is determined by momentarily removing the input current, continuously monitoring the crack length by the potential drop method was impossible. In comparison, the major advantage of the elastic compliance method was the ability to continuously monitor the load-line deflection with time; therefore, the crack length can be calculated at any point throughout the test duration. In our research, both techniques were used to measure crack extension, and crack growth rates were also calculated using both measurements for all tests.

To investigate the potential for correlation between the crack growth rate, da/dt, and K for 2519, the following equation was considered:

$$\frac{da}{dt} = C'K^q \tag{4}$$

where C' and q are regression constants. The stress intensity factor, K, is calculated from the crack lengths using Eq 5:

$$K = \frac{Pf\left(\frac{a}{W}\right)}{B_N W^{1/2}} \tag{5}$$

$$\text{where } B_N = \sqrt{B_{sg}B}$$

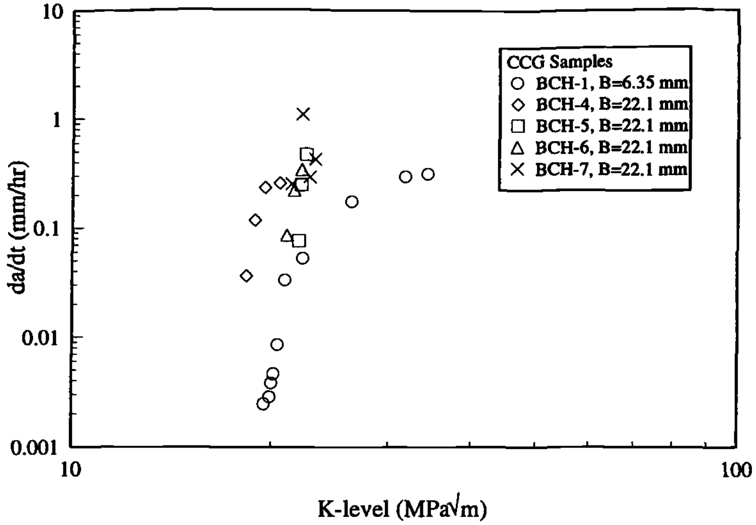

FIG. 7—*Correlation with* K *using the d-c potential drop method for crack length measurement.*

where P is the load, W is the specimen width, $f(a/W)$ is a geometric factor, B_N is the net specimen thickness, B is the original specimen thickness, and B_{sg} is the specimen thickness in the plane of the side groove [*19*]. Figures 7 and 8 plot the crack growth rate against K using the d-c potential drop data and the elastic compliance data, respectively. These figures demonstrate that an experimental correlation does exist between the creep crack growth rate and K, a result consistent with the creep-brittle characteristics of this material. A reasonable comparison exists between the data from the two crack extension measurement techniques, although there is much more scatter in the data from the compliance method. The electric potential drop

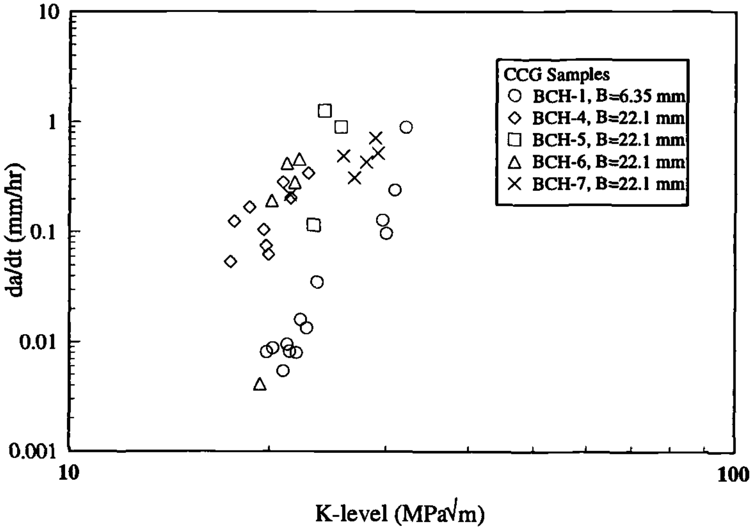

FIG. 8—*Correlation with* K *using the change in elastic compliance for crack length measurement.*

method also shows considerable scatter even without considering the thickness effect. It appears that pronounced thermal fluctuations due to the low electrical resistivity of the material are the source of this unusually high scatter of data. This problem may be resolved by using the switching d-c potential technique, which will separate the signal from the noise.

The correlation between the creep crack growth rate and C_t was also investigated. Since, 2519 displays limited creep deformation at 135°C, the accumulation of creep strain remains confined to a small region at the crack tip. Under these small-scale creep conditions, the following equation is used to calculate C_t [*2*].

$$(C_t)_{ssc} = \frac{P\dot{V}_c}{B_N W}(F'/F) \tag{6}$$

where

$$F = \left(\frac{K}{P}\right)B_N W^{1/2} \qquad F' = \frac{dF}{d\left(\frac{a}{W}\right)} \tag{7}$$

$\dot{V}_c$ is the creep deflection rate, which is determined by partitioning the entire deflection rate into contributions from creep deformation, elastic deformation ($\dot{V}_e$), and plastic deformation ($\dot{V}_p$) [*12,15,20*], i.e.,

$$\dot{V} = \dot{V}_c + \dot{V}_e + \dot{V}_p \tag{8}$$

such that

$$\dot{V}_c = \dot{V} - \frac{\dot{a}B}{P}\left[\frac{2K^2}{E} + (m + 1)J_p\right] \tag{9}$$

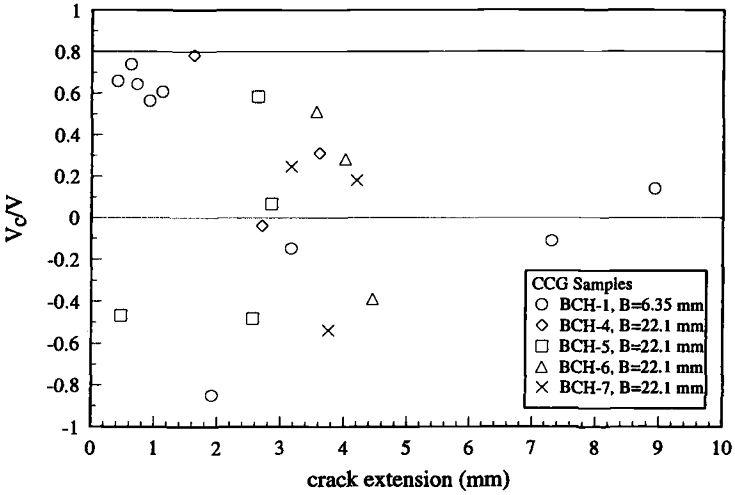

FIG. 9—*Change in normalized creep deflection rate with crack extension.*

The plastic contribution in these specimens was found to be negligible. Figure 9 plots the normalized creep deflection rate as a function of the crack extension (determined from the potential drop method) and demonstrates that, for all creep crack growth tests, the creep contribution is less than 80% of the total deflection rate. Also, as the crack length increases, the creep contribution declines as the crack growth rate increases and the elastic fracture regime is approached. Equation 8 is more accurate when the creep deflection rate dominates the total deflection rate. Thus, for creep contributions less than 80% of the total deflection, the equation lacks precision as the elastic term becomes significant [*12*]. Since the total deflection rate is experimentally measured and the elastic term is analytically determined, Eq 8 can yield negative creep deflection rates if the experimental error in the total deflection rate is significant, as seen in Fig. 9; however, the numerical analysis presented in the second part of this paper demonstrates that negative creep deflection rates are possible, especially during the early stages of crack growth.

Negative creep deflection rates lead to negative C_t values, which have no clear physical interpretation; therefore, the creep crack growth rate data displayed a lack of experimental correlation with C_t, which is consistent with creep-brittle behavior. The creep crack growth rate and the rate of creep strain accumulation in the crack tip region are comparable. Under these conditions, the assumption that the crack remains essentially stationary within an expanding creep zone is no longer valid. The movement of the crack perturbs the crack tip stress fields, invalidating the Riedel-Rice formulation [*21*]. The small-scale creep region remains embedded within a larger K-controlled zone, and the stress amplitudes remain effectively characterized by K. Therefore, K displays a unique correlation with the creep crack growth rate and is the appropriate crack tip parameter for characterizing creep crack growth in aluminum 2519-T87 at the test temperature. The unique correlation between da/dt and K implies the establishment of steady-state conditions at the crack tip in which the crack tip stress is only a function of position in front of the advancing crack tip. The second part of this paper examines the experimental results presented above through growing crack finite element analyses and suggests guidelines for K-controlled crack growth.

Mechanisms of Fracture

Examination of the fracture surfaces for all specimens revealed two distinct fracture morphologies, an intergranular region following the precrack and a transgranular region following the intergranular regime. Figure 10 contains micrographs taken of the fracture surface of specimen BCH-1 and displays the two observed morphologies. A main characteristic of the intergranular fracture region is creep cavitation along grain boundaries. Stereomicroscopy [*22*] revealed that, in general, only those grain facets oriented perpendicular to the applied load contain creep cavitation. Those facets not oriented perpendicular to the load appear smooth and did not exhibit cavitation. This result is consistent with the constrained cavity creep crack extension model outlined by Wilkinson and Vitek [*23*]. In this model, cavities nucleate and grow on grain boundaries ahead of the crack tip that are perpendicular to the applied load. Crack extension occurs when the cavities have grown to a sufficient size and coalesce, thus advancing the crack. Table 6 contains the lengths of the intergranular regions for the creep crack growth specimens.

Characteristics of the transgranular region not only include creep cavitation, but also microvoid coalescence due to ductile rupture. Elements of creep cavitation and ductile rupture appearing within the same region of the fracture surface suggest that the transgranular fracture surface is a result of complementary mechanisms of crack extension. As creep cavities grow and coalesce, the unbroken ligaments between them fail by ductile rupture, causing the crack to advance. Thus, crack extension by creep cavity coalescence may be the dominant mechanism

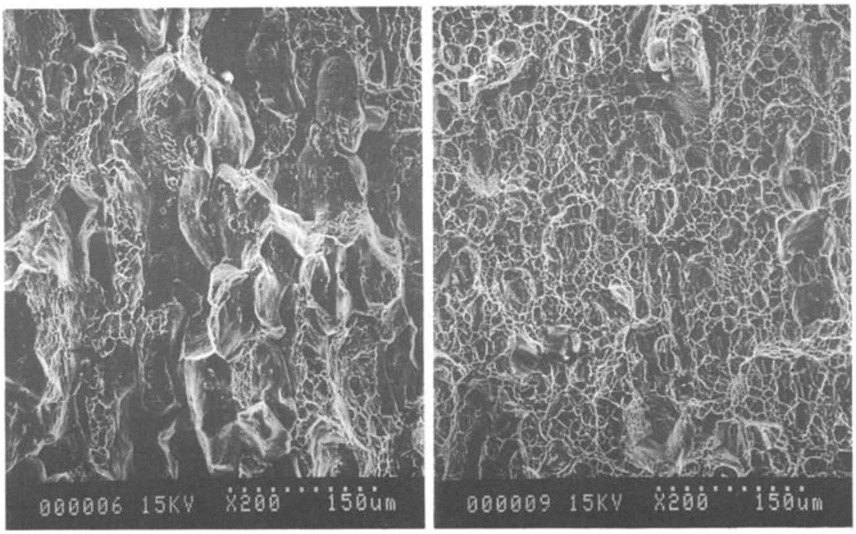

FIG. 10—*Intergranular* (left) *and transgranular* (right) *fracture surfaces for creep crack growth specimen BCH-1.*

in the intergranular regime and by microvoid coalescence associated with ductile tearing in the transgranular regime. The transition between intergranular and transgranular was found to occur at a critical K-level between 18 and 20 $\text{MPa}\sqrt{\text{m}}$. This result will be discussed in more detail in a later paper.

Incubation Period

Creep crack growth studies have shown that crack extension occurs following a specific time period, which has been termed incubation time. Incubation models based on ductility exhaustion and creep cavitation concepts have been developed [*24,25*]; however, incubation time currently lacks a precise definition among researchers since it is unknown if the crack actually remains stationary during this period or if the crack grows at an undiscernibly slow rate. In this research, an operational definition of incubation time was utilized. With a crack extension resolution of 0.1 mm, the initial incubation time was defined as the point at which an increase in the d-c potential drop output could be discerned. This definition is similar to that used by Bensussan

TABLE 6—*Lengths of intergranular crack extension regions.*

Specimen No.	Thickness, mm	Initial K-Level, $\text{MPa}\sqrt{\text{m}}$	Intergranular Crack Extension, mm
BCH-1	6.35	18.67	3.71
BCH-4	22.1	16.51	3.33
BCH-5	22.1	18.73	2.18
BCH-6	22.1	18.73	0.51
BCH-7	22.1	17.60	1.07

in which the incubation time is related to a percentage increase in the potential drop output [*17*].

If a critical amount of creep damage must accumulate ahead of the crack tip before crack growth initiates, the incubation time may be related to a critical creep zone size, r_c^*. As the initial *K*-level increases, the incubation period required to reach this creep zone size would decrease, a conclusion consistent with experimental observations. For steady-state creep conditions, the creep zone size is given by:

$$r_c = \frac{1}{2\pi}\left(\frac{(n+1)^2}{2n\alpha_n^{n+1}}\right)^{\frac{2}{n-1}}(EAt)^{\frac{2}{n-1}}K^2F_{cr}(\theta) \tag{10}$$

where $F_{cr}(\theta)$ is an angular function, α_n^{n+1} is approximately 0.69 for $3 < n < 13$, A and n are the steady-state creep constants, t is the time, and E is the modulus. Assuming that a critical creep zone size does exist, Eq 10 predicts the following correlation between the incubation time, t_i, and K for steady-state creep conditions:

$$t_i = \beta K^{1-n} \tag{11}$$

where β depends on material properties and the critical creep zone size. Creep deformation tests have demonstrated the importance of primary creep in the creep response of 2519; therefore, the creep zone size is also considered in terms of primary creep, i.e.

$$r_c = \frac{K^2}{2\pi}\left[\frac{I_{n_1}E}{2\pi(1-\nu^2}\right]^{\frac{2}{n_1-1}}[(1+n_1)(1+p)A_1]^{\frac{2}{(1+p)(n_1-1)}}t^{\frac{2}{(1+p)(n_1-1)}}\tilde{r}_c(\theta) \tag{12}$$

where $\tilde{r}_c(\theta)$ is an angular function. Equation 12 yields the following relationship:

$$t_i = \eta K^{-(1+p)(n_1-1)} \tag{13}$$

where η depends on material properties and the critical creep zone size.

Figure 11 plots the log of incubation time, utilizing the operational definition as a function of the log of the stress intensity factor and reveals a correlation between the two parameters, as suggested by Eqs 11 and 12. The data from specimen BCH-1, however, does not correlate with the remaining tests and demonstrates the dependence of the correlation on specimen thickness. This effect is not fully understood, but the plane stress conditions in specimen BCH-1 are believed to be a contributing factor. The correlation of the remaining data, however, does support the hypothesis that a critical creep zone size controls the initiation of crack growth. A regression fit to the data yields a slope of −13.84. Equations 11 and 13 predict the value of the slope as −24 and −29, respectively. Undiscernibly slow crack growth rates may contribute to this discrepancy; however, with only four data points available to study the incubation phenomenon, the regression is not rigorous. Tables 7 and 8 present the calculated creep zone sizes at which crack initiation occurs for secondary and primary creep conditions. These tables demonstrate that a critical creep zone size does exist and that the incubation time is simply the time required for the creep zone to reach this critical size. Creep zone sizes evaluated through numerical analysis show good agreement with the experimentally determined values.

Considering Figs. 7 and 11 together underscores the engineering significance of the incubation time. Figure 7 plots the correlation between the creep crack growth rate and *K*. The steep slope of the correlation indicates that the crack growth rate increases rapidly for very small increases in *K*; therefore, the *K*-range over which creep crack extension occurs prior to

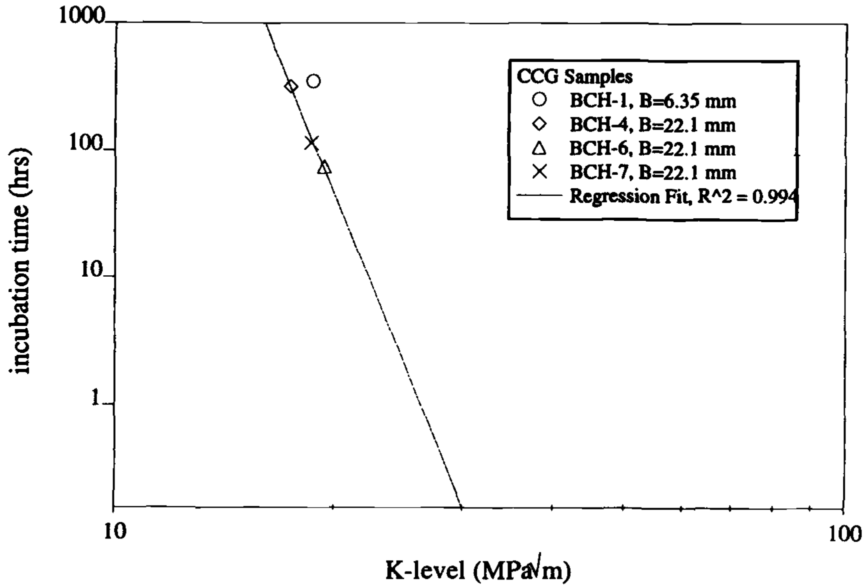

FIG. 11—*Correlation of the incubation time with the stress intensity factor.*

specimen fracture is quite small. Once the crack begins to grow, the test material cannot sustain stable crack extension for a significant duration before failure occurs, a characteristic that limits the engineering application of the material. Figure 11, however, indicates that the incubation period required prior to crack extension quickly increases for small decreases in the initial *K*-level. For very low *K*-levels, the incubation time may be so large that the crack remains effectively stationary within the testing time frame. Total time to failure, therefore, must be considered as a combination of the incubation period prior to crack initiation and the crack growth period following crack initiation. Evaluation of the test material for engineering applications cannot rely solely on the *da/dt-K* correlation, but must take into account the time required to initiate creep crack growth.

Conclusions

To characterize the creep crack growth behavior of aluminum 2519, several creep deformation and creep crack growth tests were performed at 135°C. Microscopy of fracture surfaces revealed the mechanisms controlling creep crack growth, and the phenomenon of crack incu-

TABLE 7—*Critical creep zone size in steady-state creep.*

Specimen	*K*-Level, MPa$\sqrt{m}$	Critical Creep Zone Size, mm
BCH-1	18.67	0.70
BCH-4	16.51	0.60
BCH-6	18.73	0.66
BCH-7	17.60	0.63

TABLE 8—*Critical creep zone size in primary creep.*

Specimen	K-Level, MPa$\sqrt{m}$	Critical Creep Zone Size, mm
BCH-1	18.67	0.56
BCH-4	16.51	0.48
BCH-6	18.73	0.54
BCH-7	17.60	0.51

bation was investigated. Based on the results and observations, the following conclusions are drawn:

1. Aluminum 2519 displayed limited creep ductility at 135°C. Though the material did creep, the total creep strain at failure was less than 2% for all tests. This behavior is consistent with a creep-brittle material.
2. At 135°C, creep crack growth rates correlate reasonably well with the stress intensity factor, K. No experimental correlation was found between da/dt and C_t.
3. Creep crack growth rates are very high in aluminum 2519 following incubation. Figure 5 demonstrates that once the crack has initiated (utilizing the operational definition), the time to failure is very short (on the order of tens of hours) due to the steep correlation between the creep crack growth rate and K.
4. Two fracture morphologies, intergranular and transgranular, were revealed for the test material at 135°C.
5. Incubation time in aluminum 2519 appeared to exhibit a correlation with the stress intensity factor (utilizing the operational definition). Incubation time as well as crack propagation time must be considered together to properly evaluate the material for engineering applications.

References

[*1*] Landes, J. D. and Begley, J. A., "Mechanics of Crack Growth," *Mechanics of Crack Growth, ASTM STP 590*, American Society for Testing and Materials, West Conshohocken, PA, 1976, pp. 128–148.

[*2*] Saxena, A., "Creep Crack Growth Under Non-Steady-State Conditions," *Fracture Mechanics: Seventeenth Volume, ASTM STP 905*, American Society for Testing and Materials, West Conshohocken, PA, 1986, pp. 185–201.

[*3*] Saxena, A., "Creep Crack Growth in High Temperature Ductile Materials," *Engineering Fracture Mechanics*, Vol. 40, No. 4, 1991, pp. 721–736.

[*4*] Saxena, A. and Liaw, P. K., "Remaining Life Estimations of Boiler Pressure Parts-Crack Growth Studies," Final Report, EPRI Contract RP 2253-7, EPRI, Palo Alto, CA, 1986.

[*5*] Hutchinson, J. W., *Journal of the Mechanics and Physics of Solids*, Vol. 16, 1968, pp. 13–31.

[*6*] Rice, J. R. and Rosengren, G. F., *Journal of the Mechanics and Physics of Solids*, Vol. 16, 1968, pp. 1–12.

[*7*] Bensussan, P. L. and Pelloux, R. M., "Creep Crack Growth in 2219-T851 Aluminum Alloy: Applicability of Fracture Mechanics Concepts," *Advances in Fracture Research, ICF6*, S. R. Valluri et al., Eds., Pergamon Press, Oxford, England, Vol. 3, 1984, pp. 2167–2179.

[*8*] Bensussan, P. L., Jablonski, D. A., and Pelloux, R. M., "A Study of Creep Crack Growth in 2219-T851 Aluminum Alloy Using a Computerized Testing System," *Metallurgical Transactions A*, Vol. 15A, 1984, pp. 107–120.

[*9*] Jones, K. A., "The Creep Behavior of Aluminum Alloy 8009," M.S. thesis, School of Materials Science and Engineering, Georgia Institute of Technology, Atlanta, GA, 1993.

[*10*] Dogan, B., Saxena, A., and Schawlbe, K. H. "Creep Crack Growth in Creep-Brittle Ti-6242 Alloys," *Materials at High Temperature*, Vol. 10, 1992, pp. 138–143.

[*11*] Alcoa Aerospace Technical Fact Sheet, Alloy 2519-T87, Aluminum Company of America: Sheet and Plate Division, 1990.

[*12*] Test Method for Measurement of Creep Crack Growth Rates in Metals, ASTM E 1457-92, American Society for Testing and Materials, West Conshohocken, PA, 1992.

[*13*] Johnson, H. H., *Materials Research and Standards*, Vol. 5, No. 9, 1965, pp. 442–445.

[*14*] Riedel, H., *Journal of the Mechanics and Physics of Solids*, Vol. 29, 1981, pp. 35–49.

[*15*] Saxena, A., ''Evaluation of Crack-Tip Parameters for Characterizing Creep Crack Growth: Results of the ASTM Round-Robin Programme,'' *Materials at High Temperatures*, Vol. 10, 1992, pp. 79–91.

[*16*] Bensussan, P. et al. ''Creep Crack Initiation and Propagation: Fracture Mechanics and Local Approach,'' *Journal of Pressure Vessel Technology*, Vol. 110, 1988, pp. 42–50.

[*17*] Bensussan, P., Cailletaud, G., Pelloux, R., and Pineau, A., ''Fracture Mechanics and Continuum Damage Applied to Creep Crack Initiation and Creep Crack Growth in 2219-T851 Aluminum Alloy,'' *The Mechanisms of Fracture*, V. S. Goel, E., ASM, Metals Park, OH, 1986, pp. 587–595.

[*18*] Garafalo, F., ''Properties of Crystalline Solids,'' *Properties of Crystalline Solids, ASTM STP 283*, American Society for Testing and Materials, West Conshohocken, PA, 1960, p. 82.

[*19*] Broek, D., *Elementary Engineering Fracture Mechanics*, Kluwer Academic Publishers, London, 1991, pp. 1–32.

[*20*] Saxena, A. and Landes, J. D. in *Advances in Fracture Research*, ICF6, Proceedings of the 6th International Congress on Fracture, 1985, p. 3977.

[*21*] Riedel, H. and Rice, J. R., ''Tensile Cracks in Creeping Solids,'' *Fracture Mechanics: Twelfth Conference, ASTM STP 700*, American Society for Testing and Materials, West Conshohocken, PA, 1980, pp. 112–130.

[*22*] Goldman, J. I. et al., *Scanning Electron Microscopy and X-ray Microanalysis*, Plenum Press, New York, 1984, pp. 143–146.

[*23*] Wilkinson, D. S. and Vitek, V., *Acta Metallurgica*, Vol. 30, 1982, p. 1723.

[*24*] Austin, T. S. P. and Webster, G. A., ''Prediction of Creep Crack Growth Incubation Periods,'' *Fatigue and Fracture of Engineering Materials and Structures*, Vol. 15, No. 11, 1992, pp. 1081–1090.

[*25*] Bensussan, P., ''A Critical Review of the Application of Global and Local Approaches to Creep Crack Initiation and Growth,'' *Proceeding of MECAMAT*, Vol. 3, pp. 1–17.

David E. Hall,[1] *B. Carter Hamilton,*[2] *David L. McDowell,*[3] *and Ashok Saxena*[4]

Creep Crack Growth Behavior of Aluminum Alloy 2519: Part II—Numerical Analysis

REFERENCE: Hall, D. E., Hamilton, B. C., McDowell, D. L., and Saxena, A., "**Creep Crack Growth Behavior of Aluminum Alloy 2519: Part II—Numerical Analysis,**" *Elevated Temperature Effects on Fatigue and Fracture, ASTM STP 1297,* R. S. Piascik, R. P. Gangloff, and A. Saxena, Eds., American Society for Testing and Materials, 1997, pp. 19–36.

ABSTRACT: The experimental analysis of high temperature fracture in Aluminum Alloy 2519-T87 presented in Part I of this paper highlighted the creep-brittle fracture characteristics of the material and showed reasonable correlation of crack growth rates with the stress intensity factor K. Part II continues this investigation numerically using growing crack finite element analyses. Experimentally observed crack growth histories of four aluminum 2519-T87 compact specimens are enforced by controlling the rate of release of finite element nodes along the crack growth path to gain insight into the relation of the crack tip fields to far field fracture parameters and to crack growth rates. A variable time-step, nodal-release algorithm is presented to model the high strain rates that occur during the initial stages of crack growth. The numerical results indicate an initial transient period of crack growth followed by a quasi-steady-state crack growth regime in which the crack tip fields change slowly with increasing crack length. Transition of crack growth to the quasi-steady-state regime, where similitude and small-scale creep conditions roughly exist, is given by a transition time t_g that depends on the crack growth history and material properties. Excellent correlation of the stress intensity factor K with the crack growth rates is observed after time t_g. Experimental difficulties in measuring the creep component of the load-line deflection rate are also discussed.

KEYWORDS: creep, crack, propagation, aluminum, creep-brittle, fracture, finite element analysis

High temperature quasi-static fracture may be classified as either creep-ductile or creep-brittle depending on the extent of creep deformation that accompanies crack growth. Creep-ductile fracture is characterized by crack growth rates that are slow compared to the rate of expansion of the creep zone, resulting in extensive accumulation of creep deformation in the cracked body. In contrast, creep-brittle fracture is characterized by crack growth rates comparable to the rate of expansion of the creep zone, resulting in development of a "ribbon-like" creep zone along the crack growth path.

Time-dependent fracture research has leaned heavily toward understanding the fracture behavior of creep-ductile materials. Recently, the high-temperature fracture characteristics of

---

[1] Assistant professor, Department of Mechanical and Industrial Engineering, Louisiana Tech University, Ruston, LA 71272.

[2] Graduate research assistant, School of Materials Science and Engineering, Georgia Institute of Technology, Atlanta, GA 30332.

[3] Professor, The George W. Woodruff School of Mechanical Engineering, Georgia Institute of Technology, Atlanta, GA 30332.

[4] Professor and chair, School of Materials Science and Engineering, Georgia Institute of Technology, Atlanta, GA 30332.

several creep-brittle materials have been investigated to address the potential use of these materials in critical applications [*1–6*]. These investigations have generally concluded that the stress intensity factor K is more appropriate than time-dependent fracture parameters for correlating crack growth rates in creep-brittle materials. While it appears that the issues surrounding the choice of the optimum correlating parameters for characterizing creep crack growth in creep-ductile materials is reaching a stage of consensus, much more understanding of the creep crack growth behavior in creep-brittle materials is needed [*1*]. The objective of this paper is to gain insight into the relation of the stress intensity factor K to crack growth rates in creep-brittle materials using growing crack finite element analyses. Moreover, transition times describing the onset of quasi-steady-state and K-dominated crack growth conditions must be developed.

Asymptotic Solutions for Small-Scale Power Law Creep

Consider a Mode I crack at high temperature that deforms according to an elastic-power law creep constitutive relation $\dot{\varepsilon} = \dot{\sigma}/E + A\sigma^n$. Here, $\dot{\varepsilon}$ is the strain rate, $\dot{\sigma}$ is the stress rate, E is the elastic modulus, and A and n are creep constants. The initial response of the body will be purely elastic such that the stress field is characterized by the stress intensity factor K according to standard solutions. The initially high stresses near the crack tip result in growth of a creep zone in which the accumulated creep strains dominate the elastic strains. The creep zone is surrounded by an annular region where the singular elastic fields remain valid, so that small-scale creep conditions exist. Riedel and Rice [*7*] and Bassani and McClintock [*8*] addressed crack tip stress fields under small-scale creep and showed that the amplitude of the asymptotic crack tip stress field is given by the $C(t)$ integral, i.e.,

$$\sigma_{ij} = \left(\frac{C(t)}{I_n A r}\right)^{\frac{1}{1+n}} \tilde{\sigma}_{ij}(\theta,n) \tag{1}$$

where t is time, I_n is an integration constant, $\tilde{\sigma}_{ij}(\theta,n)$ is an angular function identical to the corresponding Hutchinson, Rice, and Rosengren (HRR) angular function [*9,10*], and r and θ are crack tip polar coordinates. For small-scale power law creep, $C(t)$ is given as [*7,8*]

$$C(t) = \frac{K^2(1 - \nu^2)}{E(1 + n)t} \tag{2}$$

for plane strain where ν is Poisson's ratio. For stationary cracks, this relaxing stress field remains valid until the onset of extensive creep conditions where $C(t)$ evolves towards a value known as C^* [*11,12*].

The creep zone boundary can be defined as the locus of points where the effective stress predicted by the elastic solution is equal to the effective stress of the HRR solution in Eq 1. Along $\theta = 0°$, the radius of the creep zone is [*7*]

$$r_c(\theta = 0°) = \frac{1}{2\pi} K^2 \left(\frac{EA(n + 1)I_n t}{2\pi(1 - \nu^2)}\right)^{\frac{2}{n-1}} \left(\frac{1 - 2\nu}{\tilde{\sigma}_e(\theta = 0°)}\right)^{\frac{2(n+1)}{n-1}} \tag{3}$$

where $\tilde{\sigma}_e(\theta = 0°)$ is the HRR angular function for effective stress along $\theta = 0°$.

During crack growth, the stresses and elastic strains near the moving tip will be elevated due to the instantaneous elastic response of the material so that the creep strains near the tip no longer dominate the elastic strains. Hui and Riedel [13] showed that the competing effects of stress elevation due to crack growth and stress relaxation due to creep give rise to a field with an amplitude related to the crack growth rate (for $n > 3$), i.e.,

$$\sigma_{ij} = \alpha_n \left(\frac{\dot{a}}{AEr} \right)^{\frac{1}{n-1}} \bar{\sigma}_{ij}(\theta,n) \tag{4}$$

where $\bar{\sigma}_{ij}(\theta,n)$ is an angular function and α_n depends on n and is approximately unity for plane strain conditions. This field is commonly referred to as the Hui-Riedel (HR) field. The amplitude of the HR field is completely determined by the crack growth rate and is independent of loading and growth history.

Hawk and Bassani [14] demonstrated that the near tip fields of growing cracks can be well approximated by a straightforward "nesting" of singular crack tip solutions (HR, HRR, and K). They found that the HRR-type field dominates at short times and/or under very slow crack growth rates, while the HR field dominates as steady-state crack tip stresses are approached (under small-scale creep conditions). Hui [15] also indicated that the fields can be nested and analytically showed that the region of dominance of the HR field is exceedingly small when the crack growth rate is much smaller than the creep zone expansion rate.

The asymptotic fields mentioned above are valid only for a material deforming according to an elastic-power law creep constitutive relation. Similar asymptotic fields also exist for materials that deform according to an elastic-primary creep constitutive relation. Riedel [16] derived the form of these crack tip fields for stationary cracks under small-scale and extensive creep conditions, while Chang et al. [17] showed that the amplitude of the fields for growing cracks under elastic-primary creep conditions is given by the instantaneous rate of crack growth (HR-type fields).

Numerical Procedure

Nodal Release Algorithm

Finite element analyses are carried out using a small strain code developed by Leung and McDowell [18] based on an implicit trapezoidal time-stepping scheme. Crack growth is simulated by releasing a sequence of finite element nodes along the crack growth path at a specified rate using an algorithm similar to those of Hawk and Bassani [14] and Moyer and Liebowitz [19]. As the crack grows from one nodal position to the next, the net force on the node to be released is gradually relaxed over a number of time steps. Instead of releasing the node over a prescribed number of force decrements, an opening displacement is imposed on the node to ensure that the rate of force release due to crack growth is faster than the rate of force relaxation due to creep. Application of these displacement increments ensures that the crack immediately begins to open. Increments of displacement are continued (based on the overall y-direction displacement of previously released nodes) until the net force on the node is reduced to a fraction of its original value or until a specified time is reached. The remaining force on the node is then reduced to zero by applying force decrements over a number of time steps.

The new variable time-step nodal-release approach devised here selects a new time step for each displacement increment or load decrement according to the most conservative of three time-stepping criteria. First, the effective creep strain expected to be accumulated at any gauss point during the current time step should be less than or equal to some fraction (τ) of the total effective strain at that gauss point, so that

$$\Delta t_{\max} \leq \tau\left(\frac{\bar{\varepsilon}}{\dot{\bar{\varepsilon}}_c}\right) \tag{5}$$

where $\bar{\varepsilon}$ is the total effective strain and $\dot{\bar{\varepsilon}}_c$ is the effective creep strain rate. Another useful limit can be imposed to avoid oscillatory solutions that often occur if the time step changes too abruptly, i.e.,

$$\Delta t_{\max} \leq k\ \Delta t_{\text{old}} \tag{6}$$

where k is a specified constant and Δt_{old} is the previous time step length. The third limit on the time step requires that a minimum number of time steps be completed during the release of a node according to

$$\Delta t_{\max} \leq \frac{t_{\text{end}} - t_{\text{start}}}{N + M} \tag{7}$$

where N and M are guesses for the number of displacement increments and load decrements, respectively, and t_{start} and t_{end} are the times at which release of the current crack tip node begins and ends, respectively.

After choosing the minimum of the $\Delta t_{\max}$ values in Eqs 5 to 7 above, the displacement increment or load decrement is computed based on this time step. Displacements are prescribed until the remaining reaction at the crack tip node is less than 10% of the initial reaction *OR* until a specified amount of time (t_{switch}) has elapsed, where

$$t_{\text{switch}} = (t_{\text{end}} - t_{\text{start}})\left(\frac{N}{N + M}\right) \tag{8}$$

Here, t_{switch} is the maximum period of time during which displacements are incremented. Displacement increments are given as

$$\Delta V = V_{\text{ref}}\left(\frac{\Delta t}{t_{\text{switch}}}\right) \tag{9}$$

where V_{ref} is the y-displacement at the node behind the crack tip at $t = t_{\text{start}}$. When the reaction at the node has been reduced to 10% of its initial value or the y-displacement at the crack tip node is equal to V_{ref}, the remaining load on the node is reduced to zero over two or more time steps. The load decrements at the crack tip, denoted as ΔR_y, are given by

$$\Delta R_y = -R_y\left(\frac{\Delta t}{t_{\text{end}} - t + \Delta t}\right) \tag{10}$$

where R_y is the *remaining* nodal reaction. When $t = t_{\text{end}}$, Eq 10 shows that the remaining nodal force is reduced to zero since $\Delta R_y = R_y$.

This variable time-step nodal-release algorithm performed well for the creep-brittle material studied here, resulting in time-steps ranging from 10^{-17} to 10^{-1} h. The number of time-steps required to completely release the crack tip nodes varied from approximately 250 for the first node to 50 for other nodes. The user-defined time-step controlling parameters were chosen as $\tau = 0.04$ and $k = 1.35$ (similar to Ref *18*). Values of N and M were chosen as 10 and 2, respectively, for all releases. The relative magnitudes of N and M are important, as seen in Eq 8, while the absolute magnitudes have little effect on the overall performance since the maximum time step given by Eqs 5 or 6 usually governs the time-stepping process. However, selection of N and M values that are too small could result in accuracy and stability problems, while values of N and M that are too large could result in unnecessary computational effort.

Implementation

Experimentally observed crack growth histories of four compact tension specimens were numerically enforced to study the evolution of crack tip fields and far-field fracture parameters (a similar approach was taken by Bassani et al. [*20*] for the creep-ductile case). Details of the implementation for Specimen BCH-6 are provided below.

The time-dependent deformation characteristics for the Aluminum Alloy 2519-T87 are reasonably accurately described by the following constitutive law:

$$\dot{\varepsilon} = \frac{\dot{\sigma}}{E} + A_1(\varepsilon_{pc})^{-p}\sigma^{n_1(1+p)} + A\sigma^n + A'\sigma^{n'} \qquad (11)$$

Here, σ is stress, ε_{pc} is the primary creep strain, and A_1, p, n_1, A, n, A', and n' are creep constants. Values for these material properties, along with a plot illustrating the creep deformation response of the material at the 135°C test temperature, are given in Part I of this paper. This constitutive model was incorporated into the finite element code and used to model the response of each fracture specimen.

A constant external load of 10.5 kN was applied to Specimen BCH-6, whose width and thickness were 5.08 and 2.21 cm, respectively. The specimen was side-grooved 10% on each side (the thickness at the side grooves was 1.77 cm) so that plane strain fracture conditions were assumed to apply. Crack growth began at a crack length of 2.25 cm and ended 105 h later at a crack length of 2.52 cm (unstable fracture occurred at the final crack length). A plot of the crack growth history (Fig. 1) reveals a relatively long incubation period followed by accelerating crack growth.

The finite element mesh used to model Specimen BCH-6 consists of 1142 four-noded linear isoparametric elements (Fig. 2). Crack growth is simulated by releasing a sequence of 40 nodes along the lower boundary of the dense portion of the mesh. Crack growth begins six elements

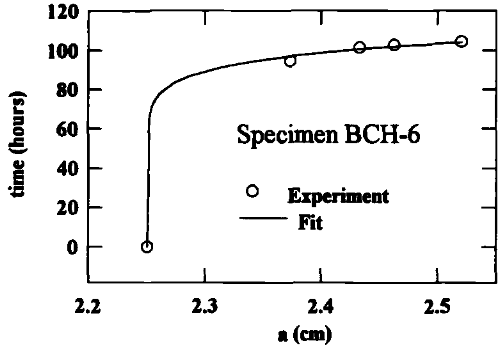

FIG. 1—*Experimentally determined crack growth history along with curve fit.*

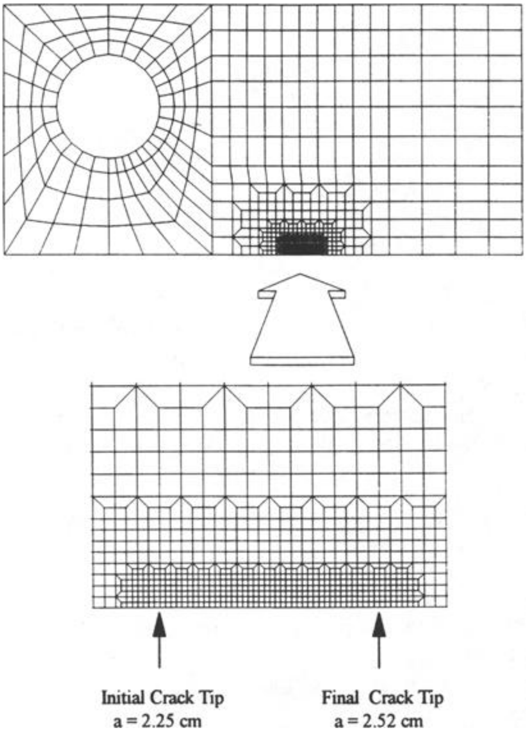

FIG. 2—*Finite element mesh for Specimen BCH-6.*

to the right of the start of the small square elements and ends six elements to the left of the end of the small square elements. The crack growth increment is 67.3 μm, which is smaller than the experimentally observed average grain size of 100 μm. The release time of each of the 40 nodes along the crack growth path is estimated using a smooth fit of the experimentally observed crack length versus time history (see Fig. 1). Load-line deflection versus time data was used to approximate the location of the knee in this curve, as well as knowledge that there was no discernable crack growth for Specimen BCH-6 by the potential drop method until after 80 h [*3*].

Numerical Results

Evolution of Crack Tip Fields

Interpretation of the finite element results is enhanced using a visualization program, developed as part of this work, to simulate the evolution of various crack tip field parameters at different stages of crack growth. Figure 3 shows contour plots of the effective creep strain and effective stress at three stages of crack growth for Specimen BCH-6. The white areas of the filled contour plots for creep strain denote regions where creep strains are greater than 0.005, while the black areas denote near zero creep strains. For the sequence of stress plots, the white areas denote regions where the effective stress is greater than 310 MPa, while the black regions denote stresses less than 103 MPa. Deflections in all of these plots are magnified by a factor

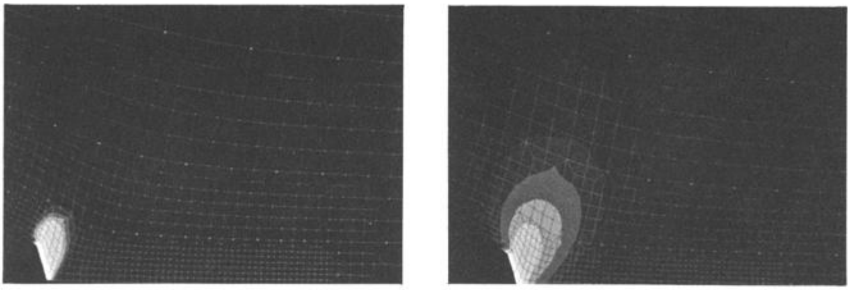

Time = 74.53 hours; Crack Length = 2.26 cm

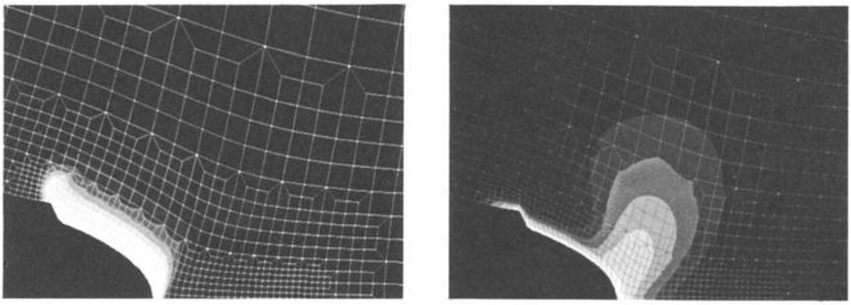

Time = 98 hours; Crack Length = 2.39 cm

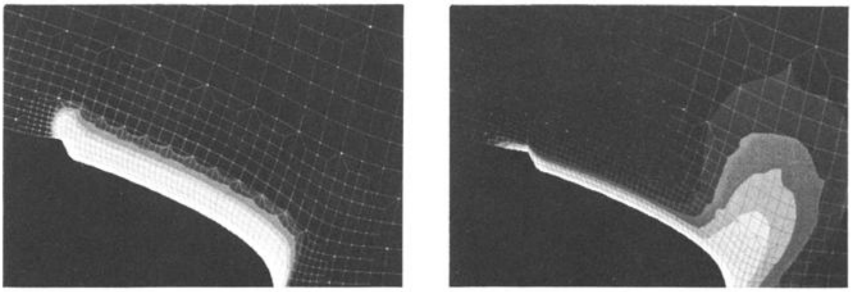

Time = 104 hours; Crack Length = 2.52 cm

Creep Zone Evolution **Stress Field Evolution**

FIG. 3—*Contour plots of effective stress and creep strain at various stages of growth.*

of 60. Significant levels of creep deformation are confined to a thin region adjacent to the crack growth path. The characteristic "knob" observed near the initial crack tip is due to the initially elastic crack tip fields that produce high creep strain rates while the crack growth is slow due to incubation. As the stresses near the crack tip relax, the driving force for creep deformation decreases, resulting in a corresponding decrease in the creep zone size. Both residual stress and residual creep strain are left in the wake of the growing crack. As the crack grows, the crack tip fields become more intense, resulting in larger creep zone expansion rates. However, the extent of the creep zone is limited by the accelerating crack growth since accumulating creep deformation is quickly left in the wake of the growing crack.

Profiles of effective stress along a radial line from the crack tip at $\theta = 90°$ reveal that stresses in a region just outside the creep zone scale with $r^{-1/2}$ throughout the crack growth history (Fig. 4). Consequently, small-scale creep conditions exist and K describes the crack tip fields in an annular region around the crack tip. Both the amplitude and the strength of the stress singularity within the creep zone ($r <\approx 0.25$ mm) increase with time. It is not clear whether the amplitude scales with K or with the crack growth rate ($\dot{a}$) since both quantities increase significantly during the test. The strength of the singularity is given by $r^{-1/16}$ just after incubation (after one crack growth increment) and approximately by $r^{-1/12}$ throughout most of the remainder of the test. Similar trends are predicted analytically when a stationary crack tip field (HRR-type field) gives way to a growing crack tip field (HR-type field) [*14,15*]. Thus, the results presented here seem to support the notion of ''nested'' crack tip fields, although the particular form of the fields and the character of the nesting cannot be compared directly with theory due to the complex constitutive law employed in this analysis.

Correlation of Crack Growth with K

Attempts are generally made to correlate creep crack growth rates with global fracture parameters that can be measured experimentally. A substantial body of experimental evidence indicates that crack growth rates in creep-brittle materials, such as Aluminum 2519-T87, correlate best with K, while crack growth rates in creep-ductile materials correlate best with the C_t parameter of Saxena [*21*]. Creep-ductile conditions are generally assumed to exist when the deflection at the load-line is dominated by creep deformation. Specifically, creep-ductile conditions prevail with $\dot{V}_c/\dot{V} \geq 0.8$ [22], where $\dot{V}_c$ is the creep component of the load-line deflection rate, and $\dot{V}$ is the total load-line deflection rate. This rule of thumb suggests that crack growth in Specimen BCH-6 does not occur under creep-ductile conditions (Fig. 5).

From an analytical viewpoint, successful correlation of crack growth with a fracture parameter requires that the deformation and damage fields surrounding the crack tip scale with the parameter in a roughly ''self-similar'' fashion. For example, the creep zone for a stationary crack under small-scale yielding expands in a self-similar fashion such that its shape does not change with time (i.e., $r_c(\theta = 90°)/r_c(\theta = 0°)$ is constant). Figure 6 indicates that the shape of the creep zone for Specimen BCH-6 changes significantly during the early stages of crack

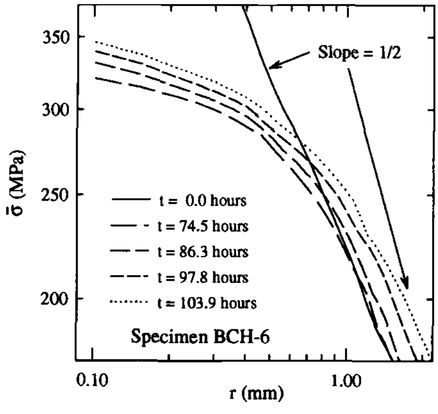

FIG. 4—*Profiles of effective stress along $\theta = 90°$.*

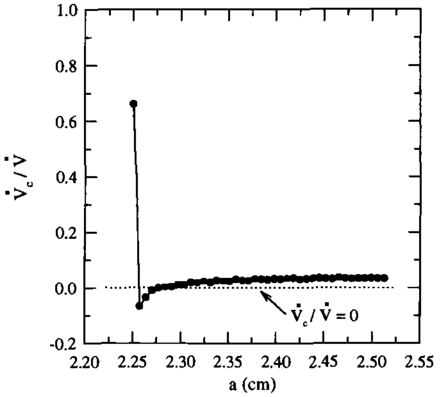

FIG. 5—*Ratio of load-line deflection rate due to creep to total load-line deflection rate.*

growth and later assumes a somewhat constant shape. Thus, crack growth for this specimen appears to approach self-similar conditions following a transient period where the character of the creep zone changes significantly (the other three specimens follow similar trends). Note, however, that self-similar growth of the creep zone does not necessarily translate into self-similar growth of the process zone within which the damage processes that govern incremental crack extension occur.

The applicability of small-scale creep conditions, coupled with the approximate existence of similitude, suggest that the later stages of crack growth can be correlated with *K* (Fig. 7). Figure 7 effectively represents smoothed out experimental data since *K* is uniquely determined by the current crack length for a given specimen geometry and loading (this plot is unaffected by the results of the finite element analyses). Specimens BCH-4, BCH-6, and BCH-7 have a thickness of 2.21 cm, while specimen BCH-1 has a thickness of 0.635 cm. All specimens are side grooved 10% on each side. Figure 7 reveals good correlation of *K* with crack growth rates after the initial period of transience for the thicker specimens. Crack growth rates also appear to have a

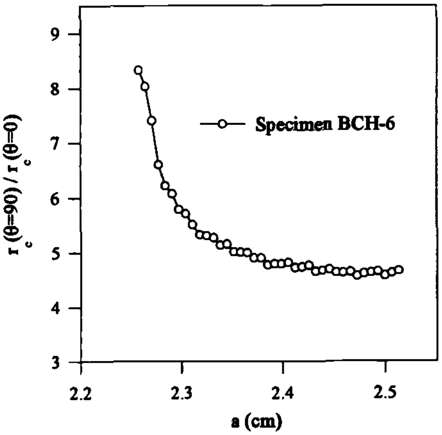

FIG. 6—*Check of similitude for Specimen BCH-6.*

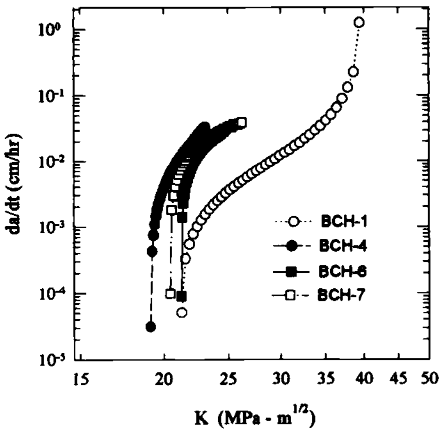

FIG. 7—*Stress intensity factor versus crack growth rate.*

power law dependence on K for the thinner specimen, although the dependence is shifted relative to the thicker specimens. The higher resistance to creep crack growth demonstrated by the thinner specimen is attributed to reduced constraint since it is believed that crack tip damage processes accelerate under increasing triaxiality levels, particularly for creep-brittle materials [*23*].

Assessment of Accuracy

Accuracy of the growing crack, finite element solutions have been verified by comparison with growing crack solutions obtained using ABAQUS, a commercial finite element code that allows for nodal release [*24*]. Discrepancies in computed load-line deflections were well within 1% for creep-brittle crack growth in a material deforming according to an elastic-power law creep constitutive relation.

The ability of the numerical approach to accurately model experimental conditions can be evaluated by comparing numerically and experimentally measured load-line deflections (Fig.

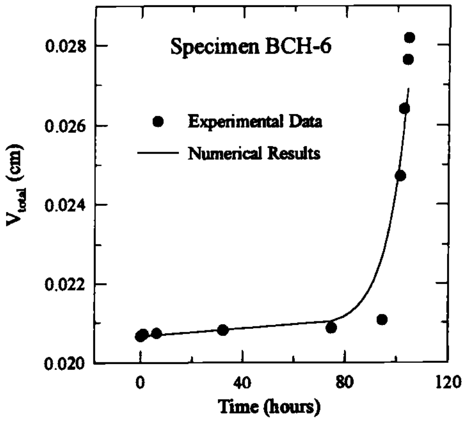

FIG. 8—*Evaluation of numerical results by comparison of experimentally and numerically determined load-line deflections.*

8). Although some deviation between the numerical and experimental results is apparent, especially near the end of the test, both measurements follow the same trends. Possible reasons for the discrepancies include (1) the influence of triaxial stress states on the creep deformation characteristics of the material, (2) plane stress effects not accounted for in the numerical model (surface effects), and/or (3) uncertainties in experimental measurements of crack length, load-line deflection, and creep deformation properties.

Discussion

Transition Times for Growing Cracks

The initial stages of crack growth in Aluminum Alloy 2519-T87 are characterized by highly transient crack tip fields (Fig. 6) and crack growth rates that do not correlate well with K (Fig. 7). These initially transient conditions are expected since the stationary crack tip fields (HRR-type fields) that develop during the incubation period are replaced by growing crack tip fields (possibly HR-type fields) as the crack extends through the initial creep zone. The numerical results indicate that the period of time after which crack growth becomes self-similar and crack growth rates correlate with K roughly corresponds to the time required for the crack to grow through the initial creep zone. Transition times that relate to the passage of the initially transient crack tip fields are presented in this section.

Due to nesting of the HR, HRR, and K fields [*14*], the expansion of the creep zone during the initial stages of crack growth is given by Eq 3 for a material deforming according to an elastic-power law creep constitutive relation. Differentiating Eq 3 with respect to time shows that $\dot{r}_c$ decreases with $(1/t)^{(n-3)/(n-1)}$. Regardless of the crack growth rate, $\dot{a}$, a unique reference time, t_g', will eventually be reached where $\dot{a} = \dot{r}_c$, even when $\dot{a}$ varies with time. The creep zone size at this reference time, denoted by r_g, approximates the distance that the crack must extend to leave the initial creep zone in the wake of the growing crack. The time required for the crack to extend a distance r_g may be considered as a transition time for growing cracks, designated here as t_g.

Examples of the evolution of $\dot{a}$ and $\dot{r}_c$ are shown in Fig. 9 for constant and varying crack

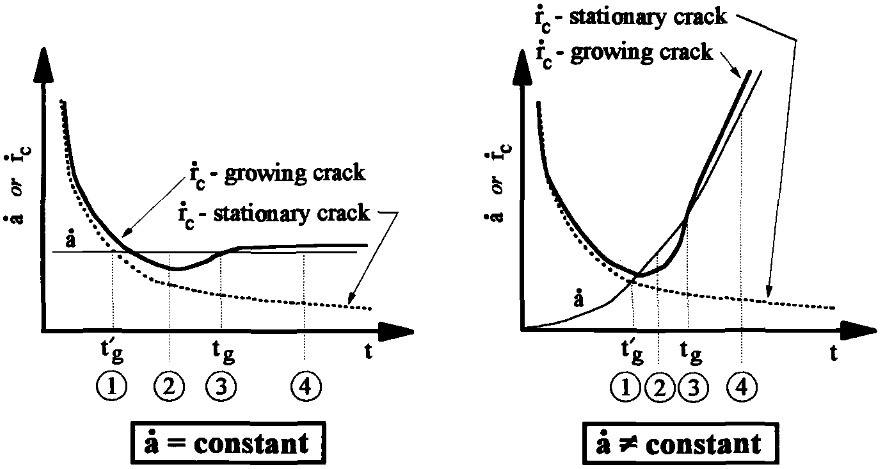

FIG. 9—*Possible relation of* $\dot{r}_c$ *and* $\dot{a}$ *for creep-brittle crack growth. Here, both constant and varying crack growth rates are examined, and* $\dot{r}_c$ *is measured relative to a fixed position (not with respect to the moving crack tip).*

growth rates. Notice that $\dot{r}_c$ for the growing crack is expected to approximately follow the stationary crack solution for $t < t'_g$. However, as the crack tip approaches the reference distance r_g, $\dot{r}_c$ becomes dominated by crack growth effects and approaches $\dot{a}$ at time t_g. The creep-brittle character of the material ensures that $\dot{a} \approx \dot{r}_c$ during the quasi-steady-state crack growth regime that occurs after time t_g, assuming the rate of expansion of the creep zone is measured relative to a fixed position along $\theta = 0°$. Here, the quasi-steady-state crack growth regime is characterized by crack tip fields that change slowly with increasing crack length.

Constant Crack Growth Rate—Closed-form expressions for t'_g and t_g can be developed when the crack growth rate is constant. The reference time t'_g is defined as the time when $\dot{r}_c$ is first equal to $\dot{a}$. Equating $\dot{a}$ with $\dot{r}_c$ and solving for time results in

$$t'_g = \left(\frac{1}{\pi(n-1)}\right)^{\frac{n-1}{n-3}} \left(\frac{EA(n+1)I_n}{2\pi(1-\nu^2)}\right)^{\frac{2}{n-3}} \left(\frac{1-2\nu}{\tilde{\sigma}_e(\theta = 0°)}\right)^{\frac{2(n+1)}{n-3}} \left(\frac{K^2}{\dot{a}}\right)^{\frac{n-1}{n-3}} \tag{12}$$

Since the creep zone radius along $\theta = 0°$ is larger than the total amount of crack extension at t'_g, additional crack growth is necessary for the crack to grow out of the influence of the initial creep zone. From Eq 3, it follows that $\dot{r}_c = ((2/(n-1)r_c/t$. Since $\dot{r}_c = \dot{a}$ and $r_c = r_g$ at time t'_g, the initial creep zone size can be written in terms of t'_g as $r_g = ((n-1)/2)\dot{a}t'_g$. The transition time for growing cracks $(t)_g$ correspond to the time required for the crack to extend a distance r_g through the initial creep zone. For a constant crack growth rate, $r_g = \dot{a}t_g$, resulting in

$$t_g = \left(\frac{n-1}{2}\right) t'_g \tag{13}$$

While Eqs 12 and 13 apply to elastic-power law creep deformation, similar expressions have been derived for a material deforming according to an elastic-primary creep constitutive relation [*25*].

A growing crack finite element analysis was carried out to evaluate the usefulness of t_g for predicting the onset of quasi-steady-state crack growth conditions. A constant crack growth rate was enforced under plane strain conditions for a compact-type specimen deforming according to an elastic-power law creep constitutive relation. An indication that creep-brittle crack

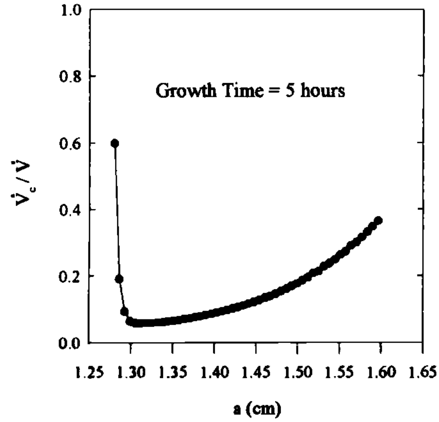

FIG. 10—*Ratio of deflection rate due to creep to total deflection rate.*

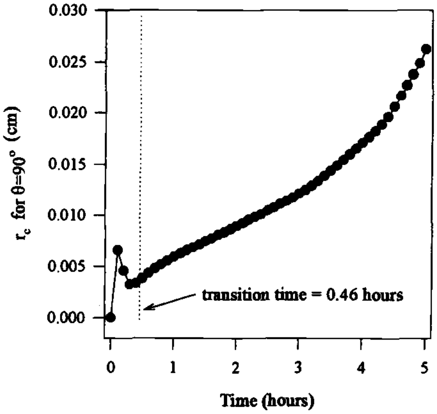

FIG. 11—*Time versus creep zone radius along $\theta = 90°$ for a constant crack growth rate.*

growth conditions were achieved is provided by Fig. 10, where $\dot{V}_c/\dot{V} < 0.4$ predominately. For this creep growth simulation, the passage of transient conditions can be examined by plotting the radius of the creep zone along $\theta = 90°$ versus time (Fig. 11). Figure 11 shows that $t_g = 0.46$ h from Eqs 12 and 13 approximately corresponds to the onset of quasi-steady-state growth of the creep zone. Notice that the highly transient changes in the creep zone size occur prior to the transition time.

Varying Crack Growth Rate—Determination of t_g for varying crack growth rates is illustrated using the crack growth history of Specimen BCH-6. Figure 12 shows a plot of the stationary crack solutions for $\dot{r}_c$ versus time, where the $\dot{r}_c$ curve resulting from each of the three creep terms in the constitutive relation (Eq 11) is considered separately. Specifically, the $\dot{r}_c$ curves are based on the elastic properties of the material along with the primary creep term, the first power law creep term with $n = 5.33$, and the second power law creep term with $n =$

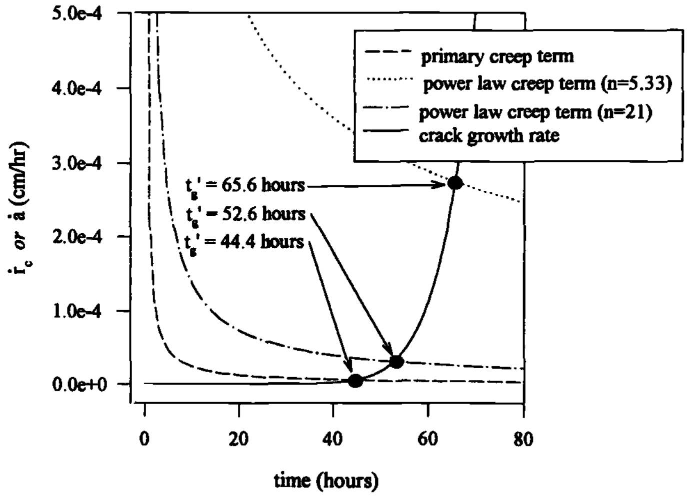

FIG. 12—*Determination of the reference time* t_g'.

21 (all material constants are given in Part I of this paper). The crack growth rate versus time for Specimen BCH-6 is also plotted in Fig. 12. The three intersections of the $\dot{r}_c$ and $\dot{a}$ curves correspond to values of the reference time t_g'. Notice that t_g' for power law creep with $n = 5.33$ governs the transition of crack growth to quasi-steady-state conditions since the required change in crack length (r_g) is largest for this term of the constitutive relation. Plotting the crack extension (Δa) for this specimen versus time along with $r_c(t = t_g', \theta = 0°)$ from Eq 3 with $n = 5.33$ results in a transition time t_g of 87.4 h (Fig. 13).

The duration of the transient regime of crack growth can also be estimated by qualitatively examining the finite element results. Figure 14 indicates that the crack has grown through the initial creep zone after 86.3 h since the creep zone radius along $\theta = 90°$ changes slowly with crack length after this time. Thus, the finite element results indicate that $t_g = 87.4$ h is a good estimate of the time required for the onset of quasi-steady-state crack growth. Repeating the analysis in Figs. 12 through 14 for the other specimens and comparing the finite element results with computed values of t_g yields Fig. 15. This comparison shows good agreement between t_g and the time required for the crack to grow through the initial creep zone. Examining r_g for Specimens BCH-1, BCH-4, BCH-6, and BCH-7 indicates that quasi-steady-state crack growth occurs after 0.89, 0.58, 0.39, and 0.43 mm of crack growth, respectively.

The boundary of the creep zone in Eq 3 is defined as the locus of points where the effective stress from the elastic solution is equal to the effective stress of the HRR solution in Eq 1. Transition times based on this definition for r_c show good agreement with the duration of the transient crack growth regime, as discussed above. However, other definitions for r_c are typically favored in time-dependent fracture analyses. For example, Riedel and Rice [7] define r_c as the locus of points where the effective creep strain is equal to the effective elastic strain. Similarly, Adefris [26] defines r_c as the locus of points where the effective creep strain is equal to 0.002. These alternate definitions for r_c are more robust than Eq 3 for use with finite element analyses since numerically determined creep zone radii based on Eq 3 may show significant irregularity. For this reason, the finite element creep zone radii along $\theta = 90°$ in Figs. 11 and 14 are based on Adefris' definition of r_c. Although these alternative definitions for r_c are better indicators of the region within which creep strains dominate elastic strains, expressions for t_g

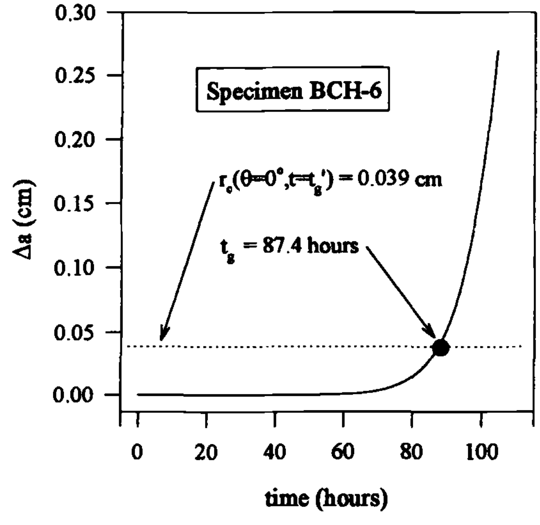

FIG. 13—*Determination of the transition time* t_g.

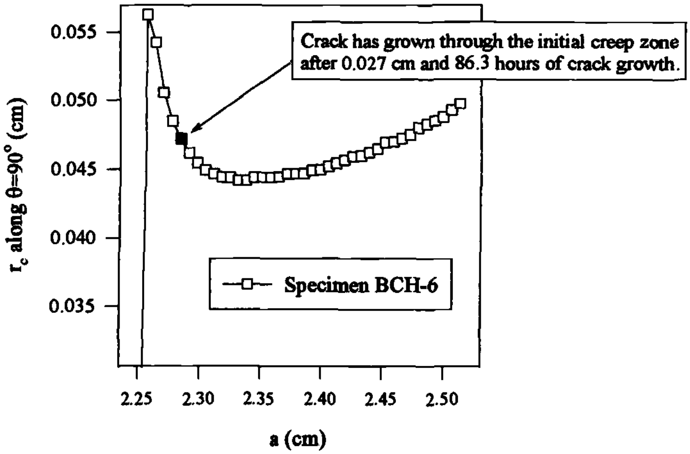

FIG. 14—*Variation of the creep zone radius with crack growth for Specimen BCH-6. The crack is estimated to grow through the initial creep zone after 86.3 h of crack growth.*

based on these definitions of r_c predict significantly smaller creep zone radii along $\theta = 0°$ than Eq 3 and consequently underestimate the duration of the transient crack growth regime. Note that the creep zone of Eq 3 predicts the region within which stresses deviate significantly from those computed using linear-elastic fracture mechanics.

The reference time t_R of Hawk and Bassani [*14*] can also be used to mark the onset of quasi-steady-state crack growth conditions. The formulation of this reference time is based on equating the radius of the creep zone for growing cracks (the HR zone, which depends on K and $\dot{a}$) to the radius of the creep zone for a stationary crack (the HRR zone, which depends on K and t) and solving for the time. When the crack growth rate is constant, the expression for t_R is similar to the expression for t_g above since both quantities scale with $(K^2/\dot{a})^{(n-1)/(n-3)}$. However, interpretation of t_R is not clear for varying crack growth rates. Moreover, t_R may not exist when crack growth is preceded by an incubation period since the creep zone predicted from stationary

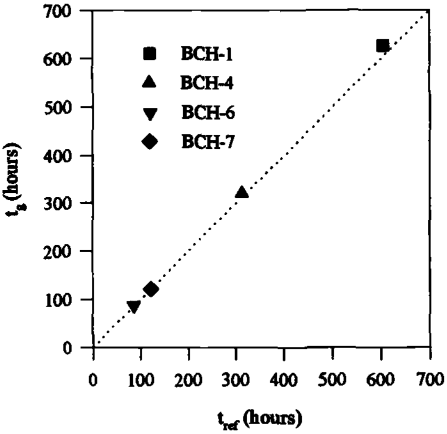

FIG. 15—*Comparison of* t_{ref} *and* t_g. *Here,* t_{ref} *is the time for the crack to grow through the initial creep zone as qualitatively estimated by examining the finite element results.*

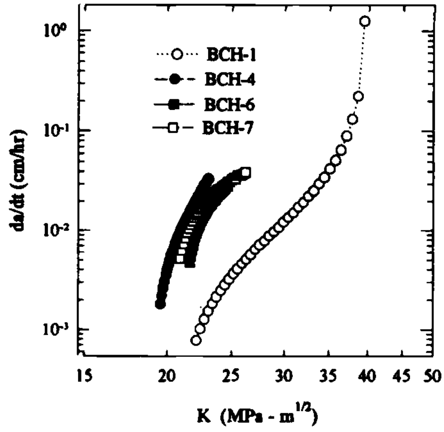

FIG. 16—*Stress intensity factor versus crack growth rate after transition time* t_g.

crack mechanics may always be greater than the creep zone predicted from growing crack mechanics.

The aim of examining these transition times is to define the region where quasi-steady-state crack growth occurs and $\dot{a}$ correlates well with K. Computing the transition times for all of the Aluminum 2519 specimens and plotting only the $(K,\dot{a})$ pairs that occur after the transition time for each specimen results in Fig. 16. Notice that the tails that occur during the initial stages of crack growth are removed when compared to Fig. 7. Consequently, the transition time t_g presented here provides a useful estimate of the time after which crack growth can be better correlated with K, at least for Aluminum 2519. The utility of this approach is that the duration of the highly transient regime of creep-brittle crack growth can be estimated based on material properties and the crack growth history without detailed information from growing crack finite element analyses. While useful, it should be emphasized that the K-controlled regime may actually comprise the minority of life [3].

Difficulties in Experimental Determination of Time-Dependent Fracture Parameters

Experimental determination of time-dependent fracture parameters, such as the C_t parameter of Saxena [21], is typically based on the creep component of the load-line deflection rate ($\dot{V}_c$). For creep-brittle materials, $\dot{V}_c$ may be a very small fraction of the total load-line deflection rate ($\dot{V}$) or even negative, as shown in Fig. 5 and discussed in a recent paper by Hall, McDowell, and Saxena [27]. These small or negative $\dot{V}_c/\dot{V}$ ratios coupled with limited accuracy in determining crack lengths and corresponding crack growth rates result in inaccurate values of $\dot{V}_c$ since $\dot{V}_c = \dot{V} - \dot{V}_e$ and $\dot{V}_e$, which is the elastic component of the load-line deflection rate, depends on measured $\dot{a}$ values, as discussed in Part I of this paper. A forthcoming paper will discuss the impact of the numerical results on correlation of time-dependent fracture parameters with creep-brittle crack growth rates.

Summary and Conclusions

The creep crack growth characteristics of Aluminum Alloy 2519-T87 were evaluated by performing growing crack finite element analyses of four compact tension specimens under constant external loading. Experimentally determined crack growth histories were enforced to gain insight into the relation of evolving crack tip fields to far field parameters and to crack growth rates. The growing crack finite element solutions were carried out using a small-strain finite element code coupled with a new variable time-step, nodal-release algorithm.

Crack growth in Aluminum 2519 was determined to be creep-brittle in nature, with an initial transient period of crack growth followed by a quasi-steady-state crack growth regime. Crack growth rates were found to correlate with the stress intensity factor K during the quasi-steady-state crack growth regime, where conditions of small-scale creep and similitude roughly exist. A transition time for growing cracks t_g was presented to signal the onset of quasi-steady-state conditions and K-dominated crack growth. This transition time successfully predicted the time required for the crack to grow through the initial creep zone for both constant and varying crack growth rates. Experimental difficulties commonly encountered in creep-brittle fracture analysis were also discussed.

Acknowledgments

This work was supported by both NSF and NASA Langley Center grants. The required computer code was developed under NSF sponsorship, while Aluminum 2519 calculations were performed under NASA sponsorship.

References

[*1*] Dogan, B., Saxena, A., and Schwalbe, K.-H., "Creep Crack Growth in Creep-Brittle Ti-6242 Alloys," *Materials at High Temperatures*, Vol. 10, No. 2, 1992, pp. 138–143.

[*2*] Bensussan, P., Maas, E., Pelloux, R., and Pineau, A., "Creep Crack Initiation and Propagation: Fracture Mechanics and Local Approach," *Journal of Pressure Vessel Technology*, Vol. 110, 1988, pp. 42–50.

[*3*] Hamilton, B. C., "Creep Crack Growth Behavior of Aluminum Alloy 2519," Master's thesis, Materials Science and Engineering, Georgia Institute of Technology, Atlanta, GA, November 1994.

[*4*] Gill, Y., "Creep Crack Growth Characterization of SA-106 C Carbon Steel," Ph.D. thesis, Materials Science and Engineering, Georgia Institute of Technology, Atlanta, GA, March 1994.

[*5*] Jones, K. A., "The Creep Behavior of Aluminum Alloy 8009," Master's thesis, Materials Science and Engineering, Georgia Institute of Technology, Atlanta, GA, September 1993.

[*6*] Leng, Y., Porr, W. C., Jr., and Gangloff, R. P., "Time Dependent Crack Growth in P/M Al-Fe-V-Si at Elevated Temperatures," *Scripta Metallurgica et Materialia*, Vol. 25, 1991, pp. 895–900.

[*7*] Riedel, H. and Rice, J. R., "Tensile Cracks in Creeping Solids," *Fracture Mechanics: 12th Conference, ASTM STP 700*, American Society for Testing and Materials, West Conshohocken, PA, 1980, pp. 112–130.

[*8*] Bassani, J. L. and McClintock, F. A., "Creep Relaxation of Stress Around a Crack Tip," *International Journal of Solids and Structures*, Vol. 7, 1981, pp. 479–492.

[*9*] Hutchinson, J. W., "Singular Behavior at the End of a Tensile Crack in a Hardening Material," *Journal of Mechanics and Physics of Solids*, Vol. 16, 1968, pp. 13–31.

[*10*] Rice, J. R. and Rosengren, G. F., "Plane Strain Deformation Near a Crack Tip in a Power-Law Hardening Material," *Journal of Mechanics and Physics of Solids*, Vol. 16, 1968, pp. 1–12.

[*11*] Landes, J. D. and Begley, J. A., "A Fracture Mechanics Approach to Creep Crack Growth," *ASTM STP 590*, American Society for Testing and Materials, West Conshohocken, PA, 1976, pp. 128–148.

[*12*] Nikbin, K. M., Webster, G. A., and Turner, C. E., "Relevance of Nonlinear Fracture Mechanics to Creep Cracking," *Cracks and Fracture (9th Conference), ASTM STP 601*, American Society for Testing and Materials, 1976, pp. 47–62.

[*13*] Hui, C. Y. and Riedel, H., "The Asymptotic Stress and Strain Field Near the Tip of a Growing Crack Under Creep Conditions," *International Journal of Fracture*, Vol. 17, No. 4, 1981, pp. 409–425.

[*14*] Hawk, D. E. and Bassani, J. L., "Transient Crack Growth Under Creep Conditions," *Journal of Mechanics and Physics of Solids*, Vol. 34, No. 3, 1986, pp. 191–212.

[*15*] Hui, C. Y., "The Mechanics of Self-Similar Crack Growth in an Elastic Power-Law Creeping Material," *International Journal of Solids and Structures*, Vol. 22, No. 4, 1986, pp. 357–372.

[*16*] Riedel, H., "Creep Deformation at Crack Tips in Elastic-Viscoplastic Solids," *Journal of Mechanics and Physics of Solids*, Vol. 29, 1981, pp. 35–49.

[*17*] Chang, T. C., Popelar, C. H., and Staab, G. H., "Creep Crack Growth in an Elastic-Creeping Material Part II: Mode I," *International Journal of Fracture*, Vol. 33, 1987, pp. 31–45.

[*18*] Leung, C.-P., McDowell, D. L., and Saxena, A., "Inclusion of Primary Creep in the Estimation of the C_t Parameter," *International Journal of Fracture*, Vol. 46, 1990, pp. 81–104.

[*19*] Moyer, T. E. and Liebowitz, H., "Creep Crack Growth Modeling and Near Tip Stress Fields," *Engineering Fracture Mechanics*, Vol. 28, No. 5/6, 1987, pp. 601–621.

[*20*] Bassani, J. L., Hawk, D. E., and Saxena, A., "Evaluation of the C_t Parameter for Characterizing Creep Crack Growth Rate in the Transient Regime," *Nonlinear Fracture Mechanics, ASTM STP 995*, American Society for Testing and Materials, West Conshohocken, PA, 1989, pp. 7–26.

[*21*] Saxena, A., "Creep Crack Growth Under Non Steady-State Conditions," *Fracture Mechanics (17th Volume), ASTM STP 905*, American Society for Testing and Materials, West Conshohocken, PA, 1986, pp. 185–201.

[*22*] Saxena, A. and Landes, J. D., "Characterization of Creep Crack Growth in Metals," *Advances in Fracture Research*, Sixth International Conference on Fracture, Pergamon Press, New York, 1984, pp. 3977–3988.

[*23*] Wu, F.-H., Bassani, J. L., and Vitek, V., "Transient Crack Growth Under Creep Conditions Due to Grain-Boundary Cavitation," *Journal of Mechanics and Physics of Solids*, Vol. 34, 1986, pp. 455–475.

[*24*] Hibbitt, Karlsson, & Sorensen, Inc., ABAQUS, Version 5.2, 1992.

[*25*] Hall, D. E., "Analysis of Crack Growth in Creep-Brittle Materials," Ph.D. thesis, Woodruff School of Mechanical Engineering, Georgia Institute of Technology, Atlanta, GA, July 1995.

[*26*] Adefris, N. B., "Creep-Fatigue Crack Growth Behavior of 1%Cr-1%Mo-1/4%V Rotor Steel," Ph.D. thesis, Materials Science and Engineering, Georgia Institute of Technology, Atlanta, GA, 1993.

[*27*] Hall, D. E., McDowell, D. L. and Saxena, A., "Some Aspects of Crack Growth in Creep-Brittle Materials," *Proceedings*, International Symposium for Inelastic Deformation, Damage and Life Analysis, Honolulu, Hawaii, 30 July–3 Aug. 1995, ASME, New York.

Matthias Sester,[1] *Ralf Mohrmann,*[1] *and Hermann Riedel*[1]

A Micromechanical Model for Creep Damage and Its Application to Crack Growth in a 12% Cr Steel

---

REFERENCE: Sester, M., Mohrmann, R., and Riedel, H., "**A Micromechanical Model for Creep Damage and Its Application to Crack Growth in a 12% Cr Steel,**" *Elevated Temperature Effects on Fatigue and Fracture, ASTM STP 1297,* R. S. Piascik, R. P. Gangloff, and A. Saxena, Eds., American Society for Testing and Materials, 1997, pp. 37–53.

ABSTRACT: If creep cavities on grain boundaries grow by the constrained diffusive mechanism, partly cavitated boundary facets act mechanically like microcracks. Two cell models, one based on a cylindrical cell and the other on a regular tetrakaidekahedron, are worked out numerically to explore the influence of a distribution of microcracks on the constitutive response of a creeping solid. The results confirm the predictions of analytical estimates based on the differential self-consistent method of Rodin and Parks [*5*]. The Rodin and Parks model is then combined with the Robinson model [*9*] to provide a comprehensive model covering primary, secondary, and tertiary creep under arbitrary loading conditions. The combined model is implemented in the finite element code ABAQUS. The model is adjusted to a set of creep curves for a 12% Cr steel (X 20 CrMoV 12 1), and tests on compact specimens are successfully modeled.

KEYWORDS: creep damage, cell models, self-consistent analyses, constitutive modeling, finite element simulation, creep crack growth

The general goal of the present work is to develop a comprehensive material model for creep and plasticity describing primary, secondary, and tertiary creep under a wide range of loading histories such as constant load tests, constant strain rate tests, relaxation tests, and cyclic loading. Special attention is paid to cavitation damage and its effect on the constitutive behavior.

The ρ Parameter and Self-Consistent Estimates of the Constitutive Behavior

Under typical long-time service conditions, many materials develop grain boundary cavities, which grow by the constrained diffusive mechanism proposed by Dyson [*1*]. A necessary consequence of constrained cavity growth is that cavitating grain boundary facets act like microcracks in the sense that they transmit no or only small tractions, although substantial material bridges may still exist between the cavities [*1–5*].

This led Hutchinson [*3*] to the definition of a damage parameter, ρ, depending primarily on the number of density, N, of cavitating facets times their diameter, d, cubed:

$$\rho = \frac{n+1}{2\sqrt{1+\frac{3}{n}}} d^3 N \tag{1}$$

---

[1] Scientist, scientist, and senior scientist and head of department, respectively, Fraunhofer Institute for the Mechanics of Materials, Woehlerstr. 11, 79108 Freiburg, Germany.

Here, n is the stress exponent of Norton's creep law, and the n-dependent factor was introduced for later convenience. Hutchinson also derived the constitutive response of a power-law viscous (i.e., Norton-type) material containing a dilute concentration of penny-shaped microcracks. For uniaxial tension his result is

$$\dot{\varepsilon} = (1 + \rho)\,\dot{\varepsilon}_s \tag{2}$$

where $\dot{\varepsilon}$ is the inelastic strain rate of the damaged material, and $\dot{\varepsilon}_s$ is the steady-state strain rate of the matrix material without damage at the same stress.

Hutchinson's solution [*3*] for the dilute limit was extended to larger microcrack densities by Riedel [*4*] and by Rodin and Parks [*5*] using self-consistent methods. The simple, approximate method applied in Ref *4* leads to

$$\dot{\varepsilon} = \frac{1}{1 - \rho}\,\dot{\varepsilon}_s \tag{3}$$

if an integral self-consistent argument is employed, while the differential self-consistent method applied in the same approximate manner yields

$$\dot{\varepsilon} = e^{\rho}\dot{\varepsilon}_s \tag{4}$$

Rodin and Parks worked out the differential self-consistent scheme in a proper multiaxial formulation developed from an analysis of axisymmetric loadings. Their result is

$$\dot{\varepsilon}_{ij} = \frac{3}{2\bar{\sigma}}\,\dot{\varepsilon}_s[1 + \alpha(n,\rho)\,X^2]^{\frac{n-1}{2}}\left\{s_{ij} + \frac{2}{3}\,\alpha(n,\rho)\,\sigma_I\,\frac{\partial\sigma_I}{\partial\sigma_{ij}}\right\} \tag{5}$$

where $\dot{\varepsilon}_{ij}$ is the inelastic strain rate tensor, and σ_{ij} is the Cauchy stress tensor. The stress deviator, s_{ij}, is given by

$$s_{ij} = \sigma_{ij} - \frac{1}{3}\,\sigma_{kk}\delta_{ij} \tag{6}$$

(summation convention applied to repeated indices) and the Mises equivalent stress by

$$\bar{\sigma} = \sqrt{\frac{3}{2}}\,s_{ij}s_{ij} \tag{7}$$

The parameter X characterizes the stress state and is defined as $X = \sigma_I/\bar{\sigma}$ with the maximum principal stress, σ_I.

The function $\alpha(n,\rho)$ has the form

$$\alpha(n,\rho) = \frac{2\rho}{(n + 1)} + \frac{(2n + 3)\rho^2}{n(n + 1)^2} + \frac{(n + 3)\rho^3}{9n(n + 1)^3} + \frac{(n + 3)\rho^4}{108n(n + 1)^4} \tag{8}$$

In the following section it will be shown that the simplified evaluation of the self-consistent scheme resulting in Eq 4, and the more elaborate treatment, Eq 5, lead to very similar results for uniaxial tension. Furthermore, cell model calculations will be presented to show that the Rodin and Parks [5] model describes the constitutive response accurately.

Cell Models

Geometry and Boundary Conditions

The constitutive response of a power-law viscous material containing penny-shaped microcracks is investigated by analyzing a representative unit cell containing one microcrack. Two such cell models are investigated. Figure 1*a* shows an axisymmetric model. The microcrack is centered in a cylindrical cell. The number density of cracks is related to the cell diameter Λ by

$$N = \frac{4}{\pi \Lambda^3} \tag{9}$$

from which ρ is calculated using Eq 1. The applied stress system is assumed to be axisymmetric with the components σ_z^∞ in axial, and σ_r^∞ in radial direction. On the surface of the cylinder and on the crack plane the following boundary conditions are prescribed:

u_r = constant, $F_r = \frac{1}{2}\Lambda^2\sigma_r^\infty$ on the mantle surface (F_r is a force per radian)

u_z = constant, $F_z = \frac{\pi}{4}\Lambda^2\sigma_z^\infty$ on the top surface

$\sigma_z = 0$ on the crack surface, $z = 0$

$u_z = 0$ on the ligament, $z = 0$

Figure 1*b* shows the second of the considered cell models. Here the unit cell is a tetrakaidekahedron, which is the Wigner-Seitz cell of the body-centered cubic (bcc) lattice. Contrary to the axisymmetric cell, the tetrakaidekahedron is space filling when repeated periodically. The number density of cracks is

$$N = \frac{2}{\Lambda^3} \tag{10}$$

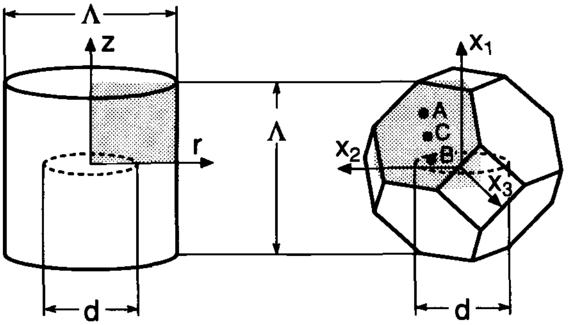

a b

FIG. 1—*Representative unit cells containing one microcrack with diameter* d*:* (a) *cylindrical cell;* (b) *tetrakaidekahedron, termed bcc cell.*

The principal stress axes are assumed to be aligned with the cubic axes, i.e., they are oriented normal to the square facets of the tetrakaidekahedron. For arbitrary values of the principal stresses, σ_I^∞, σ_{II}^∞, and σ_{III}^∞, it suffices to analyze the unit cell shaded in Fig. 1*b*. For the special case of axisymmetric loading, half of that cell would be sufficient, but all calculations were carried out with the shaded cell. Boundary conditions are prescribed as follows:

$$\begin{array}{ll}
u_1 = \text{constant},\ F_1 = \dfrac{\Lambda^2}{2}\,\sigma_I^\infty & \text{on the square facet with } x_1 = \dfrac{\Lambda}{2} \\
u_2 = \text{constant},\ F_2 = \dfrac{\Lambda^2}{2}\,\sigma_{II}^\infty & \text{on the square facet with } x_2 = \dfrac{\Lambda}{2} \\
u_3 = \text{constant},\ F_3 = \dfrac{\Lambda^2}{2}\,\sigma_{III}^\infty & \text{on the square facet with } x_3 = \dfrac{\Lambda}{2} \\
u_1 = 0 & \text{on the ligament, } x_1 = 0 \\
\sigma_1 = 0 & \text{on the crack surface, } x_1 = 0 \\
u_1^A + u_1^B = 2u_1^C & \text{on the hexagonal facet} \\
u_2^A + u_2^B = 2u_2^C & \text{on the hexagonal facet} \\
u_3^A + u_3^B = 2u_3^C & \text{on the hexagonal facet}
\end{array}$$

Point C is the center of the hexagonal facet. Points A and B are symmetric with respect to Point C.

A similar model was analyzed by Dib and Rodin [6], who consider the two cases that either one family of the square facets or one family of the hexagonal facets are cracked. These two cases correspond to two discrete values of the ρ parameter. If the square and hexagonal cracks are replaced by circular cracks of equal area, one obtains the ρ parameter from Eq 1 with $Nd^3 = 0.112$ for the cracked square facets and $Nd^3 = 0.504$ for the cracked hexagonal facets. Their results can be used as benchmarks in our analysis.

Finite Element Meshes

Figure 2 shows the finite element meshes used in the calculations. The axisymmetric model contains 124 quadrilateral eight-noded isoparametric elements and 801 degrees of freedom. The bcc model is made up of 456 20-noded brick elements and has 7388 degrees of freedom. Reduced integration is used to avoid possible mesh-locking problems. At the crack tip, the

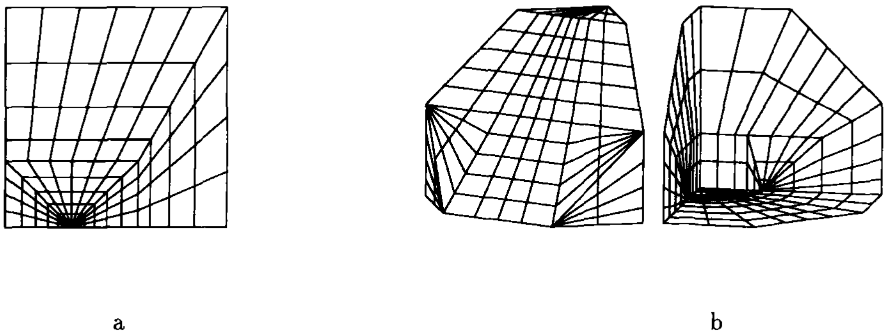

FIG. 2—*Finite element models of the unit cells:* (a) *cylindrical cell;* (b) *bcc cell, viewed as in Fig. 1*b *and in the opposite direction.*

nodes along one side of an element are collapsed into one point in the axisymmetric model and into one line in the bcc model. These elements give a strain singularity of r^{-1}, which is a good approximation to the strain singularity of $r^{-n/(n+1)}$ of the Hutchinson, Rice, and Rosengren (HRR) field.

Material Law

The material is described as elastic/nonlinear viscous, i.e., in uniaxial tension the total strain rate is

$$\dot{\varepsilon}^{\text{tot}} = \dot{\sigma}/E + A\sigma^n \tag{11}$$

where

E = Young's modulus, MPa,
n = stress exponent in Norton's creep law, and
A = coefficient in Norton's law 1/(MPa^n s):

The elastic strain rate in Eq 11 was introduced primarily for computational convenience since an algorithm for elastic/nonlinear viscous material was available. In the present paper, the steady-state solution established at long times is of primary interest. However, also the elastic solution calculated for the time $t = 0$ directly upon load application can be used to check models for elastic response of microcracked solids, e.g., Refs *7* and *8*.

Results and Comparison with Self-Consistent Estimates

The presence of the microcracks leads to an enhanced creep rate. The results of the self-consistent analyses and the cell-model calculations are presented in terms of the enhancement factor for the axial inelastic strain rate $\dot{\varepsilon}_{\text{I}}$,

$$e = \frac{\dot{\varepsilon}_{\text{I}}}{\dot{\varepsilon}_{\text{I},s}} \tag{12}$$

where $\dot{\varepsilon}_{\text{I},s}$ is the inelastic strain rate in the absence of microcracks.

Uniaxial Tension

Figure 3 summarizes the results of the self-consistent estimates and cell model calculations for uniaxial tension. The Norton exponent was chosen as $n = 4$ and 8. The figure shows the enhancement factor, e, defined in Eq 12 as a function of the damage parameter, ρ.

As one would expect, all curves merge into Hutchinson's [*3*] linear approximation at small ρ. At larger ρ, the integral and the differential self-consistent schemes lead to substantially different results. Comparing the two differential approaches, one notes that the cruder approximation, Eq 4, is practically indistinguishable from the more accurate solution, Eq 5.

The two cell models differ from one another at large ρ. This is expected since the critical values, ρ_f, at which neighboring cracks touch are different for the two crack arrangements. For $n = 4$, creep coalescence ($d = \Lambda$) corresponds to $\rho_f = 2.41$ for the cylindrical cell model and to $\rho_f = 3.78$ for the bcc model.

It is important to note that the creep rate enhancement factors predicted by the differential self-consistent method, Eqs 4 and 5, lie between the finite element results of the cell models and can therefore be considered to be good approximations for describing the creep rate at

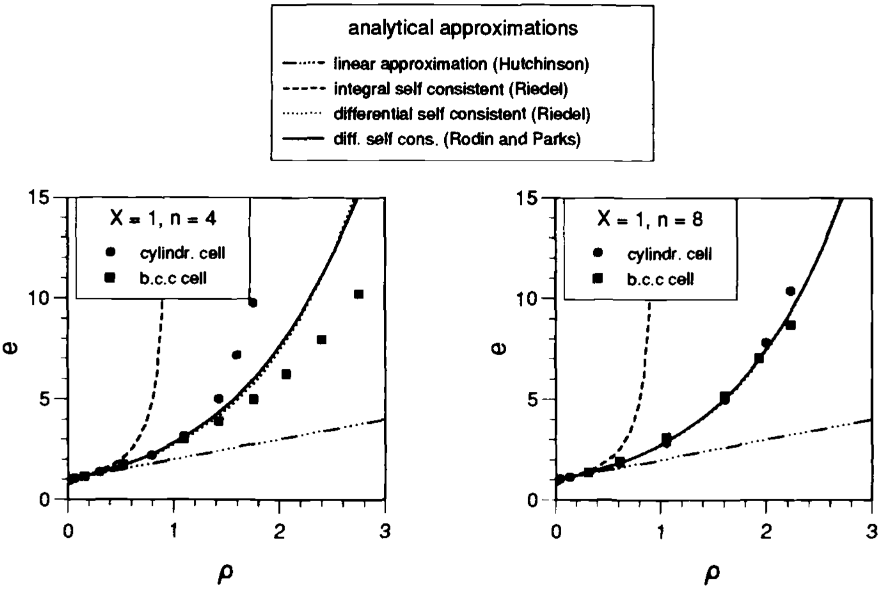

FIG. 3—*Creep enhancement factor* e *as a function of the damage parameter* ρ. *Comparison of cell model calculations (symbols) with analytical approximations (lines) for a uniaxial stress state.*

higher densities of cracks. On the other hand, the integral self-consistent method, which leads to Eq 3, is inaccurate.

Axisymmetric Loadings

In this section, the results of Rodin and Parks, Eq 5, are compared with cell model calculations for axisymmetric loading conditions. In Fig. 4, the stress state $\sigma_r^\infty = \frac{1}{2}\sigma_z^\infty$ is chosen. This corresponds to $X = 2$. The enhancement factor, e, is given as a function of ρ for $n = 3$, 5, and 8. Again, the results of Rodin and Parks lie between the finite element results of the two cell models.

From now on, only the bcc cell model will be considered. In Fig. 5, the analysis is carried out for the two special cases corresponding to the crack densities considered by Dib and Rodin [*6*]. The enhancement factor e is given as a function of the stress state parameter $X = \sigma_I/\overline{\sigma}$ for $n = 3$, 5, and 8. The results of Rodin and Parks agree well with our cell model calculations. Dib and Robin use a slightly different measure for the creep enhancement, so their results cannot be plotted with ours in a single figure. However, Dib and Rodin also found a fairly good agreement between their results and those of Rodin and Parks.

Arbitrary Loadings

The Rodin and Parks model is based on the results of a differential self-consistent analysis worked out for axisymmetric loadings [*5*]; the results were generalized to arbitrary loadings with the help of an additional simple assumption. Now, the validity of this assumption will be checked by comparing the Rodin and Parks model with the bcc cell model for arbitrary loadings.

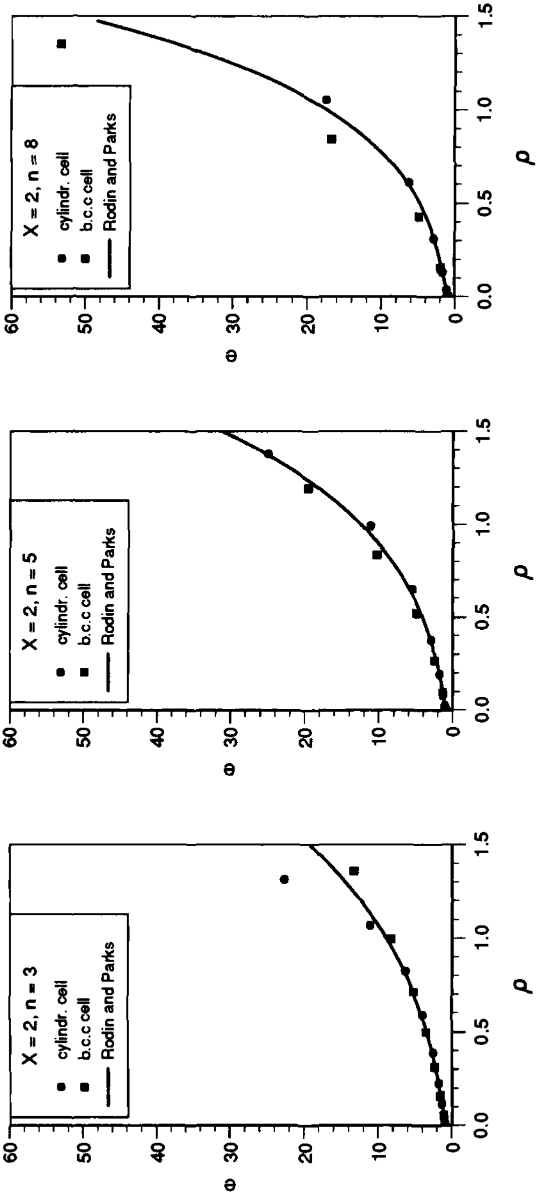

FIG. 4—*Creep enhancement factor* e *as a function of the damage parameter* ρ. *Comparison of cell model calculations (symbols) with Rodin and Parks model (lines) for an axisymmetric stress state with* X = 2.

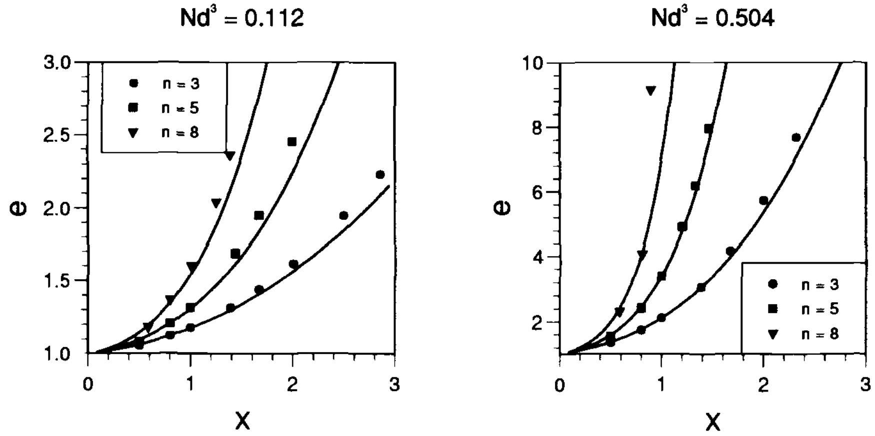

FIG. 5—*Creep enhancement factor* e *as a function of the parameter* X = $\sigma_I/\bar{\sigma}$. *Comparison of bcc cell model calculations (symbols) with Rodin and Parks model (lines) for axisymmetric stress states.*

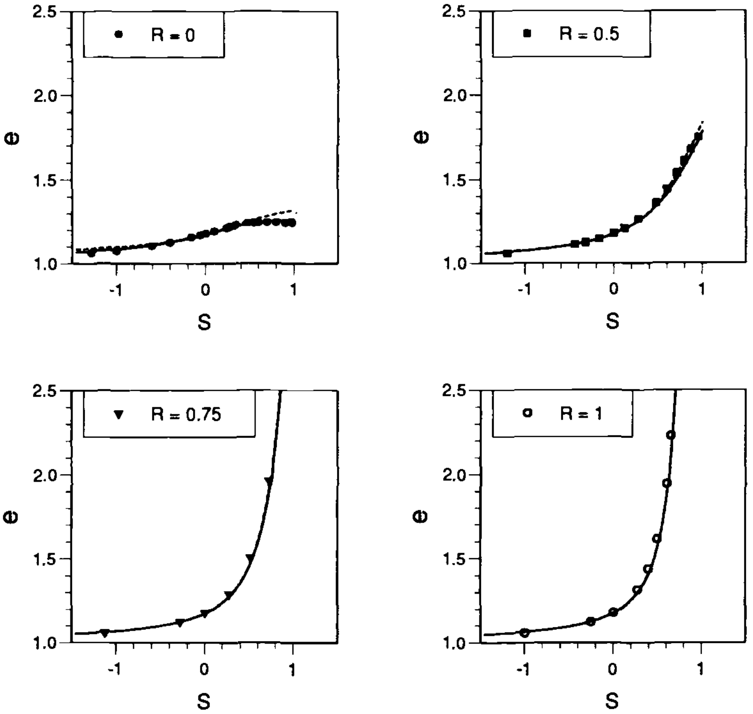

FIG. 6—*Creep enhancement factor* e *as a function of the ratio* S *and* σ_{II}/σ_I *for different values of the ratio* R = σ_{III}/σ_{II}. *Comparison of bcc cell model calculations (symbols) with the Rodin and Parks model (solid lines) and the Rodin and Parks model modified according to Eq 13 (dotted lines) for* n = *3 and* Nd^3 = *0.112.*

In order to bound the numerical effort, only the crack size, $Nd^3 = 0.112$, and the creep exponent, $n = 3$, are considered.

Arbitrary stress states are characterized by the principal stress ratios $R = \sigma_{III}/\sigma_{II}$ and $S = \sigma_{II}/\sigma_{I}$. Figure 6 shows the dependence of the creep enhancement factor e on the parameter S for $R = 0$ (biaxial stress states), $R = 0.5$, $R = 0.75$, and $R = 1$. The stress state is axisymmetric if $R = 1$ or $S = 0$, the latter case being uniaxial tension. The agreement between the cell model results and the analytical model is equally good for all loading conditions.

Hence, we consider the Rodin and Parks model the most advanced micromechanical model for cavitated creeping polycrystals at the time. In the remainder of this paper, a complete constitutive model is formulated on the basis of the Rodin and Parks model and applied to a 12% chromium steel.

Modified Rodin and Parks Model

For practical applications of the Rodin and Parks model, a slight modification of the model was found to be useful. In the original model, Eq 5, the calculation of $\partial\sigma_I/\partial\sigma_{ij}$ is necessary, and this expression is discontinuous when two or three principal stresses are equal. This causes numerical problems.

These problems can be avoided by an ad hoc modification of the model where it is not very realistic anyway. In Eq 5 we replace σ_I by $\sigma_m + 2\bar{\sigma}/3$ (where $\sigma_m = \sigma_{kk}/3$ is the mean stress) and correspondingly $X = \sigma_I/\bar{\sigma}$ by $Y = \sigma_m/\bar{\sigma} + 2/3$. For axisymmetric loading with a fixed principal stress direction, the two formulations are identical. For a variable principal stress direction, neither the original nor the modified Rodin and Parks model are completely appropriate. In reality, cavities will develop on grain boundaries with different orientations depending on the loading history. Contrary to the anisotropy resulting from such an orientation distribution, the modified model is isotropic, whereas the original model is not well defined under these conditions. The original model is based on a uniform orientation of the damaged grain boundaries, but there is no criterion for choosing that orientation when the principal stress direction rotates. Moreover, using the original formulation as it is, Eq 5 implies the assumption that the already damaged boundaries rotate with the principal stress insofar as the original model is also isotropic with the additional drawback of being numerically cumbersome. Hence we prefer to use the modified expression for the inelastic strain rate tensor

$$\dot{\varepsilon}_{ij} = \frac{3}{2\bar{\sigma}}\,\dot{\varepsilon}_s[1 + \alpha(n,\rho)\,Y^2]^{\frac{n-1}{2}}\left\{\left(1 + \frac{2}{3}\,\alpha(n,\rho)\,Y\right)s_{ij} + \frac{2}{9}\,\alpha(n,\rho)\,Y\bar{\sigma}\delta_{ij}\right\} \tag{13}$$

The symbol δ_{ij} is the Kronecker delta, and $\dot{\varepsilon}_s = A\bar{\sigma}^n$.

Figure 6 shows the creep enhancement factors, e, as given by the original and by the modified Rodin and Parks model. The differences are small.

Elastic Response of Microcracked Solids

Budiansky and O'Connell [7] and Hoenig [8] presented self-consistent estimates for the *elastic* response of microcracked solids. Budiansky and O'Connell consider penny-shaped cracks that are randomly spaced and oriented in an isotropic material, while in Hoenig's analysis the cracks are randomly spaced but aligned in parallel planes.

Their results are given in Fig. 7 in terms of the stiffness reduction in axial direction as a function of the ρ parameter, which is $\rho = ½\,Nd^3$ for $n = 1$. The data points in Fig. 7 are the results of linear elastic cell model analyses. As expected, for moderate microcrack densities the cell model results agree well with Hoenig's results for aligned penny-shaped cracks.

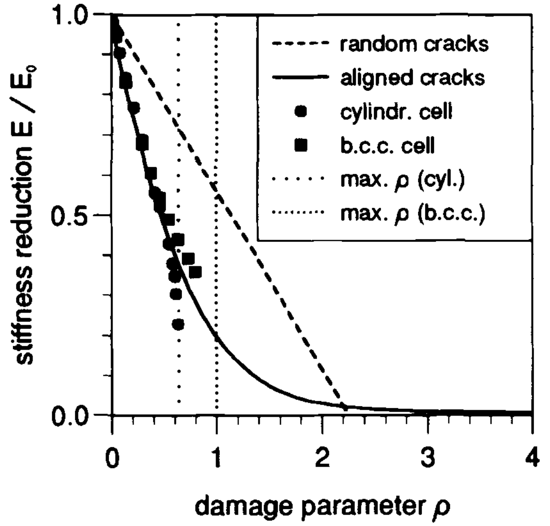

FIG. 7—*Stiffness reduction in axial direction as a function of the damage parameter ρ. Comparison of self-consistent estimates (lines) with cell model calculations (symbols).*

The dotted vertical lines mark the critical ρ values, for which in the cell models neighboring cracks touch each other. These values are $\rho = 2/\pi$ for the cylindrical cell, and $\rho = 1$ for the bcc cell. One would expect that the stiffness of the cell models is reduced drastically as ρ approaches its critical value.

The Complete Constitutive Model

In the previous sections, the effect of damage on the *stationary* creep rate was considered. In order to model transient behavior of the matrix material, the Rodin and Parks model now is combined with the viscoplastic constitutive model of Robinson [9]. The Robinson model is capable of describing essential features of high-temperature inelastic behavior such as primary and secondary creep under constant load, stress relaxation under constant strain, Bauschinger effect, and cyclic hardening under cyclic loading, among other effects.

In the combined Robinson and Rodin and Parks model, the inelastic strain rate tensor, $\dot{\varepsilon}_{ij}$, has the form

$$\dot{\varepsilon}_{ij} = \frac{A(1 + \alpha Y^2)^{\frac{n-1}{2}}}{\sqrt{J_2(\Sigma_{ij})}} \left[\frac{J_2(\Sigma_{ij})}{K} - (1 + \alpha Y^2)^{\frac{-(n+1)}{n}}\right]^{\frac{n}{2}} \left\{\left(1 + \frac{2}{3}\alpha Y\right)\Sigma_{ij} + \frac{2}{9}\alpha Y \overline{\sigma} \delta_{ij}\right\} \quad (14)$$

where J_2 denotes the second invariant of the effective stress Σ_{ij}, which is now defined as $\Sigma_{ij} = s_{ij} - a_{ij}(1 + \alpha Y^2)^{-(n+1)/2n}$. The function $\alpha(n,\rho)$ is given in Eq 8. Equation 14 is valid if both $s_{ij}\Sigma_{ij} > 0$ and $J_2(\Sigma_{ij} > K[1 + \alpha Y^2]^{-(n+1)/n}$ hold, otherwise $\dot{\varepsilon}_{ij} = 0$.

It should be mentioned that the finite element results presented below were obtained using a preliminary version of Eq 14, in which the factor $(1 + \alpha Y^2)^{-(n+1)/n}$ is replaced by 1 in the square brackets and in the definition of the effective stress. This latter formulation has the drawback that the stress is not completely relaxed when the damage parameter becomes large. This deficiency was corrected in Eq 14, but not yet in the finite element program.

The evolution laws for the internal variables, a_{ij} and K, are not changed in comparison to the Robinson model,

$$\dot{a}_{ij} = HG^{-\beta}A\left[\frac{J_2(\Sigma_{ij})}{K} - 1\right]^{\frac{n}{2}} \frac{\Sigma_{ij}}{\sqrt{J_2(\Sigma_{ij})}} - RG^{m-\beta}\frac{a_{ij}}{\sqrt{J_2(a_{ij})}} \tag{15}$$

$$\dot{K} = \frac{K_s - K_i}{3W_0}e^{-W^P/W_0}\dot{W}^P \tag{16}$$

with $\dot{W}^P = \sigma_{ij}\dot{\varepsilon}_{ij}$ and $G = J_2(a_{ij})/\kappa^2$. Equation 15 is valid, if $\Sigma_{ij}a_{ij} > 0$ as well as $G > G_0$, otherwise, G is substituted by G_0 in the first term of Eq 15.

To formulate an evolution equation for ρ, one recalls that cavity nucleation is often strain controlled [*4*]. Using a power law with an exponent γ to describe this, the evolution law becomes

$$\dot{\rho} = \frac{\rho_f}{\varepsilon_f^{\gamma}}\gamma\bar{\varepsilon}^{\gamma-1}\dot{\bar{\varepsilon}}, \text{ with } \dot{\bar{\varepsilon}} = \sqrt{\frac{2}{3}\dot{\varepsilon}_{ij}\dot{\varepsilon}_{ij}} \tag{17}$$

Experiments on creep-resistant ferritic steels give values for γ between 1 and 2 [*10*]. In the present study γ is an adjustable parameter. Its value resulting from the fit to the 12% Cr steel is $\gamma = 1.27$.

In contrast to purely phenomenological damage models, the damage variable ρ in the present model has a clear physical meaning and may be measured by suitable methods. This fact enables us to improve the above evolution equation for damage as more microstructural information becomes available.

Finally, the coupling of the stress rates and the strain rates is given by the differentially formulated Hooke's law

$$\dot{\sigma}_{ij} = E_{ijkl}(\dot{\varepsilon}_{kl}^{\text{tot}} - \dot{\varepsilon}_{kl}) \tag{18}$$

in which E_{ijkl} and $\dot{\varepsilon}_{kl}^{\text{tot}}$ are the tensor of the elastic moduli and the total strain rate tensor, respectively. Although the effect of damage on the elastic response is known (Fig. 7), this effect is neglected in the following applications of the model, and Eq 18 is used with constant elastic moduli. This is justified when elastic strain rates are negligible compared to the inelastic strain rates.

Finite Element Implementation

The above constitutive equations are generalized to finite deformations using Eq 18 as an hypoelastic relation between the elastic strain rate and the Jaumann rate of Cauchy stress. In Eq 18, $\dot{\varepsilon}_{kl}^{\text{tot}}$ is replaced by the symmetric part of the velocity gradient and $\dot{\sigma}_{ij}$ is replaced by the Jaumann rate of Cauchy stress. Equation 14 defines the inelastic contribution to the symmetric part of the deformation gradient.

The constitutive equations were implemented in the finite element code ABAQUS by writing a user material subroutine. The relation between deformation and stress is evaluated using an incrementally objective algorithm proposed by Weber [*11*], suitably generalized to include tensorial state variables [*12*]. For the integration of the first order differential Eqs 14 to 17, an explicit Runge-Kutta method, the Euler backward method, and a "semi-implicit" method analogous to Ref *13* were implemented. In the semi-implicit method, the nonlinear equations of the Euler backward method are approximated by a Taylor series expansion. In the applications that are presented later, the semi-implicit method offers the best compromise between computation cost and accuracy. For further details concerning the numerical method, the reader is referred to Ref *12*.

Adjustment of Model Parameters

The constitutive model is applied to the 12% chromium steel X 20 CrMoV 12 1. The model parameters were adjusted to the results of creep tests performed at 550°C at constant load. In these tests, primary, secondary, and tertiary creep is observed.

The 13 model parameters were optimized *simultaneously* with respect to all eleven creep curves. For details of the optimization method the reader is referred to Ref *14*. The optimized parameter set is given in Table 1. Figure 8 shows that the quality of the fit is generally good apart from the stress range 240 to 275 MPa, where the model underestimates the creep rates by up to a factor 2.

Comparison of Calculated and Measured Load Line Displacement

Finite element computational results have been obtained for two different types of compact tension (CT) specimen: CT specimen with drilled holes and CT specimen with sharp prefatigued cracks. The geometries of these specimens are shown in Fig. 9. The shaded regions are meshed with finite elements.

CT Specimen with Drilled Holes

In these specimens, the stress state in the notch root may be varied by choosing specific hole diameters, D. In Fig. 10, finite element meshes and the computed distribution of the stress state parameter Y in the notch root after load application is shown for two different specimens. In both specimens, the ligament size is $l = 17$ mm. The hole diameters are $D = 10$ mm and $D = 2$ mm, respectively. The peak of the stress multiaxiality Y is higher for the specimen with $D = 2$ mm. On the other hand, for the same external load the Mises equivalent stress $\overline{\sigma}$ in the notch root is smaller for the specimen with $D = 2$ mm due to the higher constraint.

Some experiments at different load levels were performed at 550°C. All available experi-

TABLE 1—*Numerical values of the model parameters.*

Parameter	Numerical Value
A	$9.01 \cdot 10^{-15}$
n	9.23
H	$3.66 \cdot 10^{6}$
κ	$1/\sqrt{3}$ fixed
β	0.882
R	$1.65 \cdot 10^{-7}$
m	0.959
G_0	854
K_s	909
W_0	0.139
K_i	86.2
γ	1.27
$\rho_f/\varepsilon_f^{\gamma}$	114

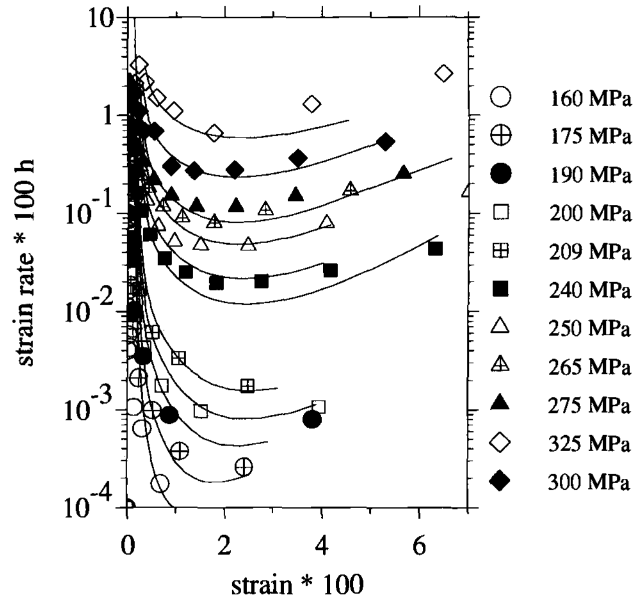

FIG. 8—*Creep data (symbols) and constitutive model (lines).*

mental results are presented in a companion paper [*15*], in which possible modifications of the evolution equation for ρ, Eq 17, are discussed. Here, as an example, only two experiments with $D = 10$ mm and $D = 2$ mm at the same load $F = 8$ kN are considered.

In Fig. 11, measured load line displacements are given together with computational results. The computed displacements are 20 to 40% lower than the measured ones. This can be explained by the limited accuracy of the fit of the material model to the data shown in Fig. 8. The Mises stress in the CT specimen exceeds 230 MPa by over about 25% of the ligament,

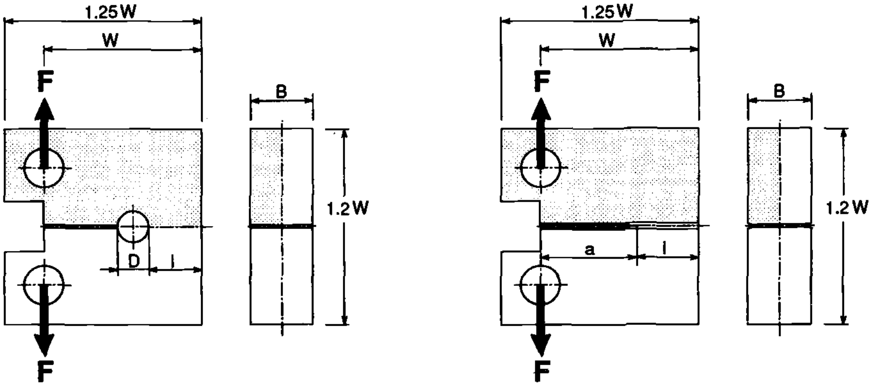

a b

FIG. 9—*Geometry of compact tension specimen. In the experiments,* W *= 50 mm and* B *= 20 mm:* (a) *specimen with a drilled hole;* (b) *specimen with a sharp crack, 20% side grooved.*

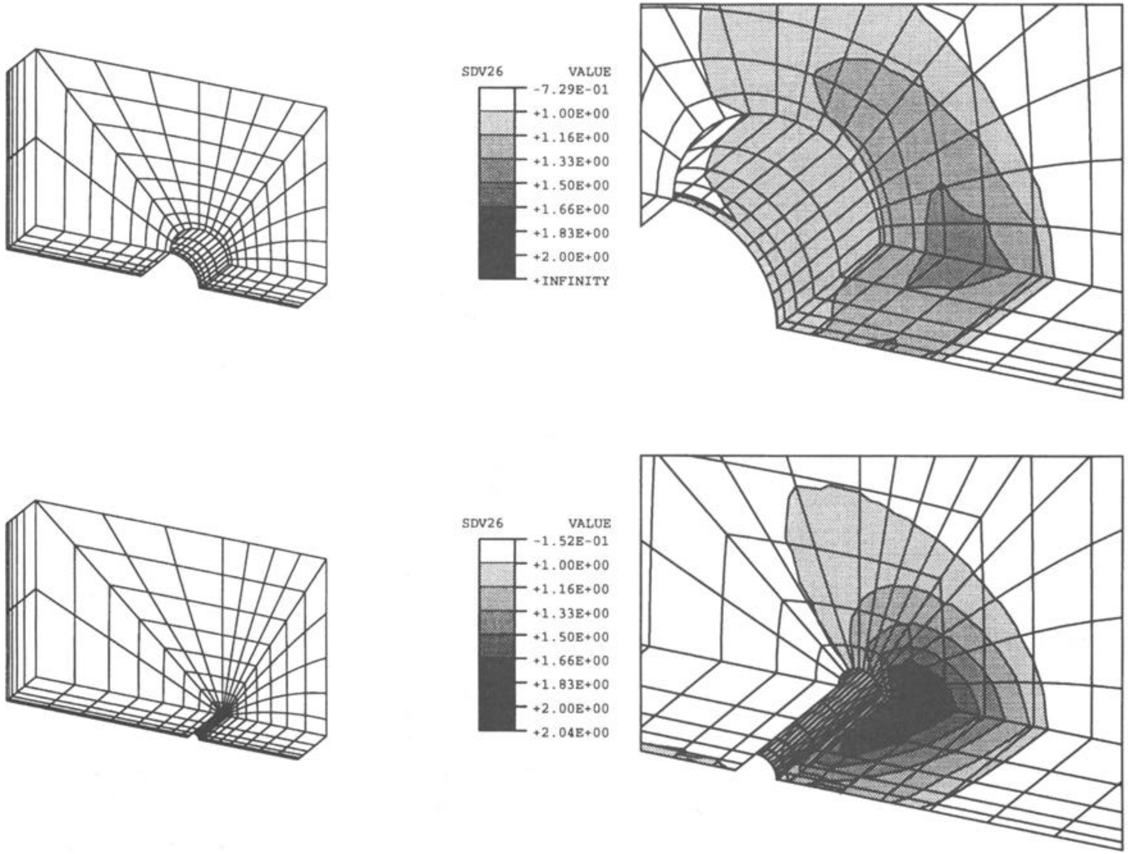

FIG. 10—*Finite element models of CT specimen with a drilled hole. Left: FE models for* D = *10 mm and* D = *2 mm. Right: Computed distribution of the stress state parameter* Y *after load application.*

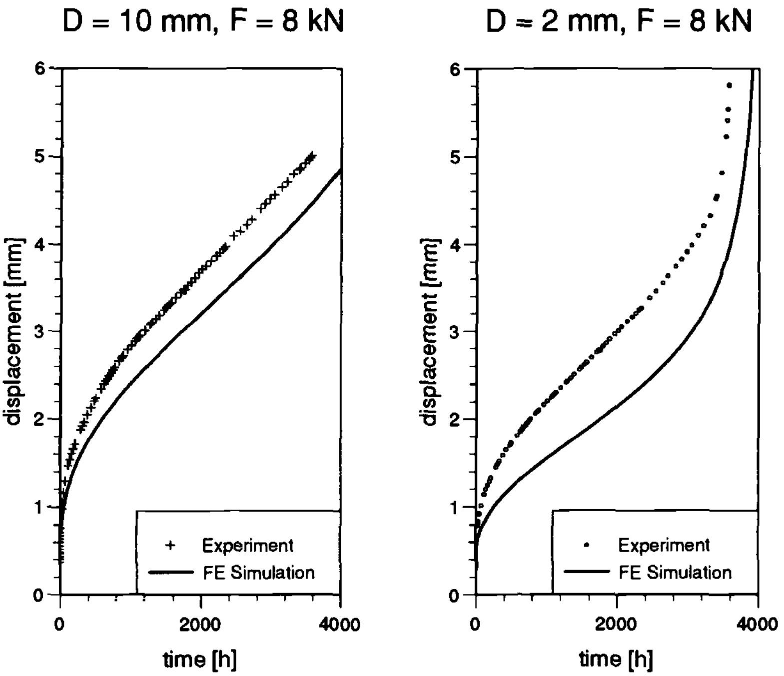

FIG. 11—*Measured and calculated load line displacement for CT specimens with drilled holes.*

and the classical reference stress in the CT specimen [*16*] is 217 MPa (for plane stress). In this stress range and above, the material model underestimates the measured strain rates to an extent that can easily explain the discrepancy between measured and calculated displacements in Fig. 11.

Apart from this discrepancy in absolute values, the calculations reproduce an interesting feature of the measured curves. During the first 2000 h, the measured displacement rates are lower for the specimen with the smaller hole. This is expected since the Mises equivalent stress in the notch region is smaller in this specimen. Later, however, the displacement rate of the specimen with the small hole accelerates, and fracture occurs after about 4000 h. The specimen with the larger hole, on the other hand, continues to creep at a nearly constant rate without any sign of imminent fracture within the test time.

A probable explanation is that initially the greater multiaxial constraint at the smaller hole dominates, while later, when damage develops, the higher multiaxiality leads to a greater creep enhancement factor. Hence the displacement of the specimen with the smaller hole finally overtakes that of the specimen with the larger hole. The calculations predict that crossover qualitatively correctly. This is taken as experimental evidence for the validity of the Rodin and Parks model and the evolution (Eq 17), which was chosen somewhat arbitrarily.

CT Specimen with Sharp Cracks

Four creep crack growth experiments with side-grooved CT specimens were performed at different load levels at 550°C. In these experiments, the load line displacement was measured online, and, in addition, the crack extension was determined after the specimen had been frac-

TABLE 2—*Measured crack extension and computed spread of damaged zone ($\rho > 5$) into the ligament in the CT specimen with sharp cracks.*

Load, kN	Initial Crack Length, mm	Measured Crack Extension, mm	Computed Spread of Damage Zone, mm
$F = 6.2$	30.9	≤ 0.02	...
$F = 9.8$	31.1	0.15	1.5
$F = 12.0$	30.8	1.2	> 3 (after 150 h)
$F = 14.8$	31.2	1.3	> 3 (after 10 h)

tured at room temperature. The loads, the initial crack lengths, and the measured crack extension are given in Table 2.

Computations were carried out with two different finite element models in which the side length of the rectangular elements ahead of the crack tip was 0.3 and 0.6 mm, respectively. Figure 12 shows a comparison of measured and calculated load line displacements in the four tests. For the tests with low load levels, $F = 6.2$ kN and $F = 9.8$ kN, the computed values agree well with the measured values. With increasing load, the discrepancy between computed and measured values is larger.

This discrepancy is linked with an overestimation of crack extension by the computations. In Table 2, the computed extension of the damaged zone into the ligament is given. The damaged zone is defined, somewhat arbitrarily, as the zone where $\rho > 5$. Clearly, the actual creep crack growth is overestimated largely by the computations.

The numerical analysis will be evaluated in terms of the C^* integral in a forthcoming paper.

Discussion and Conclusion

Cell model analyses of a creeping matrix with penny-shaped aligned microcracks give strong support for the analytical Rodin and Parks model that describes the influence of microcracks

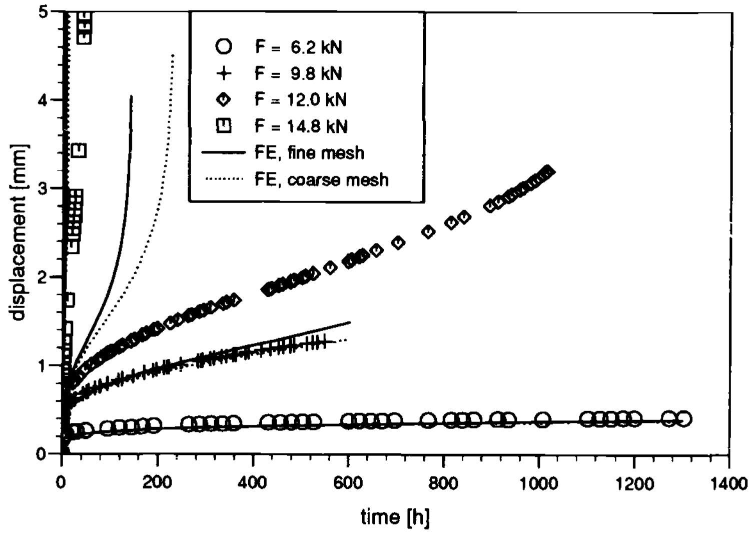

FIG. 12—*Measured and calculated load line displacement for the creep crack growth experiments.*

on the stationary creep rate in closed form. Based on the Rodin and Parks model, a comprehensive material model for creep and plasticity is formulated and applied to creep tests with a compact tension specimen. This material model is a combination of the Rodin and Parks model with the viscoplastic constitutive model of Robinson. It contains an empirical evolution law for the damage parameter, ρ.

At moderate load levels, computed displacements employing this material model agree well with measured values. The observed constraint effects are well reproduced by the model.

In the creep crack growth experiments performed at high load levels, measured displacements and crack extensions are overestimated by the computations. A possible explanation is that for the creep strain rates observed in these experiments, cavity growth may not be constrained. In that case, a basic assumption of the model would be violated.

However, for high levels of strain rate and strain, the available uniaxial creep data used for parameter adjustment are limited. It is expected that the model gives better predictions if the model parameters are adjusted to a wider range of experimental data.

Acknowledgment

We gratefully acknowledge financial support by the Deutsche Forschungsgemeinschaft (DFG) under Contract No. Schm 522/7-2.

References

[*1*] Dyson, B. F., "Constraints on Diffusional Cavity Growth Rates," *Metal Science*, Vol. 10, 1976, pp. 349–353.

[*2*] Rice, J. R., "Constraints on the Diffusive Cavitation of Isolated Grain Boundary Facets in Creeping Polycrystals," *Acta Metallurgica*, Vol. 29, 1981, pp. 675–681.

[*3*] Hutchinson, J. W., "Constitutive Behavior and Crack Tip Fields for Materials Undergoing Creep-Constrained Grain Boundary Cavitation," *Acta Metallurgica*, Vol. 31, 1983, pp. 1079–1088.

[*4*] Riedel, H., *Fracture at High Temperatures*, Springer-Verlag Berlin, Heidelberg, New York, 1987.

[*5*] Rodin, G. J. and Parks, D. M., "A Self-Consistent Analysis of a Creeping Matrix with Aligned Cracks," *Journal of the Mechanics and Physics of Solids*, Vol. 36, 1988, pp. 237–249.

[*6*] Dib, M. W. and Rodin, G. J., "Three-Dimensional Analysis of Creeping Polycrystals Using Periodic Arrays of Truncated Octahedra," *Journal of the Mechanics and Physics of Solids*, Vol. 41, 1993, pp. 725–747.

[*7*] Budiansky, B. and O'Connell, R. J., "Elastic Moduli of a Cracked Solid," *International Journal of Solids and Structures*, Vol. 12, 1976, pp. 81–97.

[*8*] Hoenig, A., "Elastic Moduli of a Non-randomly Cracked Solid," *International Journal of Solids and Structures*, Vol. 15, 1979, pp. 137–154.

[*9*] Robinson, D. N., "A Unified Creep-Plasticity Model for Structural Metals at High Temperature," ORNL report/TM-5969, 1978.

[*10*] Riedel, H., Mohrmann, R., and Sester, M., "Prediction of Residual Lifetime under Simulated Service Loads," COST 501-II Final Report, IWM report Freiburg, 1992.

[*11*] Weber, G. G., Lush, A. M., Zavaliangos, A., and Anand, L., "An Objective Time-Integration Procedure for Isotropic Rate-Independent and Rate Dependent Elastic-Plastic Constitutive Equations," *International Journal of Plasticity*, Vol. 6, 1990, pp. 701–744.

[*12*] Sester, M., Ph.D. thesis, Technische Hochschule Darmstadt, to appear.

[*13*] Peirce, D., Shih, C. F., and Needleman, A., "A Tangent Modulus Method for Rate Dependent Solids," *Computers and Structures*, Vol. 18, 1984, pp. 875–887.

[*14*] Mohrmann, R., Ph.D. thesis, Universitaet Karlsruhe, to appear.

[*15*] Mohrmann, R. and Sester, M., "The Effect of Multiaxial Stress States on the Damage Evolution in a 12% Chromium Steel at 550°C," International Conference on Materials 7, The Hague, The Netherlands, published by Delft University Press, Delft, The Netherlands, 1995.

[*16*] Kumar, V., German, M. D., and Shih, C. F., "An Engineering Approach for Elastic-Plastic Fracture Analysis," Report NP-1931 on Project 1237-1 for Electric Power Research Institute, Palo Alto, CA, 1981.

G. Graham Chell,[1] *Chris J. Kuhlman,*[1] *Harry R. Millwater,*[2] *and David S. Riha*[2]

Application of Reference Stress and Probabilistic Methodologies to Assessing Creep Crack Growth

---

REFERENCE: Chell, G. G., Kuhlman, C. J., Millwater, H. R., and Riha, D. S., "**Application of Reference Stress and Probabilistic Methodologies to Assessing Creep Crack Growth,**" *Elevated Temperature Effects on Fatigue and Fracture, ASTM STP 1297,* R. S. Piascik, R. P. Gangloff, and A. Saxena, Eds., American Society for Testing and Materials, 1997, pp. 54–73.

ABSTRACT: This paper describes the application of the reference stress approach and probabilistic methods to the determination of creep crack growth based on the time-dependent fracture mechanics parameter, $C(t)$, where t is time. This parameter is defined as the simple sum of a transient component, $C(t \rightarrow 0)$, which is applicable to short times and a steady-state component, C^*. The reference stress approach enables a relatively simple expression for C^* to be derived. A scheme is developed that optimizes the fit of the reference stress approach to published computed solutions for J_p, the fully plastic component of the J-integral. The optimization scheme involves the derivation of an engineering parameter, V. An expression for C^* is readily derived from an expression for J_p by invoking the creep-plastic analogy. Values of V are derived from the analysis of 189 sets of computed solutions. These values are statistically analyzed and used to derive a distribution function describing the uncertainty in V. This function is used together with distribution functions for other random variables (such as the creep strain rate coefficient and crack growth law coefficient) in example probabilistic analyses of flaws in welded internally pressurized pipes operating in the creep regime. Probability sensitivity factors are generated as part of the probabilistic analyses.

KEYWORDS: creep crack growth, reference stress, remaining life, weld mismatch stress, probabilistic analysis, probability sensitivity factors

A time-dependent fracture mechanics parameter that correlates creep crack growth data for different cracked geometries and loading systems is essential if laboratory-measured data are to be used in the assessment of structural components. Although the stress intensity factor, K, has been used to successfully correlate cyclic and environmental cracking, it fails to adequately correlate creep crack growth data [*1*]. Under static loading conditions, the parameter that seems to have the most success in correlating creep crack growth rates is the steady-state time dependent fracture mechanics parameter, C^* [*1*], originally proposed by Landes and Begley [*2*] based on the creep-plastic analogy and the plastic fracture mechanics parameter, J, derived by Rice [*3*]. The creep-plastic analogy states that the steady-state creep solution can be obtained from an equivalent fully plastic solution by replacing the plastic strains and displacements by

---

[1] Institute scientist and senior research engineer, respectively, Materials Engineering Department, Southwest Research Institute, 6220 Culebra Road, San Antonio, TX 78238-5166.

[2] Senior research engineer and research engineer, respectively, Aerospace and Reliability Engineering Department, Southwest Research Institute, 6220 Culebra Road, San Antonio, TX 78238-5166.

their time derivatives. However, by definition, the steady-state solution for C^* corresponding to secondary creep does not explicitly contain the time, t. Ehlers and Riedel [*27*] and Riedel [*4*] investigated a parameter, $C(t \rightarrow 0)$, which characterizes creep crack tip fields under transient conditions at short times where $C(t \rightarrow 0) \gg C^*$, and stress relaxation is occurring due to the substitution of creep strains for elastic strains. The two parameters can be linearly added to provide a simple, approximate expression for a parameter, $C(t)$, which is applicable for all times, t,

$$C(t) = C(t \rightarrow 0) + C^* \tag{1}$$

From Riedel [*4*]:

$$C(t \rightarrow 0) = \frac{J_e}{(m + 1)t} \tag{2}$$

where J_e is the linear elastic value of the J-integral given by

$$J_e = \frac{K^2}{E'} \tag{3}$$

where K is the stress intensity factor; $E' = E$; Young's modulus, in plane stress, $E' = E/(1 - \nu_e^2)$ in plane strain; and ν_e is Poisson's ratio. The parameter m is the exponent in Norton's law:

$$\dot{\varepsilon} = A\sigma^m \tag{4}$$

where A is a material constant, and σ is the applied stress.

The evaluation of C^* is more complicated. It is usually determined from fully plastic solutions for J_p, the plastic component of J, by invoking the creep-plastic analogy. Fortunately, a wide variety of J_p solutions have been derived under EPRI sponsorship using finite element methods for materials obeying the Ramberg-Osgood stress-strain constitutive law of the form

$$\frac{\varepsilon_p}{\varepsilon_o} = \alpha\left[\frac{\sigma}{\sigma_o}\right]^n \tag{5}$$

where ε_p is the plastic strain, σ is the applied stress, and ε_o, σ_o, α, and n are material constants [*5–7*].

The reference stress approach developed by Ainsworth [*8*] provides an alternative method for estimating J_p and hence C^*, which is closely related to the EPRI scheme. This method provides a powerful analytical tool for deriving solutions for J_p and hence C^* in cases where alternative computational solutions are not available.

A deterministic estimate of the life of a structure containing a creeping crack is obtained by integrating over time a crack growth rate law of the form

$$\frac{da}{dt} = B\,C(t)^q \tag{6}$$

where B and q are material constants. However, a deterministic approach can frequently lead to unacceptably low remaining life predictions because of the need to utilize conservative assessment data in order to avoid failure. In contrast, a probabilistic analysis enables uncertainties in assessment data to be represented as probability density functions that allow the corresponding uncertainties in calculated lifetimes to be quantified and used to define the reliability of a cracked component for further service.

The probability of failure for a specified extended operating time can play a major role in decision analysis related to the disposition of cracked components, the prioritization of components for maintenance, and economic considerations of whether to run, repair, or replace [*9*].

In this paper, the accuracy of Ainsworth's reference stress expression for C^* is investigated by determining the explicit dependence of C^* on engineering parameters. This is accomplished using the EPRI handbook and other published solutions for J_p and the creep-plastic analogy. A scheme is developed for deriving an optimum reference stress solution that provides the best fit to the computed solutions for J_p for a range of n values given a specific flawed structural geometry and loading system. The optimization procedure enables an "optimized" yield load, P_o^*, to be derived from the computed solutions, together with an engineering parameter, V. When $V = 1$, Ainsworth's reference stress approximation is recovered.

Discussion is also made concerning the transient and steady-state stress contributions to $C(t \rightarrow 0)$ and C^*, particularly the role of weld-related stresses such as those generated by a mismatch in creep rates between weld and base metals. In addition, consideration is given to the formulation of a probabilistic methodology for creep crack growth based on the reference stress approach and a statistical analysis of the distribution of derived values for V. Example calculations are performed to determine the probability of failure, P_f, as a function of service life using the NESSUS probabilistic computer program [*10*] interfaced with a deterministic creep-fatigue crack growth module developed at Southwest Research Institute. The advanced probabilistic analysis methods contained in the NESSUS program allow probability sensitivity factors (PSFs) to be determined, which in turn enable key random variables to be identified. Other creep crack growth calculations are performed to ascertain the consequences of restricting crack shape development of surface flaws to a constant aspect ratio compared with allowing the aspect ratio to vary as the crack grows.

Estimating *C*(*t*)

Determining C* *using the EPRI Estimation Scheme*

A widely used representation of J_p within the EPRI estimation scheme is [*5–7*]

$$J_P = \alpha\sigma_o\varepsilon_o c\left[\frac{a}{b}\right]h_1\left(\frac{a}{b},n,D\right)\left[\frac{P}{P_o}\right]^{n+1} \qquad (7)$$

where a is the crack depth, b is the section thickness, and $c = b - a$ is the uncracked ligament. Values for the functions h_1 are tabulated in the EPRI handbooks [*5–7*] for various structural geometries and depend on a/b, n, and, in general, on a normalized geometry parameter, D, that is related to the structure. (For example, in the case of a cylinder $D = R/b$, where R is the mean radius of the cylinder.) P is the applied load, and P_o a characteristic yield load defined for each structural geometry and load type in the EPRI handbooks.

By comparing Eqs 4 and 5, the creep-plastic analogy enables the creep solution for C^* to be derived by replacing n by m and $\alpha\varepsilon_o/\sigma_o^n$ by A in Eq 7. The result is

$$C^* = Ac\left[\frac{a}{b}\right]h_1\left(\frac{a}{b},m,D\right)\left[\frac{P\sigma_o}{P_o}\right]^{m+1} \qquad (8)$$

Determining C using the Reference Stress Approach*

One of the aims of the reference stress approach developed by Ainsworth [*8*] is to choose a yield load, P_o^*, so that the function $h_1(a/b,n,D)$ that appears in the EPRI scheme for J_p can be replaced by an alternative function, $h_1^*(a/b,D)$, which no longer depends on n or m (see also Refs *11* and *12*). In terms of the reference stress parameters P_o^* and h_1^*, J_p is written as

$$J_p = \alpha\sigma_o\varepsilon_o c\left[\frac{a}{b}\right]h_1^*\left(\frac{a}{b},D\right)\left[\frac{P}{P_o^*}\right]^{n+1} \tag{9}$$

Hence, the reference stress approximation to C^* is obtained as

$$C^* = c\left[\frac{a}{b}\right]h_1^*\left(\frac{a}{b},D\right)A\sigma_{ref}^{m+1} \tag{10}$$

The reference stress, σ_{ref} is defined through the equation

$$\sigma_{ref} = \left[\frac{P}{P_o^*}\right]\sigma_o \tag{11}$$

The term $A\sigma_{ref}^m$ represents the reference strain rate, $\dot{\varepsilon}_{ref}$, and hence Eq 10 can be written in a form that no longer explicitly depends on the Norton law creep rate constitutive relationship

$$C^* = c\left[\frac{a}{b}\right]h_1^*\left(\frac{a}{b},D\right)\sigma_{ref}\dot{\varepsilon}_{ref} \tag{12}$$

Ainsworth [*8*] made the simplifying approximation that $h_1^* = h_1(n = 1)$. This approximation enables h_1^* to be expressed in terms of the linear elastic solution for J_e since $J_p(n = 1) = \mu J_e$, where $\mu = (1 - \nu_p^2)/(1 - \nu_e^2)$ in plane strain, and $\mu = 1$ in plane stress, and ν_e and ν_p are the elastic and plastic values of Poisson's ratio, respectively. The result is

$$h_1^* = \frac{E\mu J_e}{\left[c\,\frac{a}{b}\right]\sigma_{ref}^2} \tag{13}$$

which, when substituted into Eq 12, yields his reference stress approximation for C^*

$$C^* = \mu E J_e\,\frac{\dot{\varepsilon}_{ref}}{\sigma_{ref}} \tag{14}$$

This result provides a simple and powerful approximate expression for evaluating C^* over a much greater range of structural and engineering parameters than is presently possible using the existing EPRI handbook solutions for J_p. The expression implies that the dependence of C^* on engineering parameters is fully accounted for by the dependence of J_e and σ_{ref} on these parameters, and that the dependence on creep deformation is simply derived from the constitutive relationship between creep strain rate and stress.

Contribution of Steady-State and Secondary Stresses to C(t)

Secondary stresses that relax with time have to be treated differently from steady-state stresses when evaluating $C(t)$. Examples of secondary stresses are residual welding stresses and thermally induced stresses. An example of a steady-state stress is a pressure-induced stress. An example of a steady-state secondary stress is that due to a mismatch in creep rates between base and weld metals. (The latter stresses have been studied in Refs *13* and *14*. These results show that a stress concentration builds up with increasing time and eventually attains a steady-state value in the region of the weld-base metal boundary. Steady-state stresses can also be induced at longitudinal welds where the cross section of the welded pipe deviates from circularity. These "peaking" stresses have been calculated for a particular pipe configuration before and after creep relaxation has occurred over 100 000 h of steady pressure loading [*15*].)

Secondary stresses that relax with time should be included in the evaluation of $C(t \rightarrow 0)$, but not in the evaluation of C^*. However, steady-state stresses should be included in the evaluation of both. It is conservative to ignore the effect of the relaxation of secondary stresses with time and to evaluate $C(t \rightarrow 0)$ using the stress distributions derived before stress relaxation begins. Steady-state stresses should be included in $C(t \rightarrow 0)$ because they contribute to the transient stress field at the crack tip, which is relaxed by creep deformation.

Transient and steady-state self-equilibrated stresses contribute to $C(t)$ through their contribution to K, but only primary stresses, such as those induced by pressure, contribute to the evaluation of the reference stress, σ_{ref}.

Derivation of an Optimum Reference Stress Solution

In this section, an "optimized" reference stress solution to J_{p} (and hence C^*) is constructed such that h_1^* is independent of the strain-hardening exponent, n. The expression for the reference stress solution for C^* involves a yield load, P_{o}^*, a function h_1^*, and a function $V(a/b,D)$. The values of these functions are derived using a simple scheme that optimizes the accuracy of the reference stress solution to reproduce known computed values of $h_1(a/b,n)$ for a range of exponents, n. Hence, the derived values of P_{o}^* and h_1^* are sometimes prefixed by the adjective "optimum" to differentiate them from values obtained using alternative methods.

Since $J_{\mathrm{p}}(n = 1) = \mu J_{\mathrm{e}}$, it cannot depend explicitly on either the yield loads P_{o} or P_{o}^*. Hence, the solutions for $n = 1$ are not used directly in the proposed optimization scheme.

An expression for h_1^* is obtained by comparing Eqs 7 and 9:

$$h_1^*\left(\frac{a}{b},D\right) = h_1\left(\frac{a}{b},n,D\right)\left[\frac{P_{\mathrm{o}}^*}{P_{\mathrm{o}}}\right]^{n+1}, \quad n \geq 2 \tag{15}$$

Although n appears in the terms on the right-hand side of this equation, the purpose of the optimization scheme is to make the product of these terms independent of n. Rearranging Eq 15 yields

$$P_{\mathrm{o}}^*(n) = P_{\mathrm{o}}\left[\frac{h_1^*\left(\frac{a}{b}\right)}{h_1\left(\frac{a}{b},n\right)}\right]^{\frac{1}{n+1}}, \quad n \geq 2 \tag{16}$$

where $P_o^*(n)$ are yield loads whose values are to be determined. The dependence of $P_o^*(n)$ on n is introduced intentionally to reflect numerical inaccuracies that occur in the computation of $h_1(a/b,n)$. If these errors were absent, then according to the reference stress approach the optimum yield load, P_o^*, would be independent of n. The aim of the optimization scheme is to reduce the dependence of the calculated $P_o^*(n)$ values on n by judicious choice of h_1^* while at the same time reproducing the computed values of $h_1(a/b,D,n)$ as closely as possible.

Equation 16 cannot be solved directly for $P_o^*(n)$ as the value of h_1^* is not known a priori. Instead, h_1^* is treated as a variational parameter whose value is chosen so as to minimize the dependence of $P_o^*(n)$ on n. Hence, the value of h_1^* is varied until a "sample variance" parameter, ρ, attains a minimum value, where

$$\rho = \sum_{n\geq 2} (P_o^*(n) - P_o^*)^2 \tag{17}$$

and the required optimum yield load, P_o^*, is given by

$$P_o^* = \frac{1}{N}\sum_{n\geq 2} P_o^*(n) \tag{18}$$

where N is the number of n values for which computed J_p solutions are available. Bloom [*11*] has used a similar scheme to derive yield loads from computed solutions for J_p, but he, like Ainsworth [*8*], assumed $h_1^* = h_1(n = 1)$, which does not necessarily optimize the accuracy of reference stress solution to reproduce the J_p solutions.

Once P_o^* and h_1^* have been determined, the value of $h_1(a/b,n)$ can be estimated for any value of n through the equation

$$h_1\left(\frac{a}{b},n\right) = h_1^*\left(\frac{a}{b}\right)\left[\frac{P_o}{P_o^*}\right]^{n+1}, n \geq 2 \tag{19}$$

Since $h_1(a/b,n = 1)$ is not used in the optimization scheme, it is not related to h_1^* through P_o^*, but through another parameter, $P_o^*(1)$, where

$$P_o^*(1) = P_o\left[\frac{h_1^*(a/b)}{h_1(a/b,n = 1)}\right]^{1/2} \tag{20}$$

Hence, from Eq 19:

$$h_1\left(\frac{a}{b},n\right) = h_1\left(\frac{a}{b},n = 1\right) V(a/b,D)\left[\frac{P_o}{P_o^*}\right]^{n-1} \tag{21}$$

where the parameter, V, is given by

$$V(a/b,D) = \left[\frac{P_o^*(1)}{P_o^*}\right]^2 = \frac{h_1^*(a/b,D)}{h_1(a/b,n = 1,D)} \tag{22}$$

Using the parameter, V, and Eqs 9 and 21, J_p can be written for $n > 1$ as

$$J_p = J_e \mu V(a/b,D)\ \alpha \left[\frac{P}{P_o^*}\right]^{n-1} \tag{23}$$

Equation 23 establishes the relationship between the plastic and elastic components of J. Furthermore, using the Ramberg-Osgood law and the reference stress, σ_{ref}, given in Eq 11, Eq 23 can be rewritten as

$$J_p = J_e \mu V(a/b,D) \left[\frac{E\varepsilon_{ref}^p}{\sigma_{ref}}\right] \tag{24}$$

where ε_{ref}^p is the reference plastic strain corresponding to the value of σ_{ref} on the uniaxial stress-strain curve. Note that J_p has been expressed in a form that is applicable to materials with arbitrary stress-strain behavior. This is an important benefit of the reference stress approach.

The equivalent expression for C^* is

$$C^* = J_e \mu V(a/b,D) \left[\frac{E\dot{\varepsilon}_{ref}}{\sigma_{ref}}\right] \tag{25}$$

which shows that the simplified form of the reference stress approximation represented by Eq 14 is only exact when $V(a/b,D) = 1$.

Validation of the Optimization Scheme

Examples of the ability of the optimization scheme to accurately represent the finite element solutions for $h_1(a/b,n)$ in terms of $h_1^*(a/b)$ and optimum yield loads is shown in Figs. 1 and 2. These figures show the computed values of $h_1(a/b,n)$ obtained from Ref *5* and Ref *16* for an

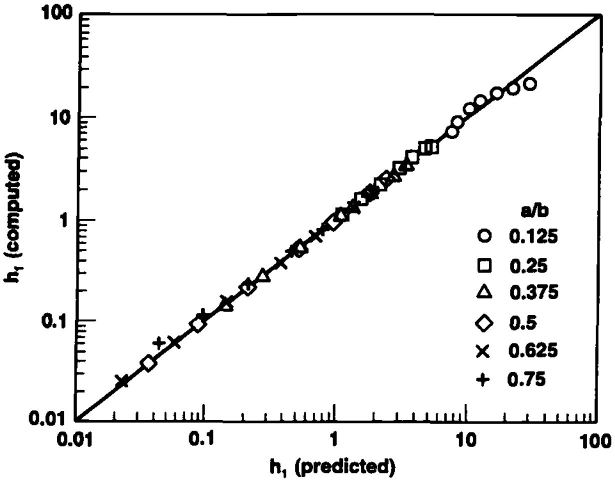

FIG. 1—*Comparison of computed plane strain values of the* $h_1(a/b,n,D)$ *functions for a single-edge-cracked plate in tension for* $n = 2, 3, 5, 7, 10, 13,$ *and 16 with the predictions of the reference stress approach derived using the optimization scheme.*

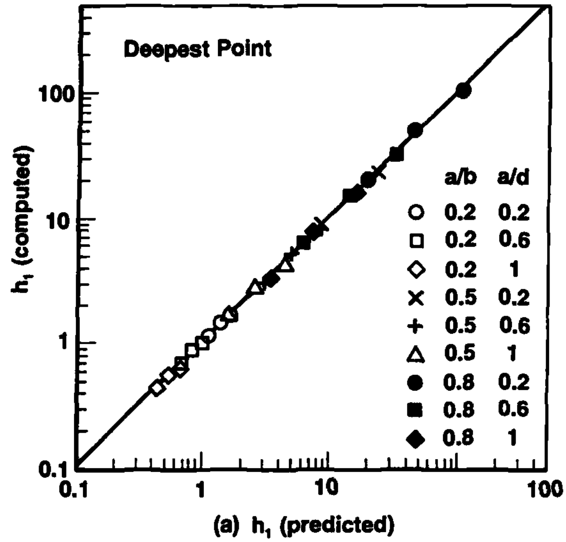

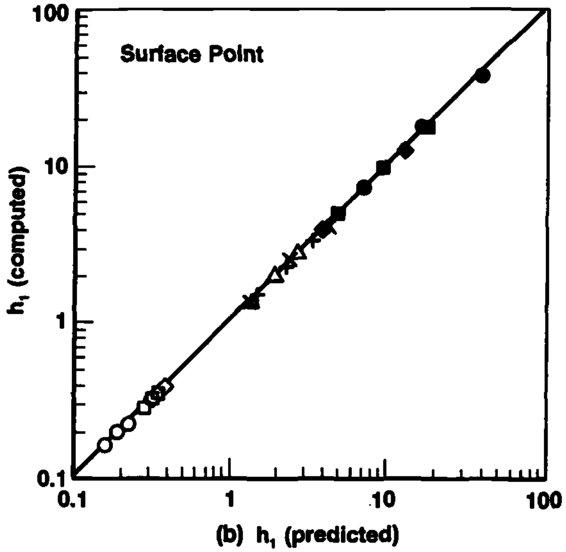

FIG. 2—*Comparison of computed values of the* $h_1(a/b,n,D)$ *functions for a surface flaw in a plate subjected to tension for* $n = 5$*, 10, and 15 with the predictions of the reference stress approach derived using the optimization scheme:* (a) *results for the deepest point on the flaw;* (b) *results for the surface point.*

edge-cracked plate in plane strain subjected to tensile loading (Fig. 1) and for a surface semi-elliptical flaw in a plate subjected to a tensile force (Fig. 2), respectively, plotted against the values predicted using Eq 21. The nearness of the points to the one-to-one line indicates the accuracy of the optimum yield approach: predictions that fall on the line are exact. The results in Fig. 1 cover six crack depths in the range $0.125 \leq a/b \leq 0.75$ and seven strain-hardening exponents in the range $2 \leq n \leq 16$. The results in Fig. 2 include three crack depths in the range $0.2 \leq a/b \leq 0.8$, three aspect ratios in the range $0.2 \leq a/d \leq 1$ where d is half the surface length, and three n values in the range $5 \leq n \leq 15$, and are presented for the deepest point (Fig. 2*a*) and the surface points (Fig. 2*b*) on the flaws.

It can be seen that the optimized reference stress method predicts $h_1(a/b,n)$ values that are in very good agreement with the computed results. The accuracies indicated in Figs. 1 and 2 are typical of the accuracies with which the method reproduces the values of $h_1(a/b,n)$ for other cracked geometries and loading systems.

Statistical Analysis of Calculated Values of *V*

To determine the dependence of V on engineering parameters, values of V and P_o^* have been derived for an extensive assortment of structural geometries, crack shapes and sizes, and applied load types from published finite element results for the function $h_1(a/b,n,D)$. The determination of the values of V and P_o^* that produce the best agreement between the reference stress approximation to J_p and the computed solutions requires that values of $h_1(a/b,n,D)$ be available for a range of strain-hardening exponents, n. From these solutions for different n, single values for V and P_o^* can be derived for a specific set of engineering features.

In all, 189 values of $V(a/b,D)$ were derived from computed $h_1(a/b,n,D)$ values for the following flawed structural geometries and engineering parameters:

Two-dimensional geometries:
1. Single edge cracks in plates subjected to tensile loads (plane stress and plane strain) [*5*].
2. Double edge cracks in plates subjected to tensile loads (plane stress and plane strain) [*5*].
3. Single edge cracks in plates subjected to bending (plane stress and plane strain) [*5*].
4. Center-cracked plates (plane stress and plane strain) [*5*].
5. Cracks emanating from an embedded round hole subjected to biaxial stressing [*5*].
6. Part-through axially cracked cylinders subjected to internal pressure [*5*].
7. Part-through circumferential cracks in cylinders subjected to tensile forces [*5*].

Three-dimensional geometries:
1. Circumferential through-wall cracks in cylinders subjected to tensile forces [*6*].
2. Circumferential through-wall cracks in cylinders subjected to applied moments [*6*].
3. Semi-elliptical flaws (deepest point) on the internal surface of a cylinder subjected to internal pressure [*17*].
4. Semi-elliptical flaws (deepest, surface, and near-surface points) in plates subjected to tensile forces [*16,18–20*].
5. Semi-elliptical flaws (deepest, surface, and near-surface points) in plates subjected to bending [*18*].

The minimum calculated value for V was 0.6, and the maximum was 2.3. It is emphasized that the variation in the values of the derived V values for different structural and engineering parameters reflects not only real explicit dependencies of V on these parameters, but also apparent dependencies due to uncertainties in the computed numerical values of h_1 and inaccuracies introduced by the method employed for deriving the fully plastic J_p solutions from the actual computed values of J, which included both linear elastic and first-order plastic components. Thus, significant differences in V values were sometimes observed in J_p values obtained by different workers for the same geometry, crack size, and load type. For example, this was the case for some of the results reported in Refs *16* and *18* for surface semi-elliptical flaws in plates. Other workers, such as Bloom and Lee [*17*], have also commented on the need for care when deducing the fully plastic component of J from its elastic-plastic value. Criteria for assessing the accuracy of computed fully plastic J_p solutions have been discussed in Ref *21*, which also discusses the accuracy of the reference stress approach in terms of load factors required to make the results of this method equal to computed solutions for J_p.

It is of interest to note that, although there are differences between the values of J_p computed by different workers for nominally the same cracked structure, within any particular set of results the values of h_1 still appear to scale as the ratio $h_1^*(P/P_o^*)^{n+1}$, even though the derived values of P_o^* may differ between sets.

The 189 derived V values were statistically analyzed by separating the data into three groups corresponding to:

1. All the data (189 samples).
2. The values of the deepest points on both the two-dimensional (108 samples) and three-dimensional (24 samples) flaws (a total of 132 samples).
3. The values for the surface (24 samples) and near-surface (33 samples) points for the three-dimensional semi-elliptical flaws (a total of 57 samples). The near-surface points corresponded to positions on the flaws at angles of 9, 10, and 18° from the free surface.

The samples in Groups 1 through 3 were statistically examined using the normal, exponential, Weibull, extreme value, and lognormal distributions. From the results of this analysis, the following conclusions were drawn:

1. Based on statistical tests [*22*], the cumulative distribution function that best described the data in Groups 1 through 3 is the Type 1 extreme value distribution (EVD). The cumulative distribution function for the Type 1 EVD is

$$F_X(x) = \exp[-\exp(-\alpha'[x - \beta'])] \tag{26}$$

where α' and β' are related to the mean, μ_x, and standard deviation, σ_x, by the equations

$$\mu_x = \beta' + \frac{0.577}{\alpha'}, \quad \sigma_x = \frac{1.283}{\alpha'} \tag{27}$$

The values of α', β', μ_x, and σ_x for each of the data samples in the three groups are shown in Table 1. The form of the empirical and derived distributions for the Group 1 data are shown in Fig. 3. The empirical distribution function was determined by the formula $F_i(v) = \frac{(i - ½)}{n}$, for $v_i \leq v < v_{(i+1)}$, in which v_i is the ith smallest value of V [*22*].

2. A linear regression analysis of the V values in Groups 2 and 3 corresponding to the deepest and surface points on three-dimensional semi-elliptical flaws indicated that the values at these two positions were not correlated (the correlation coefficient was approximately 0.01).

TABLE 1—*Type 1 EVD parameter values derived from the sample* V *values in Groups 1 through 3.*

Group	α'	β'	μ_x	σ_x
1	4.4018	1.0380	1.1691	0.2915
2	4.1776	1.0363	1.1744	0.3071
3	4.9563	1.0428	1.1592	0.2426

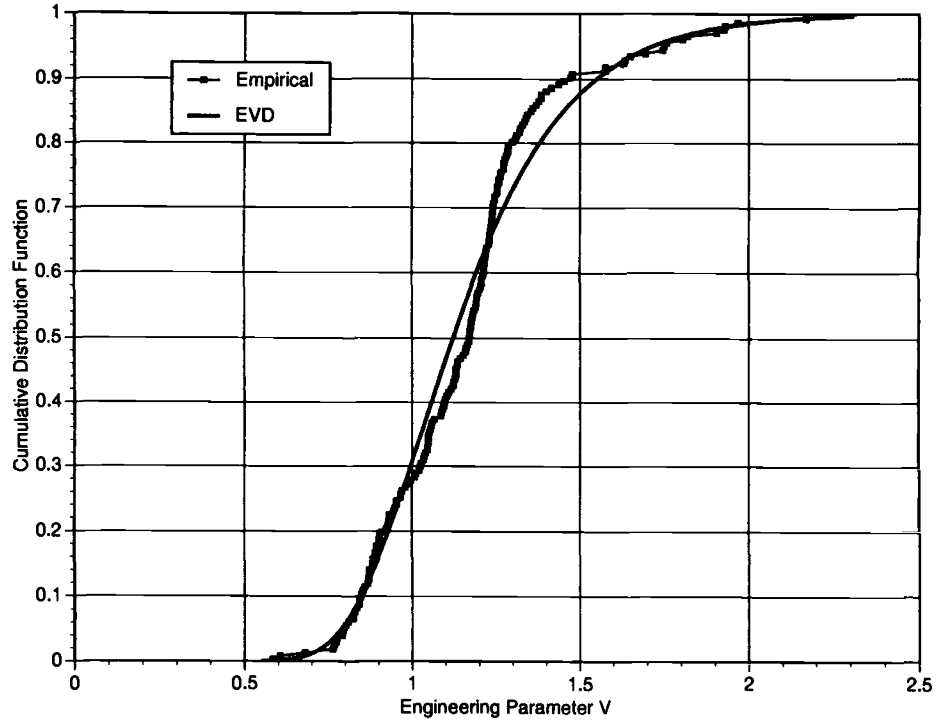

FIG. 3—*Cumulative distribution function for the engineering parameter,* V, *for Group 1 data. The Type 1 extreme value distribution best fits the empirical distribution of the derived values of* V.

Example Application: A Welded Pipe

The creep crack growth methodology is applied to calculating the remaining lives of flawed longitudinal welds in high-temperature pipes subjected to a constant internal pressure. A schematic of a welded pipe is shown in Fig. 4. The creep rates of the weld and base metals are assumed to be different, and this gives rise to a steady-state self-equilibrated stress distribution through the wall of the pipe that superposes on the hoop membrane stress, *RP/t,* due to the

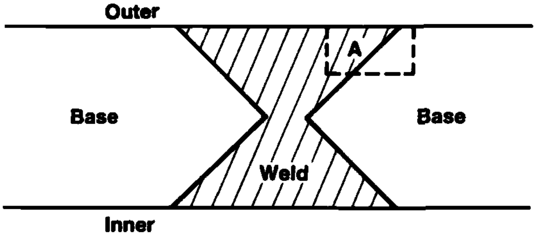

FIG. 4—*Schematic of section through a welded pipe showing Region A, which contained the surface flaws analyzed.*

internal pressure, P. R is the mean radius of the pipe and t is the wall thickness, taken to be 13.125 in. (333.4 mm) and 1.25 in. (31.75 mm), respectively. The internal pressure is assumed to be 700 psi (4.83 MPa) and the metal temperature 1000°F (538°C).

The calculations were performed for cracks emanating from the outer surface of the pipe in Region A, shown in Fig. 4. The cracks were variously assumed to be in the base or weld metal and to take on material properties consistent with these materials or in a region local to the weld-base metal interface (e.g., the heat-affected zone) that had properties different from the base and weld metals.

The work reported in Ref *14* shows that the peak values of the creep mismatch stress can occur at the surfaces of the pipe or in the interior, depending on whether the ratio $r = \dot{\varepsilon}_b/\dot{\varepsilon}_w$ is greater or less than 1, where $\dot{\varepsilon}_b$ and $\dot{\varepsilon}_w$ are the base metal and weld metal creep rates, respectively. Although both Refs *13* and *14* have investigated the form of the mismatch stresses, only a very limited number of solutions are reported, these mainly in the form of the stress concentration factors due to the creep rate mismatch rather than specific stress distributions through the pipe wall. Furthermore, the number of weld geometries analyzed is restricted to double-V type welds such as the one shown in Fig. 4 and cover only a very limited range of geometries within this class of welds.

These limited stress solutions were used to construct the approximate normalized stress distributions shown in Fig. 5. It is emphasized that, although this stress distribution is chosen mainly for calculational convenience, it contains the essential features of more specific stress distributions in terms of where the peak stress occurs and the self-equilibrated nature of the stress. In order to facilitate calculations, the two normalized distributions are assumed to remain invariant with changes in the ratios of the base and weld metal strain rates in the two regions defined by $r > 1$ and $r < 1$, respectively. The assumption of invariance was necessary given the dearth of stress distribution data available as a function of r.

Although the mean values of the base and weld metal strain rates used in the example calculations correspond to $r > 1$, the stress distribution for $r < 1$ is still needed for the probabilistic analysis because there is a finite probability of $r < 1$ occurring.

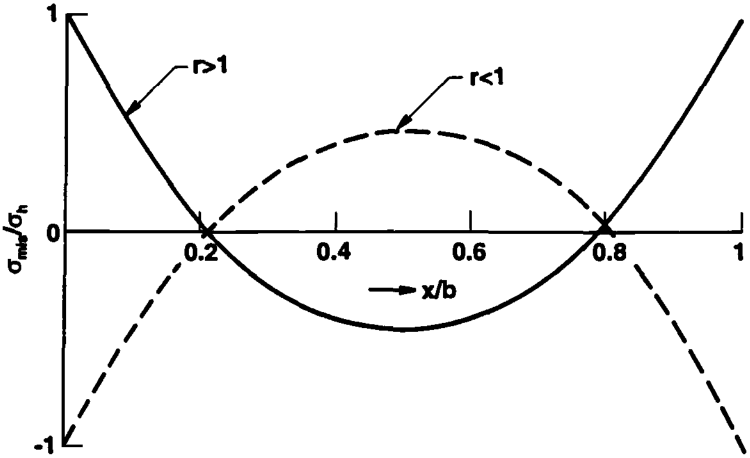

FIG. 5—*Normalized weld mismatch stress distributions used in the example application. The origin,* x/b *= 0, is at the outer surface.*

The peak value of the mismatch stresses are determined by a concentration factor, K_t, which, for a specific weld geometry, is a function of r. The relationship between r and K_t used in the example calculations is illustrated in Fig. 6. The stress distribution in the region of the weld, including the hoop membrane stress, is

$$\sigma\left(\frac{x}{t}\right) = \sigma_h\left[1 + (K_t - 1)\,\sigma^*_{mis}\left(\frac{x}{t}\right)\right] \tag{28}$$

In the probabilistic calculations, this stress takes on random values through its dependence on K_t, which in turn depends on the value of r, which will take random values if the base and weld metal strain rates are random variables.

The example calculations were performed using a deterministic creep-fatigue crack growth computer program, COBRA Version 4.0, interfaced with NESSUS [*10*], which can perform a range of probabilistic analyses based on Monte Carlo methods and more advanced methods such as the first order reliability method (FORM) [*23*], the advanced mean value (AMV) [*24*], and the adaptive importance sampling (AIS) [*25*]. Both of these programs have been developed and enhanced by Southwest Research Institute over recent years.

COBRA Version 4.0 contains a library of fracture mechanics solutions that enable the stress intensity factors, K, and reference stresses, σ_{ref}, to be determined for surface and embedded flaws. The stress intensity factors are calculated using a module, KCALC, which contains a library of influence functions for cracks in stress gradients. These solutions are not readily represented by simple analytical expressions.

Although the optimized reference stress approach provides statistical information about the value of V, the reference stress is not known a priori for flawed structural geometries and applied loads for which there are no existing J_p solutions. This is the case for the external surface flaw in a pipe. Hence, the reference stress solution used in the example was that contained in COBRA Version 4.0 and is based on the construction method described by Miller [*26*]. It has the form

$$\sigma_{ref} = \frac{P}{\left[\log\left(\frac{R_o - a}{R_i}\right) + \frac{a}{(R_o - a)(1 + 1.61\,\rho^2)^{1/2}}\right]} \tag{29}$$

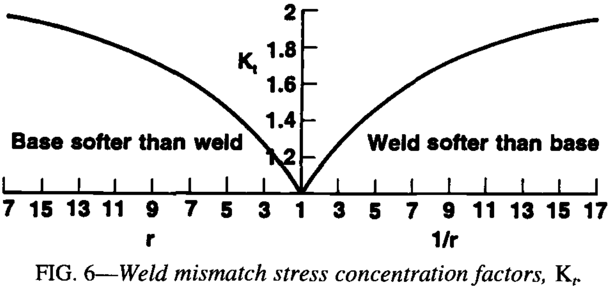

FIG. 6—*Weld mismatch stress concentration factors,* K_t.

TABLE 2—*Mean values of parameters used in the deterministic calculations. (Subscripts b, l, and w signify base, local and weld, respectively, and subscripts a and d the deepest and surface points on the flaw, respectively.)*

Parameter	Mean Value
Engineering parameter, V_a (deepest point)	1.1744
Engineering parameter, V_d (surface point)	1.1592
Base/weld metal ratio, $r = A_b/A_w$	10
Local creep rate constant, A_l	$5.00\ 10^{-15}$ ksi^{-10} h^{-1} ($2.06\ 10^{-23}$ MPa^{-10} h^{-1})
Creep crack growth constant, B	0.50 ksi^{-q} in.$^{1-q}$ h^{q-1} (4.04 MPa^{-q} m^{1-q} h^{-1})

where a is the crack depth, R_o and R_i are the outer and inner radius, respectively, and

$$\rho = \frac{d}{[(R_o - a)a]^{1/2}} \tag{30}$$

where $2d$ is the total surface flaw length.

This reference stress was used for both the deepest and surface points on the crack.

Deterministic Calculations

A series of exploratory deterministic creep life calculations were initially made based on the mean values of the parameters selected to be random variables in the probabilistic analysis (see below). A list of these mean values is given in Table 2. In all cases, the exponent, m, in the creep laws was taken as 10, and the exponent, q, in the creep crack growth law was 0.909 ($= m/(m + 1)$). The values given in Table 2 are typical of those for steels used in high-temperature pressurized components that operate at around 1000°F (538°C). For $r = 10$, the value of K_t is obtained from Fig. 6 as 1.76, and hence the peak value of the mismatch stress at the outer surface of the pipe is 1.76 σ_h.

In each case, initial flaws of depth 0.3 in. (7.62 mm) and aspect ratios (a/d) of 0, ⅓, and 1 were used. Calculations were performed for flaws in the base metal ($A_l = A_b$), in the weld metal ($A_l = A_w$), and in a local zone ($A_l \neq A_b$ and $A_l \neq A_2$). In the latter case, base and weld metal strain rates influence only the mismatch stress and can be assigned arbitrary values provided the ratio equals 10.

The results of the deterministic calculations are shown in Table 3. The results for the case

TABLE 3—*Calculated lifetimes for cracked welded pipe. (Constant aspect ratio results are shown in parentheses.)*

Crack Depth, a (in.)/Aspect Ratio, a/d	$A_b/A_w = 10$	$A_b = A_w$
0.3/0.0	630	960
0.3/0.3333	34 170 (20 710)	44 720
0.3/1.0	60 890 (127 390)	92 770

when the base and weld metals are fully matched ($\sigma_{\text{mis}} = o$) are also shown in order to indicate the effect of the weld mismatch stress on the lifetimes. Also given in brackets are results obtained assuming that the cracks propagate with constant aspect ratio, with the growth governed by the conditions at the deepest point on the flaw. A more detailed illustration of the effects of assuming propagation with a constant aspect ratio is shown in Fig. 7.

It can be seen that an accurate lifetime prediction is dependent on allowing the crack shape to change during propagation, and that, depending on the initial aspect ratio, the assumption of growth with a constant aspect ratio can either significantly underestimate, or overestimate, the lifetime. In comparison, the creep mismatch stress reduces the lifetime by about 30% with respect to the matched weld results.

The results of the example calculations indicate that the contribution to the lifetimes from the transient component of $C(t)$ is small in the present circumstances. Hence, from Eq 6, the lifetimes scale approximately as A_1^{q} since $C(t) \sim C^*$ and C^* is directly proportional to A_1. This

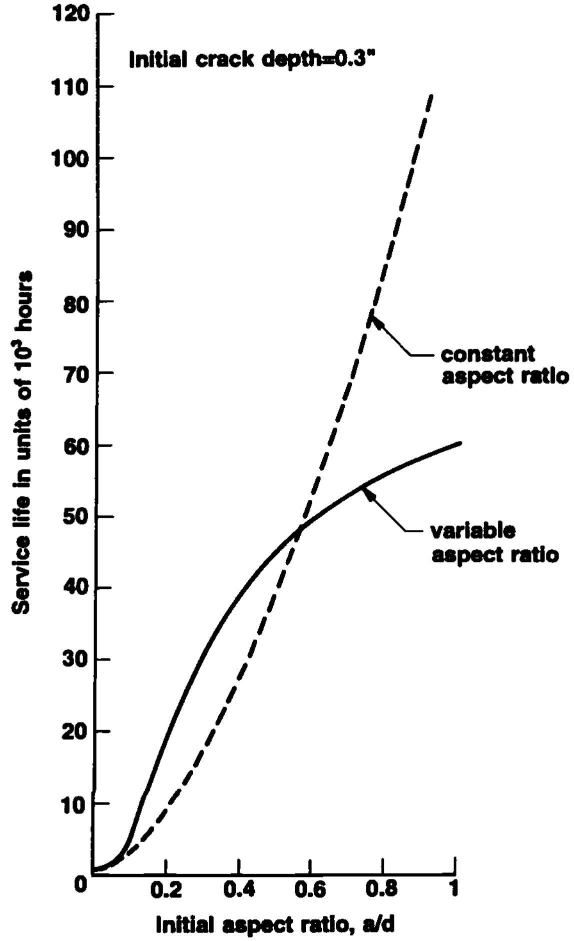

FIG. 7—*Effect of restraining crack shape development on calculated service lives.*

allows the lifetimes for different values of A_l to be readily derived from the results presented in Table 3.

Probabilistic Analysis

The random variables assumed in the analysis and their standard deviations and distribution functions are displayed in Table 4. Four sets of calculations were performed corresponding to the flaw being in a region local to the weld-base metal boundary whose creep properties were uncorrelated with either the base or weld metal properties (Case 1), in the base metal near the weld (Case 2), in the weld metal (Case 3), and far removed from the weld (Case 4, simulated by assuming no creep rate mismatch between the base and weld metals). For each case the cumulative probability of failure, P_f, was determined as a function of remaining life (see Fig. 8). Two sets of results are shown in Fig. 8. The first set was calculated using the Monte Carlo method with 100 000 samples. The second set was determined using the more computationally efficient AIS method. There is good agreement between the two sets of results.

Probability sensitivity factors (PSFs) were also determined as a function of time. These factors indicate the importance of uncertainties in each random variable with respect to their effect on the probability of failure. The value of the PSF for a random variable reflects the sensitivity of the P_f to that variable. The PSFs for each variable corresponding to a service life of 100 000 h are shown in Fig. 9 for the four cases analyzed. These values are typical of those calculated at other service lifetimes.

Discussion

A scheme has been presented that optimizes the ability of the reference stress approach to reproduce computed finite element solutions for the fully plastic component of J and, hence, through the creep-plastic analogy, computed C^* values. This scheme enables values for an optimum yield load and an engineering-dependent parameter, V, to be determined.

The results of the present work demonstrate the uncertainties associated with using the reference stress approach for estimating C^* when accurate computed solutions are not available. Even if an accurate estimate of the reference stress is known, the value of C^* is still uncertain due to the uncertainty in the value of the engineering parameter, V. 189 values of V were derived from extensive analyses performed using the optimization scheme. From these results,

TABLE 4—*Standard deviations and distribution functions used in the probabilistic calculations. The mean values are given in Table 2. (Subscripts b, l, and w signify base, local, and weld, respectively, and subscripts a and d the deepest and surface points on the flaw, respectively.)*

Parameter	Standard Deviation	Function
V_a	0.3071	Type 1 EVD
V_d	0.2426	Type 1 EVD
Base metal creep rate constant	$0.4A_b$	Lognormal
Weld metal creep rate constant	$0.4A_w$	Lognormal
Local creep rate constant, A_l	$2.00\ 10^{-15}$ ksi^{-10} h^{-1} ($0.82\ 10^{-23}$ MPa^{-10} h^{-1})	Lognormal
Crack growth constant, B	0.20 ksi^{-q} in.$^{1-q}$ h^{q-1} (1.62 MPa^{-q} m^{1-q} h^{-1})	Lognormal

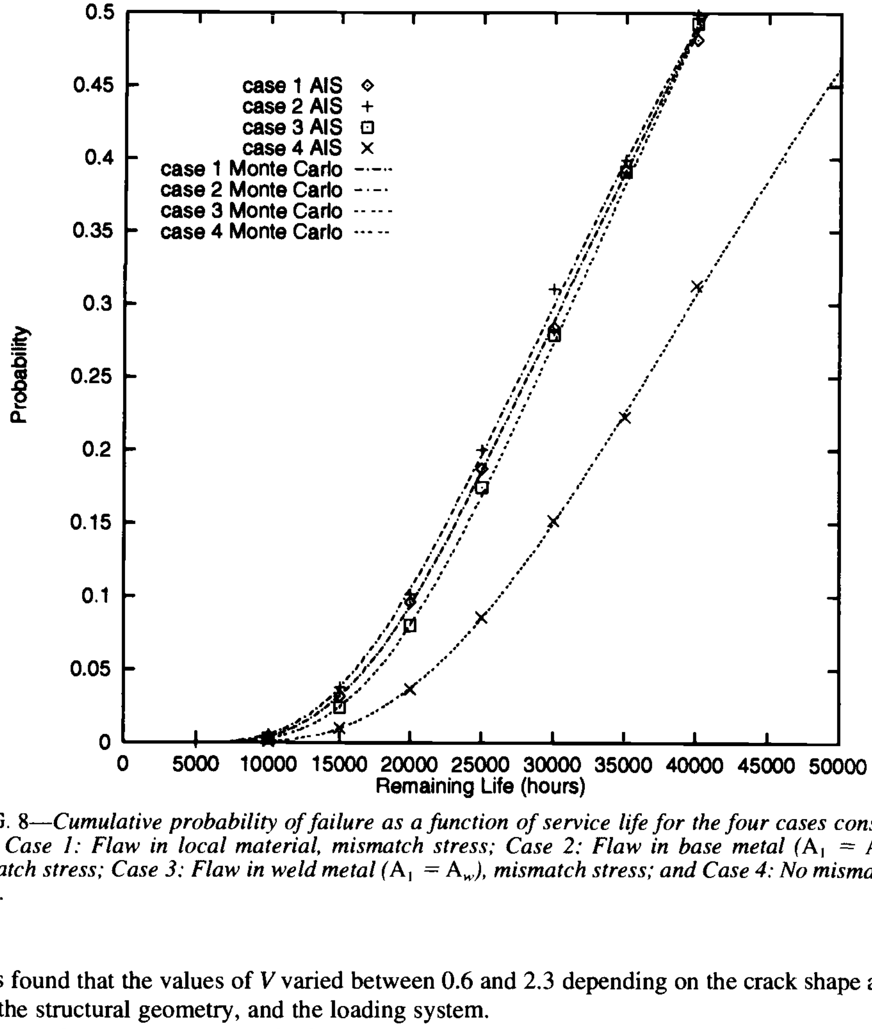

FIG. 8—*Cumulative probability of failure as a function of service life for the four cases considered: Case 1: Flaw in local material, mismatch stress; Case 2: Flaw in base metal* ($A_l = A_b$)*, mismatch stress; Case 3: Flaw in weld metal* ($A_l = A_w$)*, mismatch stress; and Case 4: No mismatch stress.*

it was found that the values of *V* varied between 0.6 and 2.3 depending on the crack shape and size, the structural geometry, and the loading system.

It is usual to assume a value of 1 for *V*, which is close to the mean value of 1.169 determined from a statistical analysis of derived *V* values. The statistical results indicate that the uncertainty in *V* can be described by a Type 1 extreme value distribution function. This function can be used in a probabilistic analysis to allow for the uncertainties in *V* and to determine the effect of these on the probability of failure for a specified service life.

An example application of the developed probabilistic creep crack growth methodology to flawed welded pipes indicates that the major variables controlling the calculated lifetimes are the creep crack growth and strain rate constants for the material in the vicinity of the flaw. This information was derived from PSFs, which were calculated by the NESSUS computer program using advanced probabilistic methods. Although of less importance, the value of *V* is still significant. In the case of the surface flaws analyzed, there was little influence on the probability of failure of uncertainties in the self-equilibrated steady-state stress induced by the mismatch in creep rates between base and weld metals. This conclusion was supported by the fact that the base and weld metal creep rate coefficients only produced significantly high PSFs when either of these was fully correlated with the creep rate at the flaw location. (In other words,

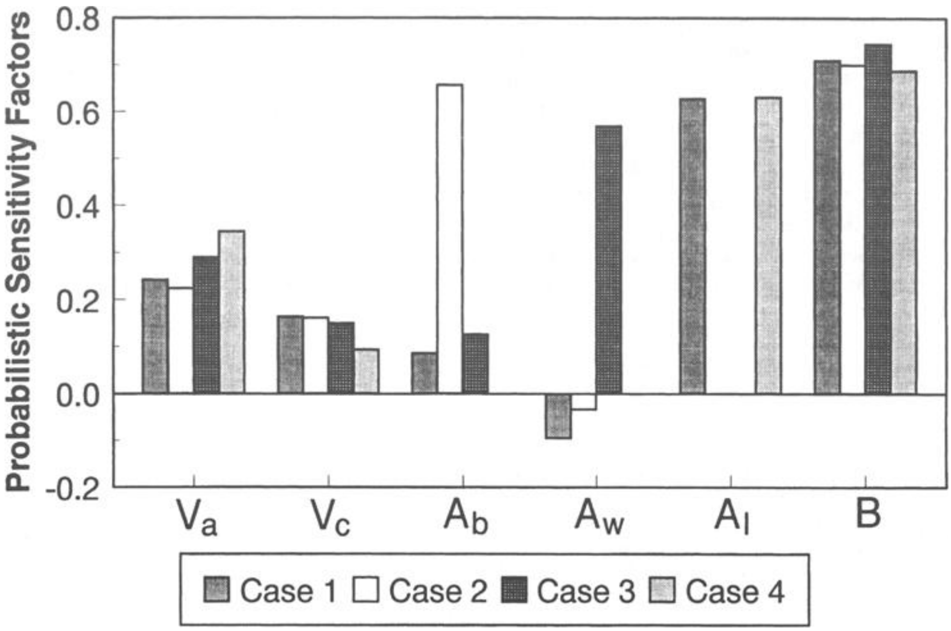

FIG. 9—*Probability sensitivity factors for a service life of 10 000 h.*

when the flaw was either in the base or weld metal. If the flaw was assumed to be in material unrelated to the base and weld metals, such as a heat-affected zone, then the PSFs of the base and weld metal creep rate coefficients were greatly reduced.) However, if the weld mismatch stress was absent, there was a significant reduction in the probability of failure for a given service life.

Conclusions

The time-dependent fracture mechanics parameter, $C(t)$, can be resolved into transient and steady-state components. Transient and steady-state stresses contribute to the transient component, but only steady-state stresses contribute to C^*, the steady-state component. Steady-state stresses can arise from primary loads, such as internal pressure, but may also be self-equilibrated stresses, such as can arise at welds due to a mismatch in creep rates between the base and weld metals.

The accuracy of the reference stress approach to calculating the steady-state component of C^* is dependent on knowing an accurate value for the applied stress intensity factor, K, the reference stress, σ_{ref}, and an engineering-dependent parameter, V. It is difficult to generalize the uncertainties associated with calculating K and σ_{ref}, and it is usual to assume $V = 1$. However, the present analysis shows that the uncertainty in the value of V arising from crack size and shape, structural geometry, and loading system can be quantified in terms of a Type 1 extreme value distribution function. This function can be used to incorporate uncertainties in the reference stress approximation for C^* into a probabilistic-based creep crack growth methodology. In the case of surface flaws, the values of V at the deepest and surface points appear not to be correlated.

An example application of the reference stress approach to a cracked welded pipe showed that service lives are significantly affected by restraints placed on crack shape development. The calculated lives for surface flaws depended on whether the defect was allowed to grow with two degrees of freedom determined by the value of $C(t)$ at the deepest and surface points or whether the growth was limited to one degree of freedom and the flaw development restricted to maintaining a constant aspect ratio. A probabilistic analysis of the pipe indicated that the main variables controlling the uncertainty in the service lives were the creep crack growth and strain rate constants in the material around the flaw. Uncertainties in the value of V were also significant in determining the probability of failure. Surprisingly, uncertainties in value of the weld stresses due to the metallurgical notch effect produced by a mismatch in creep rates between base and weld metals did not make a significant contribution to the probability of failure for a specified service life.

References

[1] Saxena, A., ''Mechanics and Mechanisms of Creep Crack Growth,'' *Mechanics, Mechanisms and Microstructure Interactions in Fracture*, S. V. Nair et al., Eds., ASM International, Metals Park, OH, 1989, pp. 283–334.

[2] Landes, J. B. and Begley, J. A., ''A Fracture Mechanics Approach to Creep Crack Growth,'' *Resource Recovery and Utilization, ASTM STP 590*, 1976, pp. 128–148.

[3] Rice, J. R., *Mathematical Analysis in the Mechanics of Fracture*, Vol. 2 of *Fracture*, E. Liebowitz, Ed., Academic Press, New York, 1968, pp. 192–311.

[4] Riedel, H., *Fracture at High Temperature*, Springer-Verlag, New York, 1987.

[5] Kumar, V., German, M. D., and Shih, C. F., ''An Engineering Approach for Elastic-Plastic Fracture Analysis,'' EPRI Report NP-1931, EPRI, Palo Alto, CA, July 1981.

[6] Kumar, V., German, M. D., Wilkening, W. W., Andrews, W. R., deLorenzi, H. G., and Mowbray, D. F., ''Advances in Elastic-Plastic Fracture Analysis,'' EPRI Report NP-3607, EPRI, Palo Alto, CA, August 1984.

[7] Zahoor, A., ''Ductile Fracture Handbook,'' EPRI Report NP-6301-D, three volumes, EPRI, Palo Alto, CA, 1989.

[8] Ainsworth, R. A., "The Assessment of Defects in Structures of Strain Hardening Material,'' *Engineering Fracture Mechanics*, Vol. 19, 1984, pp. 633–642.

[9] Mauney, D. A., ''Economic Optimization of Multiple Component/Replacement/Inspection in the Power System Environment,'' *ASME PVP*, Vol. 251, American Society of Mechanical Engineers, New York, 1993, pp. 1–16.

[10] Millwater, H. R., Wu, Y.-T., Torng, Y., Thacker, B., Riha, D., and Leung, C., ''Recent Developments of the NESSUS Probabilistic Structural Analysis Computer Program,'' *Proceedings*, 33rd Structures, Structural Dynamics and Materials Conference, Dallas, TX, 13–15 April 1992, Paper No. AIAA-92-2411, American Institute of Aeronautics and Astronautics, Washington, DC.

[11] Bloom, J. M., ''Deformation Plasticity Failure Assessment Diagram (DFFAD) for Materials with Non-Ramberg-Osgood Stress-Strain Curves,'' *Proceedings*, 1994 ASME-PVP Conference, Minneapolis, Minnesota, June 1994, American Society of Mechanical Engineers, New York.

[12] Chell, G. G., McClung, R. C., and Russell, D. A., ''Application of Failure Assessment Diagrams to Proof Test Analysis,'' *ASME PVP*, Vol. 304, American Society of Civil Engineers, New York, 1995, pp. 475–485.

[13] Stevicke, G. R., ''Failure of Welds at Elevated Temperatures,'' Welding Research Council Bulletin 390, Welding Research Council, April 1994.

[14] Samuelson, L. A., Tu, S. T., and Storesund, J., ''Life Reduction in High Temperature Structures due to Mis-Match of Weld and Parent Material Creep Properties,'' *Proceedings*, International Symposium on Mis-Matching of Welds, Luneburg, 26–28 May 1993.

[15] Buchheim, G. M., Osage, D. A., Brown, R. G., and Dobis, J. D., ''Failure Investigation of a Low Chrome Long-Seam Weld in a High-Temperature Refinery Piping System,'' *ASME PVP*, Vol 288, American Society of Mechanical Engineers, New York, 1994, pp. 35–58.

[16] Orient, G., 1994, private communication, Rockwell International Corp., Rocketdyne Division, Canoga Park, CA.

[17] Bloom, J. M. and Lee, D. R., ''Fully Plastic J-Integral Solutions for Pressurized Cylindrical Vessels Having Semi-Elliptical Surface Flaws,'' *Proceedings*, Joint IAEA/CSNI Specialist Meeting on Frac-

ture Mechanics and Verification by Large Scale Testing, Oak Ridge, TN, October 1993, NUREG Report NUREG/CP-0131, Oak Ridge Report ORNL/TM-12413.

[*18*] Yagawa, G., Kitajima, Y., and Ueda, H., "Three Dimensional Fully Plastic Solutions for Semi-Elliptical Surface Cracks," *International Journal of Pressure Vessels and Piping*, Vol. 53, 1993, pp. 457–510.

[*19*] Dodds, R. H. and Shih, C. F., "Continuum and Micromechanics Treatment of Constraint in Fracture," Structural Research Series Report No. 573, 1992, Department of Civil Engineering, University of Illinois at Urbana-Champaign.

[*20*] Wang, Y.-Y., "Analysis of Fracture Initiation in Surface Cracked Plates," M.S. thesis, 1988, MIT. (See also Parks, D. M. and Wang, Y.-Y., "Analytical, Numerical, and Experimental Aspects of Three Dimensional Fracture Processes," *AMD*, Vol. 91, 1988, American Society of Mechanical Engineers, New York, pp. 19–32.)

[*21*] Miller, A. G. and Ainsworth, R. A., "Consistency of Numerical Results for Power Law Hardening Materials and the Accuracy of the Reference Stress Approximation for J," *Engineering Fracture Mechanics*, Vol. 32, 1989, pp. 233–247.

[*22*] Wirsching, P. H. and Carlson, J. R., "Model Identification for Engineering Variables," *Journal of Engineering Mechanics*, Vol. 103, No. EM1, February 1977.

[*23*] Wu, Y.-T. and Wirsching, P. H., "New Algorithms for Structural Reliability Estimation," *Journal of Engineering Mechanics*, ASCE, Vol. 113, 1987, pp. 1319–1336.

[*24*] Wu, Y.-T., Millwater, H. R., and Cruse, T. A., "An Advanced Probabilistic Structural Analysis Method for Implicit Performance Functions," *AIAA Journal*, Vol. 28, 1990, pp. 1663–1669.

[*25*] Wu, Y.-T., "Computational Methods for Efficient Structural Reliability and Reliability Sensitivity Analysis," *AIAA Journal*, Vol. 32, No. 8, 1994, pp. 1717–1723.

[*26*] Miller, A. G., "Review of Limit Loads of Structures Containing Defects," *International Journal of Pressure Vessels and Piping*, Vol. 332, 1988, pp. 197–323.

[*27*] Ehlers, R. and Riedel, H., *Advances in Fracture Research, Proceedings of ICFS*, Vol. 2, D. Francois et al., Eds., Pergamon Press, New York, 1981, pp. 691–698.

Ming Gao,[1] *Shyuan-Fang Chen,*[1] *Gim Syang Chen,*[1] *and*
Robert P. Wei[1]

Environmentally Enhanced Crack Growth in Nickel-Based Alloys at Elevated Temperatures

---

REFERENCE: Gao, M., Chen, S.-F., Chen, G. S., and Wei, R. P., "**Environmentally Enhanced Crack Growth in Nickel-Based Alloys at Elevated Temperatures,**" *Elevated Temperature Effects on Fatigue and Fracture, ASTM STP 1297,* R. S. Piascik, R. P. Gangloff, and A. Saxena, Eds., American Society for Testing and Materials, 1997, pp. 74–84.

ABSTRACT: A recent understanding of environmentally enhanced sustained-load crack growth in nickel-based superalloys at elevated temperatures is presented. This understanding is based on the results of coordinated studies of crack growth kinetics, surface chemistry, and microstructure in a commercial Inconel 718. The results suggest that environmental enhancement of sustained-load crack growth in Inconel 718 is associated with the formation and rupture of niobium oxides at grain boundary surfaces and is controlled mainly by the rate of oxidation and decomposition of niobium carbides at the grain boundaries. Data on other nickel-based alloys in the literature appear to support this suggested role of niobium. Initial results from a study of a niobium-free Ni-18Cr-18Fe alloy (its base composition is identical to Inconel 718) confirm the possible influence of niobium and the proposed mechanism. Some open issues for further investigation are discussed.

KEYWORDS: environmentally enhanced crack growth, elevated temperature crack growth, sustained-load crack growth, environmental effect, effect of oxygen, effect of water vapor, oxidation, role of niobium

It is well recognized that the rate of sustained-load crack growth in nickel-based superalloys at elevated temperatures can be increased substantially by external environments (such as air); not all alloys, however, are equally sensitive to the environment. For example, sustained-load crack growth rates (SCGR) at 923 K in air are one to two orders of magnitude higher than those in inert environments for alloys such as Inconel 718, Rene-95, and X750 [*1–5*]. SCGR in Nimonic PE16 and Astroloy, on the other hand, are essentially unaffected by the external environment [*2,6,7*].

Extensive studies were carried out over the past two decades to understand the rate-controlling processes and mechanisms for environmentally enhanced crack growth in these alloys [*1–7*]. The increased sustained-load and fatigue crack growth rates in air were attributed to enhancement by oxygen. Two mechanisms have been proposed [*8–14*]. The first mechanism involves the oxidation of grain boundary particles and the release of "embrittling" species onto the grain boundaries [*11,12*]. Grain boundary structure and chemistry are deemed critical for embrittlement in air [*4,12*]. In the second mechanism, an increase in crack growth rate is attributed to the formation of nickel and iron oxides, although chromium oxides may inhibit

---

[1] Principal research scientist, graduate student, research scientist, and professor, respectively, Department of Mechanical Engineering and Mechanics, Lehigh University, Bethlehem, PA 18015-3085.

crack tip damage [*8–10,13,14*]. Neither mechanism, however, can explain the observed difference in the SCGR response among the various nickel-based superalloys.

In recent studies of Inconel 718 [*15,16*], niobium was found to be the principal contributor in the environmental enhancement of crack growth. Environmental enhancement was associated with the formation and rupture of niobium oxides at grain boundary surfaces and was mainly controlled by the rate of oxidation and decomposition of niobium carbides at the grain boundaries. The segregated niobium (in the form of grain boundary Ni_3Nb precipitates) may have also contributed to the embrittlement. Data on other nickel superalloys in the literature appear to be consistent with the suggested influence of niobium [*1–7*].

In this paper, the results from coordinated studies of crack growth kinetics, surface chemistry, and microstructure in a commercial Inconel 718 are reviewed and discussed in conjunction with data from the other nickel-based alloys in terms of the role of niobium. Initial results from a study of a niobium-free Ni-18Cr-18Fe alloy are then presented briefly to confirm this interpretation. Some open issues for further investigation are discussed.

Environmentally Enhanced Sustained-Load Crack Growth and Rate Controlling Process in Inconel 718

In this section, the experimental results are reviewed and discussed in terms of mechanisms and rate-controlling processes for environmentally enhanced crack growth [*15–18*].

Crack Growth Response

The results on crack growth in oxygen and moist argon at three temperatures are shown in Fig. 1 [*17*]. The rate was nearly four orders of magnitude higher in oxygen than in pure argon, near $K = 60\ \text{MPa}\sqrt{\text{m}}$, and was essentially independent of oxygen pressure between 2.67 and 100 kPa at 973 K [*17*].

The SCG response of Inconel 718 in oxygen and moist argon can be expressed by an Arrhenius relationship of the following form:

$$da/dt = A\ K^n \exp(-Q/RT)$$

where A is a constant, K and n are the stress intensity factor and its exponent, Q is the apparent activation energy associated with the environmental process(es) for crack growth, R is the universal gas constant, and T is the absolute temperature. The values of the activation energies (Q) for oxygen and moist argon were determined to be 287 ± 46 and 191 ±77 kJ/mol at the 95% confidence level, respectively (Fig. 2). The activation energy in moist argon compares well with the value of 197 kJ/mol reported for air by Floreen [*19*] and Sadananda et al. [*20*] (Fig. 2). The difference in activation energies between oxygen and moist argon reflects a difference in the rate-controlling process and perhaps a change in the deleterious species (oxygen versus hydrogen or oxygen plus hydrogen) for crack enhancement [*17*].

Surface Reaction and Niobium Enrichment

To assist in understanding the rate-controlling processes and mechanisms for the observed crack growth response, parallel studies of surface reaction with oxygen were carried out. Significant enrichment of niobium on the surfaces occurred by heating the material above 775 K both for single crystals and polycrystals. Figure 3 shows the change in surface composition as a function of temperature. It is seen that Nb enrichment was accompanied by some increase in Mo and Ti. Enrichment of these elements was coupled with a continued decrease in Ni and a

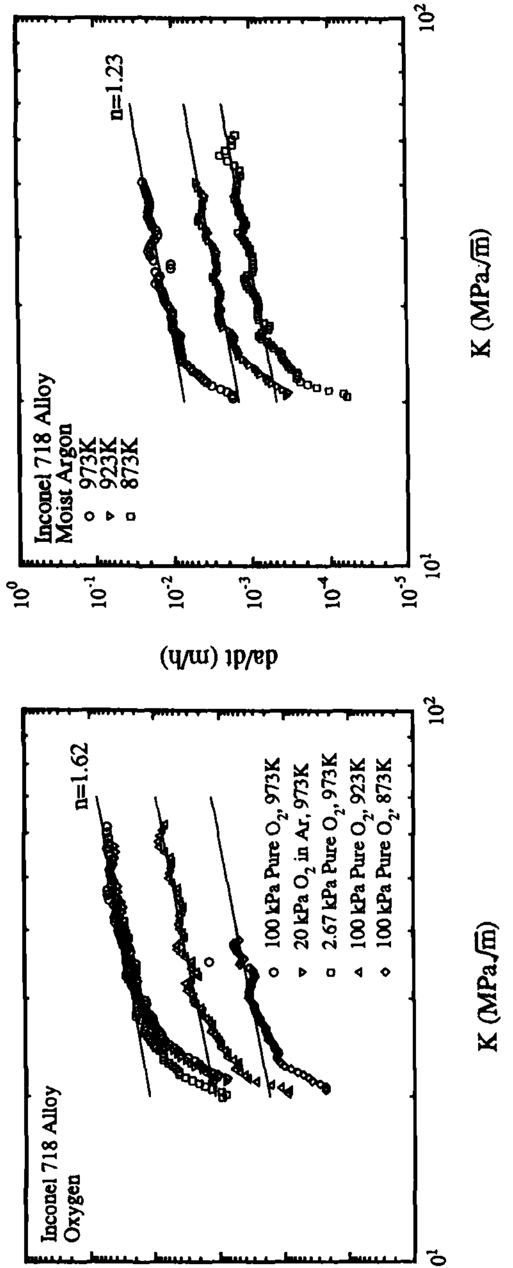

(a)

(b)

FIG. 1—*Kinetics of sustained-load crack growth (a) in pure oxygen, including the effect of oxygen partial pressure, and (b) in moist argon [17].*

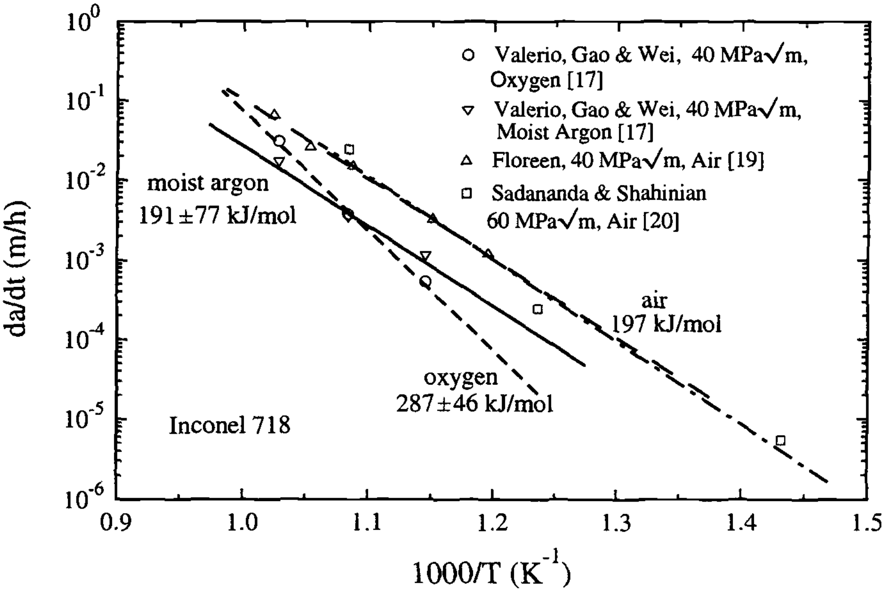

FIG. 2—*Arrhenius plots showing temperature dependence of sustained-load crack growth rates in oxygen and water vapor [17] in comparison with the data of Floreen [19] and Sadananda et al. [20].*

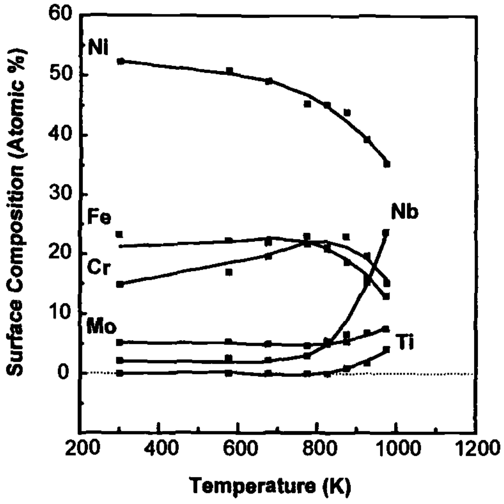

FIG. 3—*Surface composition of the Inconel 718 (100) single crystal surface after heating for 1 h in vacuum at the indicated temperature [15].*

sharp decrease in Cr and Fe. At 975 K, the Nb concentration on the sputter-cleaned surface increased from about 3 at% to over 20 at%.

More detailed studies of the kinetics of niobium enrichment on the (001) surface of Inconel 718 single crystal showed that niobium enrichment was strongly influenced by pre-adsorbed oxygen and was accompanied by the evolution of CO from the surface [*15,16*]. The lesser amounts of segregated Nb in vacuum and the formation of CO suggested that the source of Nb enrichment is associated with the oxidation and decomposition of niobium carbides (NbC) at the surface. The kinetics of NbC oxidation was then studied by using temperature programmed reaction (TPR) experiments. The activation energy for NbC oxidation was estimated to be about 266 kJ/mol by analysis of the leading edge of the TPR trace. This value is consistent with the value of 287 ± 46 kJ/mol for crack growth in oxygen [*17*]. The good agreement in activation energies is consistent with NbC oxidation as the rate-controlling process for environmentally enhanced crack growth at elevated temperatures in Inconel 718.

Analyses of the X-ray photoelectron spectroscopic (XPS) data show the chemical state of enriched niobium on the surface after high oxygen exposure to be principally associated with Nb_2O_5-type oxides. This type of oxide is known to be non-protective and brittle and is likely to be responsible for enhanced crack growth [*19*].

Preferential Oxidation of Nb at the Crack Tip

Fractographic analysis showed that crack growth was intergranular in all environments (including purified argon) and temperatures studied [*17*]. No resolvable cavities were found at magnifications up to ×10 000, suggesting that environmentally enhanced cavitation cannot be the dominant mechanism in Inconel 718. Instead, an alternate mechanism associated with some form of "interfacial embrittlement" of niobium oxide film needs to be considered.

To link surface reaction to crack growth, the oxides formed on the grain boundary facets (i.e., fracture surfaces) of a SCG specimen tested in pure oxygen at 923 K were analyzed by using XPS.

The preferential oxidation of Nb and of Fe was noted near the crack tip region (with Nb of 10 at% in the oxide versus 3 at% in the bulk and 29 at% versus 19 at% for Fe) (Fig. 4). The

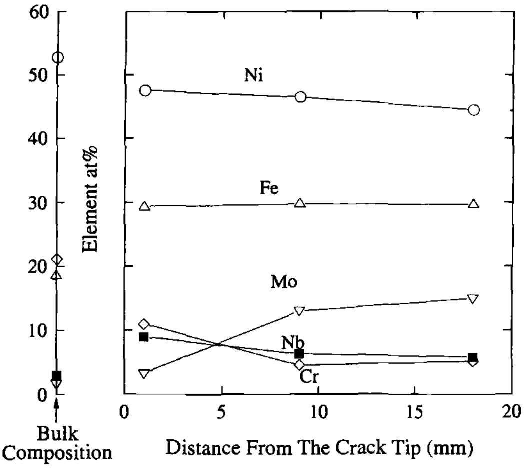

FIG. 4—*Oxide composition of fracture surface produced by SCG in pure oxygen at 923 K. The additional vertical axis on the left indicates the alloy composition.*

amount of niobium is comparable to that observed on an Inconel 718 single crystal at this temperature [*15*]. Away from the crack tip (i.e., equivalent to the longer exposure times), the concentration of niobium in the surface oxide decreased along with Ni and Cr, while that of Mo increased. The change in oxide composition with position reflects the potential for oxidation of each element and the influence of exposure time. Extrapolating the data to zero distance would suggest at higher initial concentration of niobium at the crack tip and provide support for the proposed mechanism.

NbC Carbides, γ'' Precipitates, and Segregation of Nb at Grain Boundaries

Grain boundary NbC particles were also observed directly on the fracture surface of the crack growth specimens and in the transmission electron microscopic (TEM) specimens (Fig. 5). Because of the presence of grain boundary NbC, Nb enrichment directly from the decomposition of these particles during crack growth tests is expected. There might be, however, other sources for niobium. The evidence from thermally induced surface enrichment of niobium further suggested that Nb may segregate at grain boundaries during heat treatment and participate in the subsequent environmental enhancement of crack growth. This has been confirmed by analyzing the grain boundary facets, which were produced by in situ fracturing a hydrogen-charged sample inside the UHV chamber of an XPS system. The results clearly showed a considerable grain boundary segregation of Nb (about 12 at%) [*15*]. TEM results showed that the observed Nb segregation is associated with γ''-Ni_3Nb precipitates at the boundaries [*21*].

Proposed Mechanism and Controlling Process for Sustained-Load Crack Growth in Oxygen

Based on the surface reaction data and the microstructural results, it is suggested that the segregation and enrichment of niobium at grain boundary surfaces were responsible for the environmental enhancement of crack growth in Inconel 718. Available data strongly suggest that the formation and rupture of a brittle niobium oxide (Nb_2O_5-type) film on the boundary surfaces, which reduces the alloy's crack growth resistance is the mechanism and that the

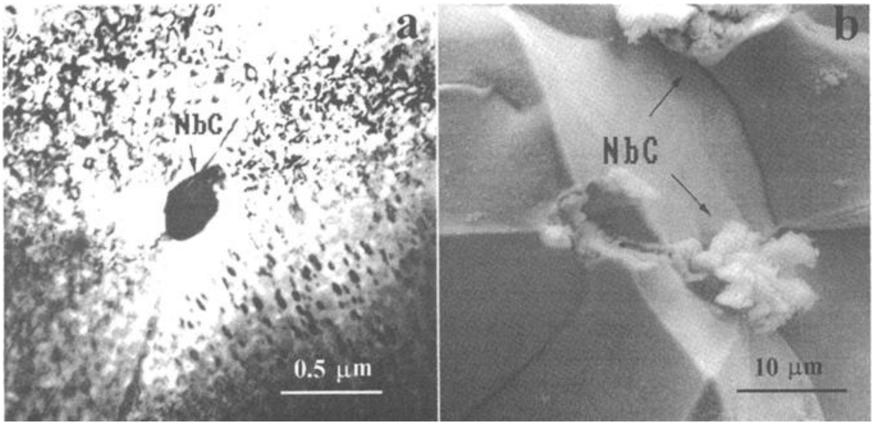

FIG. 5—*Grain boundary niobium carbides (NbC):* (a) *TEM specimen, and* (b) *fracture surface produced by creep crack growth at 973 K.*

reaction of oxygen with niobium carbides (266 versus 287 kJ/mol) or with the segregated niobium (in the form of γ''-Ni_3Nb precipitates) is the rate-controlling process for the environmentally enhanced crack growth in Inconel 718. The oxidation and decomposition of NbC particles at the grain boundaries would be the principal source for Nb enrichment. The considerable amount of γ''-Ni_3Nb particles at the grain boundaries is expected to also contribute to the enrichment. The observed independence of the crack growth rate on oxygen pressure from 2.67 to 100 kPa at 973 K is consistent with the proposed mechanism, as the source of oxygen would be that of an external (pseudo-equilibrium) surface oxide. The lower activation energy for crack growth in moist argon and air (about 190 kJ/mol) still needs to be understood and will be discussed later.

Correlations Between Environmental Sensitivity and Nb Concentration

If niobium is indeed responsible for the environmental enhancement of crack growth in nickel-based superalloys, one should expect to see a correlation between niobium concentration and its environmental sensitivity. By defining environmental sensitivity as the ratio between crack growth rates in air, $\dot{a}_e$, and the corresponding rate in an inert environment, $\dot{a}_r$, a semi-logarithmic plot of $\dot{a}_e/\dot{a}_r$ versus niobium concentration is constructed from available literature data [*1–7,17*] (see Fig. 6). The data in Fig. 6 show a good correlation and a strong dependence of environmental sensitivity on niobium concentration. For example, for the alloys containing about 5% (weight percent) niobium such as Inconel 718, the environment-sensitive factors are in the range of 100 to 1000, while, for the niobium-free alloys such as Nimonic PE16 and Astroloy, the sensitive factors reduce to less than 10. This strong dependence and correlation provides support for the suggested role of Nb and the proposed mechanism for the environ-

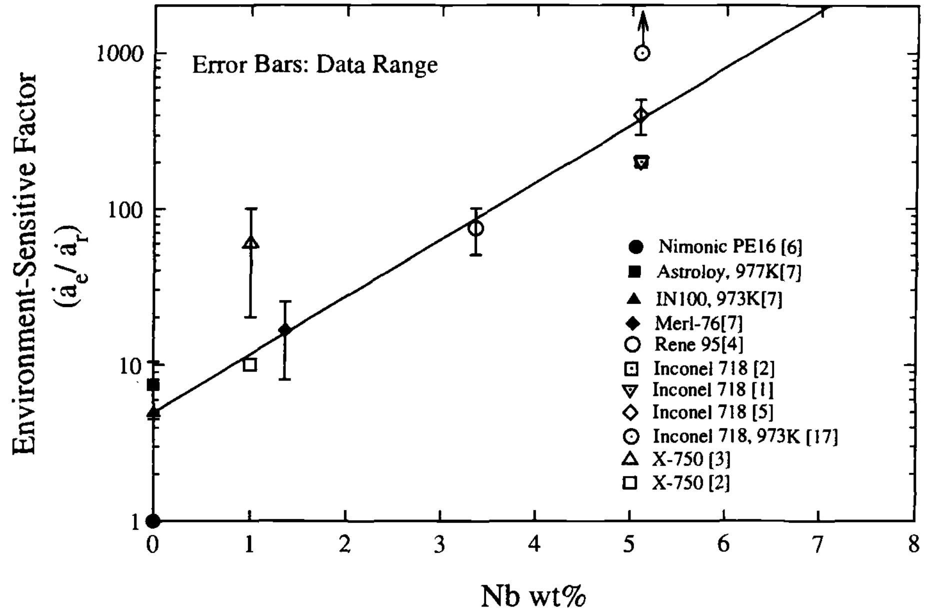

FIG. 6—*Environmental crack growth susceptibility of nickel-based superalloys as a function of niobium concentration (tests at 923 K, except as indicated in the figure) [1–7,17].*

mental enhancement of crack growth. It also provides a self-consistent explanation for the long-known difference in environmental sensitivity among the various nickel-based superalloys in terms of the role of Nb enrichment and segregation.

Crack Growth in Nb-Free Ni-18Cr-18Fe Alloy

To provide further support for the suggested role of niobium in environmentally enhanced crack growth at elevated temperatures, supplemental experiments were carried out on a Nb-free Ni-18Cr-18Fe ternary alloy [22]. The Cr, Fe, and C contents of this simple alloy (namely, 18% Cr, 18% Fe, and 0.02% C) are identical to those of Inconel 718. Although the yield strength of the ternary alloy is much lower than that of Inconel 718, yield strength per se has no effect on the intrinsic environment sensitivity of the alloy, as evidenced by data on many low-strength steels [25]. The study of this simple ternary alloy therefore should provide information on the role of niobium in the environmental enhancement of crack growth.

Because of its low strength and high ductility, crack growth experiments were carried out under cyclic loading with various frequencies at 973 K. Two environments, namely, oxygen and pure argon, were examined. The results are shown in Fig. 7. It is clearly seen that, unlike in Inconel 718 [1,2,20], oxygen essentially has no influence on either high (10 Hz) or low (0.05 Hz) frequency crack growth rates in the Nb-free Ni-18Cr-18Fe alloy (Fig. 7).

Consistent with the literature data of nickel-based superalloys [23,24], two types of behavior were observed. At high frequencies, the crack growth rate, *da/dN*, is less sensitive to frequency and the fracture mode is transgranular, while at the lower frequencies, *da/dN* increases rapidly with decreasing frequency and a change in fracture mode from transgranular to intergranular was observed. This change in fracture mode is understood in terms of cumulative damage of

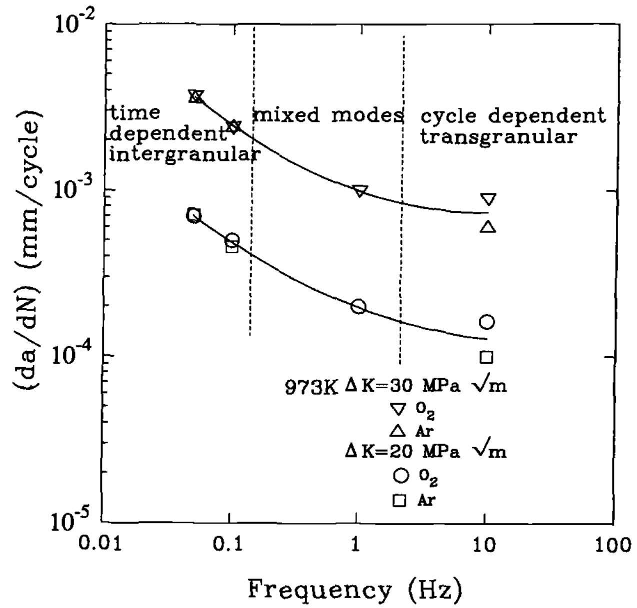

FIG. 7—*Influence of frequency and environment on crack growth rates and fracture mode of Ni-18Cr-18Fe alloy:* ΔK*: 20 and 30 MPa*$\sqrt{m}$*; 973 K [22].*

the material [*23,24*]. Typically, cycle-dependent (fatigue) crack growth is transgranular, whereas the time-dependent crack growth is intergranular. Therefore, in the absence of Nb, both cycle- and time-dependent crack growth rates would be relatively insensitive to oxygen.

Some Open Issues for Further Investigation

In the foregoing sections, we have demonstrated that niobium may be the principal contributor in environmentally enhanced crack growth in nickel-based superalloys. Environmental enhancement resulted from the formation and rupture of niobium oxides on the grain boundary surfaces and was controlled mainly by the rate of oxidation and decomposition of niobium carbides. However, some open issues need to be resolved for complete understanding. These issues may be understood in terms of the schematic diagram in Fig. 8.

The processes involved in environmentally enhanced crack growth in Inconel 718 may be as follows (Fig. 8): (1) transport of the deleterious environment (i.e., oxygen, water vapor, etc.) to the crack tip; (2) reaction of the deleterious environment with newly exposed particles (i.e., niobium carbides and, possibly, γ'' precipitates), resulting in enrichment of Nb on the newly created surfaces and formation of oxides (Nb_2O_5-type); (3) growth of oxide film into the boundaries; and (4) mechanical rupture of the oxide film. Among these, Step 2, i.e., decomposition and oxidation of niobium carbides, is the rate-controlling process for crack growth in pure oxygen [*18*].

For crack growth in moist argon, however, the lower activation energy needs to be understood. The large difference in activation energy between oxygen and moist argon (287 versus 191 kJ/mol) suggests a transfer in the controlling process and an additional embrittlement contribution from change in deleterious species (oxygen versus hydrogen or oxygen plus hydrogen). Therefore, to complete the understanding of the role of niobium in environmentally

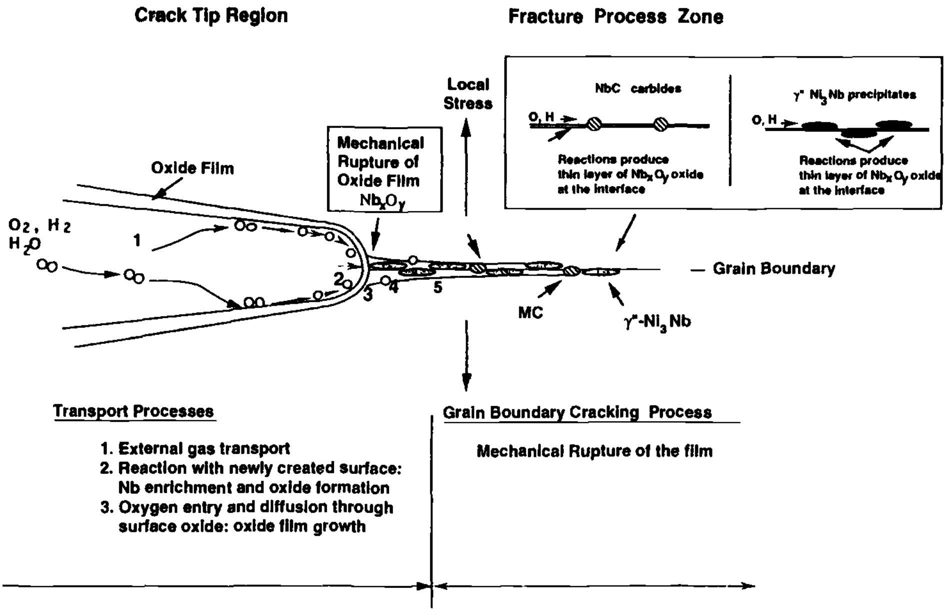

FIG. 8—*Schematic illustration of processes involved in environmentally enhanced creep crack growth in nickel-based alloys.*

enhanced crack growth, the rate-controlling process and mechanism for crack growth in moist argon needs to be addressed.

Grain boundary NbC, on the other hand, is known to be the principal contributor in environmentally enhanced crack growth [*15,16,18*]. Since the morphology, size, density, and distribution of NbC particles directly influence the source of Nb on the boundaries for chemical reaction, quantification of grain boundary niobium carbides as a function of niobium and carbon contents in terms of these parameters and their relationship to the crack growth kinetics is needed. This quantification is essential to the development of microstructurally based models for predictions of crack growth rates.

In addition to NbC particles, a considerable amount of γ'' precipitates are present in the grain boundaries [*21*]. Since γ'' precipitates contain 25 at% of niobium, the role of grain boundary γ'' precipitates in environmental enhancement of crack growth needs to be understood. Quantification of the contribution of γ'' precipitates to crack growth is also essential to the development of microstructurally based models for environmentally enhanced crack growth in nickel-based superalloys.

Summary

To better understand the mechanism and rate-controlling process for environmentally enhanced sustained-load crack growth in nickel-based superalloys, the recent results on sustained-load crack growth kinetics and surface reaction of Inconel 718 in oxygen and moist argon are reviewed and discussed in conjunction with the data from the other nickel-based superalloys. Available evidence suggests that enrichment and segregation of niobium at grain boundary surfaces played an important role in the environmental enhancement of SCG in Inconel 718. The mechanism involves the formation and fracture of a brittle niobium oxide film on the boundary surfaces that reduces the alloy's crack growth resistance. Oxidation and decomposition of NbC particles at the crack tip surfaces and at the grain boundaries is the principal source of niobium. The segregated niobium (in the form of Ni_3Nb precipitates) at the grain boundaries is expected to also contribute to the embrittlement. The reaction of oxygen with niobium carbides (266 versus 287 kJ/mol) or with the segregated niobium (in the form of Ni_3Nb precipitates) appear to be the rate-controlling process. The lower activation energy for crack growth in moist argon and air (about 190 kJ/mol) may reflect the additional embrittlement contribution from hydrogen and a transfer of the rate-controlling process. The important role of niobium in the enhancement of SCG is demonstrated by the correlation between the environmental sensitivity and niobium concentration in the series of commercial alloys and is confirmed by a recent study of the niobium-free Ni-18Cr-18Fe alloy. Issues such as the influence of microstructural parameters (e.g., the size and density of grain boundary NbC) need further study. The precise mechanism needs to be further established.

Acknowledgment

This work was supported by the Materials Research Group (MRG) Program of the Division of Materials Research, National Science Foundation under Grant No. DMR-9102093.

References

[*1*] Floreen, S. and Kane, R. H., *Fatigue of Engineering Materials and Structure*, Vol. 2, 1980, pp. 401–412.
[*2*] Sadananda, K. and Shahinian, P., *Material Science and Engineering*, Vol. 43, 1980, pp. 159–168.
[*3*] Gabrielli, F. and Pelloux, R. M., *Metallurgical Transactions A*, Vol. 13A, 1982, pp. 1083–1090.

[*4*] Bain, K. R. and Pelloux, R. M., *Metallurgical Transactions A*, Vol. 15A, 1984, pp. 381–388.

[*5*] Stucke, M., Khobaib, M., Majumdar, B., and Nicholas, T., *Advances in Fracture Research*, Vol. 6, Proceedings of the Sixth International Conference on Fracture (CFI 6), New Delhi, India, 4–10 Dec., 1984, R. Rama Rao, K. N. Raja, J. F. Knott, and D. M. R. Taplin, Eds., Pergamon Press, New York, 1984, pp. 3967–3975.

[*6*] Sadananda, K. and Shahinian, P., *Micro and Macro Mechanics of Crack Growth*, Proceedings of A Symposium, TMS 1981 Fall Meeting, 10–13 Oct., Louisville, Kentucky, K. Sadananda, B. B. Rath, and J. Michel, Eds., Metallurgical Society of AIME, Warrendale, Pennsylvania, 1982, pp. 119–130.

[*7*] Bain, K. R. and Pelloux, R. M., *Superalloys 1984*, Proceedings of the Fifth International Symposium on Superalloys, 7–11 Oct. 1984, Champion, PA, M. Gell, C. S. Kortovich, R. H. Bricknell, W. B. Kent, and J. F. Radavich, Eds., Metallurgical Society of AIME, Warrendale, Pennsylvania, 1984, pp. 1741–1749.

[*8*] Smith, H. H., Shahinian, P., and Achter, M. R., *Transactions of the Metallurgical Society, AIME*, Vol. 245, 1969, pp. 947–953.

[*9*] Cook, R. H. and Skelton, R. P., *International Metallurgical Reviews*, Vol. 19, 1974, pp. 199–221.

[*10*] McMahon, C. J., *Materials Science and Engineering*, Vol. 13, 1974, pp. 295–297.

[*11*] Woodford, D. A. and Bricknell, R. H., *Treatise on Materials Science and Technology*, Herbert Herm, Ed., Academic Press, New York, Vol. 25, 1983, pp. 157–199.

[*12*] Floreen, S. and Raj, R., *Flow and Fracture at Elevated Temperatures*, R. Raj, Ed., ASM, Metals Park, OH, 1984, pp. 383–405.

[*13*] Diboine, A. and Pineau, A., *Fatigue, Fracture of Engineering, Materials, and Structures*, Vol. 10, 1987, pp. 141–151.

[*14*] Andrieu, E., Molins, R., Ghonem, H., and Pineau, A., *Materials Science Engineering*, Vol. A154, 1992, pp. 21–28.

[*15*] Pang, X. J., Dwyer, D. J., Gao, M., Valerio, P., and Wei, R. P., *Scripta Metallurgica et Materialia*, Vol. 31, 1994, pp. 345-350.

[*16*] Dwyer, D. J., Pang, X. J., Gao, M., and Wei, R. P., *Applied Surface Science*, Vol. 81, 1994, pp. 229–235.

[*17*] Valerio, P., Gao, M., and Wei, R. P., *Scripta Metallurgica et Materialia*, Vol. 30, 1994, pp. 1269–1274.

[*18*] Gao, M., Dwyer, D. J., and Wei, R. P., *Scripta Metallurgica et Materialia*, Vol. 32, 1995, pp. 1169–1174.

[*19*] Floreen, S., *Metallurgical Transactions A*, Vol. 6A, 1975, pp. 1741–1749.

[*20*] Sadananda, K. and Shahinian, P. J., *Engineering Materials and Technology*, Vol. 100, 1978, pp. 381–387.

[*21*] Gao, M. and Wei, R. P., *Scripta Metallurgica et Materialia*, Vol. 32, 1995, pp. 987–990.

[*22*] Chen, S. F., Chen, G., Gao, M., and Wei, R. P., unpublished results, Lehigh University, Bethlehem, PA, 1995.

[*23*] Webster, G. A., *Materials Science and Technology*, Vol. 3, 1987, pp. 716–725.

[*24*] Hoffelner, W., *Materials Science and Technology*, Vol. 3, 1987, pp. 765–771.

[*25*] Wei, R. P. and Gangloff, R. P., *Fracture Mechanics: Perspectives and Directions, Twentieth Symposium, ASTM STP 1020*, R. P. Wei and P. R. Gangloff, Eds., 1989, pp. 233–264.

Fatigue

Naoya Tada,[1] Weisheng Zhou,[1] Takayuki Kitamura,[1] and Ryuichi Ohtani[1]

Analysis of the Intergranular Cracking Process Inside Polycrystalline Heat-Resistant Materials Under Creep-Fatigue Conditions

---

REFERENCE: Tada, N., Zhou, W., Kitamura, T., and Ohtani, R., "**Analysis of the Intergranular Cracking Process Inside Polycrystalline Heat-Resistant Materials Under Creep-Fatigue Conditions,**" *Elevated Temperature Effects on Fatigue and Fracture, ASTM STP 1297,* R. S. Piascik, R. P. Gangloff, and A. Saxena, Eds., American Society for Testing and Materials, 1997, pp. 87–101.

ABSTRACT: In order to investigate the intergranular failure process in polycrystalline materials under creep-dominant fatigue, numerical simulation of inner small cracks was conducted on the basis of a simple probabilistic model. Although the simulation condition is determined from experimental observation of the cross section of specimens interrupted at different fatigue cycles, the simulation is carried out continuously and reproduces inner cracking behavior throughout the fatigue life. This enables us not only to extract the spatial distribution of inner cracks at arbitrary creep-fatigue cycles, but also to calculate the propagation rate of each inner crack.

KEYWORDS: numerical simulation, inner cracking, probabilistic model, creep-fatigue

Creep-dominant fatigue of heat-resistant materials shows a variety of failure processes [*1*]. Under the creep-fatigue condition with a low tensile strain rate at an intermediate temperature, small cracks initiate and propagate along grain boundaries on the surface of the material, whereas no cracks are observed inside. This is called "surface cracking type." On the other hand, under very low tensile strain rate at relatively high temperatures, numerous small intergranular cracks initiate inside the material and frequent coalescence accelerates their following propagation. This is called "inner cracking type." The probabilistic nature in initiation and propagation of small cracks also makes the failure process complicated for both cracking types. Because there is a wide difference in the resistance against creep-fatigue fracture among grain boundaries, small cracks initiate on random grain boundaries at random times. Probabilistic treatment is necessary to discuss the results [*3*]. Moreover, in the case of the inner cracking type, available information is limited to the observation on the cross section of the specimen, such as the distribution of cracks on the cross section, since one cannot observe inner cracks directly. It is necessary to carry out a kind of inverse analysis [*4*] and to obtain the spatial distribution of inner cracks for elucidating the failure process, as schematically shown in Fig. 1.

In this study, numerical simulation is proposed on the basis of a simple probabilistic model as a convenient tool to analyze the state of distributed cracks, and the failure process in creep-fatigue is investigated by means of the simulation.

---

[1] Department of Engineering Physics and Mechanics, Graduate School of Engineering, Kyoto University, Kyoto 606-01, Japan.

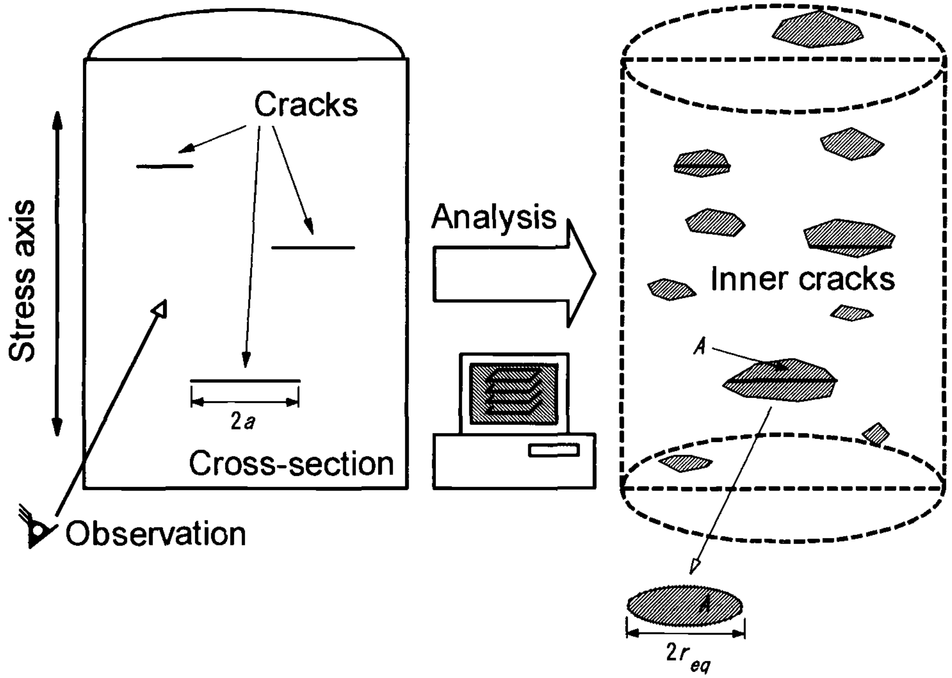

FIG. 1—*A schematic illustration showing an inverse analysis on the spatial distribution of inner cracks.*

Experimental Observation on Inner Small Cracks

Multiple inner cracks analyzed by the present numerical simulation were obtained from a creep-fatigue test. A smooth round bar specimen of a Type 304 stainless steel with a 10 mm diameter and 20 mm gage length was used. The test was carried out in an air environment at 1073 K with very slow tension (10^{-4}%/s) and a fast compression (1%/s) strain waveform of a total range of 0.7%. The failure life, N_f, which is defined as the fatigue cycles when the maximum stress is reduced to three quarters of the steady value, was 133 cycles, and six different specimens interrupted at the number of cycles, $N = 0.1N_f$, $0.17N_f$, $0.25N_f$, $0.5N_f$, $0.75N_f$, and N_f, respectively, were prepared for observation. Distribution of small inner cracks was measured on a cross section by means of an optical microscope. Details of the experiment were reported in a previous paper [*1*].

Figure 2*a* shows morphology of inner cracks on the cross section. It is found from the photographs that multiple inner cracks initiate at random locations perpendicular to the stress axis direction. The inner cracks are distributed uniformly throughout the gage section. This was substantiated by the observation of a longitudinal cross section where the number of cracks in a unit area and the distribution of crack length were independent of the position.

Figure 3 shows a change in areal crack density (i.e., the number of cracks in unit area), n_p, and the mean crack length on the cross section, $2a_m$. Individual crack length, $2a$, was measured as the length of each crack projected on the line perpendicular to the stress axis, as shown in Fig. 1. The increase in n_p implies that the small inner cracks continuously initiate from the early stage to the latter stage of fatigue life. On the other hand, the length of inner cracks shown

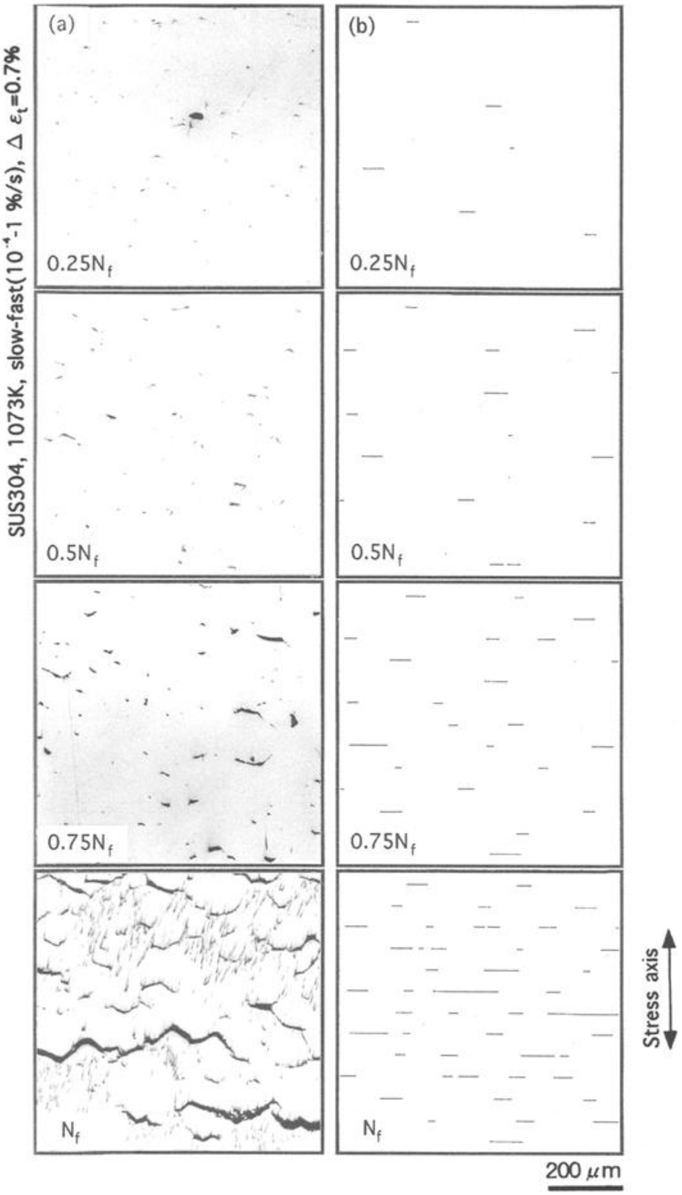

FIG. 2—*Inner cracks revealed on the cross section:* (a) *experimental result;* (b) *simulation result.*

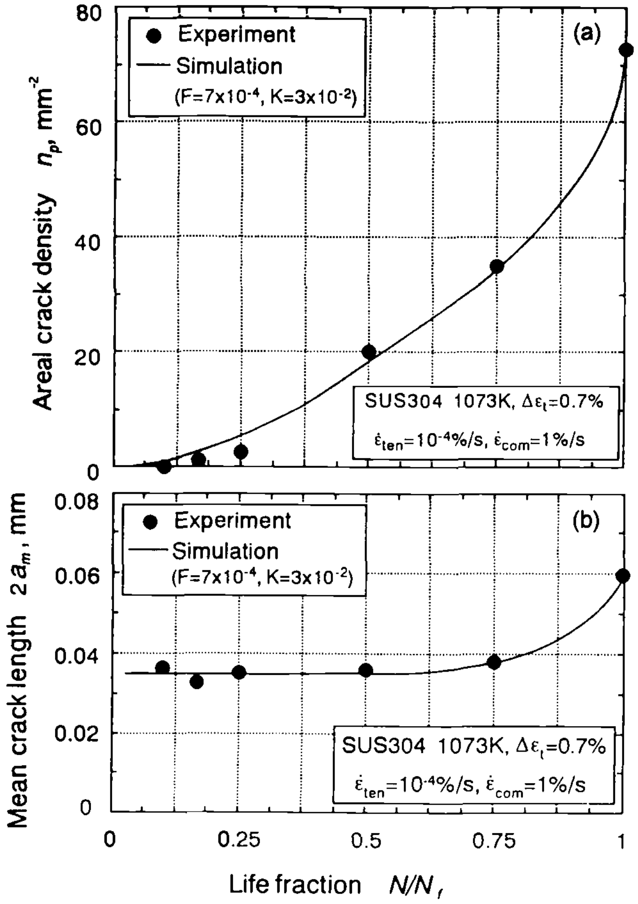

FIG. 3—*Change in areal crack density,* n_p, *and the mean crack length,* $2a_m$, *on the cross section with life fraction,* N/N_f.

in Fig. 3*b* is almost constant and corresponds to the mean length of grain boundary lines on the cross section (=37 μm) until the late middle stage of fatigue life. This suggests that inner cracks initiate by a unit of a grain boundary facet and that the initiated cracks hardly propagate at the early and middle stages.

In this paper, three-dimensional distribution of inner cracks and their changes are analyzed from the above two-dimensional information through numerical simulation.

Procedure of Numerical Simulation

Generation of Grain Boundary Facets

Three-dimensional grain boundary facets are numerically generated before the cracking simulation. The procedure can be explained as follows:

1. Three-dimensional grain boundary facets are represented by many sheets of projected grain boundary facets that are layered at equal intervals perpendicular to the stress axis

direction, as illustrated in Fig. 4. Figure 5 schematically shows one of the facet sheets in comparison with actual grain boundary facets.

2. The random grain boundary facets on each sheet are numerically made by Monte Carlo simulation on the basis of an isotropic grain growth model [5]. Details were reported elsewhere [6,7]. Choosing the proper number and growth rate of facets by trial and error and using a different set of random numbers on each facet sheet, three-dimensional grain boundary facets—the size distribution of which is identical to the actual polycrystalline structure of the Type 304 stainless steel—are reproduced numerically.
3. The space between adjacent facet sheets, h, shown in Fig. 4, is calculated by:

$$\begin{aligned} h &= (\text{mean area of grains on cross section})^{1/2} \\ &= (1/n_g)^{1/2} \end{aligned} \tag{1}$$

where n_g is the number of grains in a unit area on the cross section. In the case of Type 304 stainless steel used in the present creep-fatigue test, n_g is equal to 300 (mm^{-2}) and yields $h \approx 0.06$ (mm).

4. In this study, the size of the simulation body is set as large as 1 by 1 by 1 mm, which is composed of the 16 facet sheets, so that the converged results are obtained.

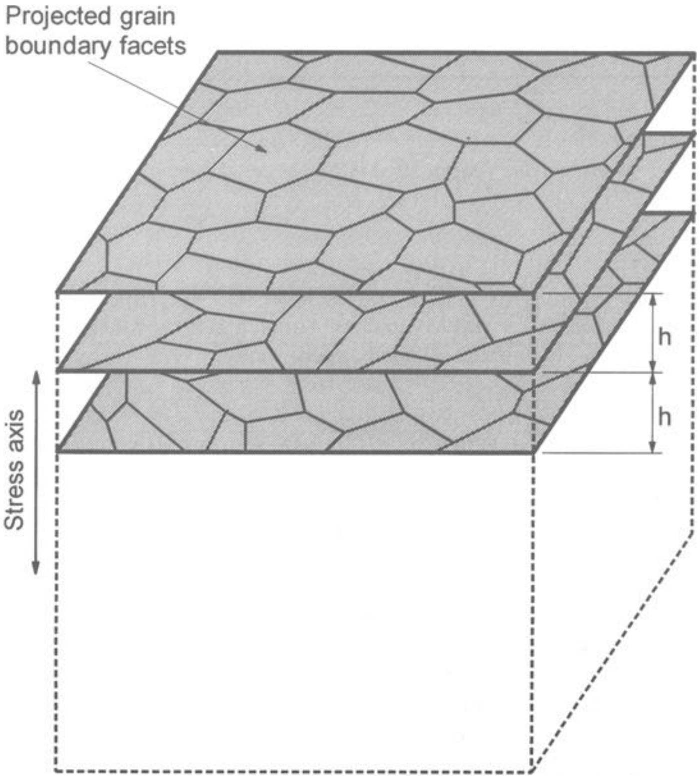

FIG. 4—*Layered sheets of grain boundary facets.*

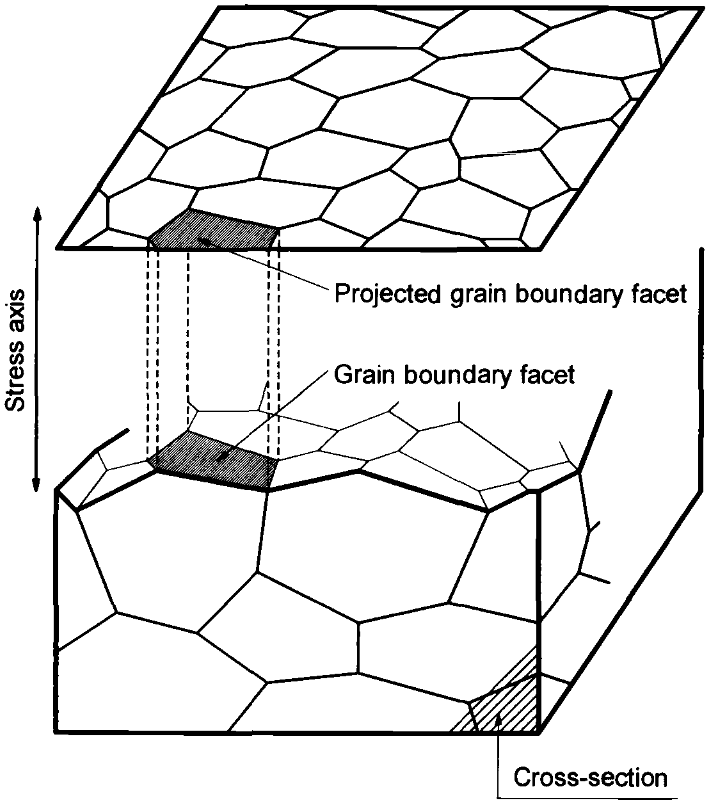

FIG. 5—*A sheet of grain boundary facets used in the model in comparison with actual facets.*

Modeling of Inner Cracking

Simulation of inner cracking is conducted on the basis of a simple probabilistic model that has previously been presented for surface cracking simulation by the authors [*8*]. The model is schematically shown in Fig. 6 and explained as follows:

1. Each grain boundary facet has its own fracture resistance, R, which takes one of the uniform random numbers ranging from 0 to 1 by means of a computer. This value is thought to be dependent on the characteristics of each grain boundary facet, such as the grain boundary structure, the angle of the grain boundary facet to the stress axis direction, etc. The uniform random number is adopted because of the simplicity and the excellent reproduction of cracking behavior on the cross section, as will be shown later.
2. The driving force for crack initiation, F, is constantly imposed on each facet, and the fracture resistance of each facet, R_i, is reduced by the magnitude of F at every fatigue cycle. Here, F is assumed to be common to every facet. In other words, the fluctuation in the variable, R, includes the randomness in F as well in this model.
3. When remaining fracture resistance becomes zero on a facet, the facet is assumed to be broken immediately and an inner crack initiates there. In other words, crack initiation occurs discretely by a grain boundary facet.
4. The driving force for the facets next to the initiated inner crack is raised by the magnitude

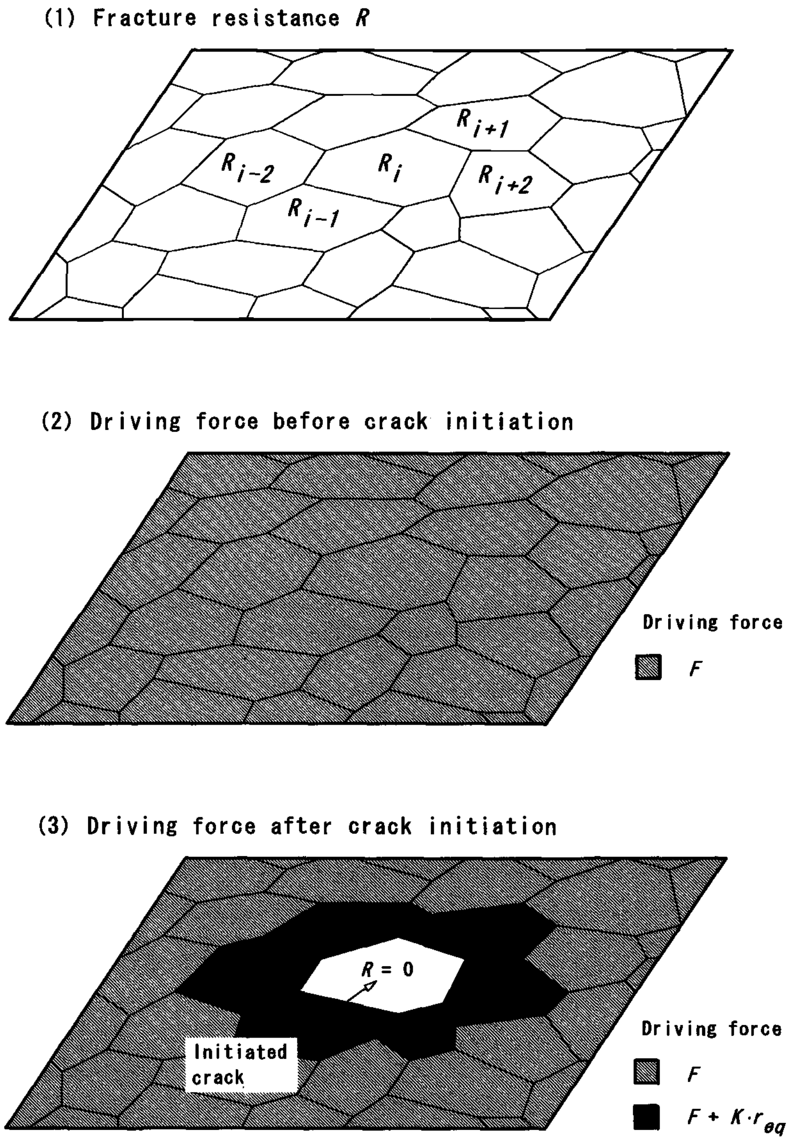

FIG. 6—*Schematic illustrations showing the procedure of numerical simulation.*

of $K \cdot r_{eq}$ due to stress intensity by the crack, where r_{eq} is an equivalent radius that is calculated from the area of the inner crack, A, as shown in Fig. 1, and K is a propagation constant, respectively. The total driving force, D, is then given by the sum of the driving force for crack initiation, F, and the one for crack propagation, $K \cdot r_{eq}$, as follows:

$$D = F + K \cdot r_{eq}, \tag{2}$$

$$r_{eq} = (A/\pi)^{1/2} \tag{3}$$

5. When the fracture resistance of the facet next to the pre-existent crack becomes zero, the crack immediately propagates. Crack propagation also occurs discretely by a grain boundary facet.

Determination of Driving Forces

Two constants, F and K, have to be determined for the simulation. As expected, the number of initiated cracks is controlled by the magnitude of F, and the following propagation is controlled mainly by the magnitude of K. Then, the following procedure is presented:

1. The value of F is tentatively determined so that the simulation result on areal crack density on the cross section, n_p, coincides with the experimental one.
2. After F is determined, an appropriate value of K is searched so that the simulation result on the mean crack length on the cross section, $2a_m$, coincides with the experimental one.
3. Adjusting the values of F and K alternately by the first two procedures, the set, which gives the best fit to cracking data on the cross section, is obtained.

The values of F and K are found to be 7×10^{-4} and 3×10^{-2}, respectively, under the present creep-fatigue test condition. The curves in Fig. 3 show the simulation results on the change in areal crack density, n_p, and the mean crack length on the cross section, $2a_m$, respectively. Each simulation curve coincides very well with the corresponding experimental results. Here, only the mean crack length is shown. It is also confirmed that the distribution of crack length obtained by the simulation is identical with the experimental one, as will be shown later. Figure 3 shows not only that the present simulation reproduces cracking behavior at the observation points of $N = 0.1N_f$, $0.17N_f$, $0.25N_f$, etc., but also that it gives a reasonable interpolation of cracking throughout the fatigue life.

Figure 2*b* shows the visualized distribution of inner cracks on the cross section obtained from the simulation. The image is also similar to the actual one.

Results of Simulation

Volumetric Density and Radius of Inner Cracks

Figure 7*a* shows the volumetric density of inner cracks, n_v, which is defined as the number of inner cracks in a unit volume by numerical analysis. While the volumetric crack density, n_v, increases in proportion to the life fraction, N/N_f, at the early stage, it saturates at approximately $0.9N/N_f$. The saturation in volumetric crack density originates mainly from the frequent coalescence of inner cracks. The most noticeable point in this figure is that the tendency in volumetric density is different from that in the areal one on the cross section shown in Fig. 3*a*. This means that the distribution of cracks on the cross section does not directly indicate the real cracking behavior inside the material. Here, a solid mark in Fig. 7*a* shows the volumetric density measured experimentally by the following technique. Shaving off the cross section of the creep-fatigued specimen repeatedly by a few micron metres and taking photographs of the cracks in a fixed area on each cross section, the spatial distribution is reconstructed from the photographs. Taking into account the difficulty in identifying each crack on different cross sections, the result is in good agreement with the analyzed one and verifies the validity of inverse analysis proposed here.

Figure 7*b* shows the mean crack radius, r_m, as a function of the life fraction, N/N_f. r_m is the average of r_{eq} of all cracks, which is calculated using Eq 3. Until the latter stage, the value of

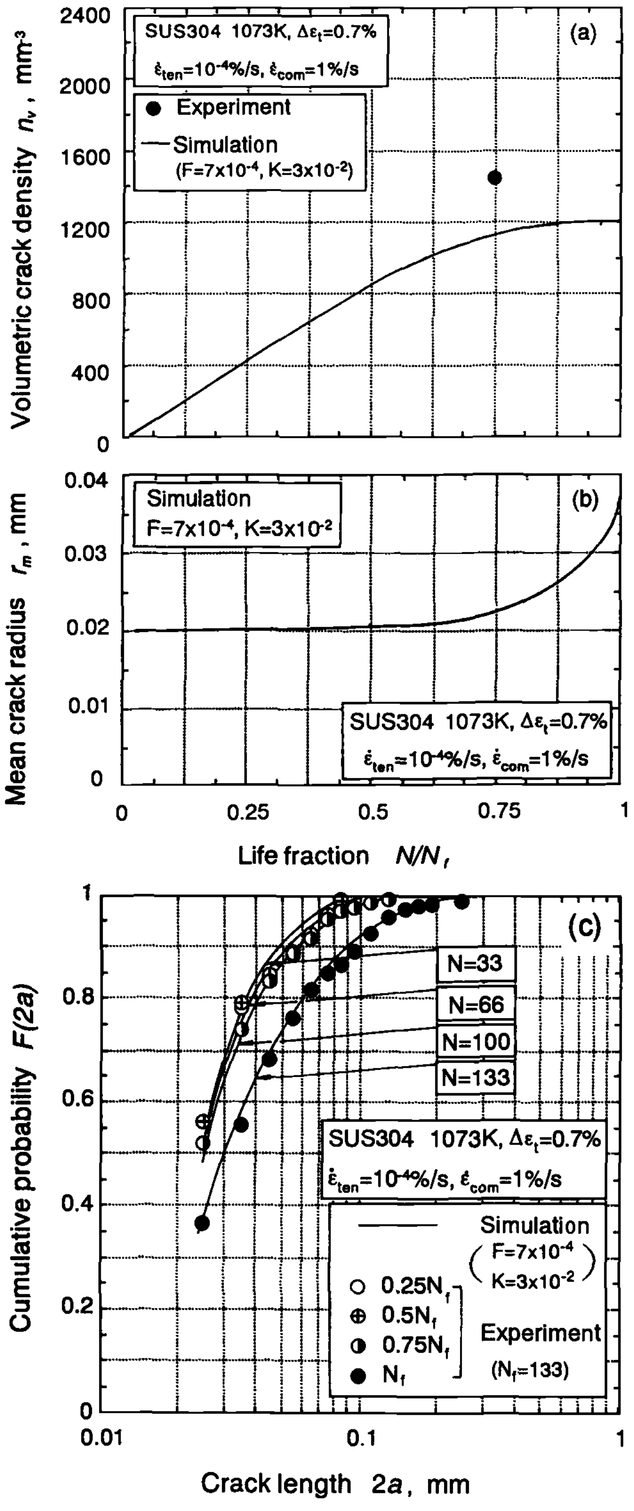

FIG. 7—*Change in the distribution of inner cracks with life fraction,* N/N_f: (a) *volumetric crack density,* n_v; (b) *mean crack radius,* r_m; (c) *distribution of crack length on the cross section.*

r_m does not change remarkably, but it increases drastically near the end of fatigue life. This also suggests that frequent coalescence of inner cracks occurs at the latter stage.

Figure 7*c* shows the distribution of the crack length, $2a$, on the cross section. Simulation and experimental results coincide well at four different life fractions. This suggests that inner cracks obtained by the simulation and those in the actual specimen are statistically identical.

Spatial Distribution of Inner Cracks

Three-dimensional distribution of inner cracks at $N/N_f = 0.75$ is shown in Fig. 8. Inner cracks are randomly and uniformly distributed throughout the material. Although many inner cracks are distributed in three dimensions, a small proportion appear on the cross section where the cracks can be observed in the experiments. Therefore, a fairly large area is necessary when one predicts the distribution of inner cracks from the cross-sectional distribution.

Figure 9 shows a change in the morphology of inner cracks on one of the layered facet sheets. Figures lined from the top left to the bottom right show the distribution of inner cracks at the points when experimental results are obtained on the cross section. Since the present numerical simulation interpolates the experimental observation on the cross section as shown in Fig. 3, it gives continuous change in the distribution of inner cracks at other arbitrary cycles, as shown at the bottom in Fig. 9. An overall look at these figures indicates that multiple inner cracks initiate at random from the early stage and coalesce to form a large crack at the latter stage, as was expected from the previous discussion on n_v and r_m.

Propagation Behavior of Inner Cracks

Additional information that can be obtained by the present simulation is the propagation behavior of inner cracks. Figure 10*a* shows propagation curves of active cracks and Fig. 10*b* those of inactive cracks that were arrested almost always after initiation. It is found from Fig. 10*a* that active cracks become large very fast not only by propagation but also by frequent crack coalescences at the latter stage of fatigue life. This kind of behavior cannot be obtained experimentally because the continuous observation of small inner cracks is impossible by any non-destructive method.

Figure 11 shows the relationship between the crack propagation rate, dr/dN, and the crack radius, r. In order to compare the propagation rates of inner cracks with the large crack propagation law, the dr/dN-r relationship was plotted only for cracks that propagated without coalescence between two successive interruptions for crack observation, ΔN (= 10 cycles). dr/dN is calculated by

$$\left[\frac{dr}{dN}\right]_i = \frac{r_{i+1} - r_i}{\Delta N}, \tag{4}$$

where r_i and r_{i+1} are the crack radii at the ith and $(i+1)$th interruptions. It is found from Fig. 11 that the propagation rate of inner cracks is distributed widely and that the highest rate is almost constant ($dr/dN \cong 3 \times 10^{-4}$ mm/cycle) independent of the crack radius. As the discrete propagation is assumed in the model, the frequency of crack propagation varies with the crack radius, but the highest propagation rate is held almost constant when the crack radius is small. As the crack radius becomes large, the distribution range of the propagation rate becomes small and converges on the large crack propagation law, which is derived based on fracture mechanics and expressed by

$$dr/dN = B \cdot r \tag{5}$$

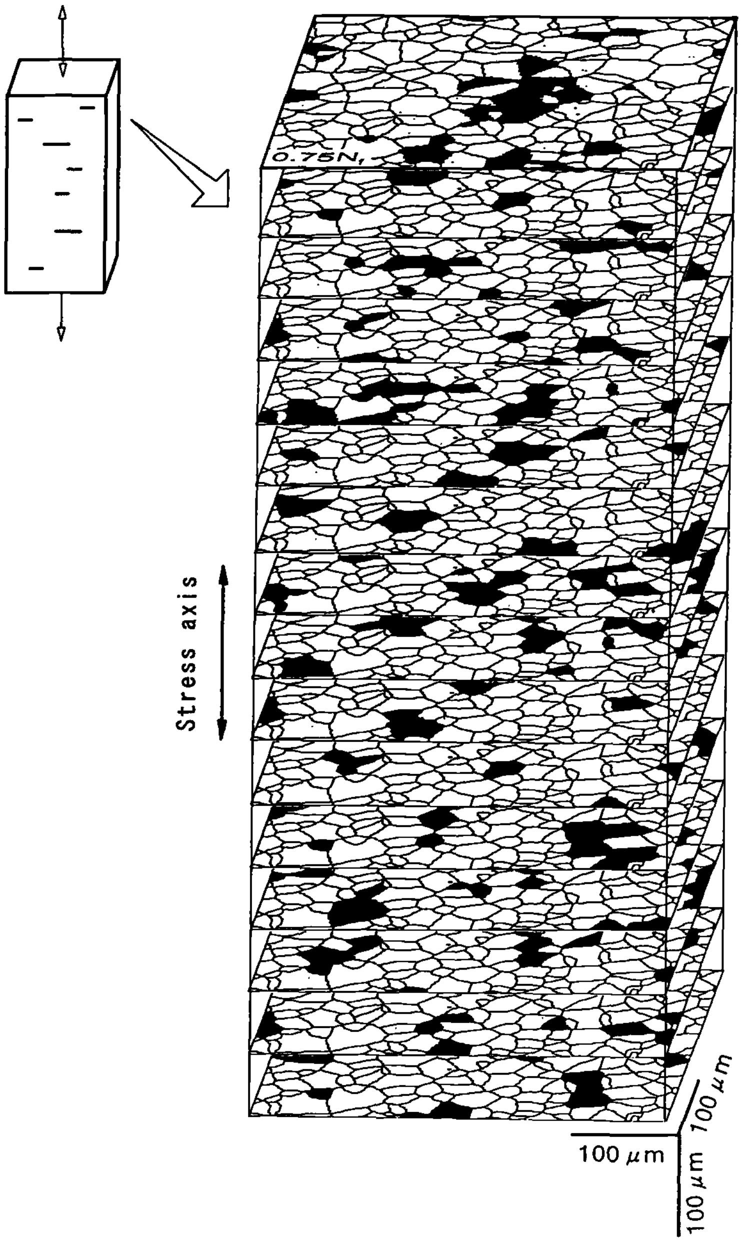

FIG. 8—*Three-dimensional visualization of inner cracks at* N/N$_f$ = *0.75.*

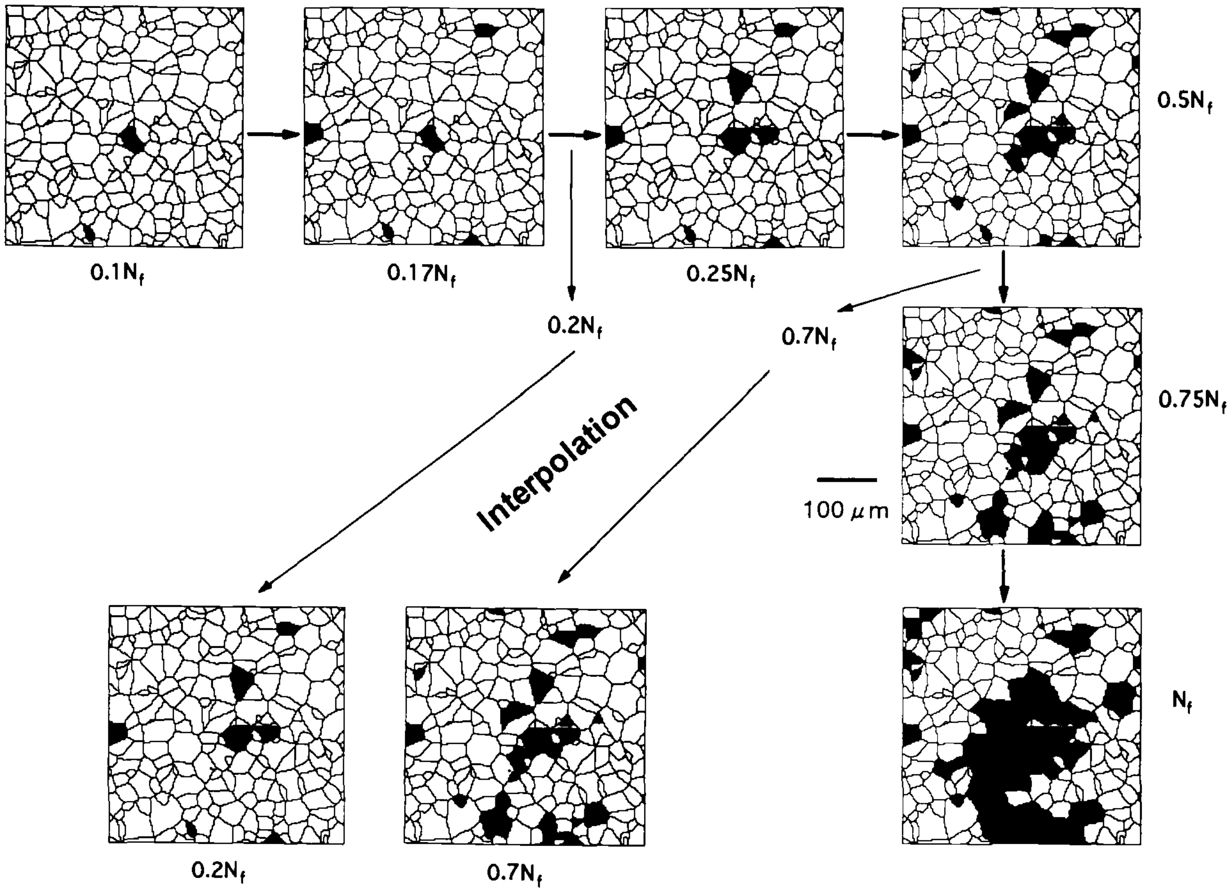

FIG. 9—*Initiation and propagation behavior of inner cracks on one of the facet sheets obtained by the simulation.*

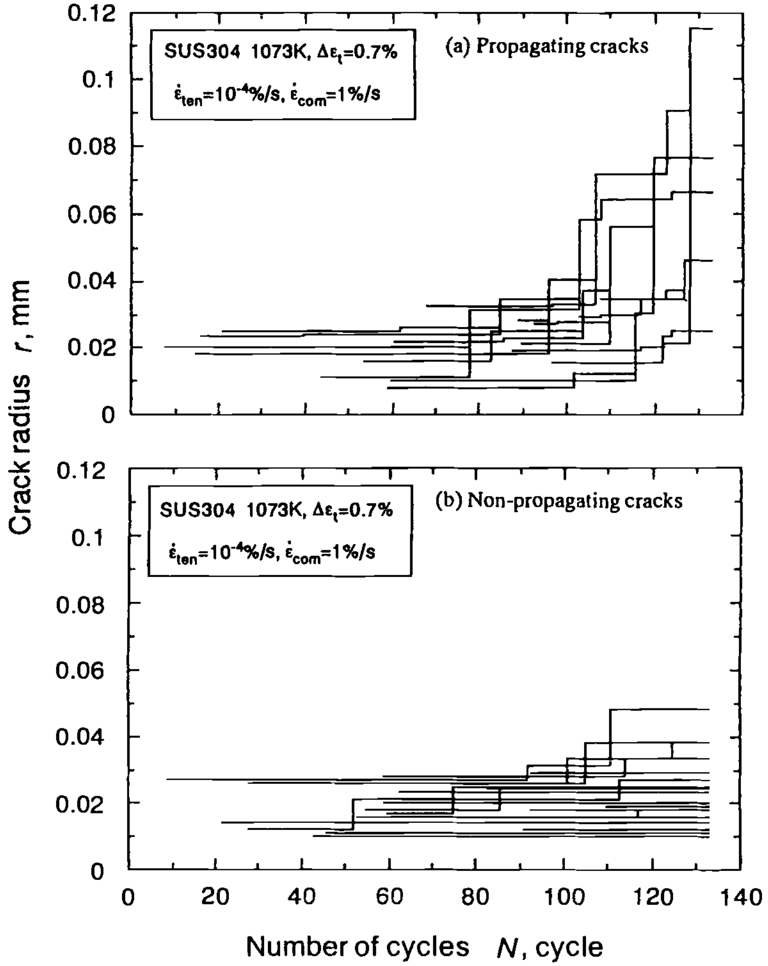

FIG. 10—*Propagation curves of inner cracks:* (a) *propagating cracks;* (b) *non-propagating cracks.*

where B is dependent on the material and test condition and is equal to 1.61×10^{-3} in this case [*1*].

Conclusions

In order to analyze the initiation and propagation behavior of multiple inner cracks in creep-dominant fatigue, the numerical simulation is conducted on the basis of a probabilistic model. Results obtained in this paper are summarized as follows.

1. A simple probabilistic model is proposed for the numerical simulation of inner cracking. The model represents microstructural inhomogeneity of grain boundary facets by the randomness in the fracture resistance, R.

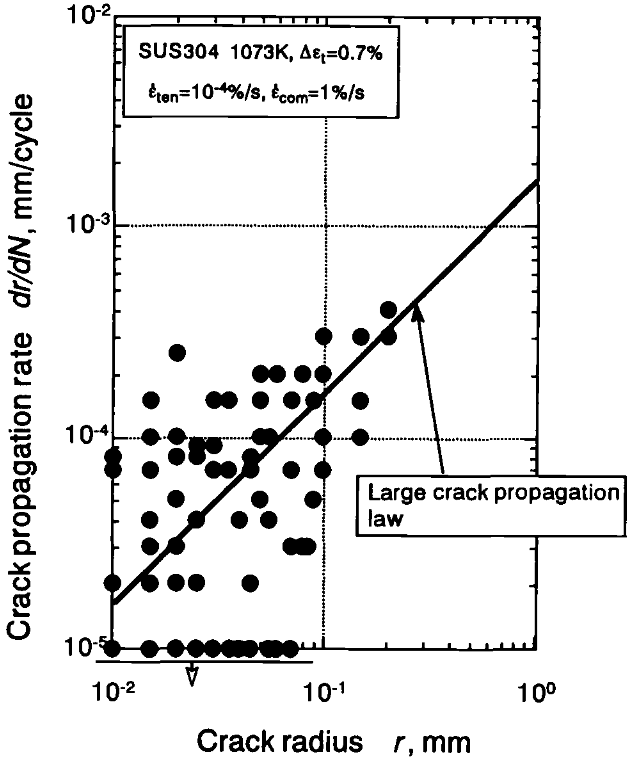

FIG. 11—*Relationship between crack propagation rate,* dr/dN, *and crack radius,* r.

2. Three-dimensional grain boundary facets, which are composed of layered facet sheets, are used in the simulation. Each facet sheet is numerically made based on an isotropic grain growth model, and the distribution of the facets obtained is identical to the actual one.
3. Two constants representing the condition of cracking simulation, i.e., the driving forces, F and K, are determined from the distribution of cracks observed on the cross section of six specimens interrupted at different life fractions, $N/N_f = 0.1, 0.17, 0.25, 0.5, 0.75$, and 1. Although the condition is determined from the discontinuous cracking data on the cross section, the simulation is carried out continuously throughout the fatigue life.
4. Three-dimensional distribution of inner cracks, namely, volumetric density (i.e., the number of inner cracks in a unit volume) and the mean radius (or the distribution of radius) of inner cracks, is analyzed by the numerical simulation. These results are obtained not only at observation points of $N/N_f = 0.1, 0.17, \cdots$, and 1 but also at other arbitrary fatigue cycles.
5. Crack propagation rate of each inner crack, *dr/dN*, is also obtained by the numerical simulation. As the cracks become large, the distributed propagation rate converges on the determinate propagation rate of large cracks, which is obtained on the basis of fracture mechanics.

References

[*1*] Ohtani, R., Kitamura, T., and Tada, N., "Experimental Mechanics on Initiation and Growth of Distributed Small Creep-Fatigue Cracks," *Recent Advances in Experimental Mechanics*, Proceedings of the 10th International Conference on Experimental Mechanics, S. Gomes et al., Eds., Balkema, Rotterdam, Vol. 2, 1994, pp. 1173–1179.

[*2*] Kitamura, T., Tada, N., and Ohtani, R., "Stochastic Simulation of Initiation and Early Growth of Small Cracks in Creep-Fatigue," *Probabilistic Structural Mechanics: Advances in Structural Reliability Methods*, Proceedings of IUTAM Symposium, P. D. Spanos and Y.-T. Wu, Eds., Springer-Verlag, Berlin, 1994, pp. 301–318.

[*3*] Ohtani, R. and Kitamura, T., "Initiation and Propagation of Microstructurally Small Cracks under Creep-Fatigue Condition," *Proceedings*, Fourth International Conference on Creep and Fracture of Engineering Materials and Structures, B. Wilshire and R. W. Evans, Eds., Institute of Metals, London, 1990, pp. 791–802.

[*4*] Tada, N., Ohtani, R., and Kitamura, T., "Inverse Analysis of Distribution of Internal Small Defects," *JSME International Journal, Series A*, Vol. 37, No. 4, 1994, pp. 450–455.

[*5*] Johnson, W. A. and Mehl, R. F., "Reaction Kinetics in Processes of Nucleation and Growth," *Transactions of AIME*, Vol. 135, 1939, pp. 416–458.

[*6*] Kitamura, T., Tada, N., Kuriyama, Y., and Ohtani, R., "Distribution of Grain-Boundary Length and Inclination of Type 304 Stainless Steel and Its Effects on Small Crack Initiation and Growth under Creep-Fatigue Conditions," *Transactions of JSME*, Vol. 56, No. 524, 1990, pp. 702–707 (in Japanese).

[*7*] Mahin, K. W., Hanson, K., and Morris, J. W. Jr., "Comparative Analysis of the Cellular and Johnson-Mehl Microstructures through Computer Simulation," *Acta Metallurgica*, Vol. 28, 1980, pp. 443–453.

[*8*] Tada, N., Kitamura, T., and Ohtani, R., "Monte Carlo Simulation of Creep-Fatigue Small Cracks Based on a Three-Dimensional Model of Random Fracture Resistance of Grain Boundaries," *Transactions of JSME*, Vol. 56, No. 524, 1990, pp. 708–714 (in Japanese).

Kee Bong Yoon,[1] *Un Bong Baek,*[2] *and Chang Min Suh*[3]

Effects of Loading Rate on Creep Crack Growth During the Succeeding Load-Hold Period Under Trapezoidal Fatigue Waveshapes

REFERENCES: Yoon, K. B., Baek, U. B., and Suh, C. M., "**Effects of Loading Rate on Creep Crack Growth During the Succeeding Load-Hold Period Under Trapezoidal Fatigue Waveshapes,**" *Elevated Temperature Effects on Fatigue and Fracture, ASTM STP 1297,* R. S. Piascik, R. P. Gangloff, and A. Saxena, Eds., American Society for Testing and Materials, 1997, pp. 102–116.

ABSTRACT: When turbines are started up in power plants, the procedures recommended by the manufacturer should be carefully followed. However, many utilities often start turbines so fast that they accelerate the crack growth of existing cracks. Hence, in order to accurately predict the crack growth life of a turbine rotor, a crack growth prediction model is needed in which the effects of load increase time on the crack growth rate during the succeeding load hold period are considered.

In this study, creep-fatigue crack growth tests were performed at 538°C using C(T) specimens of 1Cr-1Mo-0.25V rotor steel. Triangular and trapezoidal fatigue waveshapes with 0.5, 1, 10, and 100-s load rise times and 100-s load hold times were employed. The time-dependent crack growth rate during the load hold period, $(da/dt)_{avg}$, was correlated with estimated $(C_t)_{avg}$. Large data scatter was observed due to the effect of various load increase rates reaching the hold load. A new C_t estimation equation was proposed in which the effects of load increase rate are considered. The effectiveness of the proposed equation is argued by showing that the scatter of the measured $(da/dt)_{avg}$ data was reduced when the new equation was adopted. Also, characteristics of the initial transient crack growth behavior are studied and show that the cause is the oxidation-dominated crack growth mechanism during the transient period.

KEYWORDS: creep, creep fatigue, crack, Cr-Mo-V steel, C_t-parameter, oxidation

As turbine rotors of power plants become aged, cracks initiate at the root of grooves or at the inclusion near bore holes. During the operational procedures of start-up, steady operation, and shutdown of power plants, these cracks in a rotor usually experience fatigue loadings similar to trapezoidal waveshapes. The turbine start-up procedure is generally recommended by the manufacturer and should be followed strictly by utilities to reduce the magnitude of thermal stress and other damage. However, many utilities often start the turbine hurriedly and impose rapid loading on turbine components, which can cause accelerated growth of existing cracks. Hence, in order to accurately predict crack growth life of a turbine rotor or other thick section

---

[1] Associate professor, Department of Mechanical Design and Production Engineering, Chung Ang University, 221 Huksuk Dongjak, Seoul 156-756, Korea.

[2] Research engineer, Failure Prevention Research Center, Korea Research Institute of Standards and Science, P.O. Box 102 Yoosung, Taejon 305-600, Korea.

[3] Professor, Department of Mechanical Engineering, Kyungpook National University, 1370 Sankyuk Buk-gu, Taegu 702-701, Korea.

components, a crack growth prediction model is needed in which the effects of load increase rate on crack growth behavior during the succeeding load hold period are considered.

In this study, creep-fatigue crack growth rates were measured using C(T) specimens machined from a typical 1Cr-1Mo-0.25V rotor steel under trapezoidal waveshapes with different load increase times. From the test results, effects of load increase time on the crack growth rate during the succeeding load hold period are investigated. By proposing a new C_t estimation equation in which the observed effects of load increase rate are considered, the previous creep-fatigue crack growth model [*1–3*] is improved.

At early stages of creep-fatigue crack growth tests in laboratories, initial transient behavior that implies a high crack growth rate has been generally observed by some researchers [*2,4*], that is, the crack growth rate (da/dN) decreases as the applied stress intensity factor level (ΔK) is increased with crack growth. And after a certain period of the test, da/dN reaches its minimum value and then increases as ΔK is increased further. If this initial transient behavior occurs during the operation of real plant components, the remaining life of the components will be much shorter than predicted by the conventional crack growth prediction model. A cause of the initial transient behavior is also investigated in this study.

Experiments

Mechanical Testing

Specimens were machined from a forged hollow cylinder of 1Cr-1Mo-0.25V steel. Chemical composition of the test material is shown in Table 1. Tension tests were performed at 538°C using cylindrical specimens with a diameter of 6.25 mm and a gage length of 25.4 mm according to the procedures recommended in ASTM Test Methods for Tension Testing of Metallic Materials (E 8) and Test Methods for Elevated Temperature Tension Tests of Metallic Materials (E 21). In order to determine material creep constants; four creep tests were also performed at different stress levels (35, 50, 60, and 65% of yield stress) using cylindrical specimens with a diameter of 6.25 mm and a gage length of 32 mm according to ASTM standard Practice for Conducting Creep, Creep-Rupture, and Stress-Rupture Tests of Metallic Materials (E 139). Dead-weight level-type creep machines were used, and creep strain was monitored by an LVDT attached to the extensometer, which was installed on the specimen. The LVDT analog signal was converted to a digital signal and stored in a personal computer periodically. The specimen loading direction in the tension and creep test was parallel to the circumferential direction of the forged material cylinder block as shown in Fig. 1.

Creep-Fatigue Crack Growth Testing

For creep-fatigue crack growth tests, compact tension specimens with an initial crack ratio of 0.4 were machined as shown in Fig. 1. After precracking, specimens were side-grooved by 25% of their thickness to prevent crack tunneling during high-temperature fatigue crack growth testing. The d-c electric potential technique was employed for crack length monitoring [*5*]. Tests were terminated when the amount of crack growth reaches about 7 to 10 mm. The tested specimens were cooled down to liquid nitrogen temperature and fractured open. Then, the final

TABLE 1—*Chemical composition of the test material (1Cr-1Mo-0.25V steel).*

Element	C	Si	Mn	P	S	Ni	Cr	Mo	V	As	Sn	Sb
Wt%	0.31	0.23	0.76	0.006	0.001	0.36	1.11	1.32	0.27	0.006	0.005	0.001

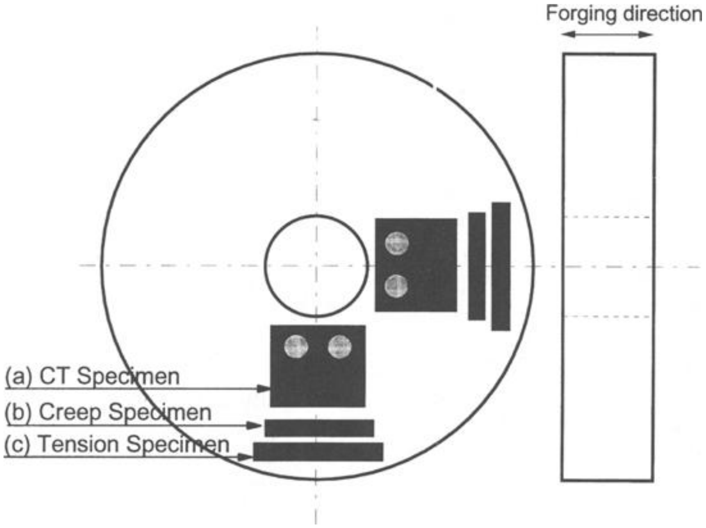

FIG. 1—*Specimen orientation.*

crack length was measured at 9 points evenly spaced in the thickness direction. In case the measured crack length was different from that predicted by the d-c potential method, the predicted crack length was corrected based on the measured value assuming the error is proportional to the amount of crack growth [5].

To measure the crack growth rate during the load rising period and load decreasing period, fatigue tests were performed under triangular waveshapes with [load rising time]/[load decreasing time] of 0.5/0.5, 1/1, 10/1, and 100/1 (unit: seconds). Detailed test conditions are shown in Table 2. On the other hand, in order to measure the time-dependent crack growth rate during the load hold period, creep-fatigue crack growth tests were also performed under trapezoidal waveshapes with a 100-s load hold period. To assess the effect of load increase rate to crack growth during the subsequent load hold period, the load hold time and the load decreasing time were kept constant but the load rising time was varied. The load decreasing time of all the tests was selected as 1 s, during which little creep deformation is expected to occur. The test conditions, i.e., [rising time]/[hold time]/[decreasing time], were 0.5/100/1, 1/100/1, 10/100/1, and 100/100/1 (unit: second) as summarized in Table 3.

Two additional tests under trapezoidal waveshapes of 1/100/1 condition were performed to investigate crack tip damage morphology. One test was interrupted at the early stage of the

TABLE 2—*Test conditions under triangular waveshapes.*

Specimen No.	Rise Time/ Decay Time, s	Initial Crack Length, mm	Final Crack Length, mm	Initial Potential, mV	Final Potential, mV	Max Load, KN	Min Load, KN	Total Cycle
1	0.5/0.5	22.17	30.10	0.333	0.475	20.6	2.1	16 185
2	1/1	21.70	31.58	0.318	0.503	20.6	2.1	14 050
3	10/1	21.88	34.01	0.345	0.559	30.0	3.0	6 362
4	10/1	21.99	28.80	0.327	0.440	30.0	3.0	5 000
5	100/1	21.79	28.45	0.317	0.413	30.0	3.0	2 214
6	100/1	26.76	30.37	0.422	0.490	20.0	2.0	1 708

TABLE 3—*Test conditions under trapezoidal waveshapes.*

Specimen No.	Rise Time/ Hold Time/ Decay Time, s	Initial Crack Length, mm	Final Crack Length, mm	Initial Potential, mV	Final Potential, mV	Max Load, KN	Min Load, KN	Total Cycle
1	0.5/100/1	21.72	29.70	0.322	0.460	30.0	3.0	5 315
2	1/100/1	22.29	...	0.318	0.508	30.0	3.0	4 400
3	1/100/1	22.06	27.99	0.334	0.434	30.0	3.0	4 010
4	10/100/1	22.06	29.08	0.323	0.446	30.0	3.0	3 607
5	100/100/1	21.11	27.98	0.322	0.440	30.0	3.0	2 358

testing when it still showed the initial transient behavior, and the other was continued until it showed normal crack growth behavior after passing the initial transient period. The tested specimens were sectioned by half in the thickness direction. The sectioned surface of the half specimen was polished, and the crack tip area was observed using an optical microscope. The other half was broken open, and the fractured surface of crack tip area was observed using a scanning electron microscope.

Results

Mechanical Properties

Tension test results are summarized in Table 4. A power law plasticity between plastic strain (ε_p) and stress (σ) is assumed as $\varepsilon_p = D\sigma^m$, and the plasticity constants, D and m, are determined by linear regression. From the creep strain versus time data of each creep test result the steady state creep strain rate, $\dot{\varepsilon}_s$, is determined and shown in Table 5. Creep constants are also determined by linear regression assuming $\dot{\varepsilon}_s = A\sigma^n$. Results are shown in Fig. 2.

Creep-Fatigue Crack Growth Behavior

Fatigue crack growth test results under the triangular waveshapes are shown in Fig. 3. In this figure, crack growth rate, *da/dN*, is characterized by ΔK. The value of ΔK is calculated by Eq 1 as proposed in ASTM Test Method for Measurement of Fatigue Crack Growth Rates (E 647)

$$\Delta K = \frac{\Delta P}{B\sqrt{W}} \cdot F\left(\frac{a}{W}\right) \tag{1}$$

where $F(a/W)$ is a dimensionless function for C(T) specimen, a is crack length, W is specimen width, B is thickness, and ΔP is load range. Figure 3 shows that crack growth characteristics

TABLE 4—*Tensile properties of the test material at 24 and 538°C.*

Test Temperature, °C	Yield Stress (0.2%), MPa	Tensile Strength, MPa	Elongation, %	Reduction of Area, %	D, MPa^{-m}	m	Young's Modulus, GPa
24	665.2	823.1	18.8	59.4	21.8E-73	25.54	209.4
538	533.5	580.6	22.7	55.5	2.82E-54	18.75	147.3

NOTE: $\varepsilon_p = D \cdot \delta^m$.

TABLE 5—*Creep properties of the test material at 538°C.*

Specimen No.	Applied Stress, MPa	Secondary Creep Rate, h^{-1}
1	346	1.27E-3
2	320	8.98E-4
3	274	7.45E-5
4	187	1.97E-6

Creep Constant	A (MPa^{-n})	n
Temperature 538°C	7.70E-27	9.13

are similar when the fatigue loading condition varies among 0.5/0.5, 1/1, and 10/1. The crack growth rate under the 10/1 condition is slightly higher than the others, but the difference is not significant. Since the crack growth rate is not increased as the load increase time is increased from 0.5 s to 10 s, it can be argued that the time-dependent crack growth due to creep does not occur during this period. A linear regression line is determined using all of the data obtained from 0.5/0.5, 1/1, and 10/1 fatigue tests as follows:

$$\frac{da}{dN} = 7.01 \times 10^{-11}(\Delta K)^{2.48} \tag{2}$$

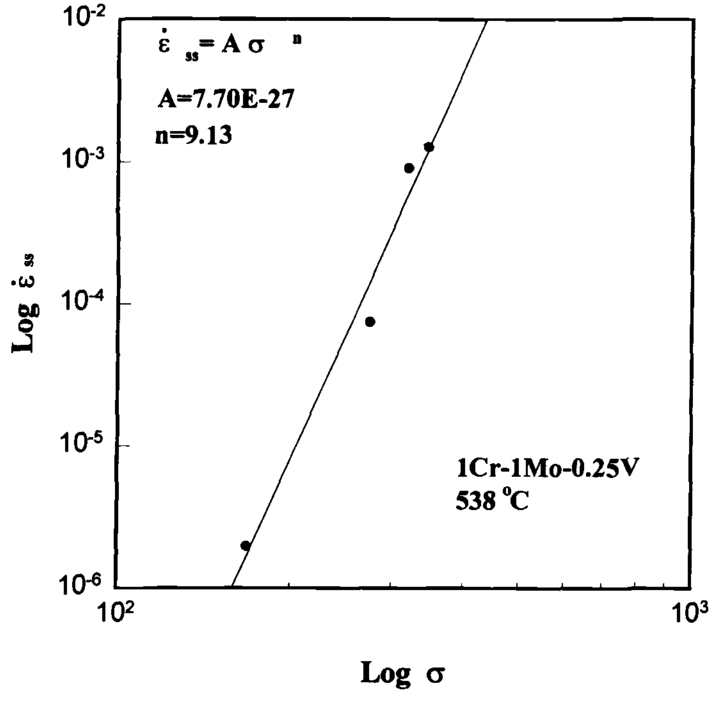

FIG. 2—*Determination of power law creep constants of 1Cr-1Mo-0.25V steel at 538°C.*

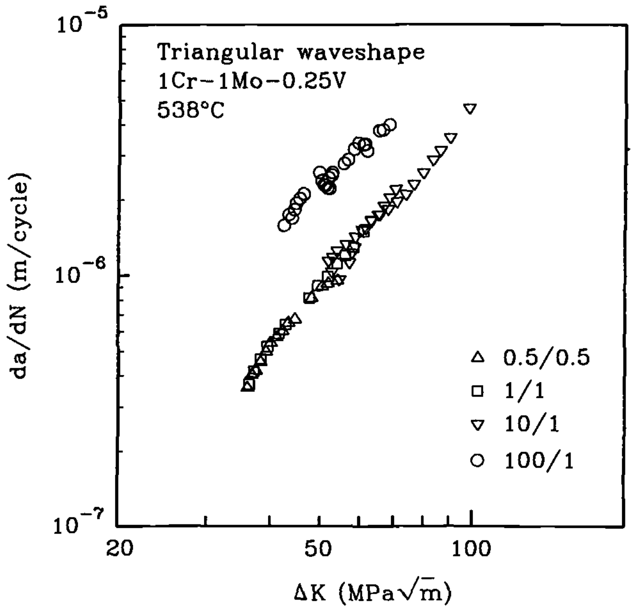

FIG. 3—*Fatigue crack growth behavior of a 1Cr-1Mo-0.25V steel at 538°C under triangular waveshapes.*

where, *da/dN* is expressed in m/cycle, and ΔK is expressed in MPa $m^{1/2}$. Equation 2 represents the cycle-dependent crack growth behavior, which excludes the time-dependent contribution. The regression line is represented as a solid line in Fig. 4. In the case in which the load increase time is changed to 100, an additional amount of crack growth appears, which must be time-dependent crack growth due to creep during the load increase time. Consequently, *da/dN* appears much higher than those of 0.5/0.5, 1/1, and 10/1 tests as shown in Fig. 3. A linear regression line is also determined from 100/1 test results and shown as a dotted line in Fig. 4. The equation for the regression line is:

$$\frac{da}{dN} = 1.59 \times 10^{-9}(\Delta K)^{1.86} \tag{3}$$

Figure 5 shows test results under trapezoidal fatigue waveshapes with a 100-s load hold period and 0.5, 1, 10, and 100-s load increase periods. In this figure, *da/dN* is characterized in terms of ΔK. To show the difference of crack growth rates of these tests from those without a load hold period, a polynomial regression line for each test is plotted in Fig. 6 with linear regression lines obtained from the tests under the triangular waveshapes. For a given ΔK value, the difference of crack growth rate between 1/100/1 test data and 1/1 test data represents the amount of time-dependent crack growth during the load hold period of 100 s after 1 s of load rise time. In a similar manner, the amount of time-dependent crack growth during the load hold period of a cycle is determined, and by dividing this value with load hold period, t_h, the average time-dependent crack growth rate, $(da/dt)_{avg}$, is subsequently determined for a given cycle.

The average time-dependent crack growth rate during the load hold period, $(da/dt)_{avg}$, is characterized by the average value of C_t, $(C_t)_{avg}$, and shown in Fig. 7. The characterizing

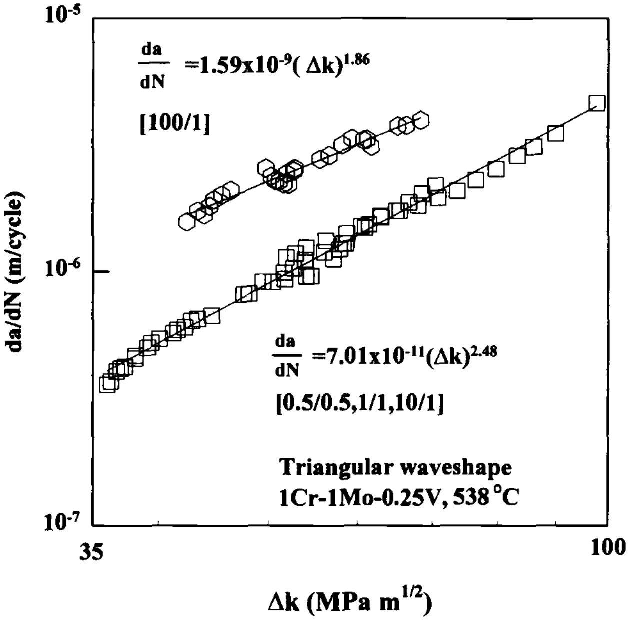

FIG. 4—*Regression results of fatigue crack growth rates of a 1Cr-1Mo-0.25V steel at 538°C under triangular waveshapes.*

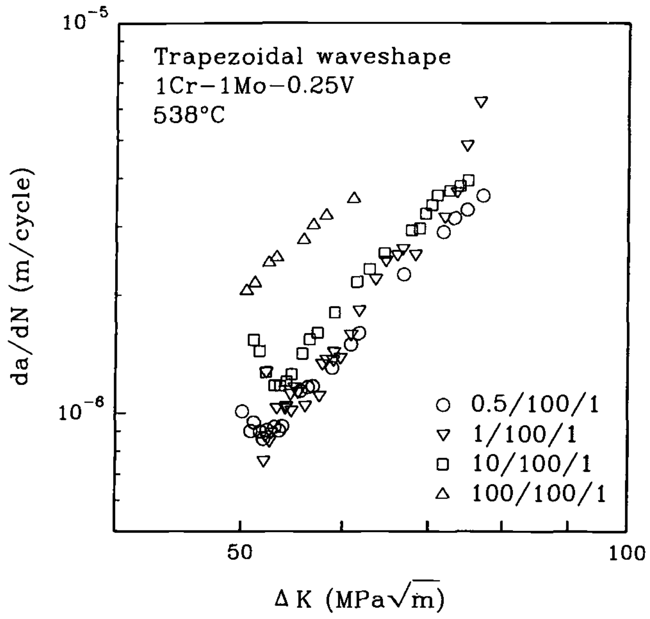

FIG. 5—*Fatigue crack growth behavior of a 1Cr-1Mo-0.25V steel at 538°C under trapezoidal waveshapes.*

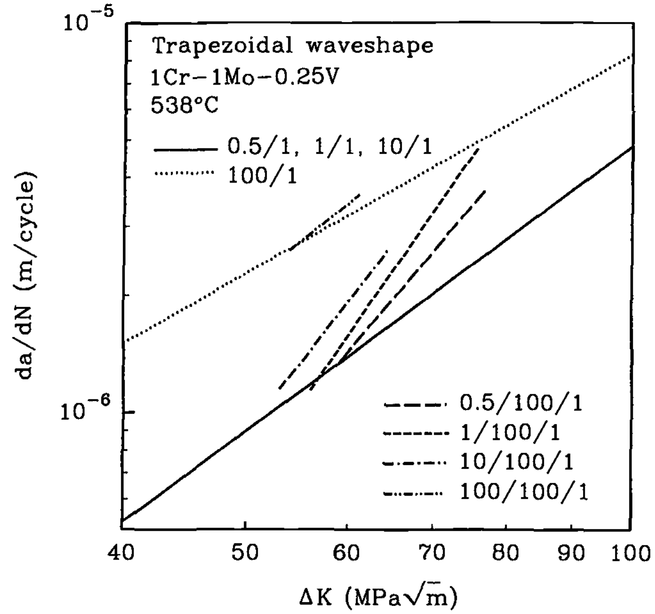

FIG. 6—*Fatigue crack growth behavior of a 1Cr-1Mo-0.25V steel at 538°C under triangular and trapezoidal waveshapes.*

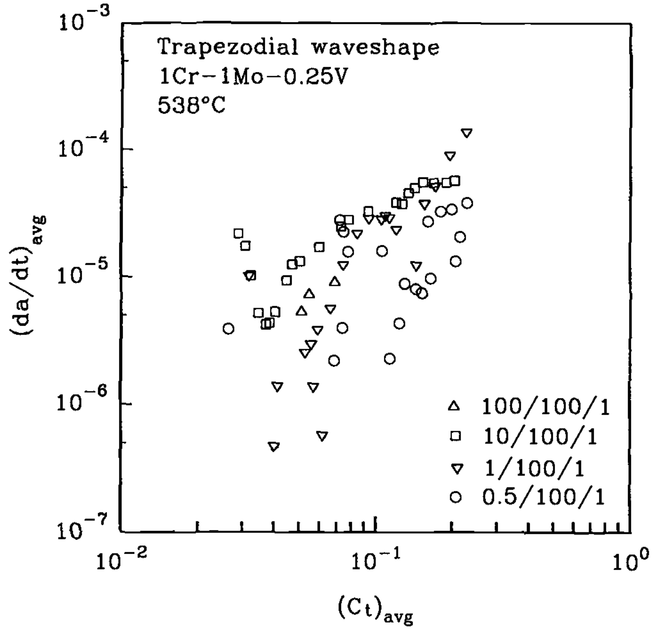

FIG. 7—*Time-dependent crack growth behavior of a 1Cr-1Mo-0.25V steel at 538 °C during load hold period of trapezoidal waveshapes.*

parameter $(C_t)_{avg}$ is estimated using Eq 4 from the measured crack length, material creep constants, and test load data. Equation 4 was deprived [2] for materials showing elastic-secondary creeping behavior.

$$(C_t)_{avg} = \frac{2\alpha\beta\hat{r}_c(\theta,n)}{E}(1 - \nu^2)\frac{\Delta K^4}{W}\frac{F'}{F}(EA)^{\frac{2}{n-1}}t_h^{-\frac{n-3}{n-1}} + C^* \qquad (4)$$

Where

$$\alpha = \frac{1}{2\pi}\left[\frac{(n + 1)^2}{2n\alpha_n^{n+1}}\right]^{\frac{2}{n-1}}, \alpha_n^{n+1} = \frac{n + 1}{n}\frac{\pi(1 - \nu^2)}{I_n}, \beta = 1/3, \hat{r}_c\,(90°, n) \approx 0.38,$$

t_h is load hold time and I_n is a dimensionless function dependent on n [6]. C^* was estimated using known J-integral solutions [7] as in Eq 5.

$$C^* = \frac{A}{(W - a)^n}h_1\left(\frac{a}{W},n\right)\left(\frac{P}{1.455\zeta B}\right)^{n+1} \qquad (5)$$

Where ζ is a dimensionless function [7], P is hold load, and h_1 is a function dependent on n. For 1Cr-1Mo-0.25V steel whose n value is 9.1, h_1 is derived as shown in Eq 6 by interpolating the h_1 data for other n values given in EPRI J- handbook [7].

$$h_1\left(\frac{a}{W}, 9.1\right) = 3.67 - 20.71\left(\frac{a}{W}\right) + 47.62\left(\frac{a}{W}\right)^2 - 45.54\left(\frac{a}{W}\right)^3 + 15.94\left(\frac{a}{W}\right)^4 \qquad (6)$$

Equation 6 is valid in the range of $0.375 < a/W < 1$. In Eq 4, employed for estimating the $(C_t)_{avg}$, load rise time effect is not considered. Hence, the data scatter observed in Fig. 7 is not surprising.

Discussion

Effect of Load Increase Rate

In the creep-fatigue crack growth models previously proposed for trapezoidal waveshapes using C_t as a characterizing parameter, various material behaviors such as secondary creep, primary creep [8], and crack tip plasticity [9] were considered in estimating C_t values. However, load history effects such as effect of load increase rate were not considered. It has been generally assumed that the load is applied instantaneously in trapezoidal fatigue waveshapes, which means that the crack tip stress field at the beginning of the load hold period is purely elastic or elastic-plastic HRR stress field.

Riedel [10] showed that the crack tip stress field at the beginning of the load hold period is affected by the load rise time, t_r. Resultingly, the crack tip stress relaxation and the crack growth rate during the succeeding load hold period are also affected by the load rise time. When the load increase time is shorter than a certain transition time [9] that is required to attain the extensive creep condition near the crack tip, the intensity of the singular stress field at the crack tip at the beginning of the load hold period is expressed by $C(t)$ as shown in Eq 7:

$$C(t) = \frac{K^2(1 - \nu^2)}{E(n + 1)[t + t_r/(1 + 2n)]} + C^* \qquad (7)$$

where E is Young's modulus, ν is Poisson's ratio, K is the stress intensity factor, n is creep exponent, and t is elapsed time after holding the load. Similarly, the magnitude of C_t, which represents the creep zone expansion rate at the crack tip during the load hold period, should also be affected by the load increase time. Using an analogy, a new estimation equation for C_t can be proposed as follows.

When the load is instantaneously applied for a trapezoidal waveshape, the small-scale creep condition is dominant at the crack tip. In this case, $C(t)$ becomes a function of t^{-1} and C_t becomes a function of $t^{-(n-3)/(n-1)}$. On the other hand, if the load is increased in t_r, $C(t)$ is a function of $(t + t_r/(1 + 2n))^{-1}$ as shown in Eq 7. Analogous to $C(t)$, the dependence of C_t on t_r can be expressed as shown in Eq 8:

$$C_t = \frac{4\alpha\beta\hat{r}_c(\theta,n)}{E(n-1)}(1-\nu^2)\frac{K^4}{W}\frac{F'}{F}(EA)^{\frac{2}{n-1}}\left(t + \frac{\delta}{1+2n}t_r\right)^{-\frac{n-3}{n-1}} \tag{8}$$

This is obtained by substituting t with $t + \delta t_r/(1 + 2n)$ in the C_t equation [2] derived for elastic-secondary creeping materials. In Eq 8, a constant δ is introduced as a scaling factor since what we can infer from the analogy between $C(t)$ and C_t is only the functional form of C_t, not the exact value of the function. The value of δ could be determined by comparing the measured C_t with that obtained from detailed finite element analysis as in the case of determining the value of β [*11*]. Equation 8 implies that crack tip stress relaxation during the time t_r under varying load conditions, i.e., from zero to the hold load, is equivalent to that during the time, $\delta t_r/(1 + 2n)$, under the constant hold load. By substituting Eq 8 to the definition of $(C_t)_{\text{avg}}$, Eq 9, a new equation for $(C_t)_{\text{avg}}$, is derived as shown in Eq 10.

$$(C_t)_{\text{avg}} = \frac{1}{t_h}\int_0^{t_h} C_t\,dt \tag{9}$$

$$(C_t)_{\text{avg}} = \frac{2\alpha\beta\hat{r}_c(\theta,n)}{E}(1-\nu^2)\frac{\Delta K^4}{W}\frac{F'}{F}(EA)^{\frac{2}{n-1}}\left[\frac{\left(t_h + \frac{\delta}{1+2n}t_r\right)^{\frac{2}{n-1}} - \left(\frac{\delta}{1+2n}t_r\right)^{\frac{2}{n-1}}}{t_h}\right] + C^* \tag{10}$$

Using this newly proposed Eq 10, $(C_t)_{\text{avg}}$ values are estimated again and the new $(da/dt)_{\text{avg}}$ versus $(C_t)_{\text{avg}}$ relation is obtained as shown in Fig. 8. The value of δ is temporarily assumed to be unity. However, a more accurate value of δ can be determined from finite element analysis, which is a future subject for this research. In Fig. 8, data scatter is reduced considerably in comparison with Fig. 7. This implies that Eq 10 effectively reflects the effect of load increasing rate on C_t values at the succeeding load hold period. Using Eq 10 and the creep-fatigue crack growth model previously proposed [*3*], the difference of crack growth rates under different conditions of load increase time can be predicted more accurately. The model can be used in assessing the severity of damage or crack growth acceleration after a sudden start-up practice of elevated temperature components such as turbines or other pressure vessels.

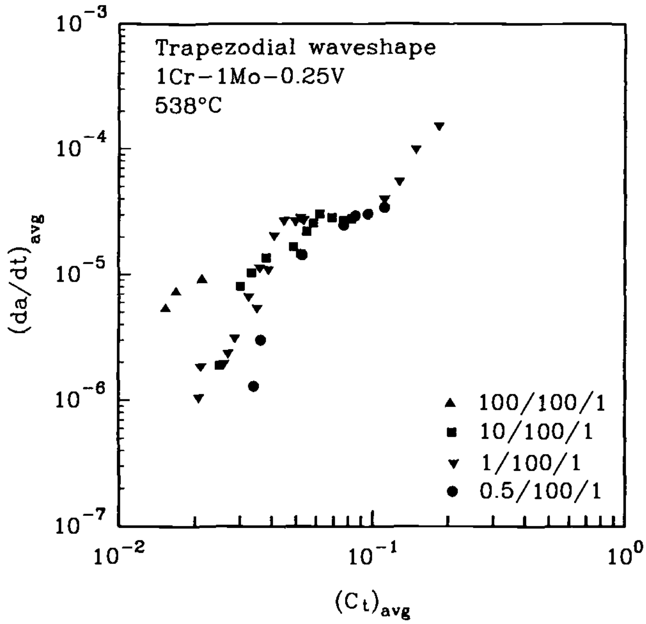

FIG. 8—*Time-dependent crack growth behavior of a 1Cr-1Mo-0.25V steel at 538°C during load hold period of trapezoidal waveshapes. (The new* C_t *estimation equation is used for data reduction.)*

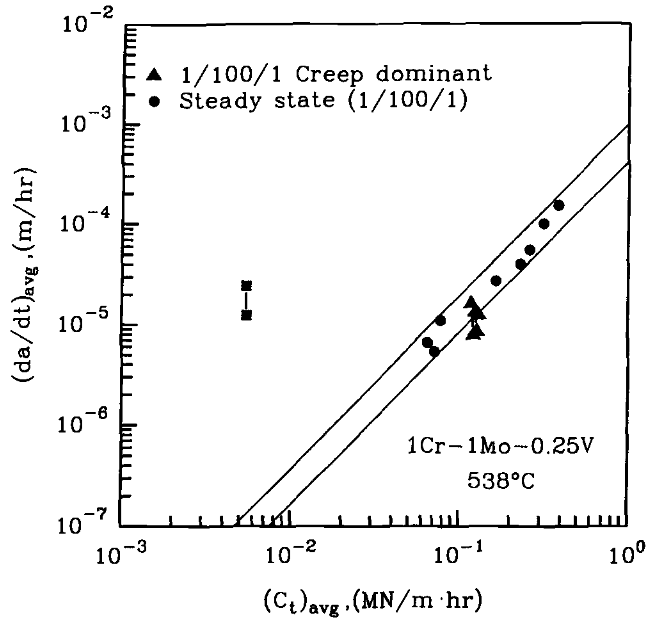

FIG. 9—*Time-dependent crack growth behavior of a 1Cr-1Mo-0.25V steel at 538°C during load hold period of 1/100/1 trapezoidal waveshapes.*

Initial Transient Behavior in Creep-Fatigue Crack Growth

Time-dependent crack growth behavior, $(da/dt)_{avg}$ versus $(C_t)_{avg}$, under the 1/100/1 condition is shown in Fig. 9 with data of two additional tests performed for investigating crack tip damage morphology. One set of crack growth data obtained from the test interrupted at the early stage of the testing when it still showed the initial transient behavior is denoted as solid rectangles (■), and the other obtained from the test continued until it showed regular crack growth behavior after passing the initial transient period is denoted as solid triangles (▲) with two lines showing the scatter band of regular crack growth trend. Figure 10 shows optical microscopy of the crack tip area of the sectioned specimen surface for both cases. The crack tip regions are enlarged and shown in Fig. 11*a* for the transient behavior specimen and in Fig. 12*a* for the regular behavior specimen. Scanning electron microscopy of the fracture surface at the corresponding crack tip region is also shown in the same figures (Fig. 11*b* and Fig. 12*b*).

The transient behavior specimen shows a considerably thick oxidation layer along the crack surface (Fig. 10*a*). The crack tip is actually embedded in the oxide layer; thus, the oxide tip is propagating through the metal matrix in advance of the crack tip. The crack tip propagation is behind the oxide tip propagation. This is clearly shown in Fig. 11. In Fig. 11*b*, the shape of

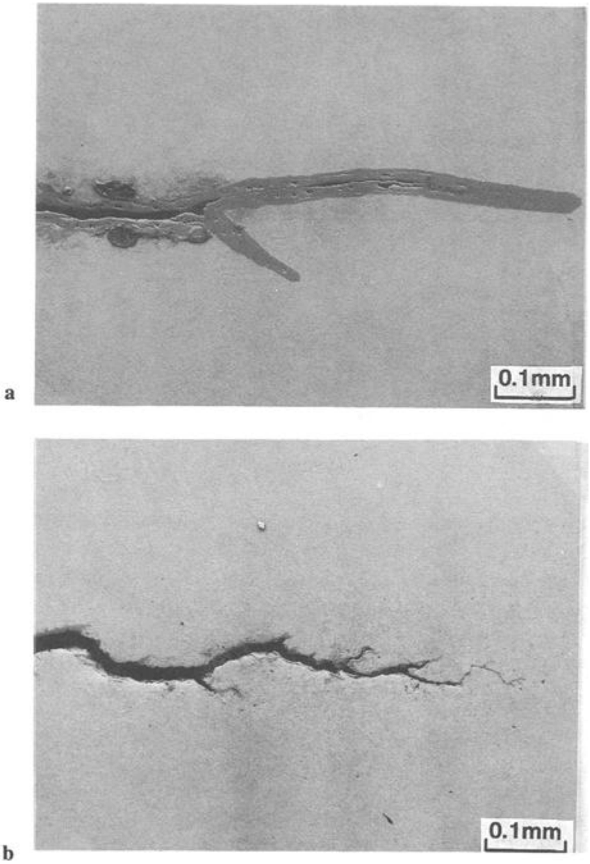

FIG. 10—*Crack growth morphology of 1Cr-1Mo-0.25V steel at 538°C:* (a) *initial transient crack growth;* (b) *regular crack growth.*

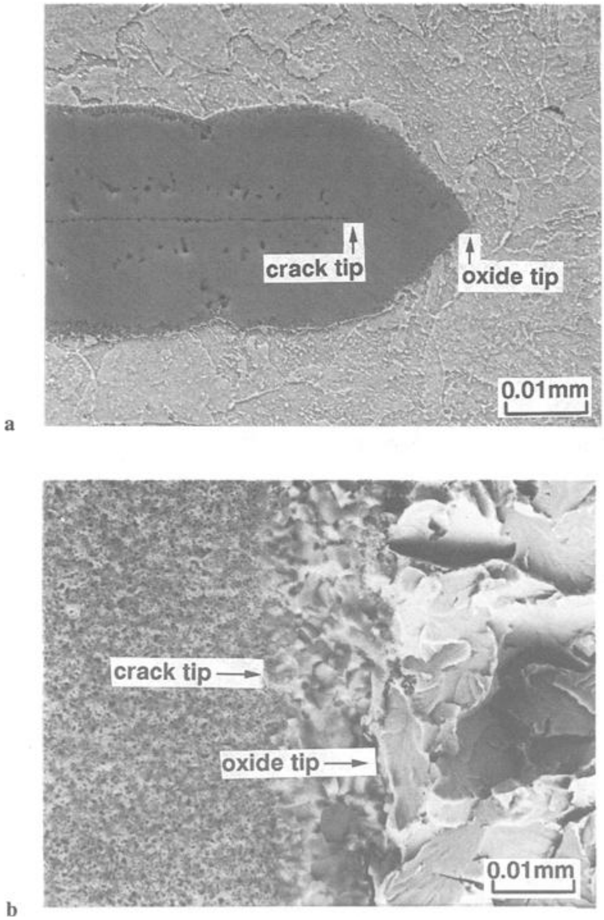

FIG. 11—*Crack tip morphology of 1Cr-1Mo-0.25V steel during initial transient crack growth:* (a) *side view;* (b) *fracture surface.*

the flat crack propagation surface is different from that of the rocky oxide fractured surface, which is also distinguished from the brittle metal fractured surface. In the regular behavior specimen, thickness of the oxidation layer is considerably decreased as the crack tip is propagating through the metal matrix. Many creep cavities are also observed on the grain boundaries near the crack tip as expected. From the above observations, it can be concluded that the initial transient behavior in Cr-Mo-V steel occurs because of the oxidation-dominant creep growth mechanism. Thus, the C_t parameter may not be used as a characterizing crack-tip parameter during the initial transient crack growth period.

Conclusions

Creep-fatigue crack growth tests were performed under triangular waveshapes and trapezoidal waveshapes with 0.5, 1, 10, and 100-s load rise times and 100-s load hold time using a typical 1Cr-1Mo-0.25V rotor steel at 538°C. The effects of load increase rate on the crack

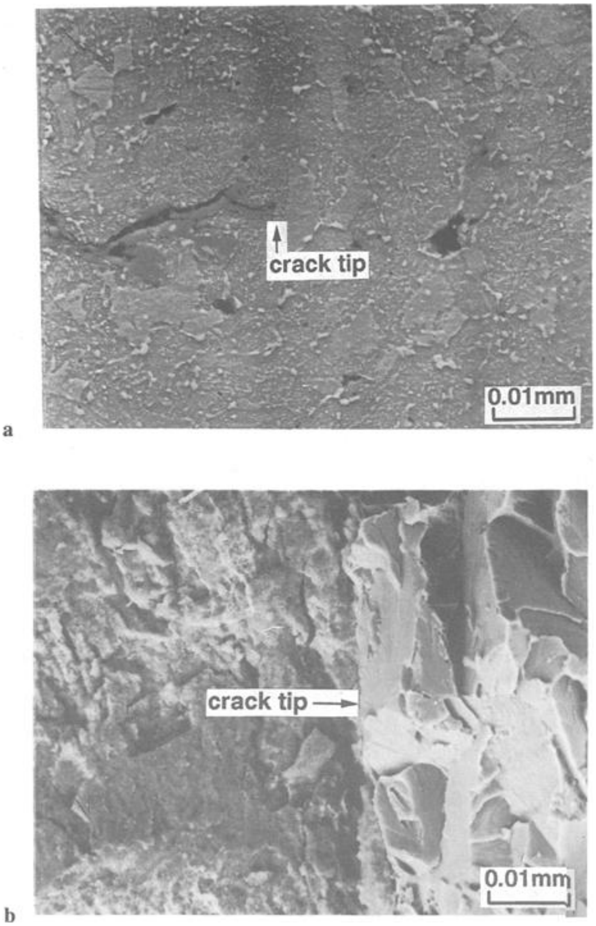

FIG. 12—*Crack tip morphology of 1Cr-1Mo-0.25V steel during regular crack growth:* (a) *side view;* (b) *fracture surface.*

growth behavior during the succeeding load hold period are investigated. The following conclusions are obtained.

1. From the fatigue test results under the triangular waveshapes with [load rise time]/[load decay time] of 0.5/0.5, 1/1, 10/1, 100/1 (unit: second), it was found that the time-dependent crack growth did not occur when the load rise time was increased from 0.5 to 10 s. However, the time-dependent crack growth due to creep occurred when the load rise time was increased to 100 s.
2. Fatigue test results under the trapezoidal waveshapes with [load rise time]/[load hold time]/[load decay time] of 0.5/100/1, 1/100/1, 10/100/1, 100/100/1 (unit: second) are reported. When $(da/dt)_{\mathrm{avg}}$ values are characterized by $(C_t)_{\mathrm{avg}}$ estimated using the equation previously derived for elastic-secondary creeping materials, data scatter is large since the effect of load increase time is not considered in the estimating equation of $(C_t)_{\mathrm{avg}}$.

3. A new C_t equation is proposed in which the effect of load increase rate on the values of C_t during the succeeding load hold period is considered. Effectiveness of the new C_t equation is argued by showing reduction of data scatter in the $(da/dt)_{avg}$ versus $(C_t)_{avg}$ relation.

4. Initial transient behavior was shown in creep-fatigue crack growth tests using 1Cr-1Mo-0.25V steel at 538°C in air. It was verified that the cause of the initial transient behavior is the oxidation-dominated crack growth mechanism during the transient period. Since the oxidation is dominant during the transient period, C_t cannot characterize the time-dependent crack growth rate, which assumes a creep-dominant crack growth mechanism.

Acknowledgment

The authors wish to acknowledge the partial support of KRISS for this study under the project entitled "Development of a General Model for Predicting Crack Growth Rate at High Temperature."

References

[*1*] Viswanathan, R., "Damage Mechanisms and Life Assessment of High-Temperature Components," ASM International, American Society of Metals, Metals Park, OH, 1989.

[*2*] Saxena, A. and Gieseke, B., "Transients in Elevated Temperature Crack Growth," EGF-6, Vol. III, Elsevier Publications, New York, 1987, pp. 19–36.

[*3*] Yoon, K. B., Saxena, A., and Liaw, P. K., "Characterization of Creep-Fatigue Crack Growth Behavior under Trapezoidal Waveshape Using C_t-Parameter," *International Journal of Fracture*, Vol. 59, 1993, pp. 95–114.

[*4*] Saxena, A., "Fracture Mechanics Approaches for Characterizing Creep-Fatigue Crack Growth," *JSME International, Series A*, Vol. 36, No. 1, 1993, pp. 1–20.

[*5*] Saxena, A. and Han, J., "Evaluation of Crack Tip Parameters for Characterizing Crack Growth Behavior in Creeping Materials," ASTM Task Group Report E 24.08.07/E24.04.08, 1986.

[*6*] Shih, C. F., "Tables of Hutchinson-Rice-Rosengren Singular Field Quantities," Brown University, Providence, RI, 1983.

[*7*] Kumar, V., German, M. D., and Shih, C. F., "An Engineering Approach for Elastic-Plastic Fracture Analysis," NP-1931, EPRI, Palo Alto, CA, 1981.

[*8*] Leung, C. P., McDowell, D. L., and Saxena, A., "Consideration of Primary Creep at Stationary Crack Tips: Implication for the C_t Parameter," *International Journal of Fracture*, Vol. 36, No. 4, 1988, pp. 275–289.

[*9*] Yoon, K. B., Saxena, A., and McDowell, D. L., "Influence of Crack-Tip Cyclic Plasticity on Creep-Fatigue Crack Growth," *Fracture Mechanics, ASTM STP 1131*, 1992, pp. 367–392.

[*10*] Riedel, H., "Crack-Tip Stress Fields and Crack Growth Under Creep-Fatigue Conditions," *Elastic-Plastic Fracture*: Vol. I, *Second International Symposium, ASTM STP 803*, 1983, pp. 505–520.

[*11*] Bassani, J. L., Hawk, D. E., and Saxena, A., "Evaluation of the C_t Parameter for Characterizing Creep Crack Growth Rate in the Transient Regime," *Nonlinear Fracture Mechanics*, Vol. I, *Time-Dependent Fracture, ASTM STP 995*, 1986, pp. 7–26.

Christine Sarrazin-Baudoux,[1] *Sandrine Lesterlin,*[1] *and Jean Petit*[1]

Atmospheric Influence on Fatigue Crack Propagation in Titanium Alloys at Elevated Temperature

REFERENCE: Sarrazin-Baudoux, C., Lesterlin, S., and Petit, J., "**Atmospheric Influence on Fatigue Crack Propagation in Titanium Alloys at Elevated Temperature,**" *Elevated Temperature Effects on Fatigue and Fracture, ASTM STP 1297,* R. S. Piascik, R. P. Gangloff, and A. Saxena, Eds., American Society for Testing and Materials, 1997, pp. 117–139.

ABSTRACT: The fatigue crack propagation behavior of a Ti-6Al-4V alloy has been investigated at room temperature and at 300°C. Tests were run in air, high vacuum, and some other environments with controlled partial pressure of water vapor and oxygen. The enhancement of the fatigue crack growth rates observed in air in comparison to high vacuum, considered as an inert environment, is clearly attributed to the presence of water vapor. Tests in a controlled environment demonstrate that very low partial pressure can accelerate crack propagation. On the basis of previous studies on Al alloys and steels, two controlling mechanisms are considered and discussed, namely, a propagation-assisted water vapor adsorption and a hydrogen-assisted propagation.

KEYWORDS: fatigue crack propagation, titanium alloy, temperature, environment

Titanium alloys present high specific strength and can be operative at elevated temperatures. Because of this, they are particularly suited to aeronautical applications and more precisely in turbine engines. For such applications, the metal can be subjected to embrittlement induced by conjugated load-environment-temperature interactions that can result in substantial loss in resistance to fatigue crack propagation (FCP). Previous investigations [*1*,*2*] have shown that crack growth rates in ambient air are invariably greater than those in vacuum, both at ambient and elevated temperatures. At 300°C and in the near-threshold range, the differences between ambient air and vacuum are more pronounced than at room temperature (RT). But the mechanisms governing environmentally assisted crack growth have not been completely elucidated, particularly the specific role of water vapor and of oxygen on titanium alloys. This paper describes an investigation of the effects of controlled gaseous environment on fatigue crack propagation on a Ti-6Al-4V alloy to determine the active species responsible for embrittlement in ambient air at 300°C.

Materials and Experimental Procedure

The material used in this investigation was a forged $\alpha + \beta$ Ti-6Al-4V alloy heat treated for 1 h at 965°C, water quenched, aged at 705°C (2 h), and air cooled. This alloy displays a heterogeneous microstructure consisting of 80% of globular primary phase, α_p (8 μm diameter), and colonies of platelets (100 μm wide and 8 μm thick), all outlined by β phase (Fig. 1). The

---

[1] Laboratoire de Mécanique et de Physique des Matériaux, URA CNRS 863, Site du Futuroscope, Chasseneuil du Poitou, BP 109, 86960 Futuroscope Cedex, France.

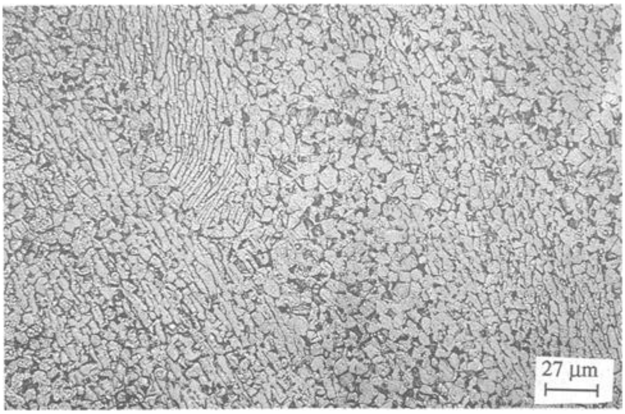

FIG. 1—*Illustration of Ti-6Al-4V microstructure.*

yield stress, ultimate strength, elongation, and Young's modulus were, respectively, 975 MPa, 1035 MPa, 16%, and 122 GPa at RT and 650 MPa, 770 MPa, 20%, and 107 GPa at 300°C.

Fatigue crack growth experiments were carried out on a compact tension specimen (10 mm thick and 40 mm wide) complying with the ASTM Test Method for Measurements of Fatigue Crack Growth Rates (ASTM E 647). Tests were conducted on a servohydraulic machine that can operate at temperatures up to 500°C under sinusoidal load time waveform and at frequencies varying from 0.5 to 35 Hz. Tests under controlled gaseous atmospheres were performed at 300°C in an environmental chamber with partial gas pressures measured by means of a mass spectrometer. A recording electrical potential system was used for monitoring crack length. The detailed experimental procedure and calibration of this method have been described elsewhere [*3*]. Crack mouth opening measurements for monitoring the crack tip opening were made at RT by means of back strain gages. At constant K_{max}, the R ratio was increased so as to eliminate crack closure and to provide the effective crack growth behavior at RT and at 300°C. Samples were fatigue precracked in ambient air in the range from 2000 to 3000 N with a load ratio of 0.1 to introduce a sharp crack approximately 0.3 mm in length. For each propagation test, cracking was performed using a shedding procedure to reach near threshold conditions, and then the propagation curves were established at increasing ΔK.

The specimens, after failure, were then submitted to scanning electron microscope (SEM) examinations of the fracture surface to establish the propagation mechanisms of the fatigue cracks.

Fatigue Crack Propagation Data

Crack propagation curves obtained from tests carried out in ambient air at RT and 300°C are shown in Fig. 2. Crack growth rates are plotted as a function of the change in the stress intensity factor (SIF) ΔK with a load ratio $R = P_{min}/P_{max} = 0.1$. This diagram displays little influence of temperature for rates higher than 10^{-8} m/cycle where RT propagation is slightly faster than at 300°C. The more significant difference is the plateau phenomenon observed at 300°C at about 10^{-8} m/cycle, which appears to be a critical rate below which temperature has

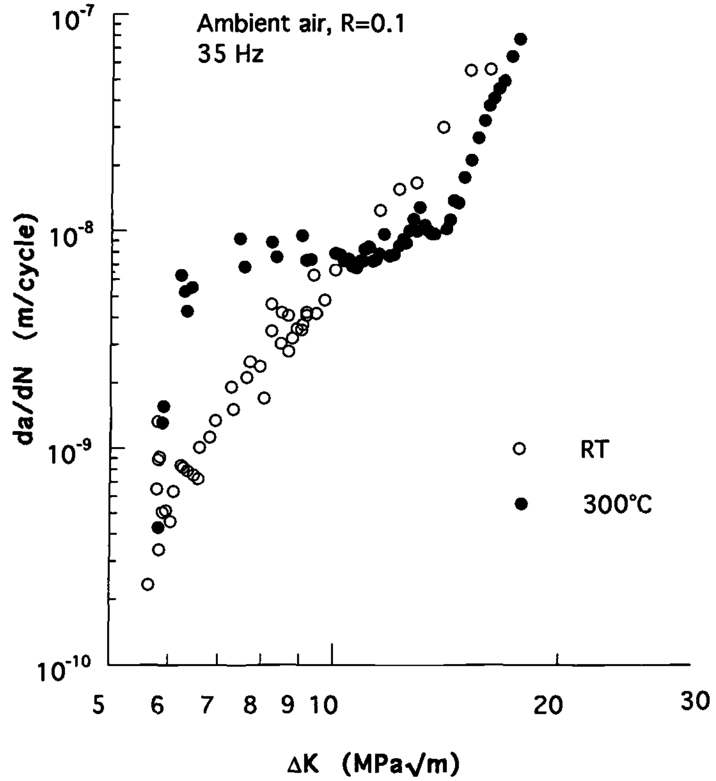

FIG. 2—*Influence of temperature on nominal fatigue crack propagation.*

a greater influence. In this rate range, increasing temperature induces crack growth rates of one order of magnitude higher than at RT at the same ΔK. Nominal threshold at both temperatures is quite similar with a value around 6 MPa$\sqrt{m}$.

In order to examine the possible role of the environment, Fig. 3 compares crack propagation behavior in air at RT and 300°C to reference tests conducted in high vacuum ($< 5 \cdot 10^{-4}$ Pa). The nominal propagation in high vacuum appears to be nearly insensitive to temperature in all the explored rate range. For crack growth rates higher than 10^{-8} m/cycle, a limited influence of environment is detected at RT and at 300°C. But at rates lower than 10^{-8} m/cycle, the reference data in high vacuum brought to light a large environmental effect when the tests are performed in ambient air. This effect is much more accentuated at 300°C, the temperature at which the growth rates in air can be two orders of magnitude higher than those in vacuum at the same ΔK range. These results are in accordance with previous observations and support coupled effects of environment and temperature on fatigue propagation in ambient air [*4–11*].

Because of the sensitivity to an aggressive environment, including ambient air, of fatigue crack growth in metallic alloys [*12–25*], a detailed analysis of fatigue crack growth behavior of titanium alloys requires experiments allowing an identification of the respective influence of environment and crack closure. For such a prospect, crack growth data including closure correction or tests performed in conditions expected without closure are considered. Experi-

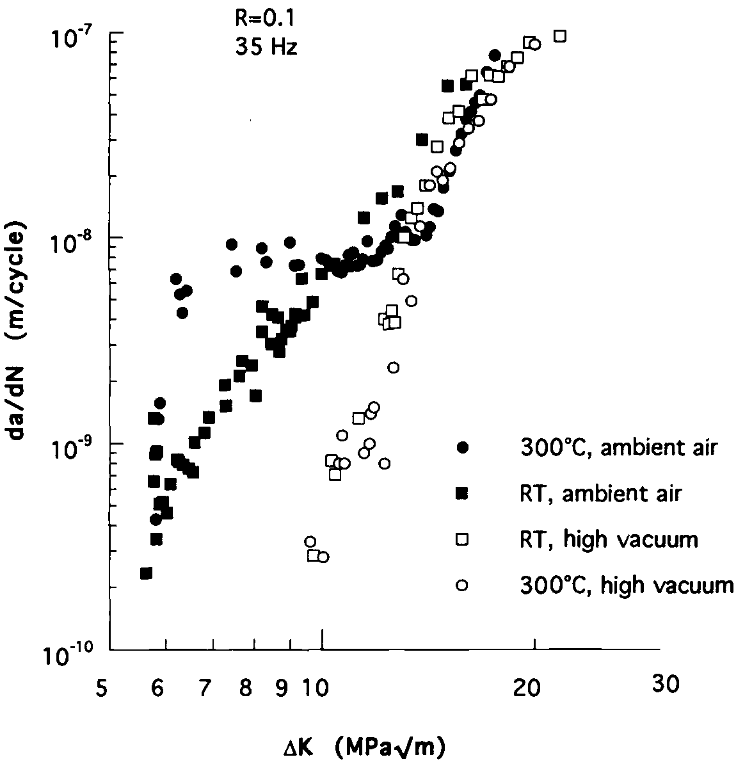

FIG. 3—*Influence of ambient air on nominal crack propagation at RT and at 300°C.*

ments performed under inert environment are then used to correlate experiments data to basic mechanisms and theories since the latter do not take the environmental influence into account. Such reference propagation will be labeled as intrinsic propagation. To go further into the analysis of the governing mechanisms, some critical experiments conducted in air and moist environments with a view to identify the active species responsible for the enhanced propagation in air will be presented and discussed.

Closure Correction

To obtain the effective crack propagation, two methods were used:

1. In the first method, the crack opening displacement δ was recorded as a function of the applied load P at a low frequency (0.35 Hz) in accordance with the mechanical performance of the X-Y plotter, and the effective propagation was then determined using the procedure proposed by Kikukawa et al. [*26*].
2. In the second method, tests were performed at variable R with constant K_{max} in conditions where K_{min} is higher than the stress intensity level for crack closure.

Comparative measurements were performed at RT using the two methods, as illustrated in Fig. 4 for tests in high vacuum. Similar effective data were obtained. The assumption was then

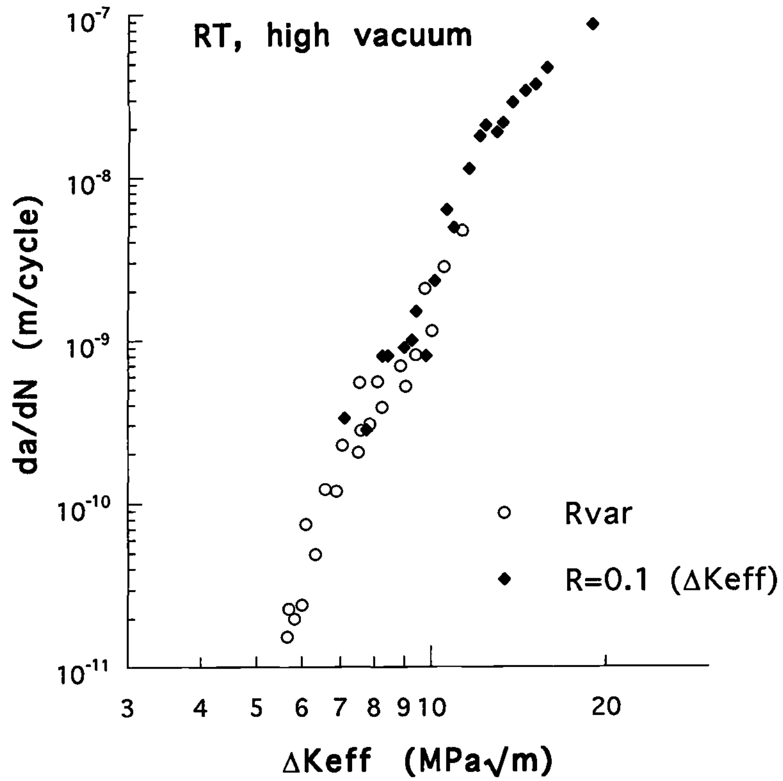

FIG. 4—*Effective crack propagation at RT in high vacuum determined by means of closure correction at* R = *0.1 or by mean of a test performed at constant* K_{max} *in condition without closure.*

made that the effective propagation at 300°C can be determined using the same constant K_{max} conditions as the ones used at RT. To check out the validity of this experimental procedure, the absence of closure was verified at different ΔK levels as illustrated in Fig. 5 for a test in humidified nitrogen. A constant growth rate was obtained for an R ratio higher than a critical R_{cut} value. The R values used during the constant K_{max} tests (26 MPa$\sqrt{m}$) were effectively higher than the R_{cut}, i.e., in the condition without closure.

In addition, Fig. 5*a* shows clearly that, when closure is eliminated, there was no influence of K_{max} or R ratio on the growth rates for the K_{max} levels used during these tests. The effective crack propagation curves (*da*/*dN* versus ΔK_{eff}) for tests performed at RT and 300°C are plotted in Fig. 6. At mid-rates ($>10^{-8}$ m/cycle), the elevation of temperature had little effect on the effective propagation; most of the difference observed on the nominal propagation can be attributed to crack closure. But, the large plateau range still observed at 300°C at about 10^{-8} m/cycle brings to light an important change in the crack growth mechanism that leads to a strong detrimental effect of temperature in the near-threshold range.

Intrinsic Behavior

To try to separate the respective influence of microstructure and of the environment, the intrinsic propagation (i.e., in the condition without closure and in high vacuum) of the Ti-6Al-

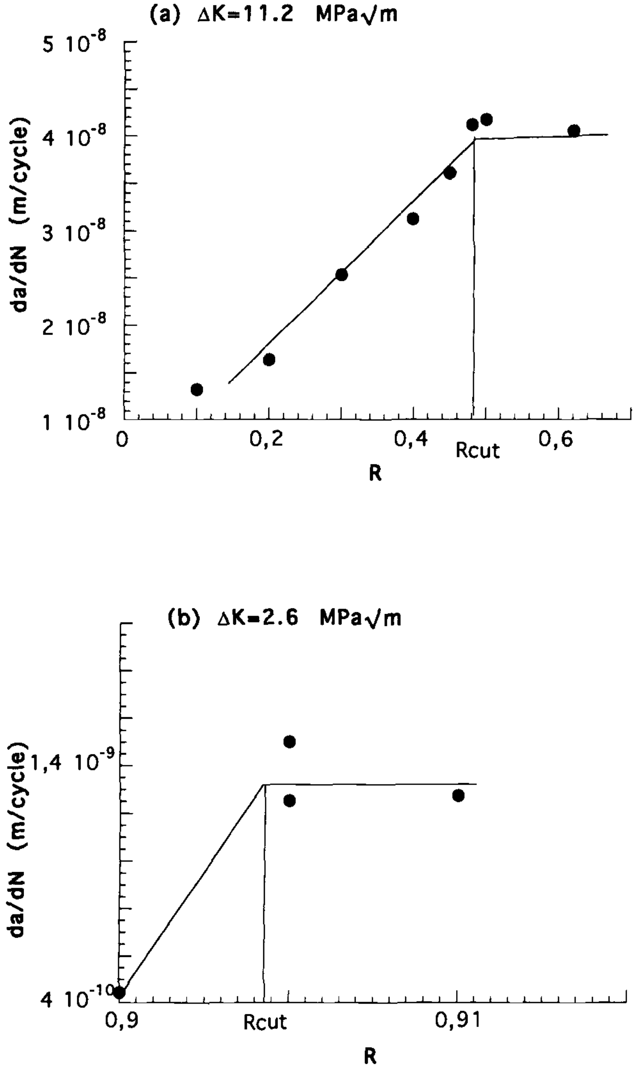

FIG. 5—*Crack growth data versus R from tests performed at 300°C in humidified nitrogen for two ΔK levels:* (a) *ΔK = 11.2 MPa√m;* (b) *ΔK = 2.6 MPa√m).*

4V alloy has been studied as described previously [27]. Figures 7*a* and 7*b* present, respectively, intrinsic data without and with correction for Young's modulus variations with temperature obtained from tests performed at decreasing ΔK (shedded load steps) or at increasing ΔK after threshold. The following conclusions have been drawn:

1. For crack growth rates higher than 10^{-8} m/cycle, the data are independent of the experimental procedure. In this rate range, intrinsic propagation plotted versus $\Delta K_{\text{eff}}/E$ (Fig.

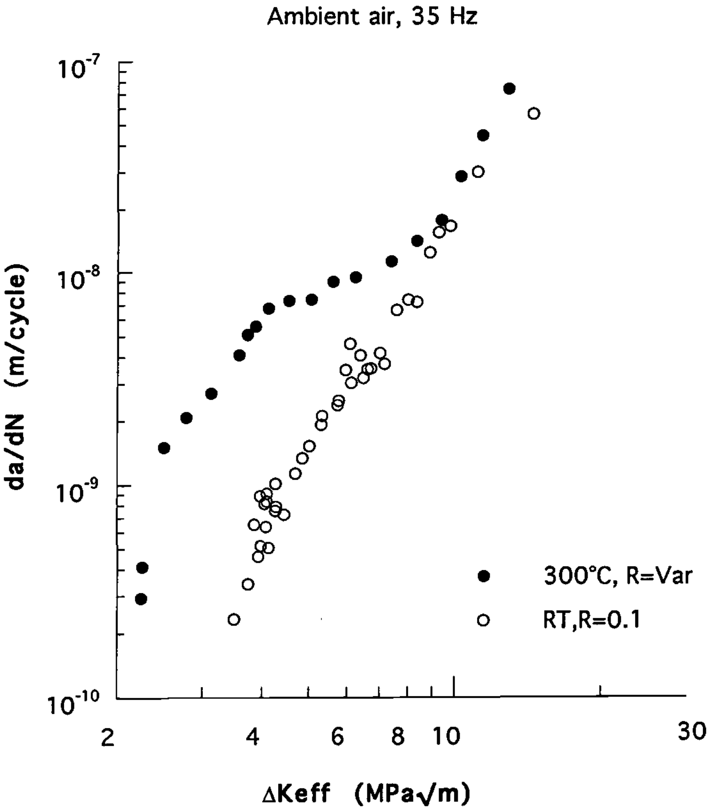

FIG. 6—*Influence of temperature on effective fatigue crack propagation in ambient air.*

7*b*) shows that temperature has no influence. In the mid-rate range, a stage II propagation is operative with a uniform transgranular morphology, as illustrated in Fig. 8. This regime results from an alternative slip mechanism that can develop along more or less symmetrical slip systems.

2. At decreasing ΔK, the intrinsic propagation in the low rate range at 300°C is slightly faster than at RT. Tests performed at constant K_{max} after the threshold were initiated by decreasing the minimum level of the stress intensity factor K_{min} (i.e., by reducing the R ratio) so as to increase the ΔK range about 5%. At 300°C, it can be noticed that, following the first increasing ΔK step after reaching the intrinsic threshold range, the crack was reinitiated in a condition corresponding to the experimental curve obtained using the shedding procedure. But afterward the crack growth rate decreased rapidly (data points into brackets), and a higher threshold range was reached very close to the intrinsic threshold at RT. Another increasing step was necessary to reinitiate the propagation. Considering all the data at 300°C, the large hysteresis existing between decreasing and increasing ΔK experiments has been attributed to a fundamental change in the crack growth mechanism from a Stage II propagation to a very slow crystallographic propagation called "Stage I-

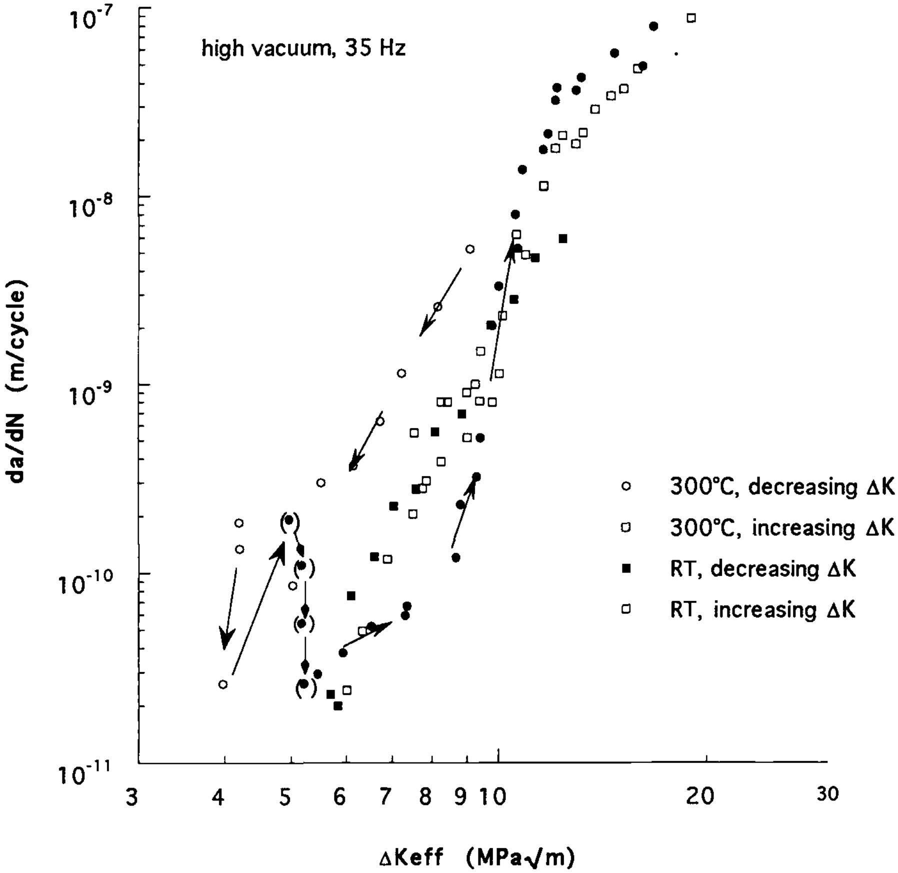

FIG. 7*a*—*Intrinsic crack growth data at RT and at 300°C.*

like" (Fig. 9*a*). Indeed, at the scale of each grain, this mechanism corresponds to a Stage I, but at a macroscopic scale, the crack remains normal to the stress axis as a Stage II crack. Recently [*28*], an identification of the involved crystallographic planes have been made by means of the technique of electron back scattering patterns (EBSP). About six points on each facet have been investigated, and five facets have been analyzed. The corresponding chaneling patterns are illustrated with related pole figures in Fig. 9 and support that all facet orientation lies within the basal planes of the α phase (Fig. 9*d*).

Intrinsic data for a GP-hardened aluminum-lithium alloy, a medium carbon structural steel type E460, an austenitic stainless steel type 316, and the present Ti-6Al-4V are plotted in Fig. 10. After correction for the Young's modulus variation for the different alloys, as reported in Ref *29* where numerous aluminum alloys and steels are considered, all data for the Stage II propagation collapse on the same line. This propagation has been identified as the intrinsic

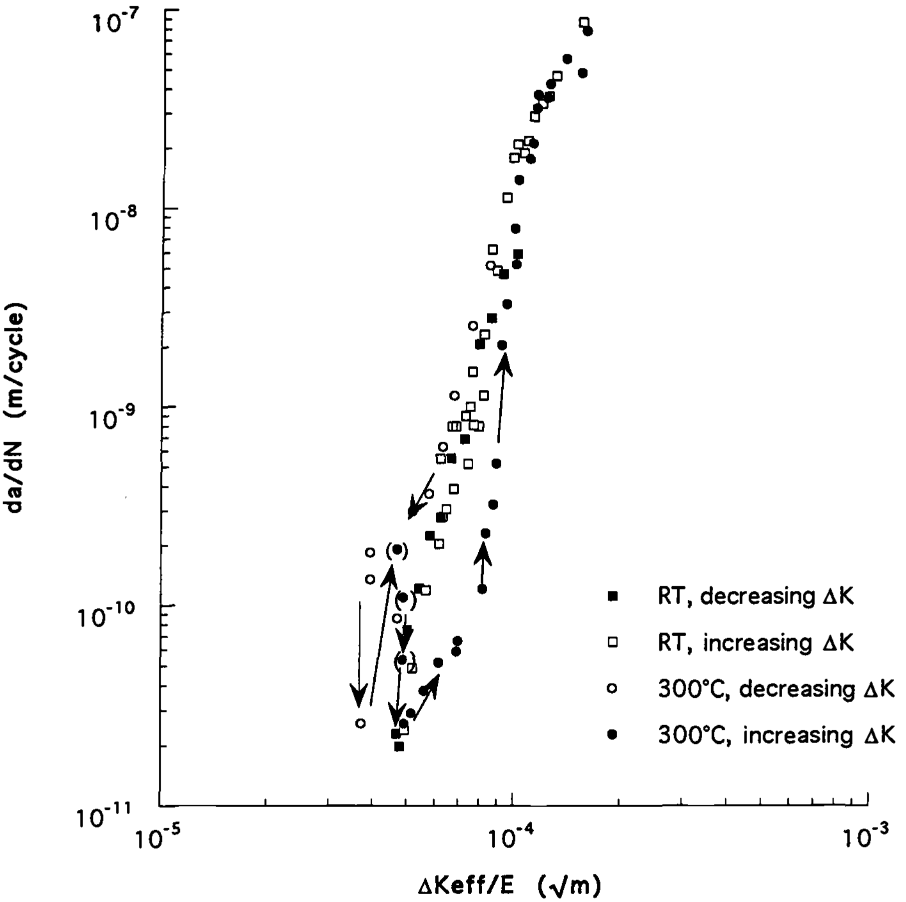

FIG. 7b—*Intrinsic crack growth data at RT and at 300°C with correction for Young's modulus with temperature.*

Stage II regime for all metallic alloys [*12,30,31*] and is described by the following relation derived from the initial models of Weertman and Rice [*32,33*]:

$$da/dN = A/D_0^*(\Delta K_{\mathrm{eff}}/E)^4 \qquad (1)$$

where A is dimensionless, and D_0^* is a critical cumulative displacement as introduced by Weertman [*32*] or Rice [*33*].

A best fit for data representative of the intrinsic Stage I-like propagation on the assumption of a slope $m = 4$ is presented. The slower growth rate can be analyzed as a lowering of ΔK_{eff} induced by crack branching and deflection, as proposed by Suresh [*34*], or by a grain boundary barrier effect, which is enhanced when a single slip mechanism is operative [*35*]. It is noticeable that the retardation effect is much larger for Ti-6Al-4V than for Al alloys. Thus, the Stage I-

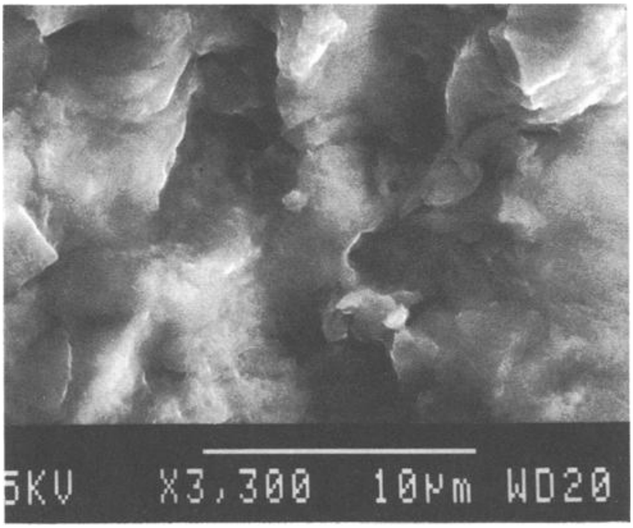

FIG. 8—*Microfractographic aspect of Stage II propagation in high vacuum in the mid-rate range at 300°C.*

like regime cannot be rationalized using a unique relation as illustrated in Fig. 10. The retardation can be very substantial when the number of available slip systems is restricted as in Ti-6Al-4V alloys or can be very limited when some secondary slips systems are activated like in Al-Li alloys [*36*]. Indeed, this crystallographic regime cannot be rationalized with respect to $\Delta K_{eff}/E$, the expected shielding effect on the Stage I-like regime being mostly dependent on the microstructure, and hence can be very different from one material to the other even with the same matrix as shown in Ref *37*.

Environmentally Assisted Propagation: Identification of Active Species

Figure 11 shows effective data obtained in ambient air and in high vacuum with correction for Young's modulus (i.e., versus $\Delta K_{eff}/E$) for the two tested temperatures. This diagram illustrates the specific influence of environment, which clearly appears deleterious at low rates ($< 10^{-8}$ m/cycle), this effect being more pronounced at 300°C.

To identify the species responsible for the embrittling processes observed in air at 300°C, experiments were carried out in atmospheres containing a controlled amount of water vapor and oxygen. A first experiment was performed at atmospheric pressure in pure nitrogen gas containing the same amount of water vapor as ambient air (1.3 kPa). The partial pressure of oxygen contained in the nitrogen environment was 1 Pa, i.e., 10^4 times lower than in air. The crack growth rate data plotted in Fig. 12 for both cases are identical for rates below 10^{-7} m/cycle. This results supports a predominant influence of water vapor.

To get more precise information on the effect of water vapor, tests were performed at different partial pressures of water vapor using nitrogen containing a low amount of water vapor or operating at low pressure by means of a controlled leak in the experimental vacuum chamber. Tests were conducted at 35 Hz and the corresponding propagation curves are presented in Fig.

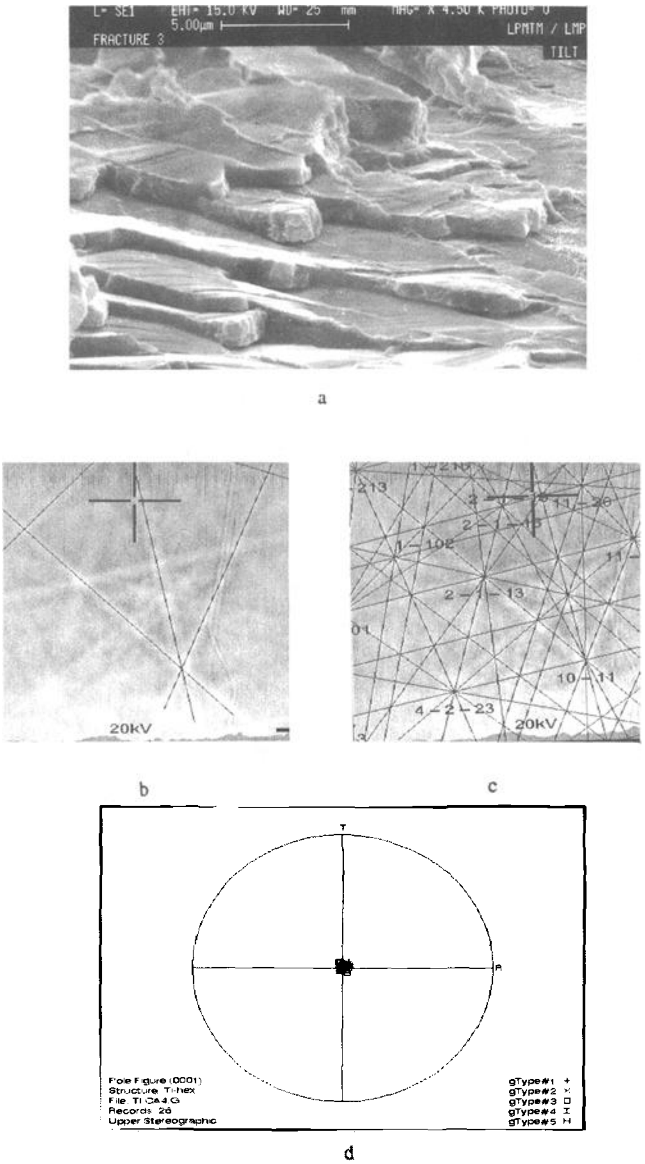

FIG. 9—*EBSP image of near-threshold crack propagation:* (a) *microfractographic aspect;* (b) *sample pattern;* (c) *indexed map;* (d) *related pole FIG.*

13*a*. The residual partial pressures of water vapor and oxygen are also mentioned in this figure for the different test. Examples of spectra given by the mass spectrometer are presented in Fig. 13*b* for high and low vacuum, respectively. When the lower partial pressure of water was increased from $2 \cdot 10^{-4}$ Pa (high vacuum) to 10^{-2} Pa (medium vacuum), a first effect was already detected consisting of an FCP acceleration in the near-threshold regime. This result

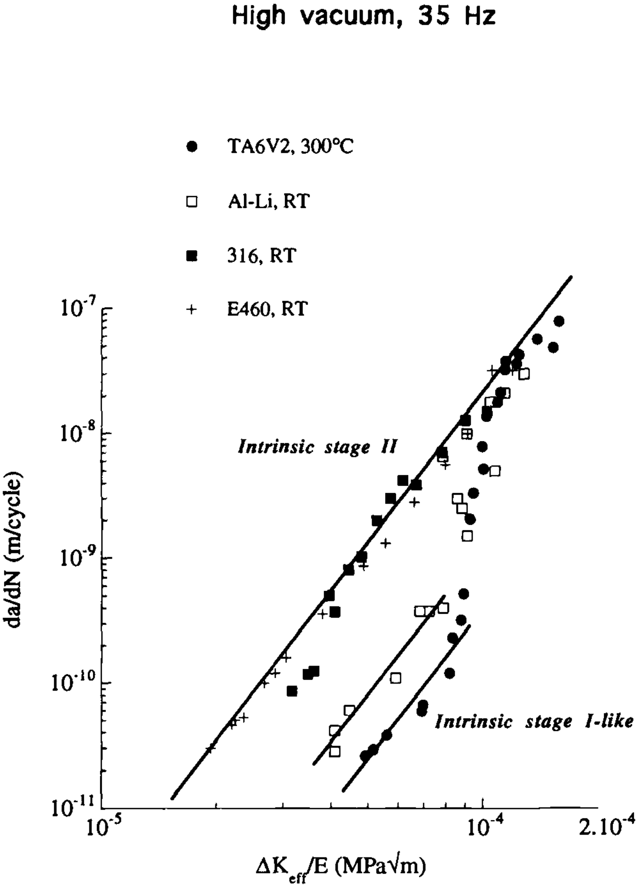

FIG. 10—*Compilation of intrinsic data.*

indicates that even a very limited number of adsorbed water vapor molecules can modify the slip conditions and favor activation of some secondary slip systems to then generate a faster propagation close to the Stage II regime. This change in the crack propagation mechanism can be associated with a partial pressure of water vapor located around 10^{-2} Pa at 35 Hz. Nevertheless, near the threshold, cracked surfaces still present large crystallographic areas, as illustrated in Fig. 14. The question is whether higher crack growth rates in medium vacuum compared to high vacuum are related to a change in the propagation mechanism or to an important softening of the grain boundaries barrier effect. A sole experiment carried out in medium vacuum cannot bring the answer. At rates higher than 10^{-8} m/cycle, little difference is observed between high and medium vacuum, and in both cases a Stage II regime is operative.

When the partial pressure of water vapor is substantially higher (from 1 Pa to 1.3 kPa), the characteristic plateau range observed in active environments becomes progressively more and more pronounced until it reaches a level and a shape similar to that observed in ambient air or humidified nitrogen. The corresponding crack growth rates are two orders of magnitude higher than in high vacuum in the near-threshold range and around three times higher in the mid-rate range.

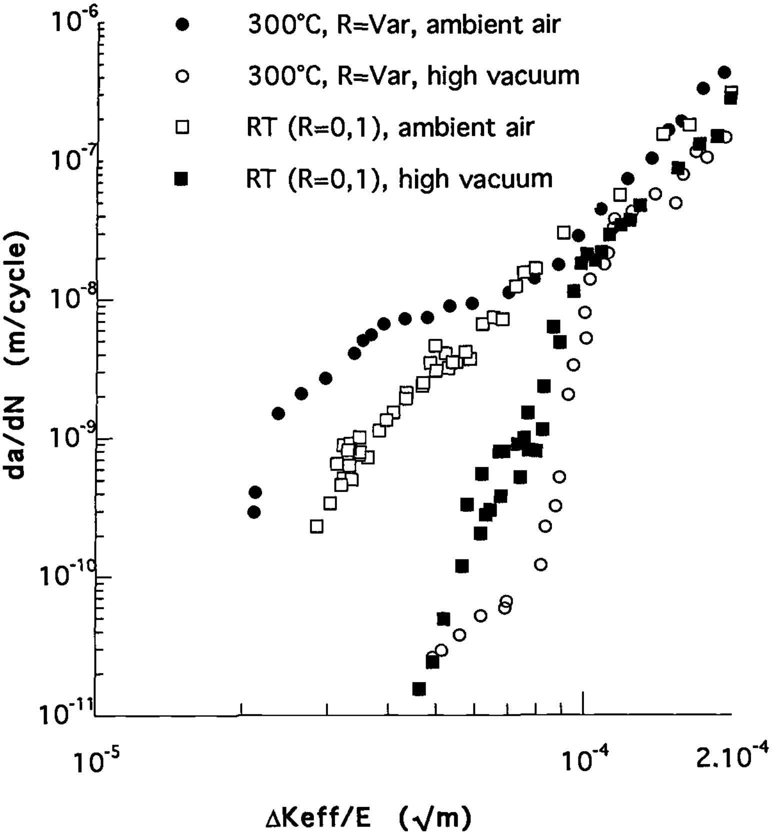

FIG. 11—*Influence of environment at RT and at 300°C on effective crack propagation after correction for Young's modulus variations.*

An analysis of the residual gas using a mass spectrometer indicates 75% of water vapor in medium vacuum and an amount of oxygen lower than the resolution of measurement ($< 10^{-5}$ Pa). Therefore, a dominant role of water vapor is highly suspected.

Discussion

In previous studies [*38–40*], the influence of environment at RT on the fatigue crack growth behavior of steels and aluminum alloys has been analyzed as the result of two mechanisms that are presented in Fig. 15:

1. *An adsorption-assisted propagation due to water vapor molecules adsorbed onto fresh surfaces.* The critical cumulative displacement at the crack tip is then reduced in accordance with the Lynch approach [*41*]. This regime, generally predominant in the mid-rate range (10^{-8} to 10^{-6} m/cycle), can be observed in a wide rate range when conditions for its occurrence are fulfilled [*40*].

	Environment	P_{H2O}	P_{O2}	Total pressure
●	Ambient air	1.3 kPa	2×10^4 Pa	10^2 kPa
○	Humidified nitrogen	1.3 kPa	1 Pa	10^2 kPa

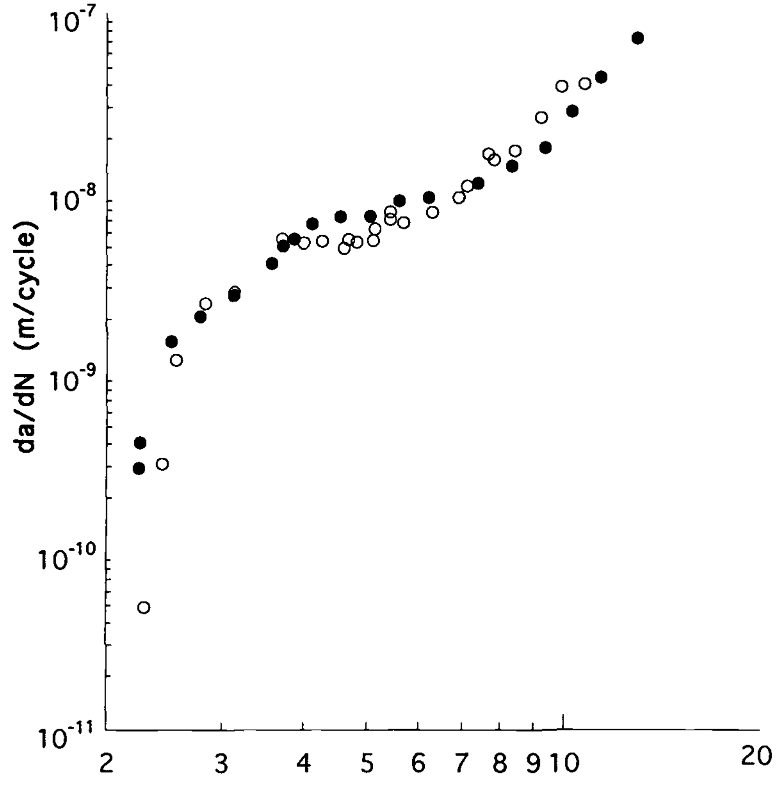

FIG. 12—*Effective propagation curves in ambient air and in humidified nitrogen.*

2. *A hydrogen-assisted propagation, hydrogen being provided by the dissociation of adsorbed water vapor molecules and then dragged within the process zone by mobile dislocations during cycling.* This process is operative in conditions leading to sufficiently high hydrogen concentration, i.e., below a critical rate $(da/dN)_{cr}$, which depends upon several parameters including the surrounding water vapor pressure, the test frequency, and the crack geometry (closure, R ratio), and generally when the deformation at the crack tip is localized within individual grains all along the crack front.

Even if the hydrogen-assistance mechanism is somewhat different in Al alloys, steels, and Ti alloys, the prominent role of water vapor on fatigue crack propagation behavior of TA6V at 300°C has been clearly demonstrated through the experiments presented here and above, and

	ENVIRONMENT	TOTAL PRESSURE	P_{H2O}	P_{O2}
△	Ambient air	10^2 kPa	1.3 kPa	$2x10^4$ Pa
▲	Humidified nitrogen	10^2 kPa	1.3 kPa	< 1 Pa
◇	Dry nitrogen	10^2 kPa	1.6 Pa	< 0.5 Pa
+	Low vacuum	1.33 Pa	1 Pa	< $4x10^{-4}$ Pa
●	Medium vacuum	10^{-2} Pa	$8x10^{-3}$ Pa	-
○	High vacuum	$3x10^{-4}$ Pa	$2x10^{-4}$ Pa	< 10^{-6} Pa

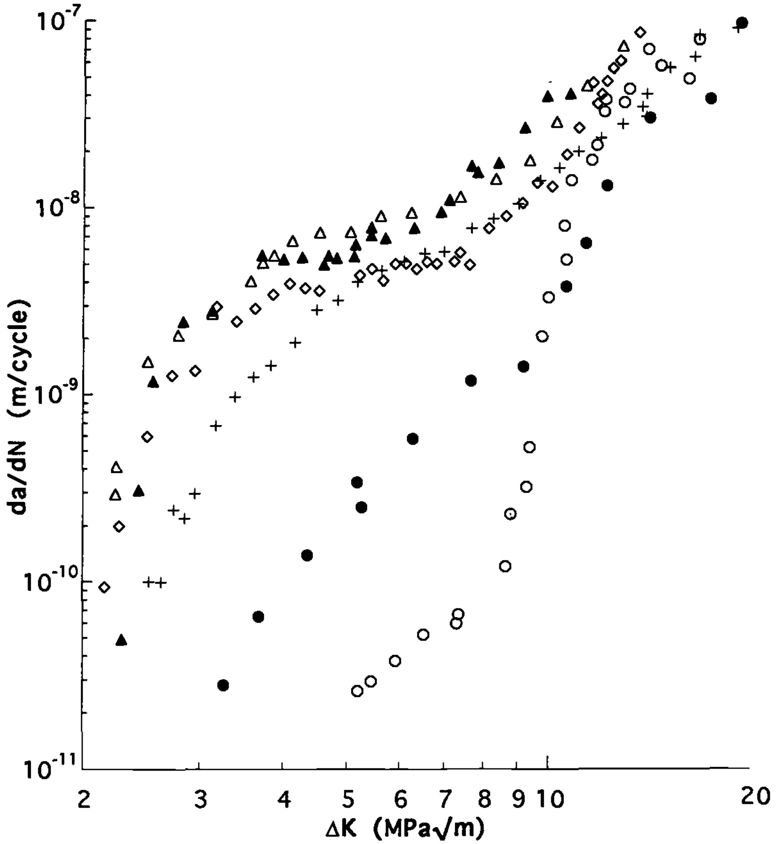

FIG. 13*a*—*Effective propagation curves in different environments containing controlled partial pressures of water vapor and oxygen.*

comparable FCP water-vapor-assisted propagation can be "a priori" considered for these metallic alloys. Figure 16 is a comparison of the effective behavior, including a correction for Young's modulus, of E460 construction steel, 316 steel, 7475T7351 and X7075 aluminum alloys all tested in air at RT, and the present Ti-6Al-4V alloy tested in air at 300°C. The intrinsic Stage II regime, identical for Al, Ti-based alloys, and steel [*38*] (see Fig. 10), is reported in this figure for comparison purposes. A sensitivity to an air environment is shown to be strongly dependent on metals with regard to propagation curves in the low crack growth rate range,

(a) High vacuum (3×10^{-4} Pa)

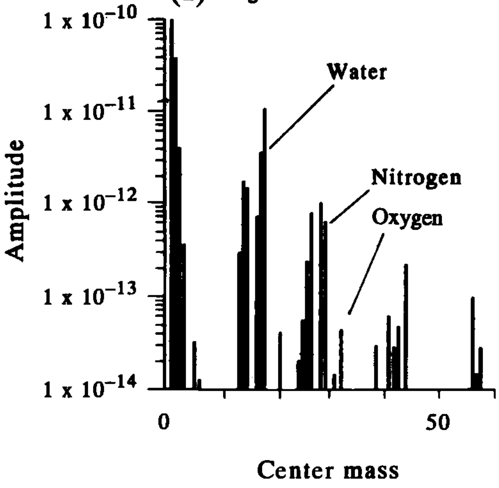

(b) Low vacuum (1.33 Pa)

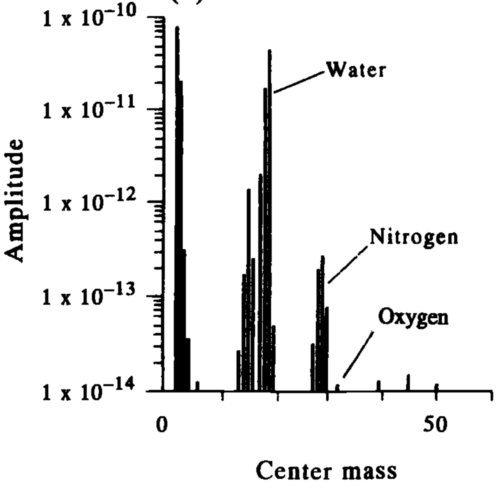

FIG. 13*b*—*Residual gas analysis of the environmental cell (nonscaled amplitudes):* (a) *high vacuum (2×10^{-4} Pa);* (b) *low vacuum (1.33 Pa).*

which differs from one alloy to the other. However, a typical common critical rate range at about 10^{-8} m/cycle can be pointed out for all materials. This critical step is associated with SIF ranges where the plastic zone size at the crack tip is of the same order as grain or subgrain diameters. In addition, there is general agreement that, for growth rates lower than this critical range, crack propagation results from a step-by-step advance mechanism instead of a cycle-by-cycle progression as generally observed in the Paris regime in air where propagation curves are nearly similar. On this basis, comparable conditions for the occurrence of a hydro-

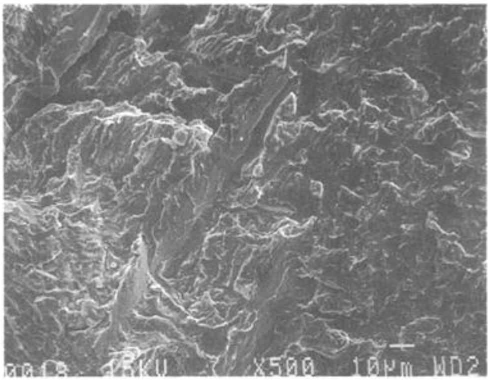

FIG. 14—*Crystallographic areas of cracked surface obtained in the near threshold range* (10^{-10} *m/cycle) from tests performed in medium vacuum* (10^{-2} *Pa).*

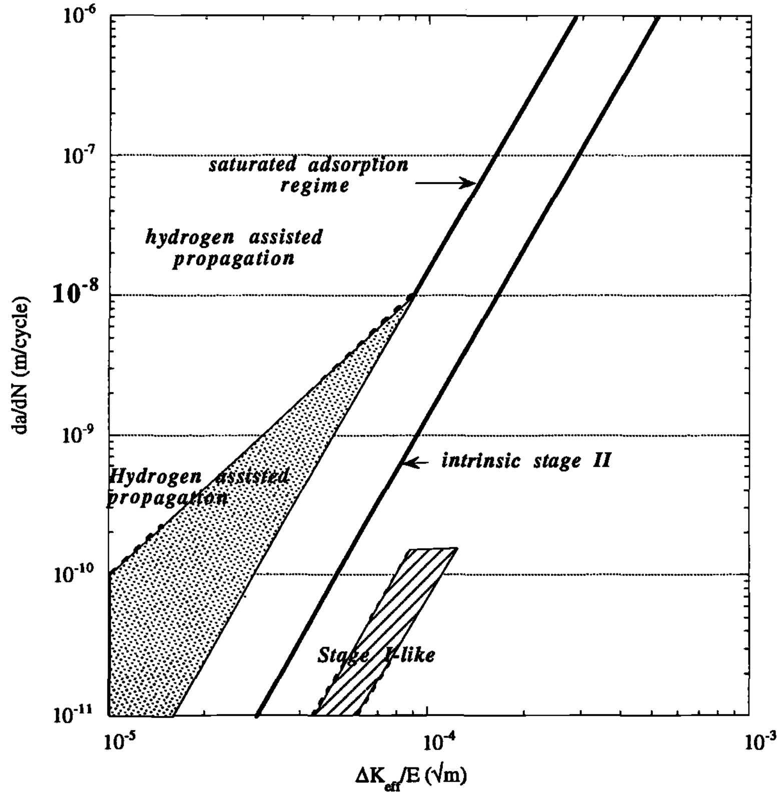

FIG. 15—*Schematic representation of the crack growth mechanisms.*

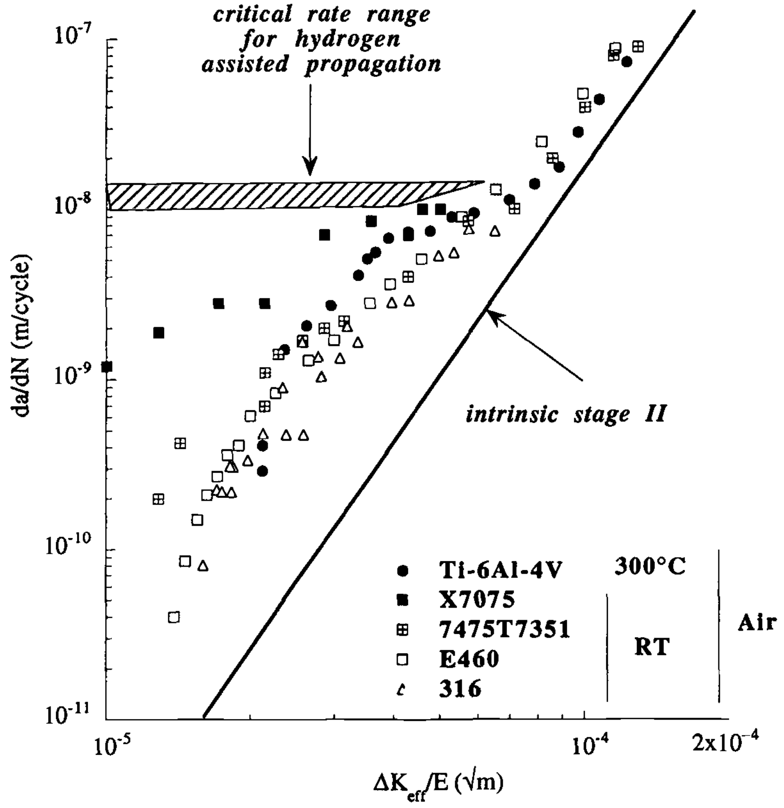

FIG. 16—*Comparison of effective behavior of E460 steel, 316 steel, X7075 and 7175T7351 Al alloys at RT, and Ti-6Al-4V at 300°C.*

gen-assisted propagation mechanism can be reasonably suggested for the Ti alloy at 300°C in the near-threshold area ($< 10^{-8}$ m/cycle) as described in previous studies [*1,16,42–44*].

The analysis of the Stage II crack propagation behavior under low partial pressure of water vapor can be developed on the basis of a recent and detailed study of fatigue crack growth under low-pressure gaseous atmospheres in a high-strength low-alloy steel [*39*]. Very low partial pressure of water vapor (10^{-3} Pa) has been proved to substantially increase the growth rates of a Stage II fatigue crack. This phenomenon has been modeled on the basic assumption that adsorption of water vapor molecules on fresh crack surfaces is the main mechanism involved in such cases. The proposed model provides a comprehensive picture of what happens at the crack tip, especially regarding the transport of active species to the tip. The adsorption-assisted regime is shown to be controlled by the competition between transport, adsorption consumption rate, and crack advance kinetics. Testing carried out on some other materials (Al alloys and steels) and some data gathered from the literature have suggested that the adsorption-assisted Stage II regime could prevail in a wide range of materials and exposure conditions (low water vapor pressure, fluid environment, etc.). In all cases, adsorption may not be viewed as an embrittling mechanism process, but rather as a mechanism inducing enhanced plasticity of the cyclically strained material at the crack tip. The consequence is interpreted as a lower value of the critical displacement D^* as defined by Weertman and Rice [*32,33*] leading to rupture and enhanced crack growth rates, the propagation being described by a relation similar to Eq 1:

$$da/dN = A/D^*(\Delta K_{\text{eff}}/E)^4 \qquad (2)$$

A recent and detailed analysis of dislocation structures near the fatigue crack tip in copper supports the fact that a unit volume of material located at a given distance from the crack tip sustains a much larger number of cycles during fatigue cracking in vacuum than in air [*45*]. A similar behavior can be considered in all ductile metallic alloys.

D^* can be correlated to the coverage rate of freshly created surfaces by adsorbed water vapor molecules as defined by Langmuir [*46*] and noticed θ. In other words, $\theta = 0$ means that no adsorption occurs (intrinsic behavior), the opposite of $\theta = 1$, when every site of the free surface is occupied by an adsorbed molecule. In such conditions, the relation between D^* and θ can be written as [*47*]

$$D^* = D^*_o \cdot D^*_1/(D^*_1 + \theta(D^*_o - D^*_1)) \qquad (3)$$

where D^*_o and D^*_1 represent the value of D^* in inert and saturated environments, respectively. This relation assumed that when θ is lower than unity, conditions for the occurrence of a hydrogen embrittlement mechanism are not satisfied and environmental influence is restricted to the sole action of adsorption. Critical conditions for the activation of a subsequent hydrogen-related mechanism, which depend on the nature of the flow inside the crack, on the total surrounding pressure, and on deformation localized within individual grains along the crack front, require at least the condition $\theta = 1$, which is necessary but could not be sufficient.

The experimental data obtained on the present Ti-6Al-4V suggest the existence of a saturated adsorption-assisted regime, as illustrated in Fig. 17. The test conducted at a partial pressure of water vapor of 1 Pa at 35 Hz gives a typical example of the transition from the adsorption-saturated regime to the intrinsic regime when θ evolved from unity near the threshold to close to zero in the mid-ΔK range when the crack grows during the test performed at increasing ΔK; hence, the area of the freshly created surfaces enlarges. Concurrently, changing the test frequency from 35 to 0.5 Hz in the same environment at a ΔK_{eff} value of 15 MPa$\sqrt{\text{m}}$ induces a propagation about ten times higher.

Another illustration of the global effect of environment is presented in Fig. 18 where crack growth data, normalized with respect to those in an inert environment, are plotted as a function of the exposure (i.e., partial pressure of water vapor P_{H_2O} divided by two times the frequency f [*1,8,21*]) at two fixed values of ΔK_{eff}. A significant increase in crack growth rates appears over the range of exposure.

At a ΔK_{eff} of 10 MPa$\sqrt{\text{m}}$, which is representative of the mid-rate range, adsorption of water vapor molecules on freshly created surfaces is assumed to be solely operative, and the growth rates for the adsorption-saturated regime are about nine to ten times higher than for the intrinsic Stage II. The critical exposure for adsorption seems to be about 10^{-1} Pa · s.

At a ΔK_{eff} range of 3 MPa$\sqrt{\text{m}}$, the sensitivity to environment is much higher. The additional acceleration can be attributed to the hydrogen assistance when the localization of the plastic deformation of the crack tip is supposed to allow the attainment of a critical hydrogen concentration condition generally encountered in the near-threshold regime ($da/dN < 10^{-8}$ m/cycle). The attainment of a saturated influence of hydrogen and the existence in itself of such a regime are questionable due to the very small number of available data. The critical exposure for the action of water vapor at $\Delta K_{\text{eff}} = 3$ MPa$\sqrt{\text{m}}$ is about 10^{-2} Pa · s. Even though the failure mechanisms are different for steels and titanium alloys, the hypothesis formulated on the role

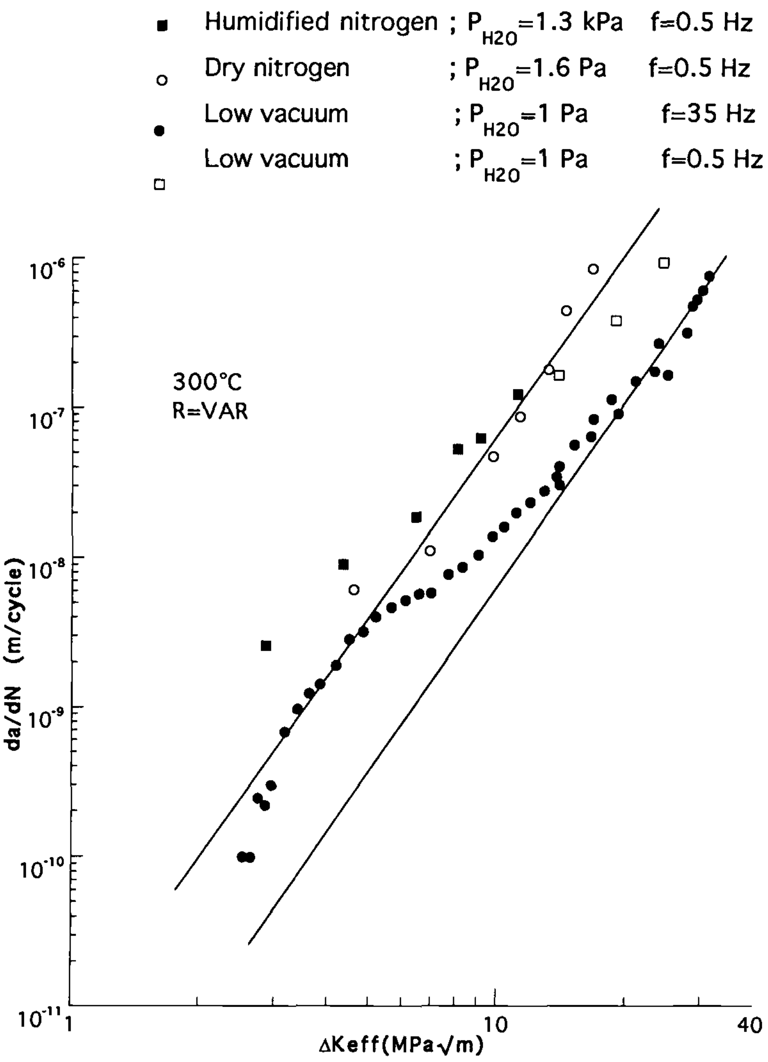

FIG. 17—*Identification of the adsorption-assisted regime at saturation* ($\theta = 1$).

of hydrogen in substantiated by the works done by several authors on hydrogen-assisted cracking in Ti alloys, which is dependent on hydrogen concentration, microstructure, yield stress, local stress intensities, and temperature [*48–52*]. Two mechanisms are often evoked: one is fracture by localized plastic deformation enhanced by the presence of hydrogen, and the other is a brittle fracture of the stress induced by titanium hydrides. The occurrence of one or the other of these mechanisms depends on several factors like the local stress intensity at the crack tip [*48*] and the tested temperature [*52*]. An understanding of crack propagation under the conditions presented in this paper requires further investigations to precisely understand the role of the different crack mechanisms.

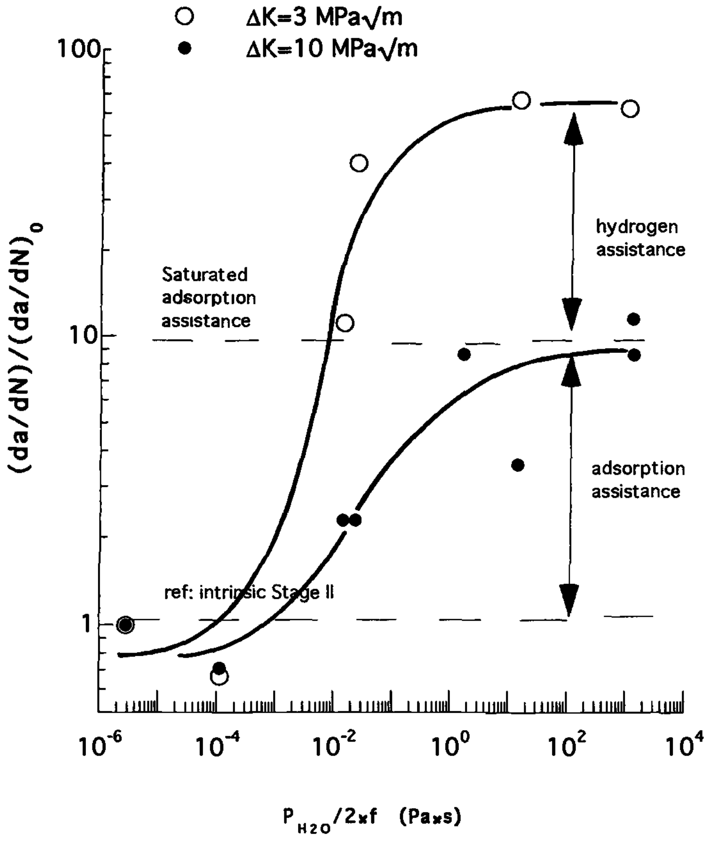

FIG. 18—*Influence of exposure ($P_{H_2O}/2 \cdot f$) on fatigue crack growth rates at 300°C at two ΔK_{eff} levels.*

Conclusion

This investigation of fatigue crack propagation in a Ti-6Al-4V alloy at RT and at 300°C and in various gaseous-controlled containments of water vapor and oxygen leads to the following conclusions:

1. In high vacuum (inert reference environment), the temperature has a very low influence on Stage II propagation which is predominant in the mid-rate regime. The slight acceleration observed at 300°C is taken into account by the variation of the Young's modulus with temperature. Near the threshold, the localization of the plastic deformation within a single slip system in each individual grain favors a retarded crystallographic Stage I-like regime highly sensitive to grain boundary barrier effects.
2. In all the other environmental conditions, a Stage II propagation is operative in the whole explored rate range (about 10^{-10} to 10^{-7} m/cycle).
3. The enhancement of fatigue crack growth rates in comparison to the intrinsic propagation is clearly attributed to the presence of water vapor.

4. Very low partial pressure of water vapor can substantially accelerate the propagation.
5. Two controlling mechanisms are proposed: an adsorption-assisted propagation and an additional hydrogen-assisted propagation.

References

[1] Gao, S. J., Simmons, G. W., and Wei, R. P., *Material Science and Engineering*, Vol. 62, 1984, pp. 65–78.
[2] Irving, P. E. and Beevers, C. J., *Metallurgical Transactions*, Vol. 5, 1974, pp. 391–398.
[3] Berata, W., Ph.D. thesis, University of Poitiers, France, 1992.
[4] Vesier, L. S. and Antolovich, S. D., *Engineering Fracture Mechanics*, Vol. 37, No. 4, 1990, pp. 753–775.
[5] Davidson, D. L. and Lankford, J., *Metallurgical Transactions*, Vol. 15A, 1984, pp. 1931–1940.
[6] Ruppen, J. A. and Hoffmann, C. L., *Proceedings*, 27th Sagamore Army Materials Research Conference, Bolton Landing, NY, J. J. Burke and V. Weiss, Eds., Plenum Press, New York, 1983, pp. 265–300.
[7] King, J. E., *Fatigue of Engineering Materials and Structure*, Vol. 5, No. 2, 1982, pp. 177–188.
[8] Wei, R. P., "On Understanding Environment-Enhanced Fatigue Crack Growth. A Fundamental Approach," *Fatigue Mechanisms, ASTM STP 675*, American Society for Testing and Materials, 1979, pp. 816–840.
[9] Lynch, S. P., "Mechanisms of Fatigue and Environmentally Assisted Fatigue," *Fatigue Mechanisms, ASTM STP 675*, American Society for Testing and Materials, 1979, pp. 174–213.
[10] Wanhill, R. J. H. and Döker, H., NLR MP 78002 U, NLR Publications, Amsterdam, Netherlands, 1977.
[11] Wanhill, R. J. H., NLR MP 76008 U, NLR Publications, Amsterdam, Netherlands, 1976.
[12] Dahlberg, E. P., *Transactions ASM Quarterly*, Vol. 58. 1965, pp. 46–52.
[13] Hartman, A., *International Journal of Fracture Mechanics*, Vol. 1, 1965, pp. 167–187.
[14] Bradshaw, F. J. and Wheeler, C., *Applied Material Research*, 1966, pp. 112–120.
[15] Ishii, H. and Weertman, J., *Scripta Metallurgica*, Vol. 3, 1960, pp. 229–232.
[16] Enochs, J. S. and Devereux, O. F., *Metallurgical Transactions*, Vol. 6A, 1975, pp. 391–397.
[17] Petit, J., "Fatigue Crack Growth Threshold Concepts," TMS-AIME, 1984, pp. 3–25.
[18] Wei, R. P., Talda, P. M., and Li, C. Y., *Fatigue Crack Propagation, ASTM STP 415*, ASTM, West Conshohocken, PA, 1967, pp. 460–485.
[19] Stegman, R. L. and Shahinian, P., *Metal Science Journal*, Vol. 6, 1972, pp. 123–127.
[20] Bignonnet, A., Petit, J., and Zeghloul, A., "Environmental Assisted Fatigue," ECF7, P. Scott and R. A. Cottis, Eds., Mechanical Engineering Pub. Ltd., London, 1990, pp. 205–222.
[21] Wei, R. P. and Ritter, D. L., *Journal of Materials*, Vol. 7, No. 2, 1972, pp. 240–250.
[22] Sugano, M., Kanno, S., and Satake, T., *Acta Metallurgica*, Vol. 37, 1989, pp. 1811–1820.
[23] Swanson, J. W. and Marcus, H. L., *Metallurgical Transactions*, Vol. 9A, 1978, pp. 291–293.
[24] Fujita, F. E., "Fracture of Solids," *Proceedings*, Metallic Solids Conference, Vol. 20, Interscience Publishers, 1963, pp. 657–670.
[25] Petit, J., de Fouquet, J., and Henaff, G., *Handbook on Fatigue Crack Propagation in Metallic Structures*, A. Carpinteri, Ed., Elsevier, New York, Vol. 2, 1994, pp. 1159–1204.
[26] Kikukawa, M., Jono, M., Tanaka, K., and Takatani, M., *Journal of Material Science*, Japan, Vol. 25, No. 276, 1976, pp. 899–903.
[27] Petit, J. Berata, W., and Bouchet, B., *Scripta Metallurgica et Materialia*, Vol. 26, 1992, pp. 1889–1894.
[28] Sarrazin-Baudoux, C., Chiron, R., Lesterlin, S., and Petit, J., *Fatigue Fracture Engineering Material and Structure*, Vol. 17, No. 12, 1994, pp. 1383–1389.
[29] Petit, J., "Modeling of Intrinsic Fatigue Crack Propagation," *Proceedings*, conference held 25–27 May 1992 at the University of Birmingham, UK, 1992, pp. 131–151.
[30] Petit, J. and Henaff, G., *Scripta Metallurgica et Materialia*, Vol. 25, 1991, pp. 2683–2687.
[31] Weertman, J., *International Journal of Fracture Mechanics*, Vol. 9, 1966, pp. 460–467.
[32] Weertman, J., *International Journal of Fracture Mechanics*, Vol. 9, 1973, pp. 125–131.
[33] Rice, J. R., *Fatigue Crack Propagation, ASTM STP 415*, ASTM, West Conshohocken, PA, 1967, pp. 247–309.
[34] Suresh, S., "Fatigue Crack Deflection and Fracture Surface Contact: Micromechanical Models," *Metallurgical Transactions A*, Vol. 16A, 1985, pp. 249–260.
[35] Miller, K. J., "Materials Science Perspective of Metal Fatigue Resistance," *Material Science and Technology*, Vol. 9, 1993, p. 453.

[*36*] Xu, Y. B., Wang, L., Zhang, Y., Gwang, Z. G., and Hu, Q. Z., "Fatigue and Fracture Behavior of an Aluminum-Lithium Alloy 8090-T6 at Ambient and Cryogenic Temperatures," *Metallurgical Transactions A*, Vol. 22A, 1991, pp. 723–729.

[*37*] Petit, J., Sarrazin-Baudoux, C., Berata, W., and Lesterlin, S., *Proceedings*, Eighth International Conference of Fracture, Ukraine, to be published.

[*38*] Petit, J. and Henaff, G., "A Survey of Near-Threshold Fatigue Crack Propagation Mechanisms and Modeling," *Proceedings*, Fatigue '93. Montréal, 3–7 May 1993, EMAS, J. P. Baïlon and I. J. Dikson, Eds., 1993, pp. 503–512.

[*39*] Petit, J. and Henaff, G., "An Analysis of the Environmental Influence on the Near-Threshold Fatigue Crack Propagation Behavior," ECF 9, *Reliability and Structural Integrity of Advanced Materials*, Vol. I, Mechanical Engineering Publications, London, 1992, pp. 433–438.

[*40*] Henaff, G., Marchal, K., and Petit, J., *Acta Metallurgica*, Vol. 43, No. 8, 1995, pp. 2931–2942.

[*41*] Lynch, S. P., "Environmentally Assisted Cracking: Overview of Evidence for an Adsorption-Induced Localized-Slip Process," *Acta Metallurgica*, Vol. 36, 1988, pp. 2639–2661.

[*42*] Shid, T.-H. and Wei, R. P., *Engineering Fracture Mechanics*, Vol. 18, No. 4, 1983, pp. 827–837.

[*43*] Weir, T. W., Simmons, G. W., Hart, R. G., and Wei, R. P., *Scripta Metallurgica*, Vol. 14, 1980, pp. 357–364.

[*44*] Tien, J. K. and Richards, R. J., *Scripta Metallurgica*, Vol. 9, 1975, pp. 1097–1101.

[*45*] Tong, Z. X. and Bailon, J. P., "Dislocation Structures Near the Fatigue Crack Tip in Copper," *Fatigue Fracture Engineering Material Structure*, Vol. 18, 1995, pp. 847–859.

[*46*] Langmuir, I., *Journal of American Chemical Society*, Vol. 40, 1918, p. 1361.

[*47*] Henaff, G. and Petit, J., *Proceedings*, CDI Conference, Fontainebleau, France, T. Magnin et al., Eds., les Éditions de Physique, 1995, p. 599.

[*48*] Shih, D. S., Robertson, I. M., and Birnbaum, H. K., "Hydrogen Embrittlement of α Titanium: In Situ TEM Studies," *Acta Metallurgica*, Vol. 36, 1988, pp. 111–124.

[*49*] Moody, N. R. and Gerberich, W. W., "The Effect of Stress State on Internal Hydrogen-Induced Crack Growth in Ti-6Al-2Sn," *Metallurgical Transactions A*, Vol. 13A, 1982, pp. 1055–1061.

[*50*] Nelson, H. G., Williams, D. P., and Stein, J. E., "Environmental Hydrogen of a-b Titanium Alloy: Effect of Microstructure," *Metallurgical Transactions*, Vol. 3, 1972, pp. 469–475.

[*51*] Gerberich, W. W. and Chen, Y. T., "Hydrogen-Controlled Cracking—An Approach to Threshold Stress Intensity," *Metallurgical Transactions A*, Vol. 6A, 1980, p. 271.

[*52*] Moody, N. R. and Gerberich, W. W., "Hydrogen-Induced Slow Crack Growth in Ti-6Al-2Sn," *Metallurgical Transactions A*, Vol. 11A, 1980, pp. 973–981.

Todd P. Albertson,[1] *Robert R. Stephens,*[1] *and Thomas D. Bayha*[2]

Fatigue Crack Growth of Two Advanced Titanium Alloys at Room and Elevated Temperature

REFERENCE: Albertson, T. P., Stephens, R. R., and Bayha, T. D., "**Fatigue Crack Growth of Two Advanced Titanium Alloys at Room and Elevated Temperature,**" *Elevated Temperature Effects on Fatigue and Fracture, ASTM STP 1297,* R. S. Piascik, R. P. Gangloff, and A. Saxena, Eds., American Society for Testing and Materials, 1997, pp. 140–161.

ABSTRACT: This paper provides fatigue crack growth information at low crack growth rates for two sheet titanium alloys: β-21S, a β alloy, and Ti-62222, an $\alpha + \beta$ alloy. Room (25°C) and elevated temperature (175°C) fatigue crack growth tests at two different stress ratios, $R = 0.1$ and 0.5, were performed. Effects of temperature and stress ratio were evaluated in order to study the complex interaction between fatigue, environment, and loading conditions. Crack-opening load was measured throughout the test from automated compliance measurements and was used to adjust fatigue crack growth data for crack closure. For β-21S, fatigue crack growth rates were similar at 175 and 25°C at a stress ratio of 0.1, while crack growth rates were lower at 175 versus 25°C at a stress ratio of 0.5 for the same nominal ΔK. Concepts associated with crack closure accounted for this as crack growth rates were found to be higher at 175°C than 25°C for both stress ratios when plotted as a function of ΔK_{eff}, showing a temperature dependency on crack growth rate. For Ti-62222, fatigue crack growth rates were comparable between 25 and 175°C for $R = 0.5$, but were different at $R = 0.1$ where crack closure was observed at 175°C. Fatigue crack growth behavior of these two titanium alloys was comparable for all loading and temperature conditions.

KEYWORDS: beta and alpha + beta titanium alloys, threshold fatigue crack growth, crack closure, elevated temperature, microstructural influences

β-21S is a metastable β titanium alloy that exhibits high strength, good ductility, and excellent corrosion and hydrogen absorption resistance and is capable of heavy cold reductions, therefore making it an excellent candidate for aerospace applications [*1,2*]. Ti-62222 was developed in the mid-1970s as a deep-hardenable, elevated-temperature $\alpha + \beta$ alloy for thick section forging in turbine engine applications [*3*]. Both materials have found numerous applications in the sheet form and are of high interest for airframe and aero-skin applications [*3,4*]. Durability and damage-tolerant analysis are required of these materials if they are to be used in critical airframe applications, and a reliable defect-tolerant approach to life prediction must be based on accurate knowledge of fatigue crack propagation and damage mechanisms. Furthermore, fatigue crack growth threshold values furnish valuable information for life prediction models and provide knowledge on crack growth rates and behavior from initially small defects.

Microstructure plays a significant roll in crack propagation in titanium alloys [*5–12*] and consequently controls the features of crack path and fracture surface morphology. Observations made regarding crack path and microstructural interaction as well as the fracture surface char-

---

[1] Graduate student, and assistant professor, respectively, University of Idaho, Moscow, ID, 83843.

[2] Material research engineer, Advanced Structures and Materials Structures Engineering, Lockheed-Martin Aeronautical Systems Company, Marietta, GA.

acteristics provide important additional information on the process of damage mechanisms. Microstructural influences on fatigue crack propagation have been used to explain closure effects of cracks due to roughness-induced closure, crack tip slip reversibility, and crack path tortuosity [*13,14*].

Temperature and environment are known to influence the fatigue crack propagation of titanium alloys [*7,12,15*]. The effect of elevated temperature on ΔK_{th} is very complex; however, the dominating mechanism is usually associated with crack closure [*16*]. This can be associated with the deposit of material on the surface as a result of fretting contact, the formation of an oxide layer, or modifications of slip character due to slip irreversibility in the presence of oxidation layers [*13*].

The purpose of this work is to present the results of near-threshold fatigue crack growth behavior for β-21S and Ti-62222 for stress ratios of 0.1 and 0.5 at 25 and 175°C. Threshold fatigue crack damage is analyzed in three manners: fatigue crack growth data, crack path morphology using standard metallurgical methods, and fractographic analysis using scanning electron microscopy. Relationships between the microstructure, temperature, stress intensity range, and crack growth rate will be provided.

Experimental Details

Materials

Fatigue crack growth tests were performed on two individual titanium alloys, β-21S (Ti-15Mo-2.7Nb-3Al-0.2Si) and Ti-62222 (Ti-6Al-2Sn-2Zr-2Mo-2Cr). The β-21S was evaluated in the solution-treated and aged (STA) condition with the heat treatment parameters reported in Table 1. The microstructure of β-21S is nearly equiaxed and essentially single-phase β; however, the aging process subsequently precipitates a fine α phase for strengthening at both the grain boundaries and within the grains [*17,18*]. The microstructure is shown in Fig. 1*a*, where the α precipitates are evident in the β matrix. The grain size varies from 10 to 50 μm with a random distribution. The Ti-62222 was also evaluated in the STA condition (Table 1). This material consists of an equiaxed alpha phase dispersed evenly throughout an $\alpha + \beta$ matrix where the estimated grain size was less than 10 μm (Fig. 1*b*). The tensile properties in the longitudinal direction at room and elevated temperature for both materials are provided in Table 2.

Specimen Design

Specimens were machined from sheet material 1.53 and 1.65 mm thick for β-21S and Ti-62222, respectively, into extended compact tension specimens [*19*] (Fig. 2). The stress intensity solution for the extended compact tension specimen is

$$K = \alpha^{1/2} \frac{P}{\sqrt{W}\,B} \frac{(1.4 + \alpha)}{(1 - \alpha)^{3/2}} (3.97 - 10.88\alpha^2 + 26.25\alpha^3 - 38.9\alpha^3 + 30.15\alpha^4 - 9.27\alpha^5)$$

TABLE 1—*Heat treatment and aging information for β-21S and Ti-62222.*

		Solution Heat Treatment		Aging		
Alloy	Thickness, mm	Temperature, °C	Time, h	Temperature, °C	Time, h	Note
β-21S	1.53	851	0.5	537	8	Air cooled
Ti-62222	1.65	732	0.5	510	10	Air cooled

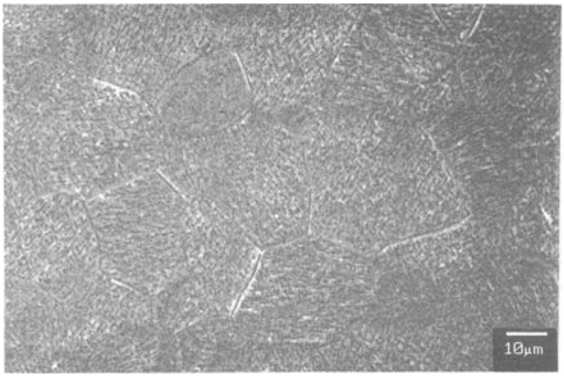

FIG. 1*a*—*β-21S microstructure showing beta phase decorated with alpha phase.*

where α is crack length normalized by specimen width (a/W). The compliance solution in terms of crack mouth opening displacement (ν), load (P), modulus, (E), and thickness (B) is

$$\alpha = 1.004 - 5.5495u + 6.0988u^2 - 16.0075u^3 + 32.3436u^4 - 22.2843u^5$$

where

$$u = \frac{1}{[(\nu BE/P) + 1]}$$

The specimens were ground on one side using progressively finer SiC paper. Polishing was carried out using a suspension of 1 μm alumna particles and water and then 0.05 μm alumna particles and water. β-21S specimens were etched using an etchant consisting of 60 parts proprionic acid, 30 parts H_2O_2, 15 parts HNO_3, 2 parts HR, and 15 parts H_2O. Keller's modified etchant was used to etch the Ti-62222. Both etchants revealed the general grain structure of the material, exposing distinct differences between the α and β phases.

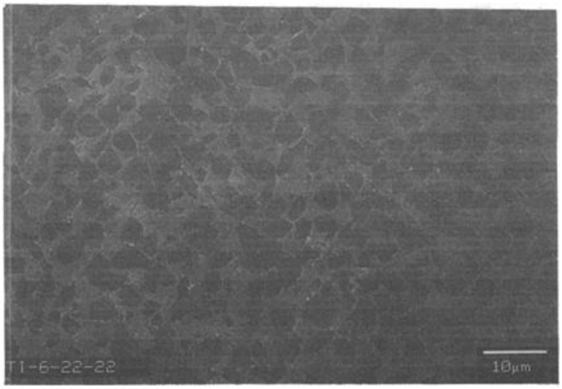

FIG. 1*b*—*Ti-62222 microstructure showing equiaxed beta phase dispersed in the alpha phase.*

TABLE 2—*Mechanical properties of β-21S and Ti-62222.*

Temperature, °C	UTS, MPa	YS, MPa	% Elongation
	β-21S		
25	1365	1268	8.6
175	1185	1068	10
	Ti-62222		
25	1341	1223	9.5
175	1237	1015	9.4

Test Procedures

All specimens were tested in accordance with the ASTM Standard Test Method for Measurement of Fatigue Crack Growth Rates (ASTM E 647) using an automated digitally controlled servo-hydraulic closed-loop testing system. Continuous load shedding with a constant load ratio was used to exponentially reduce ΔK for a given amount of crack advance using the relationship

$$\Delta K = \Delta K_0 \exp^{c(a_n - a_0)}$$

where a_0 and ΔK_0 are the beginning crack length and stress intensity range, respectively, at the start of the test, and a_n is the calculated crack length during the test. The value of the shedding constant (c) used was -0.1/mm. Crack length was monitored using a crack mouth

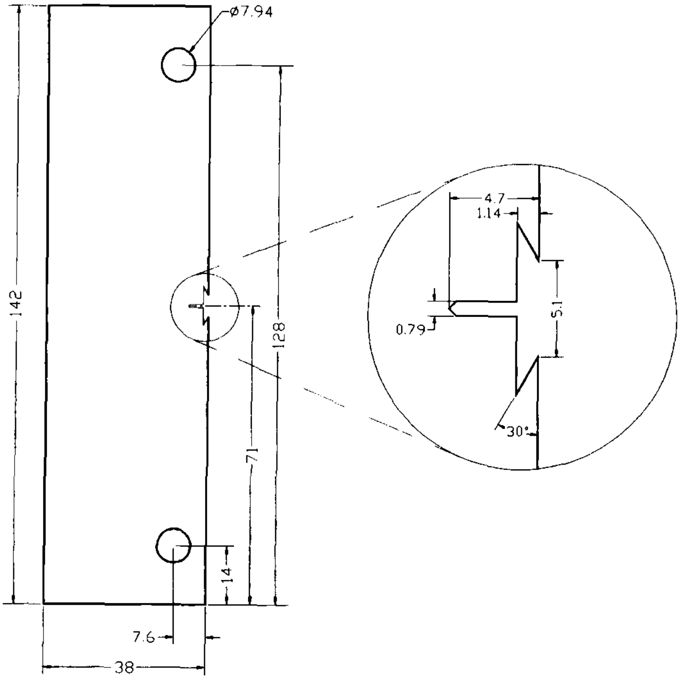

FIG. 2—*Extended compact tension specimen, dimensions in mm.*

opening displacement (CMOD) gage. Crack lengths were measured using a traveling microscope with an accuracy of 0.02 mm to confirm crack length measurements from the compliance calibration. Data were taken automatically at predetermined crack length intervals of 0.4 mm for crack growth rates above 10^{-6} mm/cycle and 0.2 mm for values of *da*/*dN* below 10^{-6} mm/cycle. A sinusoidal waveform with a frequency of 20 Hz was used for all test conditions.

Crack growth data were analyzed in terms of crack growth rate (*da*/*dN*) and Mode I stress intensity range (ΔK). Crack growth rates were calculated from crack length versus cycle data using a two-point secant method. The growth rate used to define ΔK_{th} values was 10^{-7} mm/cycle, the rate specified in ASTM E 647.

Effective stress intensity values were calculated using crack opening loads, P_{op}, using the following relationship

$$\Delta K_{eff} = \frac{\Delta K(P_{max} - P_{op})}{(P_{max} - P_{min})}$$

where P_{max}, P_{min}, and P_{op} were determined from compliance curves. Crack closure levels were monitored using the compliance method where the opening stress intensity (K_{op}) was determined from the load corresponding to first deviation in linearity of the unloading compliance curve.

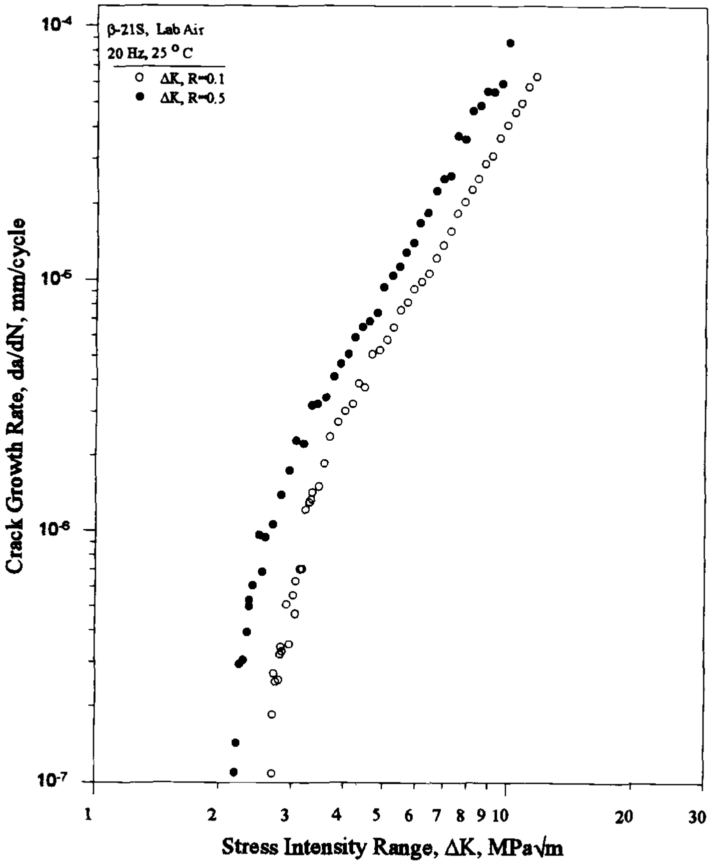

FIG. 3*a*—*Fatigue crack growth rate data for β-21S at 25°C,* R = *0.1 and 0.5.*

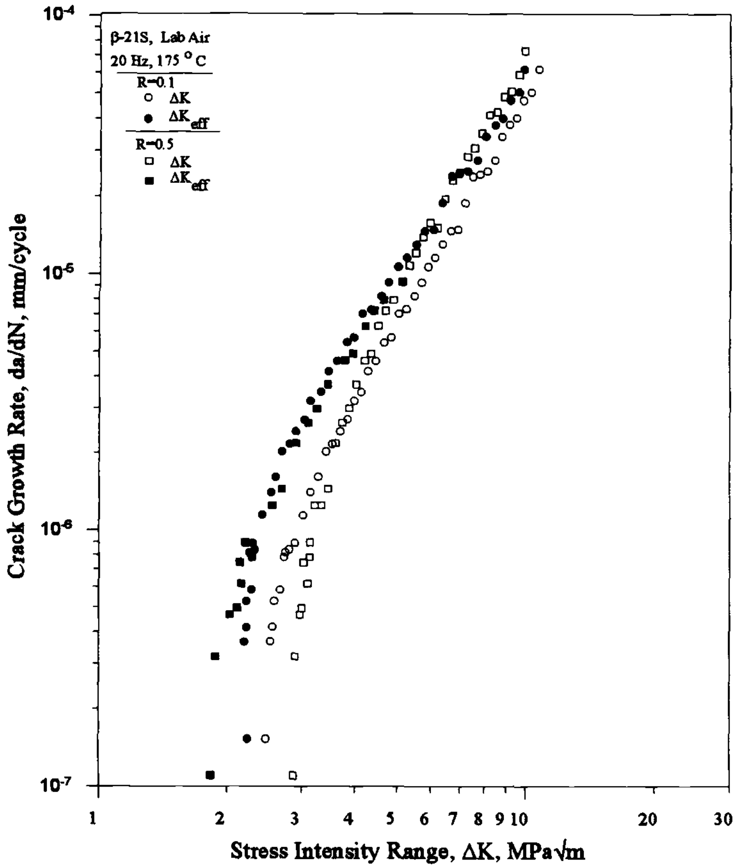

FIG. 3*b*—*Fatigue crack growth rate data for β-21S at 175°C,* R *= 0.1 and 0.5.*

Typical aero-skin temperatures experienced during subsonic and supersonic speeds were incorporated into the test matrix, those being 25 and 175°C. Heating of the specimen was accomplished using resistive heating elements that were attached by a clamping system directly above and below the mid-plane and on both sides of the specimen. Temperature variations along the crack front were within 1% of the test temperature. Temperature variations in the direction of the loading pins was minimal due to the close proximity of the heaters with respect to the crack path. In addition, tests were performed at two stress ratios, 0.1 and 0.5.

Crack path profiles were observed from the specimen using standard light microscopy, and scanning electron microscopy was used to obtain pictures of the crack path profile. Fracture surfaces were preserved by sectioning both sides of the crack path after specimen failure and were examined in a scanning electron microscope.

Results and Discussion

β-21S

Room temperature fatigue crack growth curves for stress ratios of 0.1 and 0.5 are shown in Fig. 3*a*. The threshold stress intensity range, ΔK_{th}, for a stress ratio of 0.1 was 2.7 MPa$\sqrt{m}$, whereas, for a stress ratio of 0.5, ΔK_{th} was 2.2 MPa$\sqrt{m}$, demonstrating a stress ratio dependency on crack growth rates. Crack closure was not observed for either $R = 0.1$ or 0.5 at the 25°C condition.

Elevated temperature fatigue crack growth rates for stress ratios of 0.1 and 0.5 are shown in Fig. 3*b*. The threshold stress intensity range, ΔK_{th}, for elevated temperature at a stress ratio of 0.1 was found to be 2.5 MPa$\sqrt{m}$, whereas, at $R = 0.5$, ΔK_{th} was 2.9 MPa$\sqrt{m}$. This is contrary to the stress ratio dependency observed at room temperature. This behavior, however, can be explained in terms of crack closure, as crack closure was observed for the 175°C test condition at both stress ratios. While crack closure was observed over the whole portion of the fatigue crack growth curve for low stress ratio, at high stress ratio crack closure was observed only below ΔK values of approximately 5.0 MPa$\sqrt{m}$. At a stress intensity range of approximately 3.9 MPa$\sqrt{m}$, a crossover in fatigue crack growth behavior was observed as fatigue crack growth rates became slower at $R = 0.5$ than at $R = 0.1$. At higher ΔK values, tests at $R = 0.5$ had greater crack growth rates than $R = 0.1$ tests. When corrected for crack closure, the effective threshold stress intensity value, $\Delta K_{th,eff}$, was 2.2 and 1.8 MPa$\sqrt{m}$ for $R = 0.1$ and 0.5, respectively. Thus, crack closure was able to account for most of the difference in fatigue crack growth behavior for elevated temperature at different stress ratios.

Room and elevated temperature fatigue crack growth curves for low stress ratio are compared

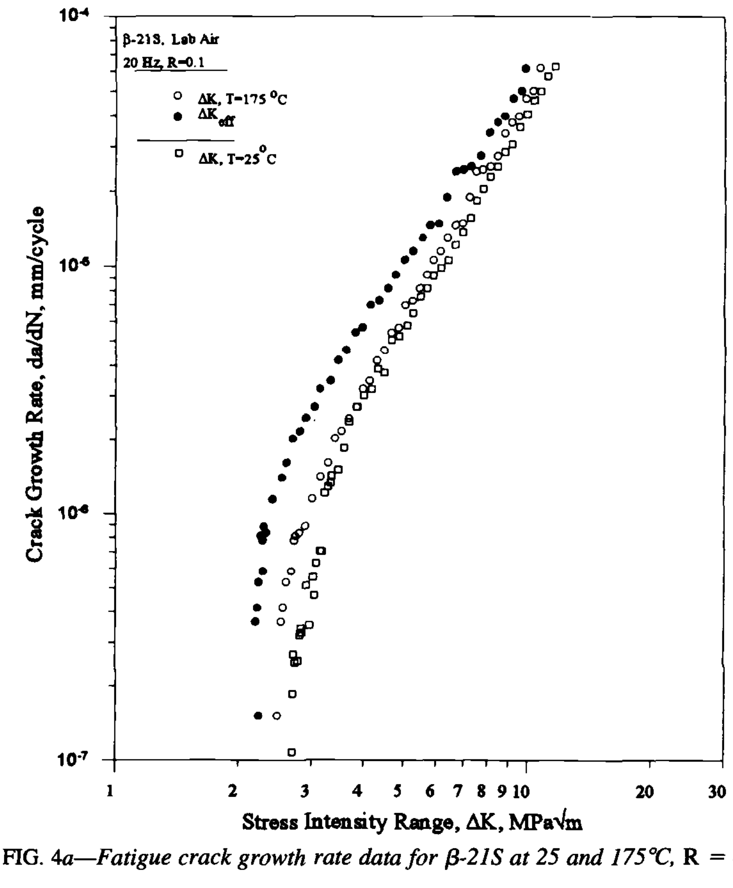

FIG. 4*a*—*Fatigue crack growth rate data for β-21S at 25 and 175°C,* R *= 0.1.*

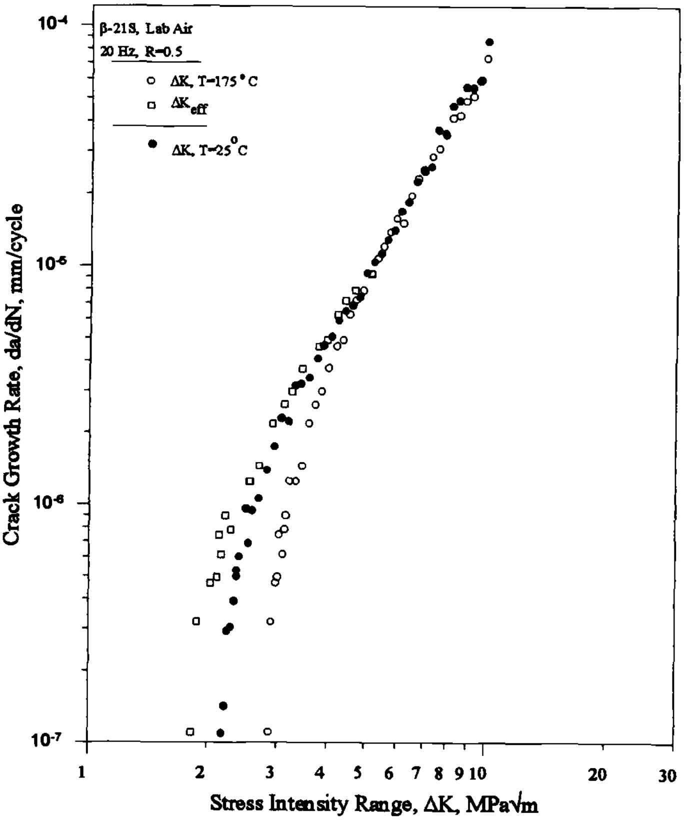

FIG. 4*b*—*Fatigue crack growth rate data for β-21S at 25 and 175°C,* R $= 0.5$.

in Fig. 4*a*. At stress intensity values greater than approximately 4 MPa$\sqrt{m}$, similar crack growth rates were observed for both temperatures, whereas, at near threshold values, moderately lower fatigue crack growth rates were observed at elevated temperature. When ΔK was corrected for crack closure at 175°C, a significant shift to the left in the fatigue crack growth curve was observed at 175°C in comparison to 25°C (Fig. 4*a*). This behavior is consistent with that reported by Petit et al. [*20*] where nominal fatigue crack growth curves were similar for room temperature and 300°C in Ti-6Al-4V. However, ΔK_{eff} crack growth rates at elevated temperature were higher than at room temperature. Thus, at low stress ratio, nominal threshold data indicated a lack of temperature influence; yet, when corrected for crack closure, the threshold data demonstrated the detrimental effect of elevated temperature.

Room and elevated temperature fatigue crack growth curves for $R = 0.5$ are shown in Fig. 4*b*. The value of ΔK at 175°C was greater than that at 25°C for the same nominal crack growth rate. However, ΔK_{eff} was less at 175°C than at 25°C for crack growth rates below about 10^{-6} mm/cycle. This behavior was similar to the lower R ratio tests. The propensity for decreased crack growth rates at elevated temperature for nominal threshold conditions can be attributed to crack tip shielding and a decline in crack tip sharpening due to crack closure. This can be explained most effectively in terms of Fig. 5, which represents the ratio of $K_{\text{op}}/K_{\text{max}}$ versus K_{max}, where K_{max} is the maximum stress intensity and K_{op} is the crack tip opening stress intensity required to overcome crack closure. The total stress cycle consists of two parts: one part is required to overcome crack closure, K_{op}, and the other is responsible for crack extension. Therefore, the crack tip driving force is decreased as the ratio of K_{op}/K_{max} increases. At elevated temperature for a stress ratio of 0.5, the driving force was reduced substantially due to crack closure as threshold conditions were approached, thus producing a slower crack growth rate. The elevated temperature tests at a stress ratio of 0.1 demonstrated a moderate decrease and then an increase in crack tip driving force as threshold was approached. This would explain the elevated temperature fatigue crack growth behavior for $R = 0.1$ and 0.5.

The fractured specimens were examined both optically and by scanning electron microscopy to relate the fatigue crack path to various microstructural features. Generally speaking, crack propagation was found to be globally flat with little deviation from the specimen centerline. Crack path tortuosity was minimal with small deflections along the crack path; however, deflections observed were usually associated with crack tip/grain boundary interaction. A distinction must be made between macro-roughness due to redirection of the crack path and micro-roughness produced by the local redirection of the cracks due to microstructural features. The latter was the typical mechanism controlling the path in which the crack followed. Crack branching and secondary cracking was not observed at $R = 0.1$ for either temperature and was limited to a few isolated cases at $R = 0.5$ but only at room temperature. A typical crack path section at near threshold for β-21S is shown in Fig. 6 for a stress ratio of 0.1 at room temperature. Fatigue crack path profiles suggest microstructural insensitive growth at intermediate ΔK, with an increase in microstructural influences as ΔK approached threshold for all test

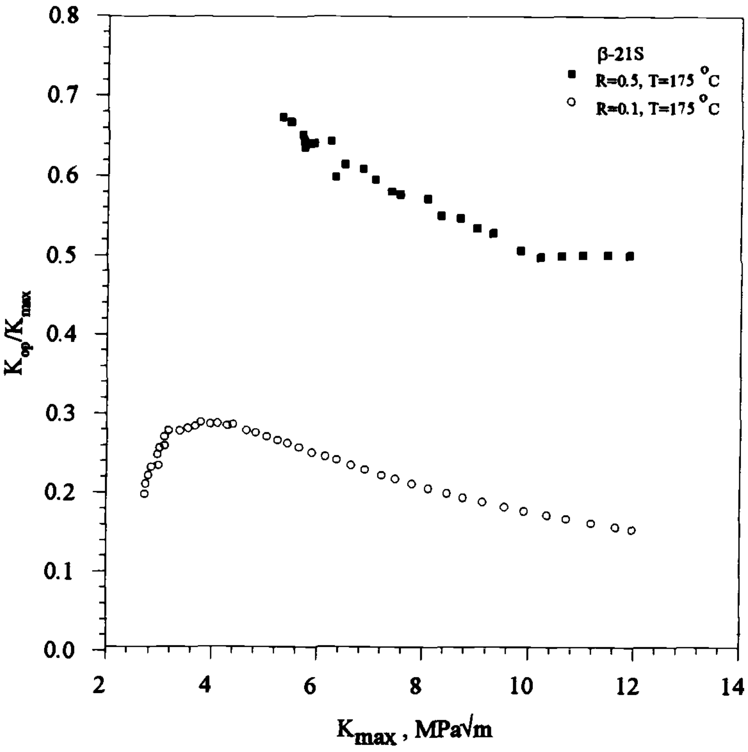

FIG. 5—*Comparison of* K_{op}/K_{max} *and* K_{max} *for elevated temperature,* $R = 0.1$ *and 0.5.*

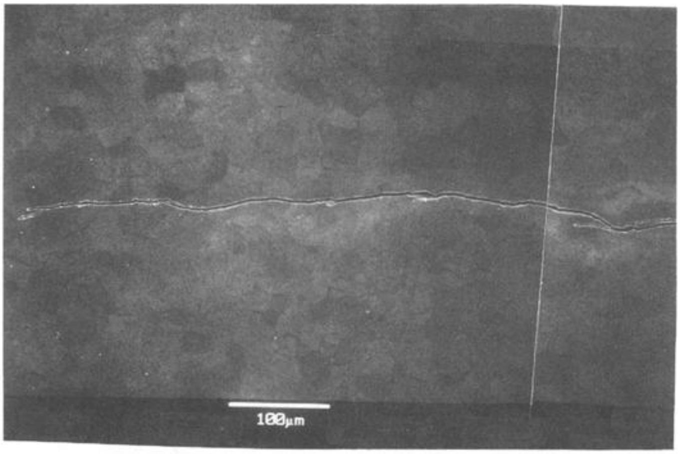

FIG. 6—*β-21S crack path at near threshold (25°C),* R = *0.1.*

conditions. Fractographs taken at near threshold revealed that fracture was crystallographic in nature for all temperatures and stress ratios in this regime. The fracture surface was characterized by transgranular facets of varying orientation on the order of the size of the *β* grain (Fig. 7).

Fracture surfaces for elevated temperature tests were examined in detail to identify the mechanisms of crack closure since large crack path deflections were absent, intuitively indicating that crack path tortuosity was not the primary cause of crack closure. Tortuosity in the direction of crack growth was eliminated as a viable argument for the crack closure observed since crack path profiles were similar for all loading and temperature conditions. However, SEM micrographs of through-thickness fatigue crack fronts provided valuable information associated with crack closure measurements made at 125°C. Through-thickness crack morphologies were deflected more at elevated temperature in comparison to room temperature tests (Fig. 8). These

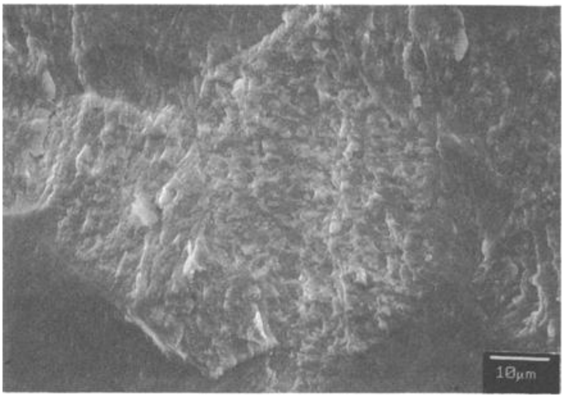

FIG. 7—*β-21S fracture surface showing fine α precipitates in β matrix (25°C),* R = *0.1.*

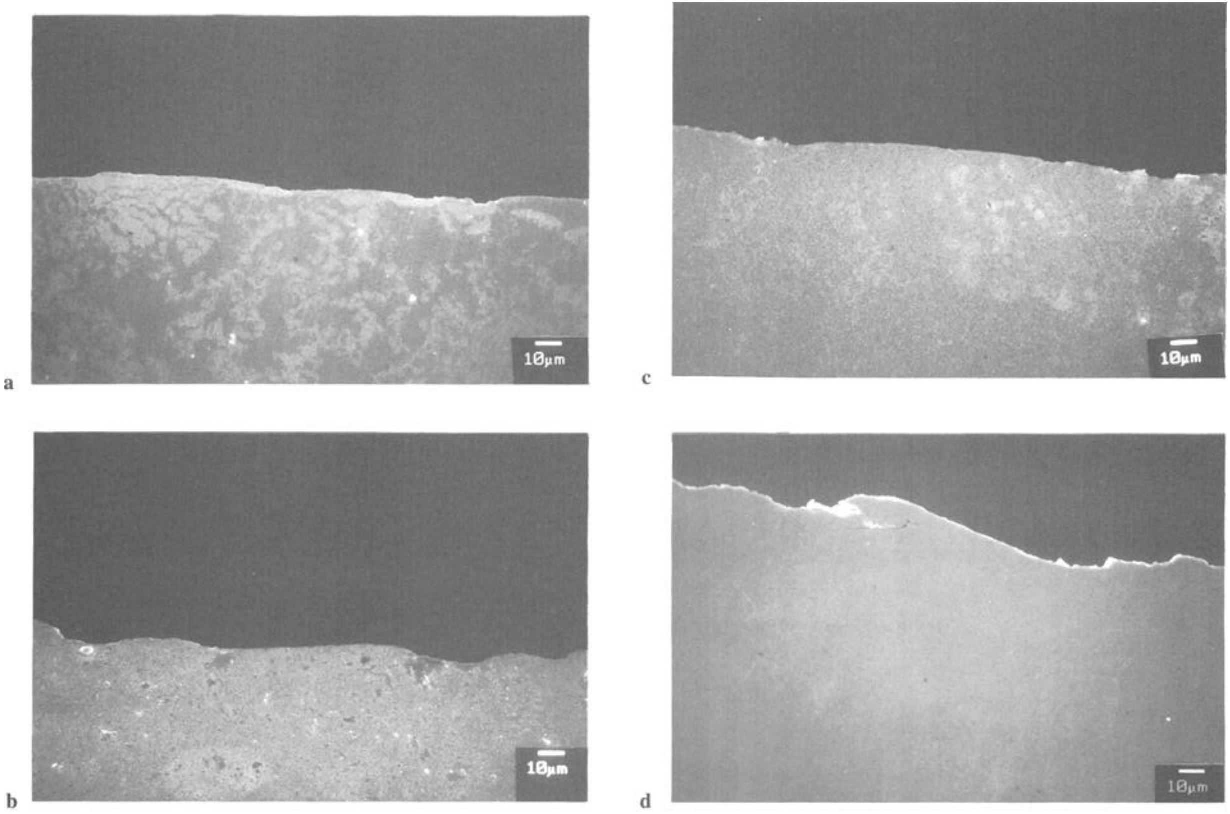

FIG. 8—*SEM micrographs of through-thickness fatigue crack front morphologies in* β*-21S at:* (a) *25°C,* R = *0.1,* $\Delta K \approx 10\ MPa\sqrt{m}$*;* (b) *175°C,* R = *0.1,* $\Delta K \approx 10\ MPa\sqrt{m}$*;* (c) *25°C,* R = *0.5,* $\Delta K_{th} \approx 2.2\ MPa\sqrt{m}$*;* (d) *175°C,* R = *0.5,* $\Delta K_{th} \approx 2.9\ MPa\sqrt{m}$*.*

larger crystallographic facets in the presence of Mode II displacement would enhance roughness-induced closure due to an increase in surface mismatch [*13*]. Roughness-induced crack closure can be identified on the fracture surface by the presence of mechanical rubbing or damage, where the surface experienced deformation and fretting [*21*]. For the 175°C tests (Figs. 8*b* and 8*d*), it can be seen that, while the facets show a greater propensity for deflection in comparison to 25°C (Figs. 8*a* and 8*c*), the edges are smoother, a result of surface contact and fretting during unloading. Fracture surface observations for room temperature samples tested at $R = 0.1$ did exhibit distinct crystallographic facets, yet no surface damage was observed (Fig. 9*a*). However, at elevated temperature the fracture surface for the same stress ratio showed evidence of mechanical damage (Fig. 9*b*). Consistently no surface damage was observed at room temperature, yet it was observed at 175°C for tests at high stress ratio. Figure 9*b* also shows the characteristic larger through-thickness faceting observed at elevated temperature.

A discoloration of the fracture surfaces was observed at 175°C due to elevated temperature oxidation. Oxide-induced closure has been associated with titanium alloys as a primary contributor to increased threshold values at elevated temperature [*20*]. Therefore it requires some discussion here. While β-21S offers superior oxidation resistance in comparison to other tita-

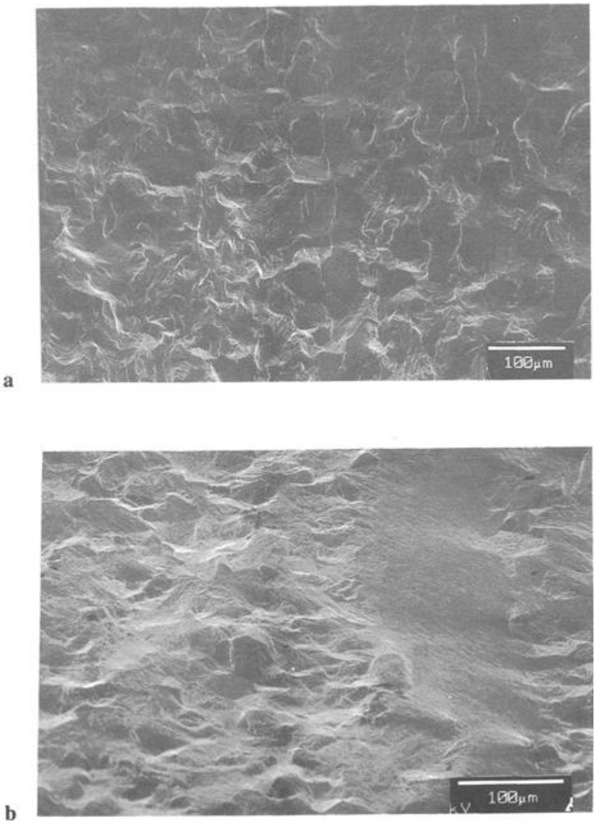

FIG. 9—*β-21S micrograph of:* (a) R = *0.1, 25°C near threshold;* (b) R = *0.1, 175°C near threshold.*

nium alloys [*1*], it is still susceptible to oxidation. Recent studies by Wallace et al. [*22*] showed oxide thickness measurements on the order of 840 nm for an exposure condition of 600°C for 72 h. Preliminary studies in this work show an oxide layer thickness on the order of 70 nm at 175°C. When oxide thickness approaches the crack tip opening displacement (CTOD $\approx K^2/\sigma_y E$), oxide-induced closure may become the dominant mechanism of crack closure. Although CTOD was not experimentally measured in this study, theoretical CTOD values at near threshold for β-21S were found to be on the order of 40 nm; thus, elevated temperature oxidation could have an effect on the crack closure observed. At a stress intensity range of approximately 4 MPa$\sqrt{m}$, the CTOD and oxide layer thickness were found to be similar. This stress intensity range value corresponds to the region on the fatigue crack growth curve (Fig. 3*b*) where crack closure levels became more pronounced at elevated temperature. A recent study by the authors [*23*] on β-21S having different heat treatments revealed various levels of crack closure under elevated temperature conditions. While oxide thickness was comparable for the different heat treatments at elevated temperature, one would expect the magnitude of crack closure to be

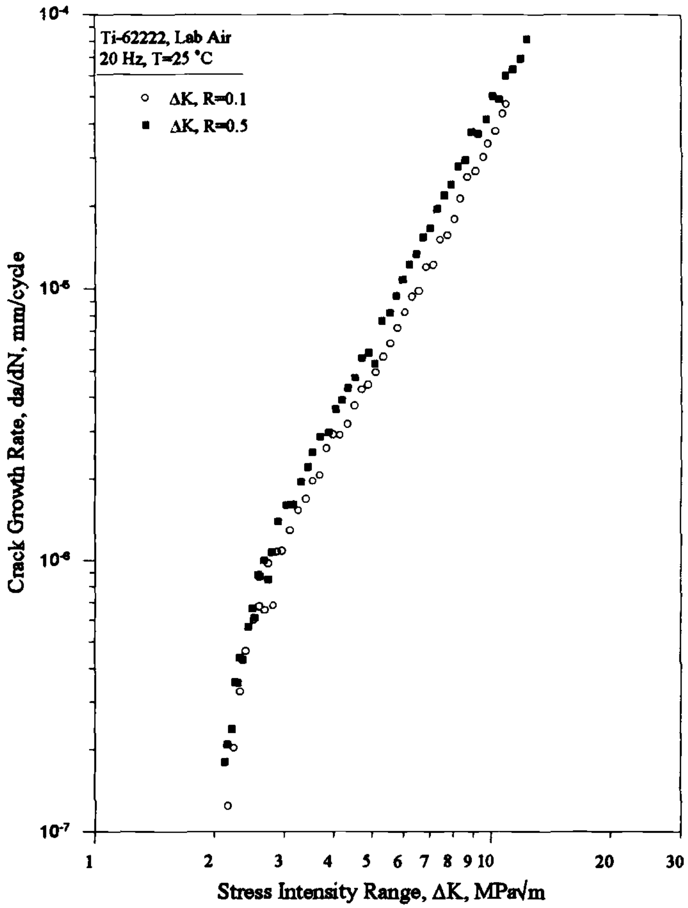

FIG. 10*a*—*Fatigue crack growth rate data for Ti-62222 at 25°C,* R *= 0.1 and 0.5.*

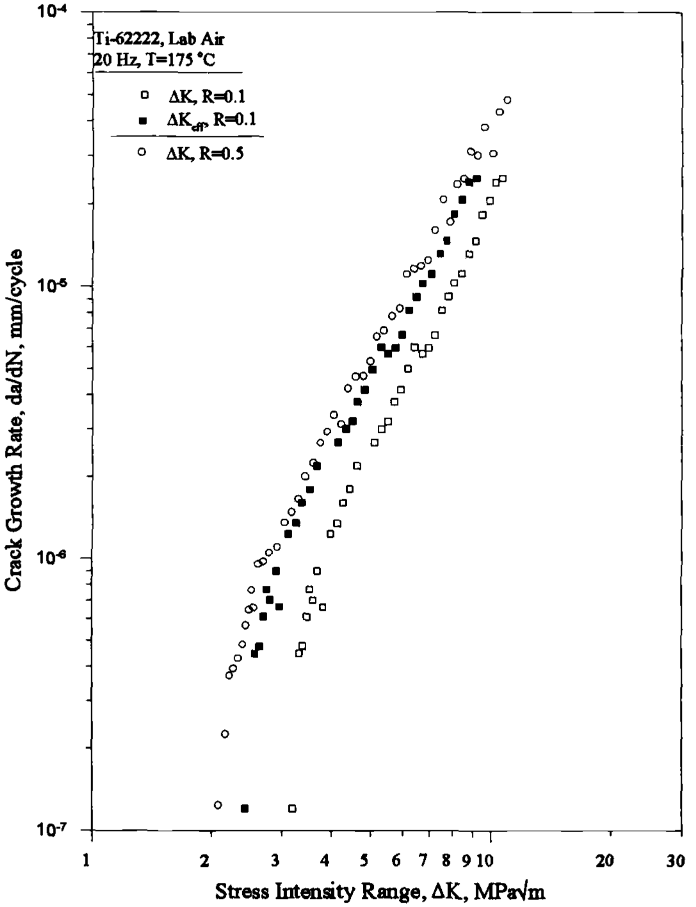

FIG. 10*b*—*Fatigue crack growth rate data for Ti-62222 at 175°C,* R = *0.1 and 0.5.*

similar for the heat treatments if oxide-induced crack closure were the dominating mechanism of crack closure. This, however, was not the case. Therefore, although oxide-induced closure may be a contributing factor to the crack closure observed, it does not appear to be the principal mechanism.

Ti-62222

Room temperature fatigue crack growth curves for stress ratios of 0.1 and 0.5 are shown in Fig. 10*a*. The threshold stress intensity range values for stress ratios of 0.1 and 0.5 were 2.1 and 2.2 MPa$\sqrt{m}$, respectively. Comparison of the different stress ratios indicated a behavior nearly independent of mean stress at near threshold conditions. The similarity for the different stress ratio tests at room temperature would indicate the absence of closure, which was in fact the case. Elevated temperature fatigue crack growth rates for stress ratios of 0.1 and 0.5 are shown in Fig. 10*b*. The threshold stress intensity range values for R = 0.1 and 0.5 were 3.1

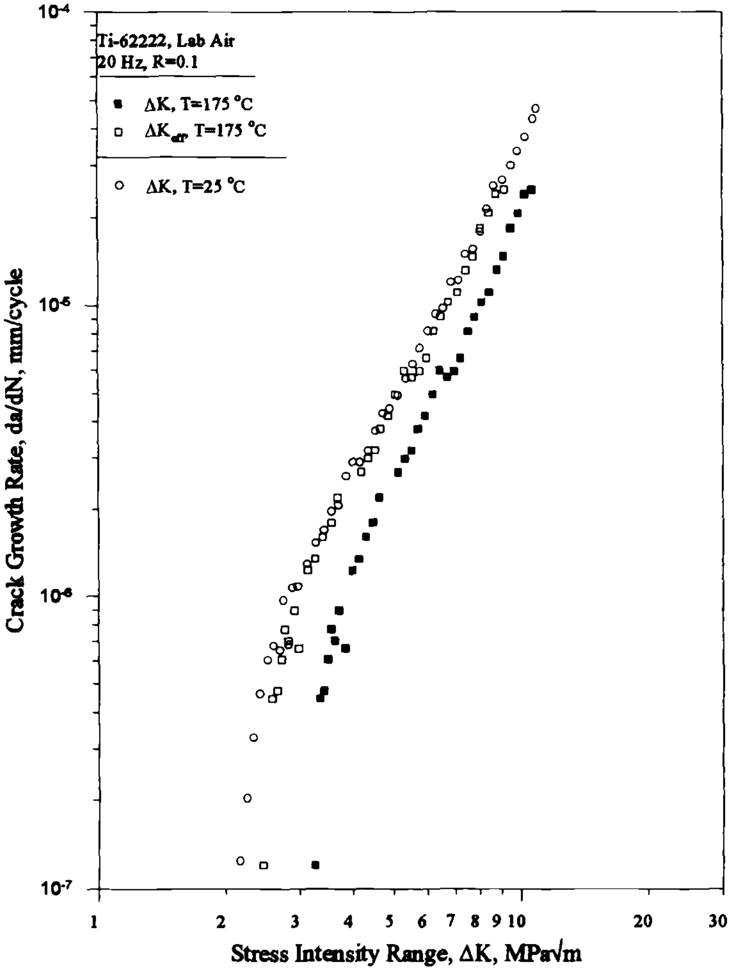

FIG. 11*a*—*Fatigue crack growth rate data for Ti-62222 at 25 and 175°C,* R *= 0.1.*

and 2.2 MPa$\sqrt{m}$, respectively. Crack closure was observed at 175°C at $R = 0.1$, yet not at $R = 0.5$, which yielded slower crack growth rates at $R = 0.1$. However, when accounting for closure, crack growth rates as well as $\Delta K_{eff,th}$ were very similar for both load ratios.

Room and elevated temperature fatigue crack growth curves for a stress ratio of 0.1 are shown in Fig. 11*a*. Nominal threshold crack growth rates were found to be lower at elevated temperature than at room temperature, producing a higher ΔK_{th}. Effective threshold crack growth rates for 175°C, however, produced similar behavior in comparison to room temperature. Room and elevated temperature tests for a stress ratio of 0.5 (Fig. 11*b*) showed no noticeable difference in fatigue crack growth behavior, indicating a lack of temperature dependence. This supports the findings observed at lower load ratio.

Examination of crack path profiles for all loading and temperature conditions revealed microstructurally influenced crack growth at low ΔK levels (Fig. 12*a*) with minimal microstructurally sensitive crack growth at intermediate ΔK levels (Fig. 12*b*). At intermediate ΔK levels,

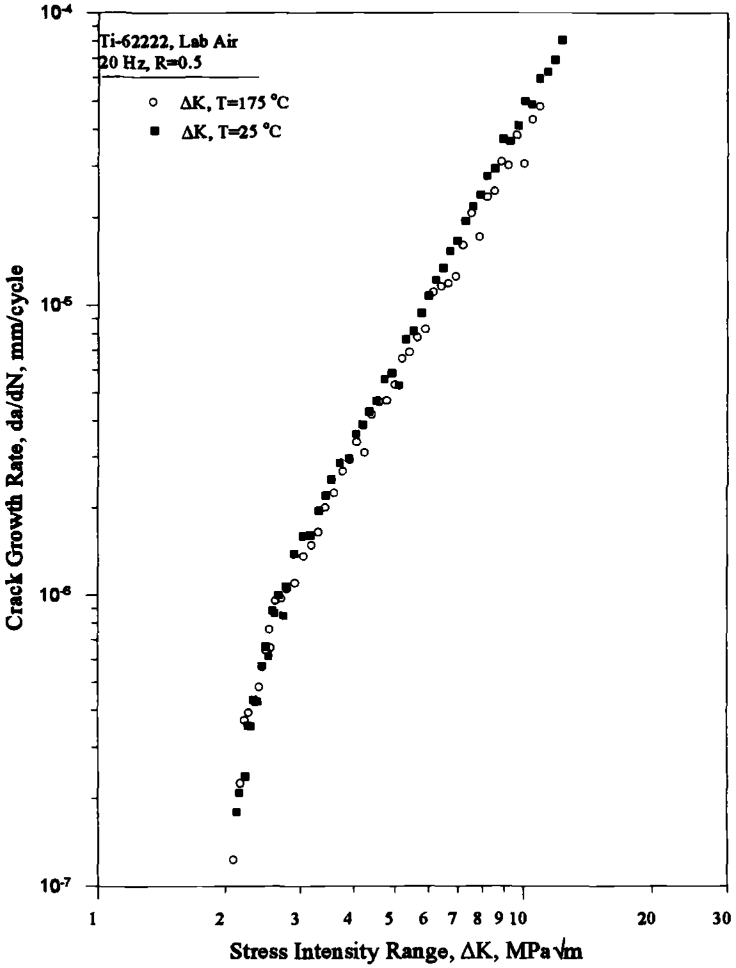

FIG. 11*b*—*Fatigue crack growth rate data for Ti-62222 at 25 and 175°C,* R *= 0.5.*

the crack path profile was observed to be flat with evidence of transgranular fracture. There was, however, evidence of out-of-plane deflections, where extruded material was observed along the crack path, specifically at elevated temperature (Fig. 12*b*).

Examination of the fracture surface revealed small planar facets intermixed with ductile-like features at near ΔK_{th} values (Fig. 13*a*). This appearance is consistent with the microstructure, where the small faceted region represents fracture of the α composition and the ductile-like regions are associated with fracture of the β composition. At intermediate stress intensity values, the fracture surface exhibited a pronounced decrease in faceting (Fig. 13*b*). Comparison of the fracture surfaces for the room and elevated temperature conditions did not show any significant differences regardless of temperature or stress ratio. A change in the fracture surface appearance was not observed for a stress ratio of 0.5. However, at elevated temperature for $R = 0.1$, there were isolated regions on the fracture surface where mechanical rubbing occurred (Fig. 13*c*). The frequency of this behavior, however, was much less than that observed for the β-21S.

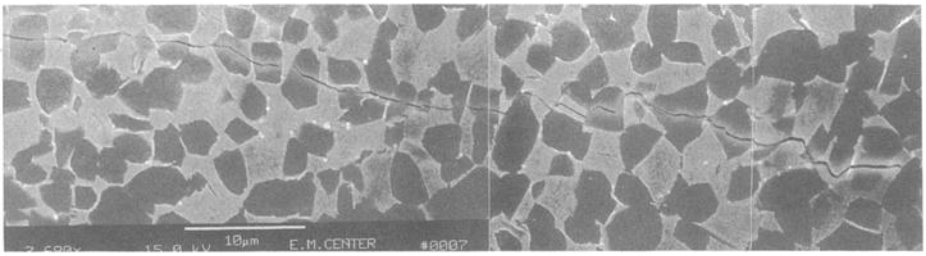

FIG. 12*a*—*Typical crack path profile for Ti-62222 at threshold.*

β-21S and Ti-62222 Comparison

While initial application concepts for these materials were different, their potential use as aero-skin materials are similar; therefore, a general comparison between the two materials will be performed. Ti-62222 and β-21S exhibited similar fatigue crack growth behavior at room temperature regardless of stress ratio (Fig. 14). At $R = 0.1$, β-21S showed higher crack growth rates in comparison to Ti-62222 for the same nominal ΔK_{th} values at elevated temperature (Fig. 14*a*), yet effective crack growth rates for the two materials were very similar. At elevated temperature, β-21S showed lower crack growth rates in comparison to Ti-62222 at the same nominal ΔK for $R = 0.5$ at crack growth rates below about 10^{-5} mm/cycle (Fig. 14*b*). This difference can be attributed to the closure behavior observed at high load ratio at elevated temperature for β-21S but not for Ti-62222. Table 3 is a summary of the fatigue crack growth threshold values for each test condition evaluated.

Crystallographic structure appeared to play a more significant role in fatigue crack threshold behavior than did grain size, where one would expect higher ΔK_{th} values for larger grain size [*16*]. The significant difference in grain size between the two materials would predict higher threshold values for β-21S, but for all test conditions a significant difference in ΔK_{th} was not observed. Since ΔK_{th} values were similar for the two materials, each having significantly different grain sizes, the combined composition of the $\alpha + \beta$ alloy compensated for the smaller

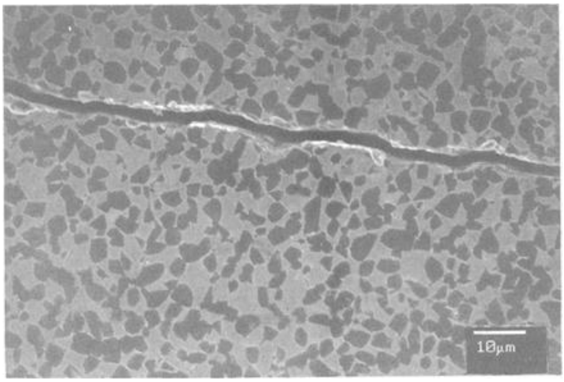

FIG. 12*b*—*Typical crack path profile for Ti-62222 for intermediate stress intensity values.*

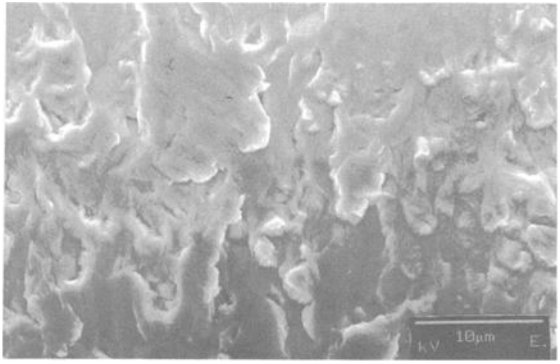

FIG. 13*a*—*Ti-62222 fracture surface at near threshold (25°C),* R *= 0.1.*

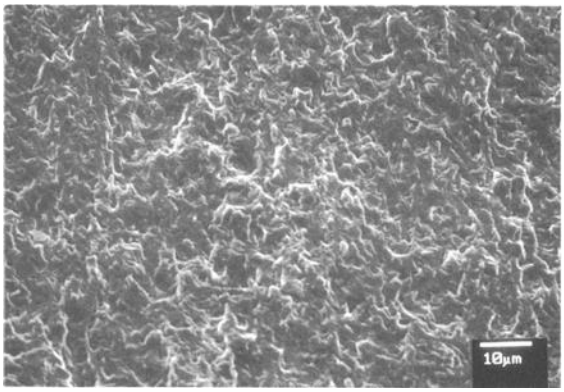

FIG. 13*b*—*Ti-62222 fracture surface at intermediate crack growth rates (25°C),* R *= 0.1.*

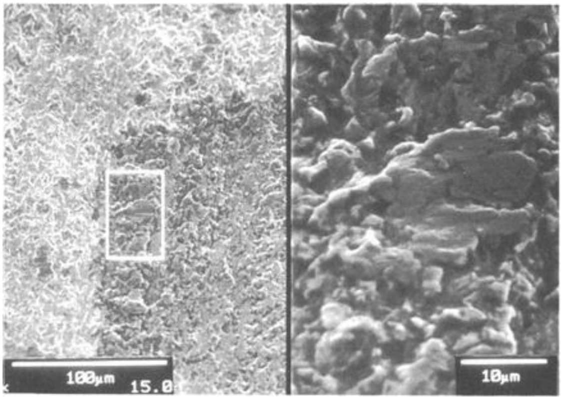

FIG. 13*c*—*Ti-62222 fracture surface showing surface damage (175°C),* R *= 0.1.*

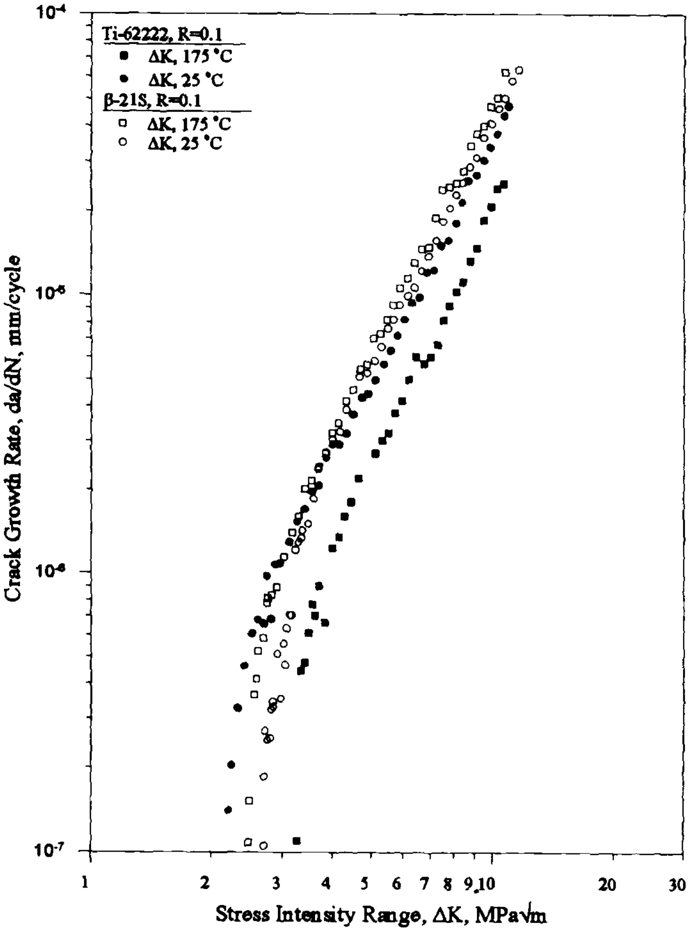

FIG. 14*a*—*Fatigue crack growth rate data for β-21S and Ti-62222 (25°C, 175°C),* R *= 0.1.*

grain size in comparison to the large-grained β alloy. The α/β composition of the Ti-62222 provides strength, toughness, and ductility, while the α composition promotes the greatest resistance to crack growth. This makes it a comparable material to β-21S, which promoted a slightly rougher crack path due to a larger grain size.

Summary and Conclusions

β-21S exhibited lower fatigue crack growth rates at elevated temperature than at room temperature under nominal stress intensity values. This was attributed, in part, to a reduced crack tip driving force caused by crack closure. Fracture surface observations confirmed this behavior for room and elevated temperature conditions. β-21S exhibited transgranular fracture defined by crystallographic planes at low and intermediate ΔK levels for room temperature conditions.

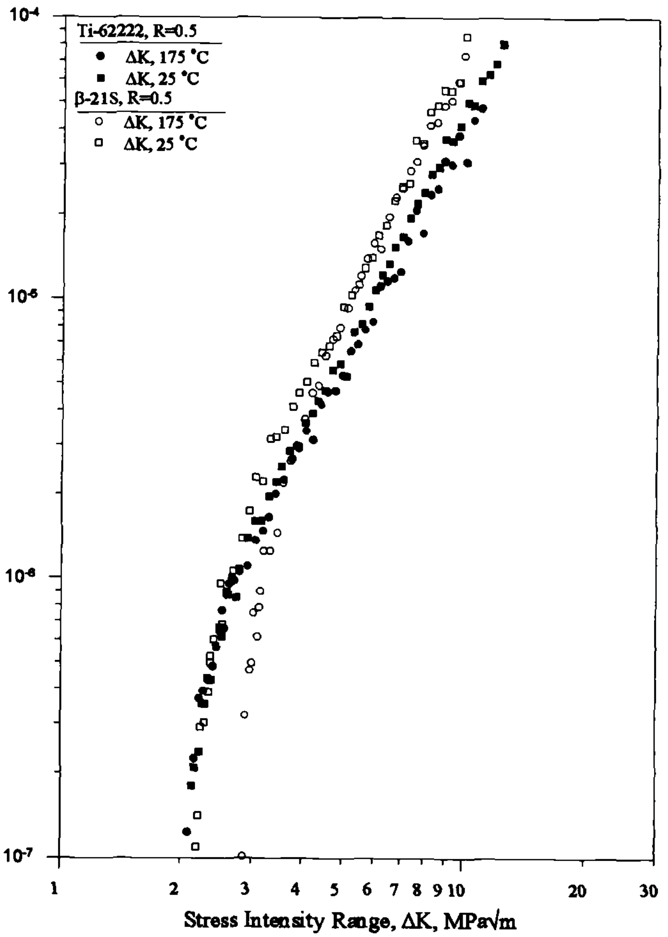

FIG. 14*b*—*Fatigue crack growth rate data for β-21S and Ti-62222 (25°C, 175°C),* R *= 0.5.*

However, the fracture surfaces examined for the elevated temperature test conditions revealed mechanical damage due to Mode II displacement and larger through-thickness facets that produced roughness-induced closure. This caused a reduction in the driving force at the crack tip. Elevated temperature oxidation was found to contribute to the crack closure observed.

Ti-62222 exhibited very similar fatigue crack growth behavior at both test temperatures at high stress ratio. At low stress ratio, crack closure was observed at 175°C but not at 25°C, resulting in moderate differences in nominal crack growth rates. Crack path profiles showed little influence of microstructure at intermediate ΔK values with an increase in microstructural influences as lower ΔK values were approached.

Fatigue crack growth behavior was similar for both materials. Microstructural differences played an important role in determining the overall fatigue crack growth behavior of these two titanium alloys. Crack closure contributed to the overall fatigue crack growth behavior in both materials, specifically at elevated temperature.

TABLE 3—*Fatigue crack growth rate threshold for different test conditions.*

Stress Ratio, R	Test Temperature, °C	ΔK_{th}	$\Delta K_{th,eff}$
	β-31S		
0.1	25	2.7	2.7[a]
0.5	25	2.2	2.2[a]
0.1	175	2.5	2.2
0.5	175	2.9	1.8
	Ti-62222		
0.1	25	2.1	2.1[a]
0.5	25	2.2	2.2[a]
0.1	175	3.1	2.2
0.5	175	2.1	2.1[a]

[a] Crack closure was not observed, thus $\Delta K_{th} = \Delta K_{th,eff}$.

Acknowledgments

The authors gratefully acknowledge research funding from Lockheed-Martin Aeronautical Systems Company through NASA Contract-20015. Mr. D. L. Dicus and Mr. E. P. Phillips are the NASA Technical Monitors for the research program. Special thanks are also due to the Idaho Space Grant Consortium for financial support during this project.

References

[*1*] Bania, P. J. and Paris, W. M., "Beta-21S: A High Temperature Metastable Beta Titanium Alloy," *Proceedings*, Seventh World Conference on Titanium, San Diego, CA, June 1992.

[*2*] Boyer, R. R., "Aerospace Applications of Beta Titanium Alloys," *Journal of Metals*, July 1994.

[*3*] Alcoa Forging Division, "Beta Processed Ti-6Al-2Sn-2Zr-2Mo-2Cr + Si Data Sheet," Mechanical Properties Data Report, Alcoa.

[*4*] "Technical Requirements of Titanium for the HSCT," Technical Report, Advanced Structures and Materials Division, Lockheed-Martin Aeronautical Co., Marietta, GA.

[*5*] Williams, J. C., Boyer, R. R., and Blackburn, M. J., "The Influence of Microstructure on the Fracture Topography of Titanium Alloys," *Electron Microfractography, ASTM STP 453*, American Society for Testing and Materials, West Conshohocken, PA, 1969, pp. 215–235.

[*6*] Yoder, G. R., Cooley, L. A., and Crooker, T. W., "Enhancement of Fatigue Crack Growth and Fracture Resistance in Ti-6Al-4V and Ti-6Al-6V-2Sn Through Microstructural Modification," *Journal of Engineering Materials and Technology*, Vol. 99, 1977, pp. 313–318.

[*7*] Ruppen, J. A. and McEvily, A. J., "Influence of Microstructure and Environment on the Fatigue Crack Growth Fracture Topography of Ti-6Al-2Sn-4Zr-2Mo-0.1Si," *Fractography and Material Science, ASTM STP 733*, L. N. Gilbertson and R. D. Zipp, Eds., American Society for Testing and Materials, West Conshohocken, PA, 1981, pp. 32–50.

[*8*] Yoder, G. R., Cooley, L. A., and Crooker, T. W., "50-Fold Difference in Region II Fatigue Crack Propagation Resistance of Titanium Alloys: A Grain Size Effect," *Journal of Engineering Materials and Technology*, Vol. 101, *1979*, pp. 86–90.

[*9*] Shechtman, D. and Elyon, D., "On the Unstable Shear Fatigued β-Annealed Ti-11 and IMI-685 Alloys," *Metallurgical Transactions*, Vol. 9A, 1978, pp. 1018–1020.

[*10*] Yoder, G. R., Cooley, L. A., and Crooker, T. W., "Observations on Microstructurally Sensitive Fatigue Crack Growth in Widmanstätten Ti-6Al-4V Alloy," *Metallurgical Transactions*, Vol. 8A, 1977, pp. 1737–1747.

[*11*] Irving, P. E. and Beevers, C. J., "The Effects of Air and Vacuum Environments on Fatigue Crack Growth Rates in Ti-6Al-4V," *Metallurgical Transactions*, Vol. 5, 1974, pp. 391–395.

[*12*] Elyon, D., Hall, J. A., Pierce, C. M., and Ruckle, D. L., "Microstructure and Mechanical Properties Relationships in the Ti-11 Alloy at Room and Elevated Temperatures," *Metallurgical Transactions*, Vol. 7A, 1976, pp. 1817–1826.

[13] Suresh, S. and Ritchie, R. O., "Near-Threshold Fatigue Crack Propagation: A Perspective on the Role of Crack Closure," *Metallurgical Society of ASME*, S. Suresh and D. L. Davidson, Eds., 1983, pp. 227–261.

[14] Beevers, C. J., Bell, K., and Carlson, R. L., "Fatigue Crack Closure and the Fatigue Threshold," *Metallurgical Society of ASME*, S. Suresh and D. L. Davidson, Eds., 1983, pp. 327–340.

[15] Salivar, G. C., Heine, J. E., and Haake, F. K., "The Effect of Stress Ratio on the Near-Threshold Fatigue Crack Growth Behavior of Ti-8Al-1Mo-1V at Elevated Temperature," *Engineering Fracture Mechanics*, Vol. 32, No. 5, pp. 807–817.

[16] Taylor, D., *Fatigue Thresholds*, Butterworths and Co., London, 1989.

[17] Upadhyaya, D., Blacketter, D. M., Suryanarayana, C., and Froes, F. H., "Microstructure and Mechanical Properties of β-21S Titanium Alloy," *Titanium Science and Technology*, F. H. Froes et al., Eds., The Minerals, Metals, and Materials Society, Warrendale, PA, 1993, pp. 447–454.

[18] Chaudhuri, K. and Perepezko, J. H., "Microstructural Study of the Titanium Alloy Ti-15Mo-2.7No-3Al-0.2Si (TIMETAL 21S)," *Metallurgical and Material Transactions*, Vol. 25A, June 1994, pp. 1109–1117.

[19] Underwood, J. H., Kortshot, M. T., Lloyd, W. R., Eidinoff, H. L., Wilson, D. A., and Ashbaugh, N., "Translaminar Fracture Toughness Test Methods and Results from Interlaboratory Tests of Carbon/Epoxy Laminates," *Fracture Mechanics: 26th Volume, ASTM STP 1256*, W. G. Reuter, J. Underwood, and J. C. Newman, Jr., Eds., American Society for Testing and Materials, West Conshohocken, PA, 1995.

[20] Petit, J., Berata, W., and Bouchet, "Fatigue Crack Growth Behavior of Ti-6Al-4V at Elevated Temperature," *Titanium Science and Technology*, F. H. Froes et al., Eds., The Minerals, Metals, and Materials Society, Warrendale, PA, 1993, pp. 1819–1826.

[21] Metals and Ceramics Information Center, *SEM/TEM Fractography Handbook*, McDonnell-Douglas Astronautics Company, Huntington Beach, CA, December 1975.

[22] Wallace, T. A., Wiedemann, K. E., and Clark, R. K., "Oxidation Characteristics of Beta-21S in Air in the Temperature Range 600 to 800°C," *Titanium '92 Science and Technology*, The Minerals, Metals, and Materials Society, Warrendale, PA, 1992, pp. 2177–2184.

[23] Albertson, T. P., Stephens, R. R., and Bayha, T. D., "The Effect of Aging and Forming on the Fatigue Crack Growth Characteristics of β-21S at Ambient and Elevated Temperature," *Proceedings*, Eighth World Conference on Titanium, Birmingham, England, 1995.

Fracture

Michael J. Haynes,[1] *Brian P. Somerday,*[1] *Cynthia L. Lach,*[2] *and Richard P. Gangloff*[3]

Micromechanical Modeling of Temperature-Dependent Initiation Fracture Toughness in Advanced Aluminum Alloys

---

REFERENCE: Haynes, M. J., Somerday, B. P., Lach, C. L., and Gangloff, R. P., "**Micromechanical Modeling of Temperature-Dependent Initiation Fracture Toughness in Advanced Aluminum Alloys,**" *Elevated Temperature Effects on Fatigue and Fracture, ASTM STP 1297,* R. S. Piascik, R. P. Gangloff, and A. Saxena, Ed., American Society for Testing and Materials, 1997, pp. 165–190.

ABSTRACT: The temperature dependence of the plane-strain initiation fracture toughness (K_{JICi}) is modeled micromechanically for a variety of advanced aluminum alloys that fail by microvoid processes. Materials include precipitation-hardened ingot metallurgy, spray formed, submicron-grain-size powder metallurgy, and metal-matrix composite alloys. A critical-plastic-strain-controlled model, employing tensile yield strength, elastic modulus, work hardening, and reduction of area measurements, successfully predicts K_{JICi} versus temperature for eight alloys, providing a strong confirmation of this approach. Modeling shows that K_{JICi} is controlled by the interplay between the temperature dependencies of the intrinsic failure locus $\bar{\varepsilon}_f^p(\sigma_m/\sigma_{fl})$ and the crack-tip stress/strain fields governed by alloy flow properties. Uncertainties in $\bar{\varepsilon}_f^p(\sigma_m/\sigma_{fl})$, as well as the critical distance (volume) for crack-tip damage evolution, hinder absolute predictions of K_{JICi}. Critical distance (calculated from the model) correlates with the nearest-neighbor spacing of void-nucleating particles and with the extent of primary void growth determined from quantitative fractography. These correlations suggest a means to predict absolute plane-strain fracture toughness.

KEYWORDS: fracture toughness, ductile fracture, micromechanical modeling, aluminum alloys, elevated temperature

Recent research has focused on measuring the plane-strain initiation fracture toughness, as well as plane-strain and plane-stress crack-growth resistances, of advanced plate and sheet aluminum alloys [*1–6*]. Experimental *J*-integral (*J*) versus crack extension (Δa) curves were established using elastic-plastic fracture mechanics (EPFM) and precision crack length monitoring by direct-current potential difference (DCPD) or unloading compliance [*7,8*]. The DCPD technique more effectively detected microscopic damage constituting initial crack extension compared to standardized offset methods, particularly in thin-sheet or high-tearing-resistance alloys [*5,8*]. The linear-elastic plane-strain fracture toughness calculated from *J* at the DCPD-detected initial crack extension (K_{JICi}), as well as the *J* (or equivalently *K*) versus Δa curves,

---

[1] Graduate research assistant, Department of Materials Science and Engineering, University of Virginia, Charlottesville, VA 22903.

[2] Research engineer, NASA Langley Research Center, Hampton, VA 23681.

[3] Professor, Department of Materials Science and Engineering, University of Virginia, Charlottesville, VA 22903.

were reported as a function of temperature for experimental and commercial aluminum alloys, including advanced 2XXX precipitation-hardened alloys [*1*,*4*], submicron-grain-size powder metallurgy alloys [*2*,*3*], a spray-formed 2XXX alloy, and a 2XXX alloy reinforced with SiC particulate [*5*,*6*]. In all cases, fracture was based on microvoid damage.

It is important to model fracture toughness in order to understand the basic microstructural and deformation properties that govern K_{JICi} and K versus Δa, particularly as a function of temperature. Measured K_{JICi} versus temperature data for aluminum alloys vary widely, and temperature dependencies of K_{JICi} and tensile ductility often differ. These trends must be understood. The critical-plastic-strain-controlled model is most pertinent for predicting aluminum alloy initiation fracture toughness and is detailed below. Although this model is simple conceptually, model accuracy has not been established over a range of flow properties and microstructures. Some model parameters are difficult to define unambiguously.

The objective of this work is to apply the strain-controlled model to predict the temperature dependence of plane-strain initiation fracture toughness for eight advanced aluminum alloys based on measured deformation and fracture properties. This study aims to understand the continuum and microstructural origins of the measured temperature dependencies of fracture toughness. In addition, the variation of model parameters with temperature and microstructure offers a unique opportunity to test the model critically.

Review of Strain-Controlled Fracture-Toughness Modeling

Micromechanical models of fracture toughness must couple three elements [*9–11*]: (1) an estimate of the intrinsic fracture resistance, (2) solutions for the crack-tip stress and strain fields that drive microscopic fracture, and (3) a microstructural distance pertinent to the fracture process. These models overcome the limitations of earlier work, which considered only the crack-tip driving force and critical distance [*12*,*13*].

Fracture Resistance

For the aluminum alloys considered, fracture is by microvoid nucleation, growth, and coalescence (MNG) involving second-phase particles. A critical strain should characterize fracture resistance regardless of the relative contributions of void nucleation and growth. While strain explicitly drives void growth [*14–18*], the void-nucleation criterion is couched typically in terms of a critical stress. The stress that concentrates near the particle/matrix interface is, however, a function of the remote strain [*10*,*19*,*20*].

Ideally, the effective plastic strain to failure ($\bar{\varepsilon}_f^p$) is the void-nucleation strain plus the strain required to grow the voids to the critical event characterized by K_{JICi}. There are two approaches for estimating the critical fracture strain: modeling and direct measurement. The critical strain for each stage of MNG is affected by stress-state triaxiality (characterized by σ_m/σ_{fl}, where σ_m is mean stress and σ_{fl} is flow stress) [*14–16*]. Since a gradient of σ_m/σ_{fl} exists ahead of a crack tip [*11*,*12*], a stress-state-dependent failure-strain locus ($\bar{\varepsilon}_f^p(\sigma_m/\sigma_{fl})$) must be determined.

Models exist for predicting both the nucleation and growth strains [*14–16*]; however, calculating $\bar{\varepsilon}_f^p(\sigma_m/\sigma_{fl})$ is complicated in the following ways. First, some MNG modeling parameters (such as the void-nucleating particle fracture strength or interface decohesion strength and the solution for stress local to a particle) are uncertain [*19–21*]. Second, when primary void growth contributes substantially to $\bar{\varepsilon}_f^p(\sigma_m/\sigma_{fl})$, voids coalesce by two means: impingement or shear-based strain localization [*14*,*22*]. Strain-localized coalescence criteria are uncertain and depend on the spacing of "primary" void-nucleating particles [*23*,*24*], strain hardening and strain rate hardening [*15*,*23–26*], σ_m/σ_{fl} [*27*,*28*], and the volume fraction of "secondary" void-nucleating particles [*4*,*14*]. Third, the contribution of each MNG stage to $\bar{\varepsilon}_f^p(\sigma_m/\sigma_{fl})$ can vary among alloys. Finally, particle and void interactions in three dimensions, as well as local triaxial stress from elastic constraint on matrix plastic flow, complicate prediction of $\bar{\varepsilon}_f^p$.

A reasonable estimate of $\bar{\varepsilon}_f^p(\sigma_m/\sigma_{fl})$ is obtained by integrating the Rice and Tracey void growth equation at constant σ_m/σ_{fl} [*16,17,29*]:

$$\bar{\varepsilon}_f^p = \alpha \exp\left(-\beta \frac{\sigma_m}{\sigma_{fl}}\right) \tag{1}$$

α is a material constant inversely related to the inclusion content, and β is the stress-triaxiality sensitivity. For many steels and other alloys, β equals 1.5 as predicted by Rice and Tracey [*29,30*]. However, β may change if void nucleation contributes significantly to $\bar{\varepsilon}_f^p$, if $\bar{\varepsilon}_f^p$ is insensitive to global σ_m/σ_{fl}, or if void growth is aided by localized strain.

Direct measurement of $\bar{\varepsilon}_f^p(\sigma_m/\sigma_{fl})$ avoids the complexities associated with MNG modeling. The $\bar{\varepsilon}_f^p(\sigma_m/\sigma_{fl})$ locus is measured typically by straining notched tensile specimens having a range of imposed σ_m/σ_{fl} values [*18,31*]. Alternately, measurements of fracture-surface microroughness are used to estimate $\bar{\varepsilon}_f^p(\sigma_m/\sigma_{fl})$ [*11,32*]. Measured $\bar{\varepsilon}_f^p(\sigma_m/\sigma_{fl})$ includes the three stages of MNG and thus cannot offer insight into MNG mechanisms.

Crack-Tip Plastic Strain and Stress-State Triaxiality Fields

The solutions for effective plastic strain ($\bar{\varepsilon}^p$) and stress-state triaxiality (σ_m/σ_{fl}) crack-tip fields should be consistent with the observed Mode I crack-tip profile geometry, as well as the angular orientation of void-damage sites ahead of the stationary crack tip. Hutchinson, Rice, and Rosengren (HRR) derived the stress and strain fields for a crack tip undergoing small geometry change (i.e., no blunting) where *J*-dominance prevails [*33,34*]. Solutions for $\bar{\varepsilon}^p$ and σ_m/σ_{fl} ahead of a blunted crack tip [*12,35–37*] are assumed to be more relevant for fracture of high-strength aluminum alloys [*8*]. The finite-strain, flow-theory, finite-element-modeling (FEM) results of McMeeking for a smoothly blunting crack tip are used in this study [*35*]. The following function is fit to $\bar{\varepsilon}^p$ results reported for a work-hardening exponent (n from $\sigma \propto \varepsilon^n$) of zero, a σ_{ys}/E ratio of 0.003, and an angular orientation of 0° from the crack plane

$$\bar{\varepsilon}^p = 0.3511\left[0.2571^{\left(\frac{x}{\delta}\right)}\right]\left(\frac{x}{\delta}\right)^{-0.5309} \tag{2}$$

The variable x is the distance from the crack tip, and δ is the Mode I crack-tip-opening displacement defined by a 90° included angle. The crack-tip strain field is insensitive to work hardening; fields for n of 0.1 and 0.2 were nearly identical to the perfect plasticity case [*35*].

McMeeking's stress fields at 0° are plotted as crack tip opening stress ($\sigma_{\theta\theta}$ or σ_{yy}) normalized by the uniaxial yield stress. For perfect plasticity, the flow stress equals the yield stress, and σ_m/σ_{fl} equals $(\sigma_{yy}/\sigma_{fl} - 1/\sqrt{3})$ [*38*]. σ_m/σ_{fl} was determined from FEM-calculated σ_{yy}/σ_{fl}, and the following function was fit to the σ_m/σ_{fl} field:

$$\frac{\sigma_m}{\sigma_{fl}} = 0.5796 + 1.9053\left(\frac{x}{\delta}\right) - 0.7311\left(\frac{x}{\delta}\right)^2 + 0.1303\left(\frac{x}{\delta}\right)^3 - 0.01118\left(\frac{x}{\delta}\right)^4 + 0.0003694\left(\frac{x}{\delta}\right)^5 \tag{3}$$

This field is assumed to approximate σ_m/σ_{fl} for aluminum alloys due to their low work-hardening rates. For modest to high work hardening ($0.1 < n < 0.2$), the field is still adequate since σ_m and σ_{fl} increase by similar amounts as n increases [*38*].

Critical Distance

The critical distance (l^*) over which MNG damage occurs is an essential model element since the crack-tip strain singularity precludes defining the failure criterion at the point of maximum strain [*11,12,18*]. An accepted definition of l^* for initial crack extension by MNG is some multiple of the nearest-neighbor interparticle spacing [*11,31*]. Equating l^* with the average spacing of void-nucleating particles is not correct because more than one particle may participate in void link-up during crack extension and coalescence may depend on particle properties. It is not possible to determine l^* *a priori* by metallographic or fractographic measurements. Thus this parameter is often used as a curve-fitting constant to match experimental toughness data [*2–4,10,31*]. If the MNG mechanisms are constant as temperature varies, then l^* may be invariant. This assumption must be examined critically.

Model Formulation

The critical-plastic-strain-controlled model criterion states that the plane-strain initiation toughness corresponds to the applied stress-intensity (K) level required for the crack-tip plastic strain to exceed the stress-state-dependent fracture resistance over a microstructural distance [*11,18,31,38*]. A graphical illustration of this model is shown in Fig. 1, where $\bar{\varepsilon}^p$ (Eq 2), $\bar{\varepsilon}^p_f$

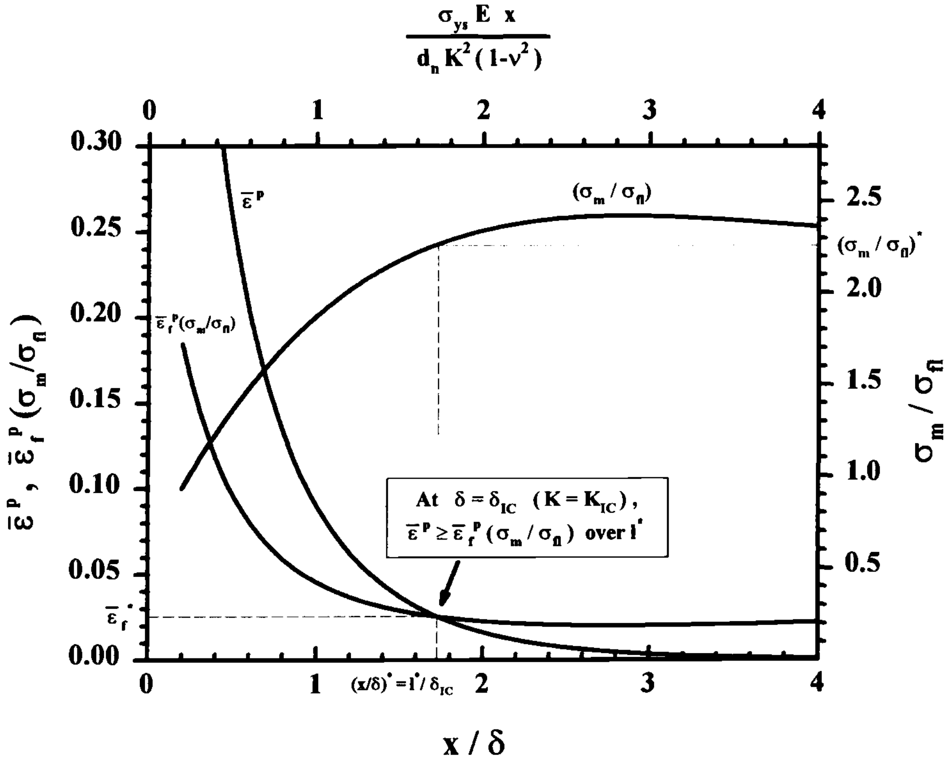

FIG. 1—*Illustration of the critical-plastic-strain-controlled model. The crack-tip effective plastic strain ($\bar{\varepsilon}^p$) and stress-state-triaxiality fields (σ_m/σ_{fl}) [35] are plotted with a typical failure strain locus ($\bar{\varepsilon}^p_f(\sigma_m/\sigma_{fl})$) ahead of the crack tip. For fracture initiation, $\bar{\varepsilon}^p$ must exceed $\bar{\varepsilon}^p_f(\sigma_m/\sigma_{fl})$ over a critical distance (l*).*

(σ_m/σ_{fl}), and σ_m/σ_{fl} (Eq 3) are plotted as a function of normalized distance ahead of the crack tip, x/δ. $\bar{\varepsilon}_f^p(\sigma_m/\sigma_{fl})$ ahead of the crack tip is obtained by substituting Eq 3 into Eq 1. The fracture criterion is satisfied at the intersection of the $\bar{\varepsilon}^p$ and $\bar{\varepsilon}_f^p(\sigma_m/\sigma_{fl})$ curves, yielding an intrinsic fracture strain $(\bar{\varepsilon}_f^*)$, a characteristic stress-state triaxiality $(\sigma_m/\sigma_{fl})^*$, and a ratio of critical distance to critical crack-tip opening displacement $(x/\delta)^*$. A computer program was written to determine $\bar{\varepsilon}_f^*$ and $(x/\delta)^*$ iteratively from Eqs 1 through 3. The $\bar{\varepsilon}^p$ and σ_m/σ_{fl} fields were the same for each alloy and testing condition, while $\bar{\varepsilon}_f^p(\sigma_m/\sigma_{fl})$ was given by Eq 1 applied to smooth and notched tensile bar reduction of area data.

At a critical distance ahead of the crack tip ($x = l^*$), $\bar{\varepsilon}^p$ increases to $\bar{\varepsilon}_f^*$ as applied δ increases to δ_{IC}, where fracture initiates by void impingement or void sheeting between the void nucleation sites and the crack tip. δ_{IC} is expressed implicitly in terms of l^* and $\bar{\varepsilon}_f^*$ by employing Eq 2 with $\bar{\varepsilon}^p$ equal to $\bar{\varepsilon}_f^*$ and x/δ equal to l^*/δ_{IC}

$$\bar{\varepsilon}_f^* = 0.3511\ [0.2571^{\left(\frac{l^*}{\delta_{IC}}\right)}]\left(\frac{l^*}{\delta_{IC}}\right)^{-0.5309} \tag{4}$$

The following relationships relate δ_{IC} to K_{JICi} [*35,39,40*]

$$\delta = d_n \frac{J}{\sigma_{ys}} \tag{5}$$

$$J = \frac{K^2(1 - \nu^2)}{E} \tag{6}$$

The quantity, ν, is Poisson's ratio. The dimensionless constant, d_n, is a function of n, stress state, σ_{ys}/E, and the definition of δ. Values of d_n are related linearly to n between 0.0 and 0.2 ($d_n = 0.58 - 1.4n$) [*35*] and are similar to those given by analytical solutions [*39*].

Effects of temperature-dependent alloy deformation and fracture properties on K_{JICi} are not shown explicitly by the iterative solution, but such effects can be seen from simpler modeling approaches [*10,11*]

$$K_{JICi} \sim \sqrt{\frac{\sigma_{ys}\, E\, l^*\, \bar{\varepsilon}_f^*}{(1 - \nu^2)\, d_n}} \tag{7}$$

The parameters σ_{ys}, E, $\bar{\varepsilon}_f^*$, and d_n are temperature dependent, while l^* and ν are assumed constant.

Determination of Model Parameters

Alloy Systems

Extensive data on microstructure, as well as temperature-dependent deformation properties, stress-state-governed fracture strains, and initiation fracture toughnesses were obtained for nine aluminum alloys. The nine alloys belong to four systems: (1) ingot metallurgy (I/M) [*1,4,41*], (2) spray formed (SF), (3) powder metallurgy (P/M), SiC particulate-reinforced metal-matrix composite (MMC) [*5,10,42*], and (4) P/M, submicron grain size (SM/GS) [*1–3*]. Alloy designation, product form, and nominal composition are listed in Table 1. The I/M alloys, MMC matrix, and SF alloy are precipitation hardened, and the tempers are indicated. AA2134 was characterized in both the underaged (UA) and overaged (OA) conditions [*41*]. The SM/GS

TABLE 1—*Aluminum alloys studied.*

Alloy Designation	Alloy System[a]	Product Form	Nominal Alloy Composition, weight %
AA2095-T8	I/M	Plate	Al-4.6Cu-1.5Li-0.4Ag-0.4Mg-0.15Zr
AA2195-T8	I/M	Plate	Al-4.0Cu-1.0Li-0.4Ag-0.4Mg-0.15Zr
AA2618-T851	I/M	Plate	Al-2.6Cu-1.6Mg-1.0Fe-1.2Ni-0.2Si
AA2519-T87(+Mg+Ag)	I/M	Sheet	Al-5.8Cu-0.5Mg-0.5Ag-0.3Mn-0.15Zr-0.1V
AA2134-type (+Mn)	I/M	Plate	Al-4.0Cu-1.5Mg-0.15Zr (0, 0.3, 0.6, 1.0 Mn)
N203-T6	SF	Extrusion	Al-5.0Cu-0.5Mg-0.5Mn-0.4Zr-0.4Ag-0.2Ti-0.2V
CM Al	SM/GS	Extrusion	Al + 2.5 vol% Al_2O_3
AA8009	SM/GS	Extrusion	Al-8.5Fe-1.3V-1.7Si
2009/SiC/20p-T6	PM/MMC	Plate	Al-3.6Cu-1.3Mg + 19.5 vol% SiC

[a] I/M = ingot metallurgy, SF = spray formed; SM/GS = submicron grain size; PM/MMC = powder metallurgy, metal-matrix composite.

alloys were processed by two different P/M techniques: cryogenic milling (CM Al) or rapid solidification by melt spinning (AA8009), followed by powder compaction, hot extrusion, and rolling [*2*,*3*]. Thicknesses of sheet, plate, and extrusion range from 3.2 to 25.4 mm. Processing and microstructural details for each alloy are reported elsewhere [*1–5*,*43*,*44*].

Fracture Toughness

Longitudinal-transverse-oriented (LT) compact-tension (CT) specimens were precracked by fatigue to crack length-to-width ratios (a/W) between 0.5 and 0.6. The CT thickness was 3.2 mm for AA2519+Mg+Ag and N203, 3.9 mm for AA2095 and AA2195, 6.3 mm for CM Al and AA2009/SiC/20p, and 7.6 mm for AA2618 and AA8009. The 6.3 and 7.6-mm-thick specimens were sidegrooved by 20% of the gross thickness. Fracture-toughness temperatures ranged from -185 to 325°C, depending on the alloy system. Specimens were tested at a constant actuator displacement rate of between 0.26 and 2.5 μm/s.

The J versus Δa behavior for AA2618, AA2519+Mg+Ag, N203, CM Al, AA8009, and AA2009/SiC/20p was characterized using the ASTM Test Method for Determining J-R Curves (E 1152) and the DCPD technique without partial unloading [*1*,*6–8*]. The first deviation from the baseline trend of the DCPD versus load-line displacement data was associated with initial crack extension. Values of K_{JICi} were calculated at this point from the applied J using Eq 6. J-dominance and plane strain prevailed for each alloy at initial crack extension according to ASTM E 1152 [*40*]. Details of these experiments are reported elsewhere [*1–6*,*8*].

The J versus Δa curves for AA2095 and AA2195 were measured using ASTM E 1152 and unloading-compliance-based crack-length measurements. The 0.2-mm offset-blunting-line construction from ASTM Test Method for J_{IC}, A Measure of Fracture Toughness (E 813) defined the applied J associated with initial crack extension. Significant crack extension accompanies the blunting-line definition of initiation fracture toughness (K_{JIC}), leading to an overestimate compared to K_{JICi} values from the DCPD method [*5*,*8*]. The provisional initiation fracture toughness (K_Q) from ASTM Test Method for Plane-Strain Fracture Toughness of Metallic Materials (E 399) was reported for AA2134 [*41*]. Initiation toughness from K_Q reflects stable crack growth and overestimates K_{JICi}.

TABLE 2—*Temperature-dependent tensile properties for aluminum alloys.*

Alloy Designation	Temperature Range, °C	σ_{ys}, MPa	E, GPa	n	%RA
AA2095-T8 [*46*]	−140/135	621/524	79.3/69.0^a	0.059/0.005	11/22
AA2195-T8 [*46*]	−185/135	693/538	80.3/69.0^a	0.066/0.005	15/44
AA2618-T851 [*45*]	25/225	450/365	75.3/60.0	0.05/0.005	23/35
AA2519-T87(Mg+Ag) [*4*]	25/175	504/404	72.4/63.7^b	0.045/0.013	40/57
N203-T6	25/190	447/342	72.1/66.0	0.085/0.028	28/61
CM Al [*3*]	25/325	265/150	72.0/58.0^b	...	38/13
AA8009 [*2*]	25/316	395/270	83.4/61.5	0.077/0.040	51/39
2009/SiC/20p-T6 [*10*]	25/316	410/90	108/60^b	0.125/0.042	2.6/23

[a] Based on precision modulus measurements at 25°C and −185°C.

[b] Based on temperature-dependent E for pure aluminum [*47*].

Deformation Properties

Based on uniaxial tensile tests, the 0.2% offset yield strength (σ_{ys}), elastic modulus (E), work-hardening exponent (n), and percent reduction of area (%RA) were reported for each alloy as a function of temperature [*1–4,10,41,45,46*]. Table 2 summarizes results corresponding to the lowest and highest test temperatures for each alloy. Values of σ_{ys}, E, and n decrease monotonically for each alloy as temperature increases. Values of %RA show two temperature dependencies: increasing %RA as temperature increases for the I/M, SF, and MMC systems [*4,10,45,46*] and decreasing %RA as temperature increases for SM/GS alloys [*2,3,45*].

Void-Nucleating Particle Spacings

The size and spacing of primary void-nucleating particles were evaluated. Measured volume-fraction (f_v) and average radius ($\bar{r}$) data for void-nucleating particles in AA2618, AA2134, and AA2009/SiC/20p were taken from the original studies [*1,6,41*]. For AA2095, AA2195, AA2519, and N203, measurements of $\bar{r}$ and f_v were averaged over longitudinal, transverse, and through-thickness metallographic sections. With the exception of AA2195, particles smaller than 2 μm in diameter were assumed to not participate in primary void nucleation and were ignored. In AA2195, constituent particles were small, and the lower-bound diameter was 0.5 μm.

Three measures of interparticle spacing were obtained for each alloy. The mean free path (λ), which is independent of particle shape and distribution, is equal to $(4/3)\bar{r}(1 - f_v)/f_v$ [*48*]. The center-to-center nearest-neighbor spacings of a random distribution of spherical particles on a plane (Δ_2) and in a volume (Δ_3) are given by [*48*]:

$$\Delta_2 = \bar{r}\left(\frac{\pi}{6f_v}\right)^{\frac{1}{2}} \tag{8}$$

$$\Delta_3 = 1.18\bar{r}\left(\frac{\pi}{6f_v}\right)^{\frac{1}{3}} \tag{9}$$

TABLE 3—*Characteristics of primary void-nucleating particles.*

Alloy Designation	Primary Void Nucleating Particles[a]	f_v	$\bar{r}$, μm	λ, μm	Δ_2, μm	Δ_3, μm
AA2095-T8 [*43*]	T_1, Al_7Cu_2Fe	0.037	3.80	132	14.3	10.8
AA2195-T8 [*43*]	C	0.0066	1.39	279	12.4	7.0
AA2618-T851 [*1*]	$FeNiAl_9$	0.08	3.75	58	9.6	8.3
AA2519-T87(Mg+Ag) [*4*]	Θ, C	0.012	2.85	313	18.8	11.9
N203-T6	...	0.022	2.44	145	11.9	8.3
AA2134(+0.00 wt%Mn)	S, C′	0.0175	2.55	190	13.9	9.3
AA2134(+0.31 wt%Mn)	S, C′	0.0196	2.65	180	13.7	9.3
AA2134(+0.61 wt%Mn)	S, C′	0.0220	2.50	150	12.2	8.5
AA2134(+1.02 wt%Mn)	S, C′	0.0407	2.90	91	10.4	8.0
2009/SiC/20p-T6 [*6*]	SiC	0.195	1.5	8.3	2.5	2.5

[a] where T_1 = primary Al_2CuLi.
Θ = Primary Al_2Cu.
C = Impurity (Fe,Si) constituents.
S = Primary Al_2CuMg [*41*].
C' = Mn-bearing constituents [*41*] ($Al_{20}Cu_2Mn_3$, $Al_{20}Cu_2(Mn,Fe)_3$.

The area fraction measured by image analysis is assumed to equal f_v. For AA2134, the average constituent-particle radius for the four different Mn contents was calculated from published values of f_v and λ [*41*]. The results of the particle-spacing analysis are summarized in Table 3. The types and compositions of constituent particles are listed for each alloy and discussed elsewhere [*1,4,6,41,43*].

Stress-State-Governed Intrinsic Fracture Resistance

In order to determine the failure locus, $\bar{\varepsilon}^{p}_{f}$ was measured or estimated for a wide range of σ_m/σ_{fl}. Failure in this context is defined as the measured strain at the "critical void damage event" characteristic of the coalescence of void damage at a notch root or crack tip [*18,49*].

$\bar{\varepsilon}^{p}_{f}$ was calculated from fractured tensile bars using the following expression [*18,50–52*]:

$$\bar{\varepsilon}^{p}_{f} = 2\ln\left(\frac{d_o}{d_f}\right) = -\ln\left(1 - \frac{\%RA}{100}\right) \tag{10}$$

The initial and final diameters at the minimum cross section, d_o and d_f, respectively, are measured for each smooth or notched round tensile specimen [*18,27*]. Measured %RA at fracture was used in Eq 10, resulting in overestimated $\bar{\varepsilon}^{p}_{f}$ compared to the strain at the critical damage event. Experimental and computational studies suggest that this error is small because reduction of the minimum cross-sectional area is limited after the critical damage event [*18,49*].

Stress-state triaxiality is governed by the ratio of the notch-root diameter (d) to the profile radius of the notch (R) [*18,27,51,52*]:

$$\left(\frac{\sigma_m}{\sigma_{fl}}\right) = \frac{1}{3} + \ln\left(\frac{d}{4R} + 1\right) \tag{11}$$

The initial profile radius and d_o were used to estimate σ_m/σ_{fl}.

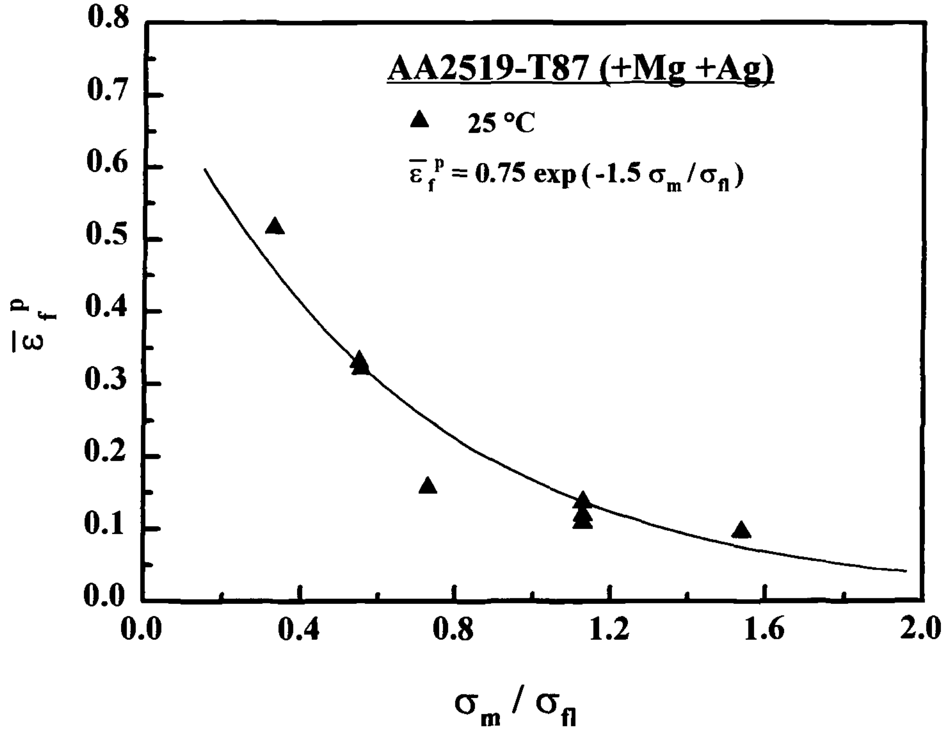

FIG. 2—*Stress-state-dependent failure strain for AA2519+T87(+Mg+Ag) at 25°C [4]. A theoretical prediction from integration of Rice and Tracey's void growth law is indicated by the solid line [*16,17*].*

The dependence of $\bar{\varepsilon}_f^p$ on σ_m/σ_{fl} varies significantly for different aluminum alloys. Figure 2 shows a failure locus for AA2519+Mg+Ag measured at 25°C compared to a model prediction based on Eq 1. Least squares curve fitting was employed to determine an α of 0.75, and the Rice-Tracey (R-T) dependence was observed ($\beta = 1.5$) [*16,17*]. Figure 3 displays failure loci for AA2134 and AA2009/SiC/20*p*. In overaged AA2134 (0.6% Mn), $\bar{\varepsilon}_f^p$ also follows a R-T dependence, while $\bar{\varepsilon}_f^p$ in underaged AA2134 is less sensitive to σ_m/σ_{fl} ($\beta = 0.70$) [*41*]. Values of $\bar{\varepsilon}_f^p$ for AA2009/SiC/20*p* are insensitive to global σ_m/σ_{fl} at 25°C (i.e., $\beta = 0$) because local constraint on matrix plastic flow dominates $\bar{\varepsilon}_f^p$ [*42*]. These loci demonstrate that β varies from 0 to 1.5 depending on alloy microstructure and the mechanisms of void nucleation through coalescence.

Measured failure loci do not exist for all the alloys or all the temperatures of interest; it is necessary to employ simplifying assumptions to facilitate modeling of K_{JICi}. For alloys where a failure locus was measured for only one temperature, α and β were determined from least squares regression based on Eq 1 and β was assumed to be temperature invariant. The available %RA data at other temperatures were employed to calculate an α value for each temperature. Figures 4 and 5 display smooth and notched $\bar{\varepsilon}_f^p$ versus temperature for AA2519+Mg+Ag and AA2009/SiC/20p, respectively, and list calculated α and β values. $\bar{\varepsilon}_f^p$ is equally sensitive to σ_m/σ_{fl} at all temperatures for AA2519+Mg+Ag, as evidenced by a constant ductility-constraint

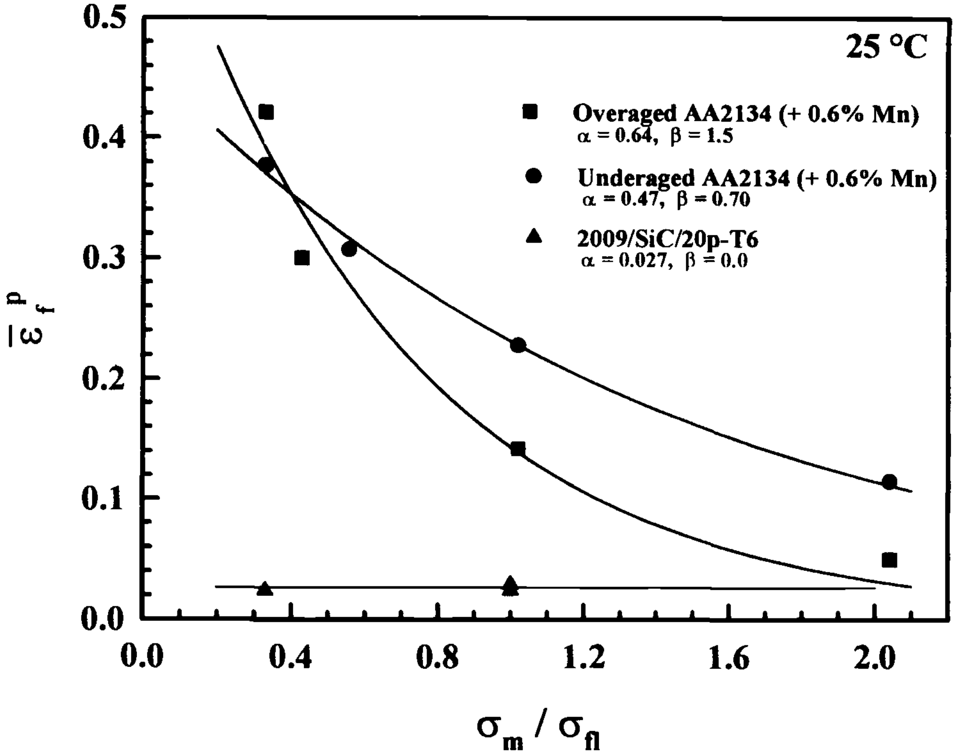

FIG. 3—*Ambient temperature, stress-state-dependent failure loci for AA2009/SiC/20p-T6 [42] and AA2134 in the underaged and overaged tempers [41].*

ratio, r_{sn}. (r_{sn} is defined as the ratio of smooth to notched $\bar{\varepsilon}_f^p$ and is measured from the least squares regression of the two temperature dependencies.) For AA2009/SiC/20p, $\bar{\varepsilon}_f^p$ is insensitive to global σ_m/σ_{fl} to 175°C and β equals zero (Fig. 5). Between 175 and 316°C, β increases from 0 to 1.5 as local constraint on matrix plastic flow is relaxed.

In alloy systems where notched tensile ductility is not available, an R-T exponential dependence is assumed ($\beta = 1.5$). In most cases $\bar{\varepsilon}_f^p$ is measured from uniaxial tensile specimens ($\sigma_m/\sigma_{fl} = 0.33$) and α is calculated from Eq 1. Replicate $\bar{\varepsilon}_f^p$ measurements were averaged to determine one value of α for each test temperature.

Given measured or estimated $\bar{\varepsilon}_f^p(\sigma_m/\sigma_{fl})$ for each alloy and temperature (Eq 1) as well as Eqs 2 and 3, the model criterion is applied to determine $\bar{\varepsilon}_f^*$ (Fig. 1). Values of $\bar{\varepsilon}_f^*$ are plotted in Figs. 6 through 8 for the I/M and SM/GS aluminum alloys over the temperature ranges given in Table 2. Fracture strains for AA2519+Mg+Ag and N203 rise sharply as temperature increases and are significantly higher than the values for AA2618, which increase only modestly with increasing temperature (Fig. 6). Values of $\bar{\varepsilon}_f^*$ increase monotonically from cryogenic to elevated temperatures for AA2195 (Fig. 7). For AA2095, $\bar{\varepsilon}_f^*$ is insensitive to temperature between −140 and 25°C and increases between 25 and 135°C. Fracture strains decrease from 25 to 175°C for CM Al and AA8009 (Fig. 8), consistent with observations for other SM/GS aluminum alloys [*53,54*]. The intrinsic damage mechanisms controlling the temperature dependencies of $\bar{\varepsilon}_f^*$ for the various aluminum alloys are considered elsewhere [*2–4,42*].

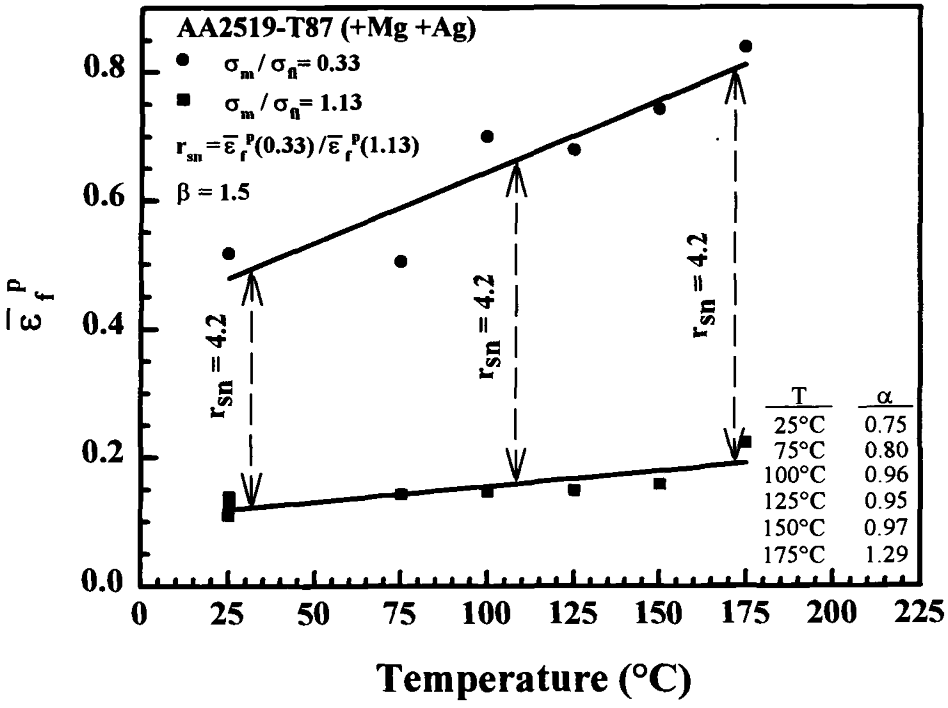

FIG. 4—*Effective plastic strain to failure of smooth and notched bars of AA2519+Mg+Ag, demonstrating the temperature independence of the constraint ratio,* r_{sn} *[4].*

Micromechanical Modeling Results

With the parameters σ_{ys}, E, $\bar{\varepsilon}_f^*$, and d_n determined as a function of temperature, K_{JICi} is predicted from Eqs 4 through 6. A single adjustable parameter, l^*, is calculated by equating measured and predicted K_{JICi} at 25°C. This constant is assumed to be temperature independent.

Temperature Dependencies

AA2519-T87 (+Mg+Ag)—The temperature dependence of K_{JICi} for AA2519+Mg+Ag is predicted successfully, as shown in Fig. 9, based on $\bar{\varepsilon}_f^p$ measured over a range of σ_m/σ_{fl} (Figs. 2 and 4) [*4*]. Variability in the measured tensile properties (e.g., %RA) leads to variability in predicted K_{JICi}. A linear-regression fit to the K_{JICi} measurements agrees reasonably with the fit to predictions, as shown in Table 4. A 95% confidence interval estimate of the slope (m) using the student t-distribution indicates that there is no significant difference between m for the measurements ($-0.044 < m < 0.0$) and predictions ($-0.028 < m < 0.0$). An l^* value of 23.7 μm was calculated from average measured K_{JICi} at 25°C and was used to predict K_{JICi} from 75 to 175°C. The calculated value of l^* correlates with the planar nearest-neighbor spacing of undissolved Al_2Cu and Fe-bearing constituent particles ($\Delta_2 = 18.8$ μm) and is twice the nearest-neighbor spacing in a volume ($\Delta_3 = 11.9$ μm).

AA2618-T851 and N203-T6—Agreement between model-predicted and measured temperature dependencies of K_{JICi} is fair for AA2618 and N203. Figure 10 shows modeling results

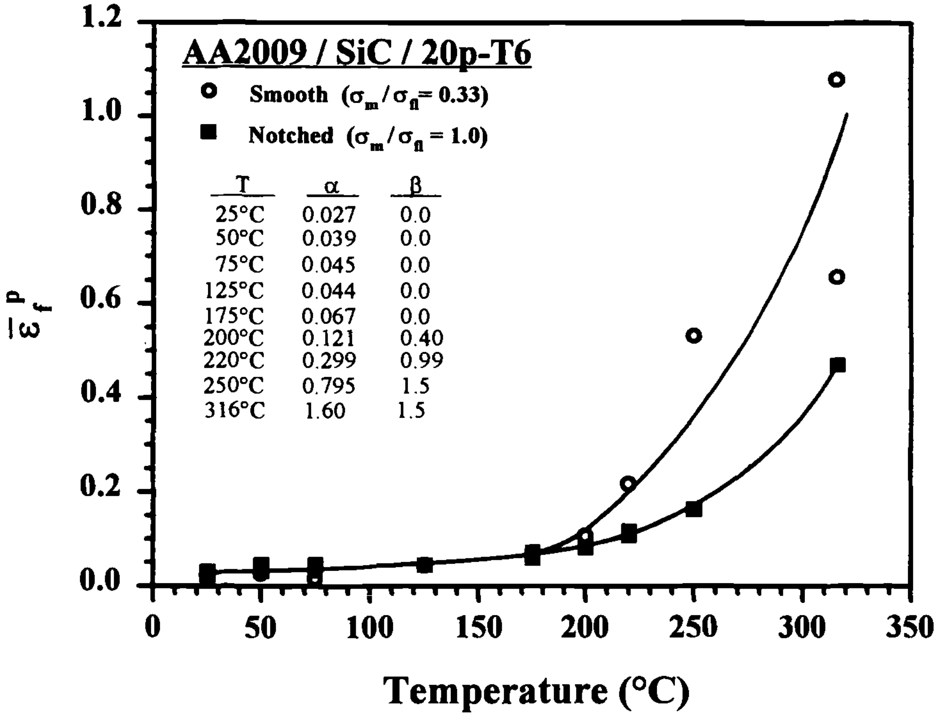

FIG. 5—*Effective plastic strain to failure of smooth and notched bars of AA2009/SiC/20p-T6 plotted as a function of temperature, demonstrating the insensitivity of* $\bar{\varepsilon}_f^p$ *to global stress-state triaxiality at temperatures up to 175°C [42].*

based on uniaxial tensile tests and an assumed β of 1.5. The model predicts that K_{JICi} increases as temperature increases for N203, but the slopes are not equal (Fig. 10 and Table 4). For AA2618, predicted K_{JICi} declines slightly from 25 to 175°C compared to a temperature-invariant-measured K_{JICi}. Measured K_{JICi} increases mildly between 175 and 225°C, while predicted K_{JICi} continues to decline. Calculated values of l^* are 11.9 μm for AA2618 and 17.9 μm for N203, equivalent to $1.4\Delta_3$ and $2.2\Delta_3$, respectively.

AA2095-T8 and AA2195-T8—Considering a wider temperature range including cryogenic levels, modeling using uniaxial-tensile properties predicts that K_{JIC} is nearly temperature insensitive for AA2095 ($m = -0.01$) and AA2195 ($m = -0.005$). The predicted trends agree with measured trends for both alloys, as shown in Fig. 11 and Table 4. Measured K_{JIC} for AA2195 is variable, resulting in uncertainty in the temperature dependence. This variability could be an artifact associated with the offset definition of initiation toughness coupled with the difficulty in measuring the steeply rising J versus Δa curve for small Δa [*8*]. Calculated values of l^* are 27.9 μm for AA2195 and 13.5 μm for AA2095, equivalent to $4.0\Delta_3$ and $1.25\Delta_3$, respectively.

AA2009/SiC/20p-T6—Prediction of K_{JICi} is challenging for the complex microstructure of the MMC, which contains a high-volume fraction of void-nucleating SiC particles distributed inhomogenously [*10*]. Due to the inherent variability in measured K_{JICi}, upper-bound and lower-bound l^* values were calculated at 25°C and used for toughness predictions from 50 to 316°C,

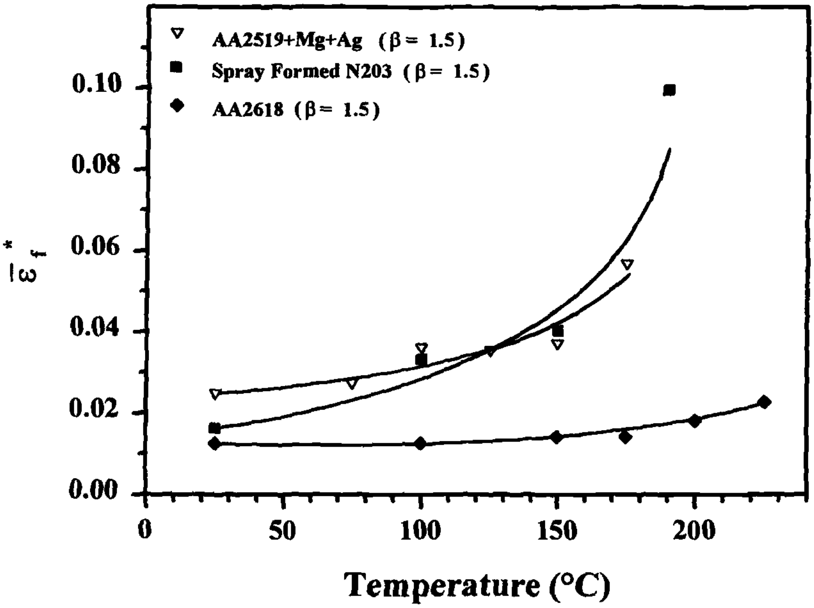

FIG. 6—*The critical fracture strain for spray-formed N203-T6, AA2618-T851 [1,45], and AA2519-T87(+Mg+Ag) [4] as a function of temperature.*

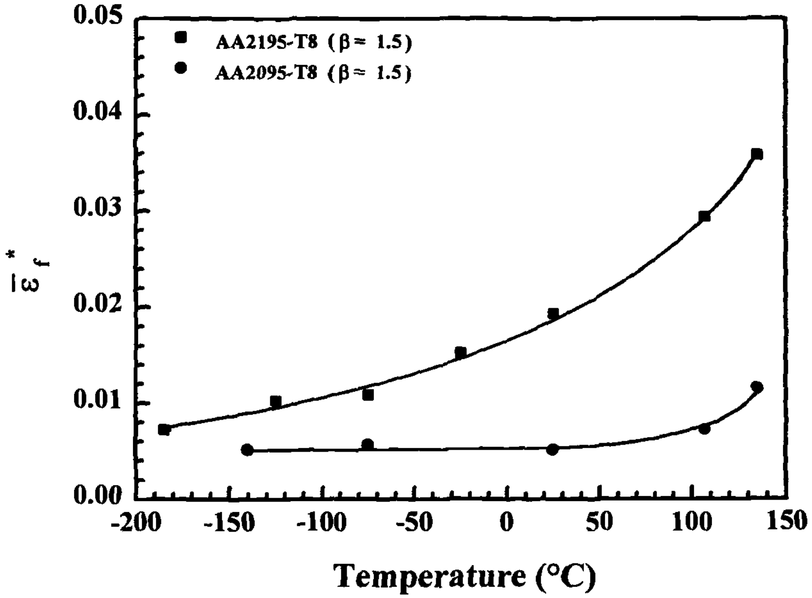

FIG. 7—*The critical fracture strain for AA2095-T8 and AA2196-T8 from cryogenic to slightly elevated temperatures [46].*

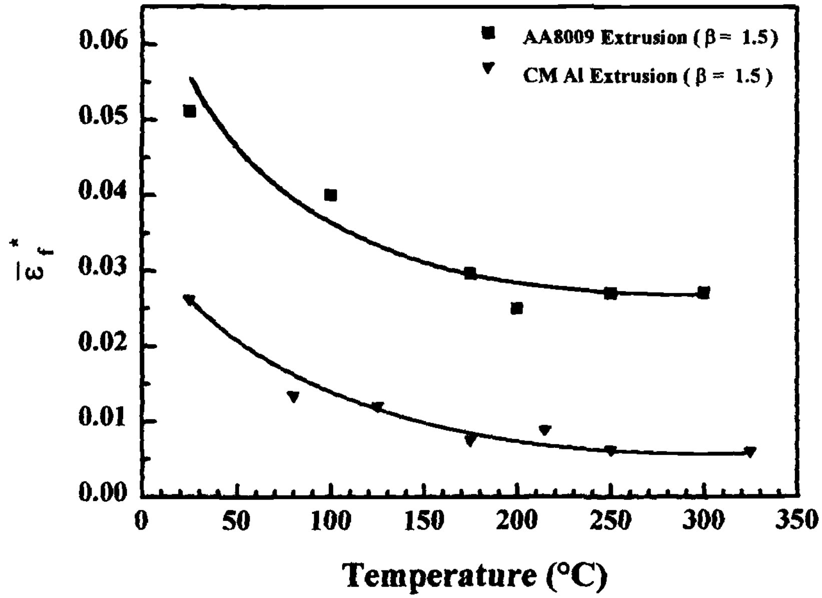

FIG. 8—*Critical fracture strain versus temperature for submicron-grain-size AA8009 [2] and cryogenically milled aluminum [3].*

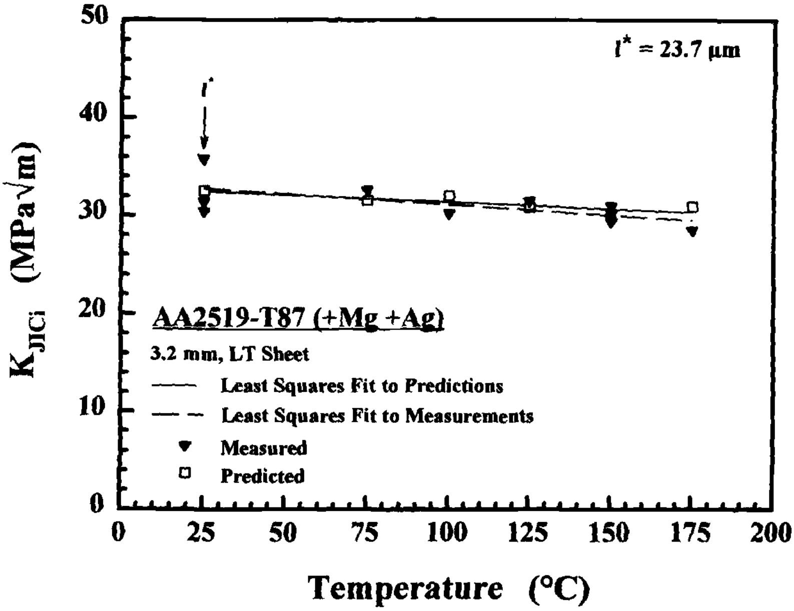

FIG. 9—*Critical-plastic-strain-controlled model predictions and experimentally measured values of the initiation toughness (K_{JICi}) as a function of temperature for AA2519-T87(+Mg+Ag) [4].*

TABLE 4—*Linear regression fits to predicted and measured* K_{JICi} *versus temperature.*

Alloy Designation	Temperature Range, °C	Predicted Fit, K_{JICi} =	Measured Fit, K_{JICi} =
AA2095-T8	−185/135	21.9MPa$\sqrt{m}$ − 0.010*T^a	21.4 MPa$\sqrt{m}$ + 0.005*T
AA2195-T8	−185/135	36.9 MPa$\sqrt{m}$ − 0.005*T	38.5 MPa$\sqrt{m}$ − 0.007*T
AA2618-T851	25/175	20.5 MPa$\sqrt{m}$ − 0.016*T	20.4 MPa$\sqrt{m}$ − 0.004*T
AA2519-T87(+Mg+Ag)	25/175	32.8 MPa$\sqrt{m}$ − 0.014*T	33.3 MPa$\sqrt{m}$ − 0.022*T
N203-T6	25/190	26.0 MPa$\sqrt{m}$ + 0.014*T	25.4 MPa$\sqrt{m}$ + 0.038*T
CM Al	25/125	14.1 MPa$\sqrt{m}$ − 0.026*T	15.0 MPa$\sqrt{m}$ − 0.040*T
CM Al	175/325	13.1 MPa$\sqrt{m}$ − 0.017*T	9.6 MPa$\sqrt{m}$ − 0.015*T
AA8009	25/100	34.1 MPa$\sqrt{m}$ − 0.053*T	34.5 MPa$\sqrt{m}$ − 0.068*T
AA8009	175/316	28.5 MPa$\sqrt{m}$ − 0.028*T	22.5 MPa$\sqrt{m}$ − 0.037*T

[a] T is temperature in degrees Celsius.

as plotted in Fig. 12 [*10*]. Two symbols are used for measured K_{JICi}: error bars represent the standard deviation among replicate results, and solid squares show single measurements. While upper-bound predictions exceed measured K_{JICi} to 200°C, the lower-bound predictions agree with measured values. The agreement is worse above 200°C, but the decline in K_{JICi} is predicted. Upper- and lower-bound l^* values of 2.9 and 5.2 μm equal 1.2 and 2.1 times the nearest-neighbor SiC particle spacing. The unique issues associated with modeling K_{JICi} of an MMC are considered elsewhere [*10*].

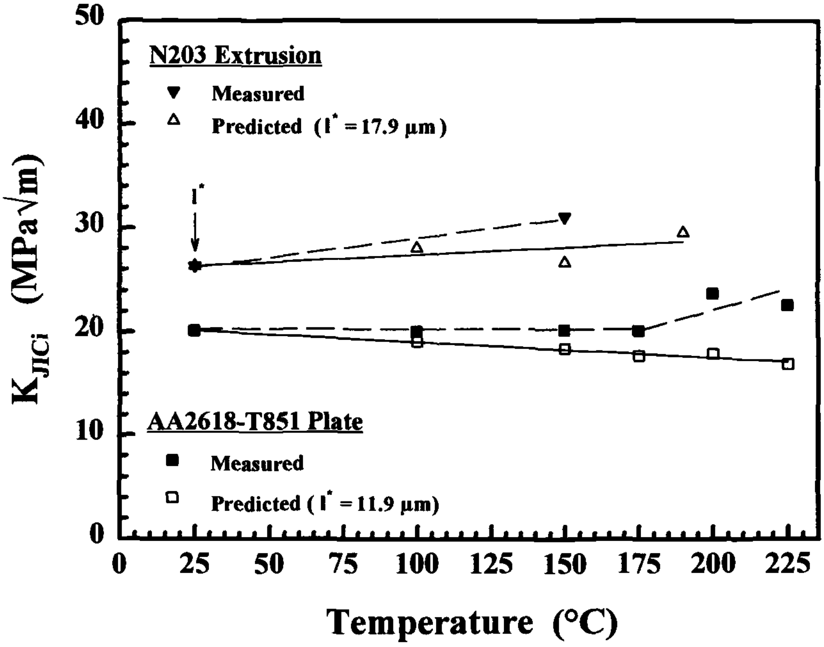

FIG. 10—*Critical-plastic-strain-controlled model predictions and experimentally measured values of* K_{JICi} *as a function of temperature for AA2618-T851 and spray-formed N203-T6.*

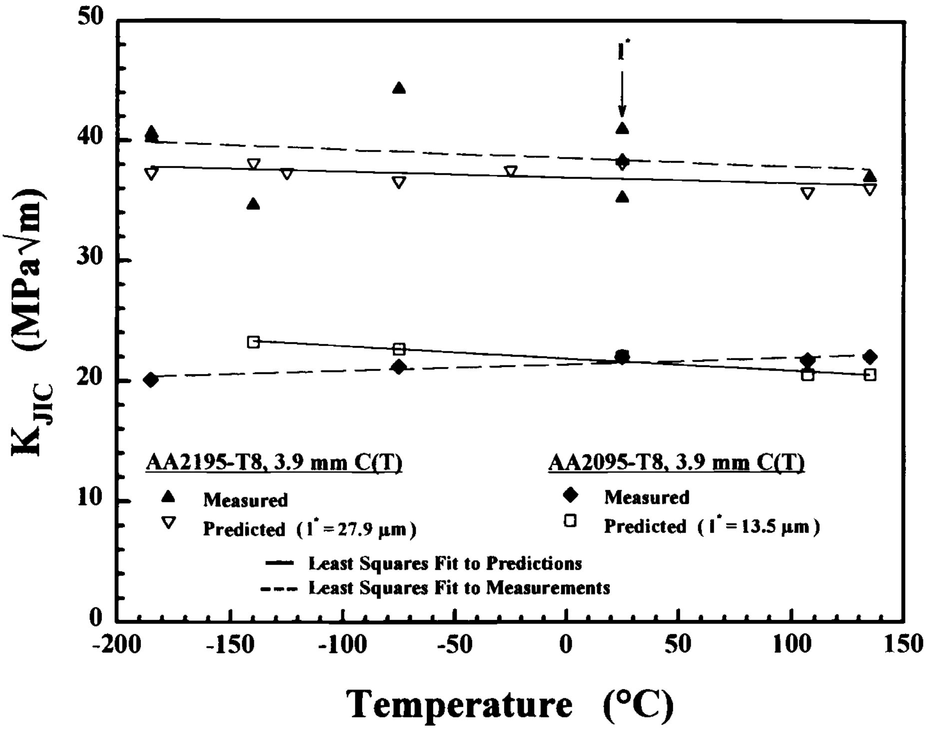

FIG. 11—*Critical-plastic-strain-controlled model predictions and experimentally measured values of* K_{JICi} *as a function of temperature for AA2095-T8 and AA2195-T8.*

Submicron-Grain-Size Alloys—Submicron-grain-size alloys suffer losses in σ_{ys}, E, n, and $\bar{\varepsilon}_f^*$ as temperature increases, as demonstrated by uniaxial-tensile results (Table 2 and Fig. 8) [*2*,*3*]. Because each of these material properties decreases as temperature increases, K_{JICi} is predicted to decrease, as illustrated in Fig. 13 [*2*,*3*]. The temperature dependencies of predicted K_{JICi} for CM Al over two temperature ranges agree reasonably with the measured trends, as presented in Table 4. The model also predicts the temperature dependence of measured K_{JICi} over similar temperature ranges for AA8009 (Fig. 13 and Table 4). At 25°C, l^* is calculated as 8.3 μm for CM Al and 18.3 μm for AA8009. The magnitude of K_{JICi} is overpredicted at 175°C and above for both alloys.

Microstructural Influences on Initiation Toughness

Literature data on UA and OA AA2134-type alloys establish the dependence of toughness on Mn content and aging condition [*41*]. Measured values of K_Q are plotted for both aging conditions as a function of Mn content in Fig. 14; such value exceed K_{IC} because the thickness criterion in ASTM E 399 was not satisfied. K_Q increases mildly as Mn is added to 0.6 wt%, then decreases sharply between 0.6 and 1.0% [*41*]. The initial rise in K_Q was attributed to the formation of submicron Mn-rich dispersoids that homogenized slip, while K_Q declined as excess Mn formed large constituents [*41*]. This trend was observed in both the UA and OA conditions, with a lower measured K_Q in the overaged condition.

Predicted K_Q from measured uniaxial and notched tensile properties for the UA and OA tempers is plotted in Fig. 14. The model predicts the toughness maximum and subsequent

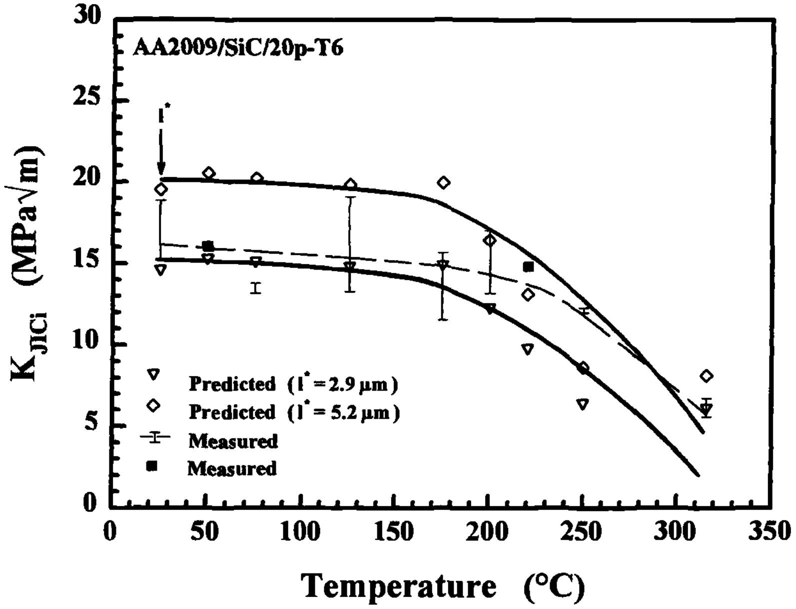

FIG. 12—*Critical-plastic-strain-controlled model predictions and experimentally measured values of* K_{JICi} *as a function of temperature for AA2009/SiC/20p-T6 [10].*

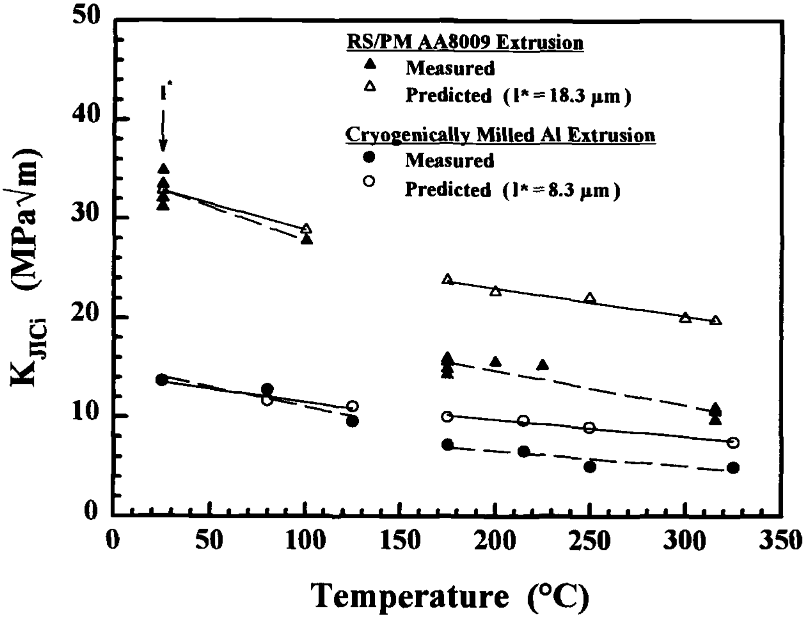

FIG. 13—*Critical-plastic-strain-controlled model predictions and experimentally measured values of* K_{JICi} *as a function of temperature for AA8009 [2] and CM Al [3].*

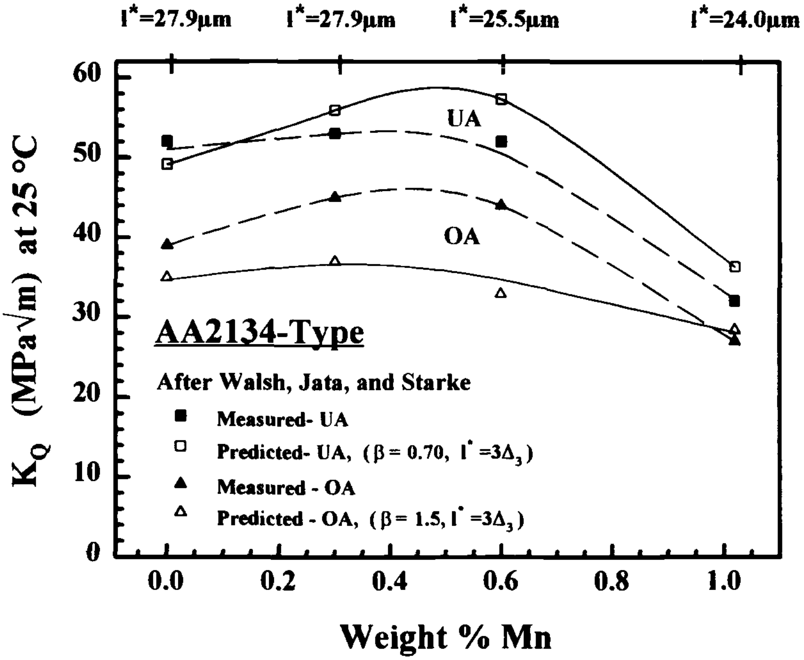

FIG. 14—*Critical-plastic-strain-controlled model predictions and experimentally measured values of* K_Q *as a function of Mn content for underaged and overaged AA2134 [41].*

decline in K_Q as Mn content is increased, as well as the lower toughness in the OA temper. Agreement between predicted and measured K_Q temperature dependencies is good for UA AA2134 and fair for OA 2134. Values of l^* were not calculated by equating measured and predicted K_Q at one Mn content; rather, such values were assumed to be a constant multiple of Δ_3, with the best agreement obtained at $l^* = 3\Delta_3$. The l^* corresponding to each Mn content is listed on the top abscissa in Fig. 14 and is identical for the UA and OA tempers because constituent size and distribution are not affected by aging. At the two lower Mn contents, voids nucleated at undissolved Al_2CuMg particles. For 0.6% and 1.0% Mn, the volume fraction of Mn-containing constituents increased; voids nucleated at these particles, and Δ_3 decreased [*41*].

Discussion

Temperature Dependence of K_{JICi}

The strain-controlled model quantifies the temperature-dependent interplay between alloy fracture resistance and crack-tip strain driving force, which governs initiation fracture toughness. δ_{IC} represents temperature-dependent alloy fracture resistance, while the temperature dependence of the driving force is represented by $\sigma_{ys}E/[d_n(1 - \nu^2)]$ or ψ. The temperature dependence of δ_{IC} is governed by $\bar{\varepsilon}_f^p(\sigma_m/\sigma_{fl})$, since l^* is assumed to be temperature invariant. The parameter ψ represents the temperature dependence of crack-tip strain through conversion of δ_{IC} to K_{JICi} (Eqs 5 and 6). As temperature increases, ψ and K decline for a fixed δ_{IC}. Physically, σ_{ys} and E decrease, d_n increases, and $\bar{\varepsilon}^p$ is increased for a fixed x and applied K. The dependence of crack-tip $\bar{\varepsilon}^p$ on K, σ_{ys}, E, and d_n is derived by substituting Eqs 5 and 6 into Eq 2 and is represented by the top abscissa in Fig. 1.

Temperature-insensitive K_{JICi} arises when δ_{IC} and ψ counterbalance. For AA2519+Mg+Ag, predicted δ_{IC} increases by 38%, from 13.7 μm at 25°C to 18.9 μm at 175°C. Over the same temperature range, σ_{ys} and E decrease by 20 and 12%, respectively (Table 2), while d_n increases by 8%. The parameter ψ decreases by 35%, from 7.7 × 10^7 MPa^2 at 25°C to 5.1 × 10^7 MPa^2 at 175°C. Values of K_{JICi}, expressed as $(\delta_{IC} \times \psi)^{1/2}$, are approximately equal at 25 and 175°C; the ratio of predicted K_{JICi} from uniaxial-tensile data at 25°C to that at 175°C is 1.05. The increased intrinsic fracture resistance at 175°C is effectively offset by the enhanced crack-tip strain field at a given K. A similar competition between the temperature dependencies of δ_{IC} and ψ results in approximately temperature-insensitive K_{JICi} for AA2618, AA2095, and AA2195 (Figs. 10 and 11).

Values of K_{JICi} decrease above 200°C for AA2009/SiC/20p despite the dramatically increasing intrinsic fracture resistance (Fig. 5), which demonstrates the strong influence of temperature-dependent crack-tip $\bar{\varepsilon}^p$ on K_{JICi}. Higher $\bar{\varepsilon}^p_f$ above 200°C is offset by an increased sensitivity to σ_m/σ_{fl}, and sharply decreasing σ_{ys}, E, and n dominate the temperature dependence of K_{JICi}. Interplay between δ_{IC} and ψ also governs the elevated-temperature degradation of K_{JICi} for SM/GS aluminum alloys. Because of uniquely decreasing $\bar{\varepsilon}^p_f$ as temperature increases (Fig. 8), δ_{IC} and ψ cooperatively degrade K_{JICi}.

The interplay between δ_{IC} and ψ is a necessary component for modeling temperature-dependent K_{JICi}. Micromechanical models that consider only the temperature-dependent plastic-strain field [*12,13*] predict declining fracture toughness with increasing temperature for precipitation-hardened AA2519+Mg+Ag, AA2618, AA2095, AA2195, and N203, counter to the mildly rising, mildly declining, or temperature-insensitive K_{JICi} measured for these alloys. For the SM/GS alloys, AA8009 and CM Al, only a mild decline in K_{JICi} would be predicted. For AA2009/SiC/20p, the measured temperature dependence of K_{JICi} is predicted solely from declining σ_{ys}, E, and n due to the dominance of $\bar{\varepsilon}^p$ [*10*], but this agreement is fortuitous.

Microstructural Influences on K_{JICi}

The effect of microstructure on initiation toughness is understood from the strain-controlled model via the interplay between the deformation-property-dependent crack-tip strain-field term, ψ, and the intrinsic crack initiation resistance term, δ_{IC}. For AA2134, changes in ψ with the addition of manganese are small in both the underaged and overaged tempers [*41*]. Effects of Mn on K_Q reflect trends in δ_{IC} and hence $\bar{\varepsilon}^p_f(\sigma_m/\sigma_{fl})$ and l^*.

Lower toughness is measured and predicted for the OA temper despite higher uniaxial-tensile $\bar{\varepsilon}^p_f$ compared to the UA temper because $\bar{\varepsilon}^p_f$ is less sensitive to stress triaxiality in the UA condition (Fig. 3). This complexity illustrates the danger in predicting initiation toughness solely from uniaxial-tensile data. Microstructural changes may alter $\bar{\varepsilon}^p_f(\sigma_m/\sigma_{fl})$, and β does not necessarily equal 1.5.

Uncertainties in $\bar{\varepsilon}^p_f(\sigma_m/\sigma_{fl})$

Strain-based micromechanical modeling of initiation fracture toughness yields reasonable values of l^*, as well as accurate temperature dependencies of K_{JICi}. Absolute values of K_{JICi} are not predicted due to uncertainties in $\bar{\varepsilon}^p_f(\sigma_m/\sigma_{fl})$ and l^*. Four uncertainties in $\bar{\varepsilon}^p_f(\sigma_m/\sigma_{fl})$ are discussed.

Damage Correlation—Initiation-toughness models predict the K level for coalescence of process-zone void damage with the crack tip. Standard measures of initiation toughness are not modeled accurately if the measurement reflects stable crack extension [*5,8,10*]. Rather, model predictions are best compared to a high-resolution indication of the K level for initial crack extension. Initiation toughness determined from DCPD measurements, K_{JICi}, is well suited for this purpose. In contrast, K_Q and K_{IC} (from ASTM E 399) or K_{JIC} (from ASTM E 813) reflect some stable crack growth and overestimate initiation toughness, especially for alloys with large tearing resistance or thin-sheet specimens [5,8]. The temperature dependencies of toughness are predicted from the model (Figs. 11 and 14), but l^* values may be overestimated.

The comparison between measured and modeled initiation toughness is an exercise in equating damage for different stress and strain fields, particularly those for a crack tip versus a blunt notch or smooth tensile specimen. The most relevant experiments are those that detect equivalent levels of microvoid damage at $\bar{\varepsilon}_f^p$ for smooth and notched tensile bars and at K_{JICi} for a precracked specimen. $\bar{\varepsilon}_f^p$ calculated in this study is based on %RA at fracture (Eq 10), which overestimates the strain at a damage level corresponding to K_{JICi}. A technique was developed to detect the formation of a central flaw within smooth and notched tensile specimens deformed at a constant strain-gage extensometer rate [18,27], but this procedure has not been correlated with microvoid damage in the crack-tip process zone at K_{JICi}.

Approximation of $\bar{\varepsilon}_f^p$—The use of Bridgman's [50] analysis to calculate $\bar{\varepsilon}_f^p$ (Eq 10) may overestimate the strain required to damage and fracture a notched tensile specimen [6,42,51]. Finite element modeling demonstrated that strains on the surface and in the center of a notched specimen are underestimated and overestimated, respectively, by Bridgman's equations [51]. The degree of error is insensitive to work hardening, but increases for larger strains and more severe notch acuity [51]. Since this error is independent of work hardening and, hence, temperature, it is accounted for by calculating l^* at 25°C and does not affect significantly the predicted values of K_{JICi} at elevated temperatures. If the $\bar{\varepsilon}_f^p$ values in Figs. 5 through 8 are corrected based on FEM results [51], then $\bar{\varepsilon}_f^*$ decreases significantly, calculated l^* is larger, and process zone damage at K_{JICi} is predicted over more average particle spacings.

Deformation History—As strain accumulates in smooth or notched tensile bars, the ratio of the notch root diameter to profile radius (d/R) continually changes, thus altering σ_m/σ_{fl} as given by Eq 11 [55]. The change in σ_m/σ_{fl} is small, so the error is accounted for by calculating l^* at 25°C and does not affect significantly the predicted trends of K_{JICi}. Another difficulty with deformation histories is that the mild change in σ_m/σ_{fl} for deforming smooth and notched tensile bars does not correspond to the rapid decline of σ_m/σ_{fl} as δ and $\bar{\varepsilon}^p$ increase at a given distance ahead of the crack tip (Fig. 1) [18]. This discrepancy is an inherent limitation of the critical-plastic-strain-controlled model.

Stress-Triaxiality Sensitivity—The sensitivity of $\bar{\varepsilon}_f^p$ to σ_m/σ_{fl} varies among engineering alloys. The *R-T* exponential dependence derived from void-growth modeling ($\beta = 1.5$) is commonly observed for alloys where void nucleation strains are small and MNG is characterized by uniform void growth [29,30,56]. The *R-T* dependence is observed for AA2519 (Fig. 2) and OA AA2134 (Fig. 3) and is assumed for AA2095, AA2195, AA2618, N203, AA8009, and CM Al. The *R-T* dependence is not always observed. For three low-alloy, quenched and tempered steels, $\bar{\varepsilon}_f^p$ is more sensitive to σ_m/σ_{fl} ($\beta > 1.5$) [27]. For UA AA2134 (Fig. 3) and AA2009/SiC/20p (Figs. 3 and 5), $\bar{\varepsilon}_f^p$ is less sensitive to σ_m/σ_{fl}.

The value of β for a given alloy depends on the stress-triaxiality sensitivity and strain accumulated in each MNG stage [57]. In commercial aluminum alloys, the true strain required to nucleate the majority of voids at large, brittle constituents is a small fraction of $\bar{\varepsilon}_f^p$ [58,59], and the *R-T* exponential dependence is a reasonable assumption. However, if the void nucleation stage contributes substantially to $\bar{\varepsilon}_f^p$, β will change. The void nucleation strain ($\bar{\varepsilon}_{nuc}^p$) can depend strongly on σ_m/σ_{fl} [60] or be insensitive to it [41], causing β to increase or decrease, respectively. For example, Walsh et al. sectioned deformed smooth and notched tensile specimens of OA AA2134 to show that the void nucleation rate ($dN_a/d\varepsilon$) is independent of σ_m/σ_{fl} [41]. For the failure locus, β equals 1.5 since voids nucleate at small strains.

Three other factors may affect β. First, a high-volume fraction of large brittle void-nucleating particles precludes global stress-triaxiality sensitivity because local constraint of matrix deformation promotes high levels of local σ_m/σ_{fl} [42]. Global constraint-insensitive $\bar{\varepsilon}_f^p$ is observed in AA2009/SiC from 25 to 175°C (Figs. 3 and 5). Second, slip localization can accelerate void growth and diminish the effect of hydrostatic stress. Walsh et al. reported that slip localization in UA AA2134 accelerates void growth and leads to void coalescence at a lower critical volume fraction of voids [*41*]; β for this alloy is less than 1.5 (Fig. 3). Third, mean stress can affect the critical condition for void coalescence [*27,28*], limiting the strain accumulated during primary void growth and altering β.

Because the stress-state-dependent failure locus varies significantly among alloys, rigorous fracture toughness modeling must include $\bar{\varepsilon}_f^p$ measurements over a wide range of global σ_m/σ_{fl}. Determining $\bar{\varepsilon}_f^p(\sigma_m/\sigma_{fl})$ from a single global-constraint level and Eq 1—as for AA2618, AA2095, AA2195, N203, and CM Al—is an oversimplification. There is no guarantee that β equals 1.5 or is invariant with increasing temperature.

Interpretation of Calculated l^*

The critical distance, the sole adjustable parameter in the strain-controlled model, is calculated by equating measured and predicted K_{JICi} at a single temperature and hence depends on accurate determination of measured initiation toughness and each model input. This parameter is affected mainly by uncertainties in $\bar{\varepsilon}_f^p(\sigma_m/\sigma_{fl})$; generally $\bar{\varepsilon}_f^p(\sigma_m/\sigma_{fl})$ is overestimated, causing l^* to be underestimated.

Ultimately, l^* must be determined by an independent means for absolute toughness prediction. This distance should relate to the primary void-nucleating particle spacing for alloys that fail by microvoid fracture and may represent the distance required for void coalescence at K equaling K_{JICi}. Calculated l^* for each Al alloy is given in Figs. 9 through 14, while primary void-nucleating particle spacings are given in Table 3. The nearest-neighbor spacing of primary void-nucleating particles, Δ_2 or Δ_3, governs void coalescence and should correlate with l^*.

Tensile and K_{IC} data for steels are sufficient to predict l^* from the model for comparison to Δ_3 [*61–64*][4] Smooth-tensile bar %RA was employed to estimate $\bar{\varepsilon}_f^p(\sigma_m/\sigma_{fl})$, with β assumed to equal 1.5. Figure 15 shows correlations between l^* and Δ_3 for steels (solid symbols) and six of the aluminum alloys included in this work (open symbols). The distance, l^*, was calculated at each temperature where K_{JICi} was both measured and predicted. Error bars indicate plus/minus one standard deviation of l^* for the aluminum alloys, including the effect of temperature on l^*. For each Al alloy except AA2195 and AA2009/SiC, voids nucleated at 2 to 20 μm diameter and widely spaced particles (Table 3). Voids nucleated at small (0.5 to 1.0 μm) and more closely spaced particles in AA2195 and at large (3 μm) and closely spaced particles in the MMC. For each steel but one, microvoid fracture was governed by small (0.2 to 0.4-μm diameter), closely spaced sulfides or carbides [*61–64*]. The exception is a low-alloy steel (plus Ni and Si) with larger 0.7-μm-diameter sulfide particles that served as more widely spaced void-nucleation sites [*62*].

Figure 15 suggests two trends between l^* and Δ_3: one for alloys where microvoid fracture is controlled by both widely spaced (large) particles and a second population of interdispersed submicron particles[5] (dashed line) and another for alloys where microvoid fracture is controlled by void damage associated with a single size distribution of relatively closely spaced particles (solid line). For the former case, l^* is proportional to $1.8\Delta_3$, while for the latter case, l^* is about five times Δ_3. One intercept is close to the expected value of zero, while the other is negative. These correlations remain reasonable at about $1.8\Delta_3$ and $3.8\Delta_3$ if forced through zero. Alternatively, l^* may not be a fixed multiple of Δ_3; the relationship may depend on microstructure and the details of MNG.

---

[4] The crack-tip strain and stress fields used in modeling (Eqs 2 and 3) are for a smoothly blunted crack tip, so only steels with a smoothly blunted crack tip were considered. Fields have been calculated for cracks that blunt to vertices [*36*].

[5] Voids nucleated from submicron particles soften the ligament between large microvoids growing from primary particles and promote the onset of strain-localized coalescence [*4*].

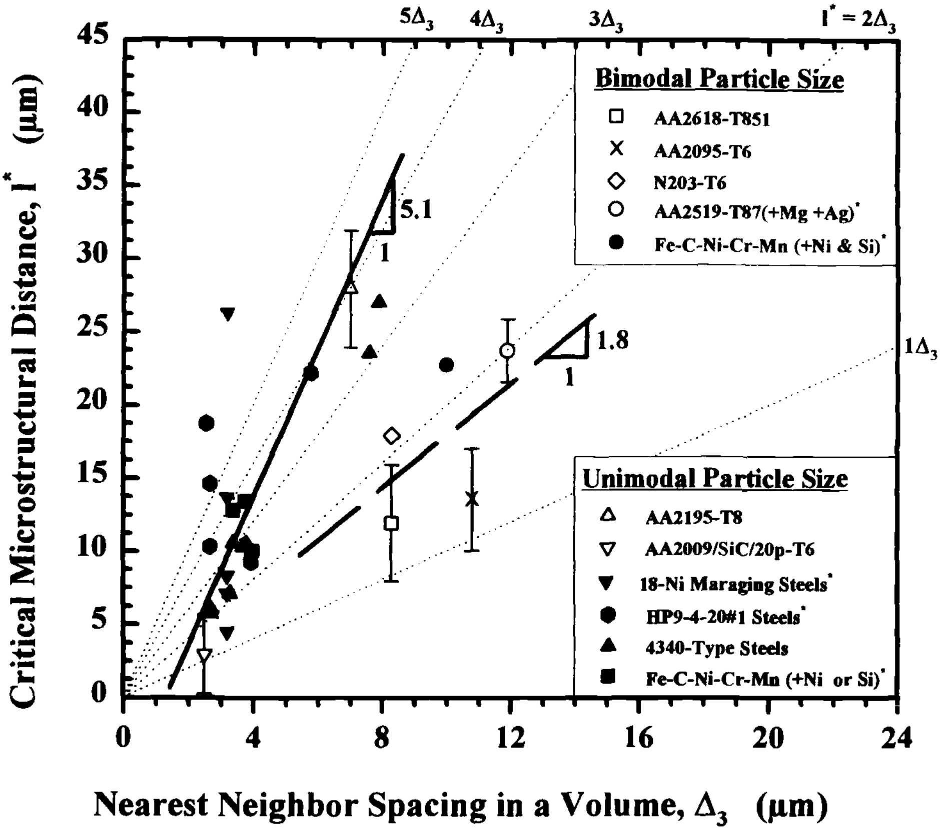

FIG. 15—*Correlations between nearest-neighbor particle spacing in an volume (Δ_3) and the calculated critical distance* (1*) *in steels [61–64] and aluminum alloys for single and bimodal distributions of void-nucleating particles.*

The data in Fig. 15 are analyzed further based on the extent of primary void growth prior to coalescence. Data legends with an asterisk represent alloys where primary void growth was quantified by the ratio of the final void radius (R_V) to the nucleating-particle radius (R_I). Values of R_V and R_I were measured from fracture-surface dimples in high-constraint regions, directly ahead of the specimen fatigue precrack [*61,62*]. Figure 16 displays a unique relationship between R_V/R_I and l^*/Δ_3. The function $l^*/\Delta_3 = 1.24 + 0.038(R_V/R_I)^2$ was obtained by least squares curve fitting, with a coefficient of determination (r^2) equal to 0.71. For no primary void growth ($R_V/R_I = 1$), voids coalesce spontaneously upon nucleation, and l^*/Δ_3 is expected to equal 1. The quadratic fit yields an l^*/Δ_3 value of 1.28 at R_V/R_I equal to 1.

The effect of primary void growth on l^*/Δ_3 in Fig. 16 is interpreted as follows. The critical distance for each alloy is a fixed multiple of Δ_3, with the multiple dependent on R_V/R_I. The parameter R_V/R_I is a direct measure of resistance to void coalescence. The steels in Fig. 16 exhibit higher R_V/R_I ratios relative to AA2519+Mg+Ag due to higher work hardening (which retards coalescence) and/or a unimodal particle distribution (which precludes strain softening between primary voids). For the high R_V/R_I case, primary void growth allows particles further from the crack tip to nucleate voids as K increases and the plastic strain distribution spreads.

More particles are involved in the critical coalescence event that constitutes K_{JICi}, and l^* is a larger multiple of Δ_3. For the low R_V/R_I case, the void-coalescence condition is satisfied before void damage accumulates over more than one or two particle spacings. The bimodal particle distribution favors this behavior because secondary void damage from small particles promotes void sheeting between primary voids [*4,14*]. The ratio, l^*/Δ_3, is relatively low due to this strain-localized coalescence.

The results in Fig. 16 suggest that l^* is temperature dependent because R_V/R_I changes with temperature. In I/M, spray-formed, and MMC alloys, l^* should increase mildly with temperature as R_V/R_I increases. For example, void sheeting is retarded in AA2519+Mg+Ag as temperature is increased from 25 to 150°C, and R_V/R_I increases from 3.2 to 3.8 [*4*]. Based on the correlation, l^*/Δ_3 should increase slightly from 1.6 to 1.8. A mildly increasing l^* would improve the predicted K_{JICi} temperature dependencies for N203, AA2618, AA2095, and AA2009/SiC, but would worsen agreement for AA2519+Mg+Ag and AA2195.

The rapid degradation in K_{JICi} with temperature for AA8009 and CM Al (Fig. 13), which is underpredicted by the model employing a constant l^*, is rationalized based on changing l^* due to a fracture mode change near 175°C. A change in deformation mode was postulated for AA8009, and a change in dimple morphology (from spherical and well developed at 25°C to shallow above 175°C) was observed [*1*]. A similar change in dimple morphology, from spherical at 25°C to faceted at 175°C, was observed in CM Al [*3*]. The change in dimple morphology

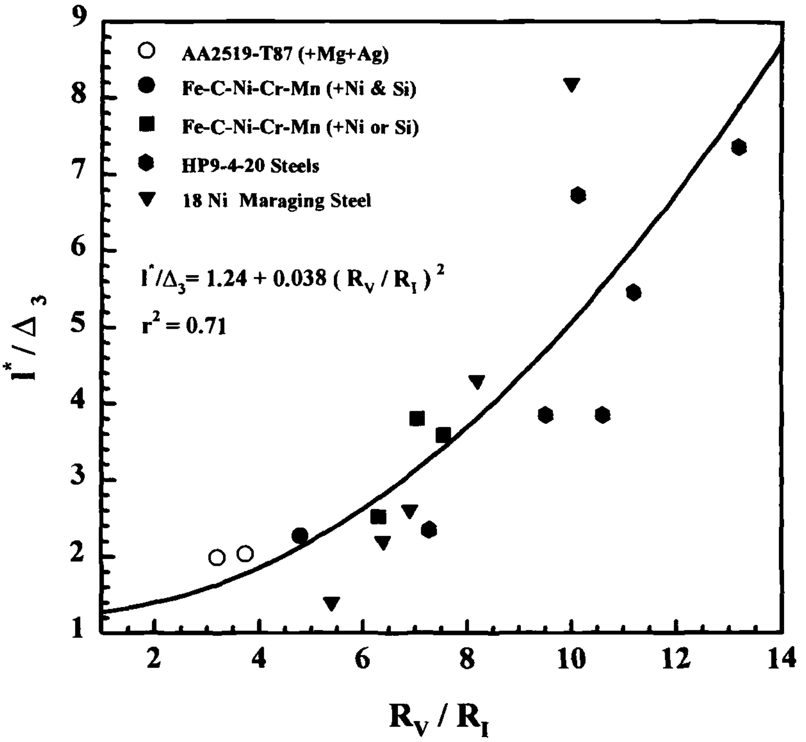

FIG. 16—*Relationship between the extent of primary void growth, quantified by the ratio of final void radius to initial void-nucleating particle radius, and* l* *normalized by particle spacing in a volume. Data are for steels [61,62,64] (solid symbols) and a single aluminum alloy (open symbol).*

is consistent with intravoid instability and strain-localized void coalescence in SM/GS alloys, where increased temperature reduces work hardening and causes strain softening between growing primary voids [3]. Strain-localized coalescence occurs at lower macroscopic $\bar{\varepsilon}^p_f$ and may occur over a smaller microstructural scale. If a second l^* (7.4 μm) is calculated for AA8009 from measured K_{JICi} at 175°C, predicted and measured values of K_{JICi} agree for temperatures from 200 to 316°C [2]. If a second l^* (4.2 μm) is calculated for CM Al at 175°C, predicted K_{JICi} agrees more closely with measured values.

The correlations shown in Figs. 15 and 16 provide a means of estimating l^* *a priori* and predicting absolute values of K_{JICi} from microstructural (Δ_3) and fractographic observations (R_V/R_I). Caution is dictated. More detailed microscopic studies of the evolution of MNG as a function of alloy microstructure and temperature are required to understand the correlations in Figs. 15 and 16. Measurements of Δ_3 are complicated by the three-dimensional distribution of primary void-nucleating particles that can be nonuniform due to particle clustering or banding from processing. A Dirichlet cell tessellation procedure describes the local geometric properties of inclusions in a steel [65,66], but has not been integrated with a model of crack-tip fracture. This problem is formidable because of the strong distance and angular dependencies of crack-tip $\bar{\varepsilon}^p$ and σ_m/σ_{fl}, coupled with a heterogeneous distribution of one or more populations of void-nucleating particles.

Because $\bar{\varepsilon}^*_f$ and R_V/R_I are measures of intrinsic alloy fracture resistance, critical fracture strain and critical distance are not independent. It is reasonable to speculate that l^*/Δ_3 is a unique monotonically increasing function of $\bar{\varepsilon}^*_f$, analogous to the trend in Fig. 16. Accordingly, it may be possible to eliminate l^* from the model by substituting the dependence of this parameter on $\bar{\varepsilon}^*_f$ and Δ_3. For the alloys in Fig. 15, l^*/Δ_3 correlates with $\bar{\varepsilon}^*_f$, but the data are too scattered to provide a quantitative correlation. More precise measurement of $\bar{\varepsilon}^p_f(\sigma_m/\sigma_{fl})$ and $\bar{\varepsilon}^*_f$ are required to confirm this notion. If future studies can relate l^*/Δ_3 and $\bar{\varepsilon}^*_f$, then absolute predictions of temperature and microstructure effects on K_{JICi} will be possible based on measured $\bar{\varepsilon}^p_f(\sigma_m/\sigma_{fl})$, σ_{ys}, E, n, and Δ_3.

Conclusions

1. The critical-plastic-strain-controlled model successfully predicts the temperature dependence of plane-strain initiation fracture toughness (K_{JICi}) for a variety of advanced aluminum alloys that crack by microvoid processes. Predictions are based on smooth-bar tensile deformation properties, an estimate of the exponential decay of the fracture strain ($\bar{\varepsilon}^p_f$) with stress-state triaxiality (σ_m/σ_{fl}), and a single adjustable parameter (l^*).
2. Approximately temperature-insensitive K_{JICi} is predicted and observed for 2000 series precipitation-hardened alloys from cryogenic to elevated temperatures, while a degradation of K_{JICi} with increasing temperature is correctly modeled for submicron-grain-size alloys.
3. The temperature dependencies of K_{JICi} are traceable to the interplay between thermally sensitive intrinsic fracture resistance and the crack-tip strain field, which is temperature dependent through σ_{ys}, E, and n. Both components are necessary to predict temperature-insensitive initiation toughness in precipitation-hardened aluminum alloys, where the fracture strain ($\bar{\varepsilon}^p_f$) generally rises with temperature while σ_{ys}, E, and n decline.
4. Uncertainties in the critical distance (l^*) and the failure loci ($\bar{\varepsilon}^p_f(\sigma_m/\sigma_{fl})$) preclude predictions of absolute values of K_{JICi}. Accurate determination of $\bar{\varepsilon}^p_f(\sigma_m/\sigma_{fl})$ is complicated by the need to correlate damage at the initiation event within tensile specimens and the process zone ahead of a crack tip.
5. Model-calculated critical distance correlates with the nearest-neighbor particle spacing (Δ_3) for several aluminum alloys and steels, and l^*/Δ_3 correlates with the extent of primary void growth. Both correlations suggest an approach to predict absolute toughness values from tensile properties coupled with microstructural and fractographic observations.

Acknowledgments

This research was sponsored by the NASA Langley Research Center under Grant NAG-1-745 with D. L. Dicus and W. B. Lisagor as technical monitors, and by NASA headquarters, under Grant NAGW-250 with T. W. Crooker as technical monitor. This financial support, as well as the help of E. Richey with computer programming and plotting, are gratefully acknowledged.

References

[*1*] Porr, W. C., Jr., "Elevated Temperature Fracture of Advanced Powder Metallurgy Aluminum Alloy 8009," Ph.D. thesis, University of Virginia, Charlottesville, VA, 1992.
[*2*] Porr, W. C., Jr. and Gangloff, R. P., *Metallurgical Transactions A*, Vol. 25A, 1994, pp. 365–379.
[*3*] Kim, S. S., Haynes, M. J., and Gangloff, R. P., *Materials Science and Engineering A*, Vol. 203, 1995, pp. 256–271.
[*4*] Haynes, M. J. and Gangloff, R. P., "Elevated Temperature Fracture Toughness of Al-Cu-Mg-Ag Alloy Sheet: Characterization and Modeling," *Metallurgical Transactions A*, in review, 1996.
[*5*] Somerday, B. P., Leng, Y., and Gangloff, R. P., *Fatigue and Fracture of Engineering Material Structures*, Vol. 18, 1995, pp. 565–582.
[*6*] Somerday, B. P., "Elevated Temperature Fracture Toughness of a SiC Particulate-Reinforced 2009 Aluminum Composite," Masters thesis, University of Virginia, Charlottesville, VA, 1993.
[*7*] Donald, J. K. and Ruschau, J. in *Fatigue Crack Measurement: Techniques and Applications*, K. J. Marsh et al., Eds., EMAS, West Midlands, UK, 1991, pp. 11–37.
[*8*] Haynes, M. J. and Gangloff, R. P., "High Resolution R-Curve Characterization of the Fracture Toughness of Thin Sheet Aluminum Alloys," *Journal of Testing and Evaluation*, in press, 1996.
[*9*] Chan, K. S., *Acta Metallurgica*, Vol. 37, 1989, pp. 1217–1226.
[*10*] Somerday, B. P., Leng, Y., and Gangloff, R. P., *Fatigue and Fracture of Engineering Material Structures*, Vol. 18, 1995, pp. 1031–1050.
[*11*] Ritchie, R. O. and Thompson, A. W., *Metallurgical Transactions A*, Vol. 16A, 1985, pp. 233–248.
[*12*] Rice, J. R. and Johnson, M. A. in *Inelastic Behavior of Solids*, M. F. Kanninen et al., Eds., McGraw-Hill, New York, NY, 1970, pp. 641–672.
[*13*] Hahn, G. T. and Rosenfield, A. R., *Metallurgical Transactions A*, Vol. 6A, 1975, pp. 653–668.
[*14*] Van Stone, R. H., Cox, T. B., Low, J. R., and Psioda, J. A., *International Metallurgical Reviews*, Vol. 30, 1985, pp. 157–179.
[*15*] Thomason, P. F., *Ductile Fracture of Metals*, Pergamon Press, Oxford, UK, 1990, pp. 105–111.
[*16*] Garrison, W. M., Jr. and Moody, N. R., *Journal of Physics and Chemistry of Solids*, Vol. 48, 1987, pp. 1035–1074.
[*17*] Rice, J. R. and Tracey, D. M., *Journal of Mechanics and Physics of Solids*, Vol. 17, 1969, pp. 201–217.
[*18*] Mackenzie, A. C., Hancock, J. W., and Brown, D. K., *Engineering Fracture Mechanics*, Vol. 9, 1977. pp. 167–188.
[*19*] Argon, A. S., Im, J., and Safoglu, R., *Metallurgical Transactions A*, Vol. 6A, 1975, pp. 825–837.
[*20*] Goods, S. H. and Brown, L. M., *Acta Metallurgica*, Vol. 27, 1979, pp. 1–15.
[*21*] LeRoy, G., Embury, J. D., Edwards, G., and Ashby, M. F., *Acta Metallurgica*, Vol. 29, 1981, pp. 1509–1522.
[*22*] Cox, T. B. and Low, J. R., Jr., *Metallurgical Transactions A*, Vol. 5A, 1974, pp. 1457–1470.
[*23*] Dubensky, E. M. and Koss, D. A., *Metallurgical Transactions A*, Vol. 18A, 1987, pp. 1887–1895.
[*24*] Yamamoto, H., *International Journal of Fracture*, Vol. 14, 1978, pp. 347–365.
[*25*] Pan, J., Saje, M., and Needleman, A., *International Journal of Fracture*, Vol. 21, 1983, pp. 261–278.
[*26*] Becker, R. and Smelser, R. E., *Journal of Mechanics and Physics of Solids*, Vol. 42, 1994, pp. 773–796.
[*27*] Hancock, J. W. and Mackenzie, A. C., *Journal of Mechanics and Physics of Solids*, Vol. 24, 1976, pp. 147–169.
[*28*] Ohno, N. and Hutchinson, J. W., *Journal of Mechanics and Physics of Solids*, Vol. 32, 1984, pp. 63–85.
[*29*] Pineau, A., in *Topics in Fracture and Fatigue*, A. S. Argon, Ed., Springer-Verlag, New York, NY, 1992, pp. 197–234.
[*30*] Marini, B., Mudry, F., and Pineau, A., *Engineering Fracture Mechanics*, Vol. 22, 1985, pp. 989–996.

[31] Ritchie, R. O., Server, W. L., and Wullaert, R. A., *Metallurgical Transactions A*, Vol. 10A, 1977, pp. 1557–1570.
[32] Thompson, A. W. and Ashby, M. F., *Scripta Metallurgica et Materials*, Vol. 18, 1984, pp. 127–130.
[33] Hutchinson, J. W., *Journal of Mechanics and Physics of Solids*, Vol. 16, 1968, pp. 13–31, 337–347.
[34] Rice, J. R. and Rosengren, G. F., *Journal of Mechanics and Physics of Solids*, Vol. 16, 1968, pp. 1–12.
[35] McMeeking, R. M., *Journal of Mechanics and Physics of Solids*, 1977, Vol. 25, pp. 357–381.
[36] McMeeking, R. M., *Journal of Engineering Materials and Technology, Transactions of the ASME*, Vol. 99, 1977, pp. 290–297.
[37] Bates, R. C. in *Metallurgical Treatises*, J. K. Tien and J. F. Elliot, Eds., TMS-AIME, Warrendale, PA, 1982, pp. 551–570.
[38] Hancock, J. W. and Cowling, M. J., *Metal Science*, 1980, pp. 293–304.
[39] Shih, C. F., *Journal of Mechanics and Physics of Solids*, Vol. 29, 1981, pp. 305–326.
[40] Hutchinson, J. W., *Journal of Applied Mechanics, Transactions of the ASME*, Vol. 50, 1983, pp. 1042–1051.
[41] Walsh, J. A., Jata, K. V., and Starke, E. A., Jr., *Acta Metallurgica*, Vol. 37, No. 11, 1989, pp. 2861–2871.
[42] Somerday, B. P. and Gangloff, R. P., *Metallurgical Transactions A*, Vol. 25A, 1994, pp. 1471–1479.
[43] Blankenship, C. P., Jr. and Starke, E. A., Jr., *Acta Metallurgica*, Vol. 42, 1994, pp. 845–855.
[44] Chellman, D. F., Bayha, T. D., Li, Q., and Wawner, F. E., Jr. in *Proceedings of Fourth International Conference on Aluminum Alloys*, Vol. 2, T. H. Sanders, Jr. and E. A. Starke, Jr., Eds., Georgia Institute of Technology, Atlanta, GA, 1994, pp. 2–9.
[45] Leng, Y., Porr, W. C., Jr., and Gangloff, R. P., *Scripta Metallurgica*, Vol. 24, No. 11, 1990, pp. 2163–2168.
[46] Gangloff, R. P., "NASA-UVA Light Aerospace Alloy and Structures Technology Program," UVA Report No. UVA/528266/MS94/117, University of Virginia, Charlottesville, VA, 1995, pp. 65–79.
[47] Mondolfo, L. F., *Aluminum Alloys Structure and Properties*, Butterworth and Co., Woburn, MA, 1976, p. 82.
[48] Corti, C. W., Cotterill, P., and Fitzpatrick, G. A., *International Metallurgical Reviews*, Vol. 19, 1974, pp. 77–88.
[49] Tvergaard, V. and Needleman, A., *Acta Metallurgica*, Vol. 32, 1984, pp. 157–169.
[50] Bridgman, P. W., *Studies in Large Plastic Flow and Fracture*, McGraw-Hill Book Co., New York, NY, 1952, pp. 9–37.
[51] Hancock, J. W. and Brown, D. K., *Journal of Mechanics and Physics of Solids*, Vol. 31, 1983, pp. 1–24.
[52] Earl, J. C. and Brown, D. K., *Engineering Fracture Mechanics*, Vol. 8, 1976, pp. 599–611.
[53] Wilsdorf, H. G. F., Wawner, F. E., Jr., and Wert, J. A., *Very High Temperature Aluminum Materials Concepts*, Wright Laboratory Report No. WL-TR-91-4022, Wright Patterson Air Force Base, OH, 1991.
[54] Gilman, P. S. in *Thermal Structures and Materials for High Speed Flight*, E. A. Thornton, Ed., AIAA, Washington, DC, Vol. 140, 1992, pp. 141–160.
[55] Thomson, R. D. and Hancock, J. W., *International Journal of Fracture*, Vol. 26, 1984, p. 99–112.
[56] Pineau, A. in *Advances in Fracture Reserach, ICF5*, D. Francois et al., Eds., Pergamon Press, Oxford, UK, 1981, pp. 553–577.
[57] Miller, T. C. and Anderson, T. L. in *Fracture Mechanics: Twenty-Fourth Volume, ASTM STP 1207*, J. D. Landes, D. E. McCabe, and J. A. M. Boulet, Eds., American Society for Testing and Materials, West Conshohocken, PA, 1994, pp. 87–107.
[58] Van Stone, R. H., Merchant, R. H., and Low, J. R., Jr., in *Fatigue and Fracture Toughness-Cryogenic Behavior, ASTM STP 556*, C. F. Hickey, Jr. and R. G. Broadwell, Eds., American Society for Testing and Materials, West Conshohocken, PA, 1974, pp. 93–124.
[59] Tanaka, J. P., Pampillo, C. A., and Low, J. R., Jr., in *Review of Developments in Plane Strain Fracture Toughness Testing, ASTM STP 463*, W. F. Brown, Jr., Ed., American Society for Testing and Materials, West Conshohocken, PA, 1970, pp. 191–215.
[60] Argon, A. S. and Im, J., *Metallurgical Transactions A*, Vol. 6A, 1975, pp. 839–851.
[61] Bray, J. W., Handerhan, K. J., Garrison, W. M., Jr., and Thompson, A. W., *Metallurgical Transactions A*, Vol. 23A, 1992, pp. 485–496.
[62] Garrison, W. M., Jr., *Metallurgical Transactions A*, Vol. 17A, 1986, pp. 669–678.
[63] Lee, S., Majno, L., and Asaro, R. J., *Metallurgical Transactions A*, Vol. 16A, 1985, pp. 1633–1648.
[64] Psioda, J. A., "The Effect of Microstructure and Strength on the Fracture Toughness of an 18 Nickel 300 Grade Maraging Steel," Ph.D. thesis, Carnegie Mellon University, Pittsburgh, PA, 1977.
[65] Spitzig, W. A., *Acta Metallurgica*, Vol. 33, 1985, pp. 175–184.
[66] Spitzig, W. A., Kelly, J. F., and Richmond, O., *Metallography*, Vol. 18, 1985, pp. 235–261.

Anthony P. Reynolds[1] *and Roy E. Crooks*[2]

The Effect of Thermal Exposure on the Fracture Behavior of Aluminum Alloys Intended for Elevated Temperature Service

REFERENCE: Reynolds, A. P. and Crooks, R. E., "**The Effect of Thermal Exposure on the Fracture Behavior of Aluminum Alloys Intended for Elevated Temperature Service,**" *Elevated Temperature Effects on Fatigue and Fracture, ASTM STP 1297,* R. S. Piascik, R. P. Gangloff, and A. Saxena, Eds., American Society for Testing and Materials, 1997, pp. 191–205.

ABSTRACT: Because of their ease of fabricability, durability, and good specific properties, precipitation-hardened aluminum alloys have been the materials of choice for subsonic aircraft for over 50 years. At the present time, precipitation-hardening alloys are being evaluated for use in elevated temperature applications such as supersonic transport aircraft. These applications require stability of mechanical properties, implying stable microstructures. In this study, it has been shown that for three materials of interest, microstructural evolution at relatively low temperatures may result in complex changes in mechanical properties with fracture resistance being a salient example. Changes in amounts and kinds of grain boundary fracture, probably related to growth of grain boundary precipitate phases or segregation of embrittling species to the boundaries, appear to dominate the behavior.

KEYWORDS: fracture, aluminum alloys, elevated temperature exposure

Precipitation-hardened aluminum alloys present special problems with regard to elevated temperature service. Generally, the microstructure of such alloys is not stable for long times at elevated temperature [*1–5*]. Previous studies have shown that tensile strength and ductility are not adequate indicators of microstructural stability [*6*]. While tensile properties remain nearly constant, fracture toughness may show significant degradation after elevated temperature exposure. The use of these alloys for elevated temperature applications will therefore require better understanding of the related mechanisms of microstructural evolution and property degradation. The objective of the present study is to assess the effect of elevated temperature exposure on the fracture properties of several aluminum alloys and to correlate the observed changes to microstructural features.

Materials

Three ingot metallurgy, precipitation-strengthened aluminum alloys were chosen for examination in this study. Their microstructures differ in grain structure, crystallographic texture, and precipitate type. Comparison of the performance of these alloys may help to determine the optimum microstructure for elevated temperature service.

Alloy 1 has a nominal composition in weight % of aluminum-5.4 copper-0.5 magnesium-

---

[1] Assistant professor, University of South Carolina, Department of Mechanical Engineering, 300 Main Street, Room A224, Columbia, SC 29208.

[2] Senior research scientist, Analytical Services and Materials, 107 Research Drive, Hampton, VA 23666.

0.5 silver-0.12 Zirconium-0.3 manganese. The grain structure of Alloy 1 is nearly equiaxed (aspect ratio 1.3:1) with a mean grain diameter of approximately 24 μm. Alloy 1 is recrystallized and exhibits a weak crystallographic texture [*7*]. The primary strengthening phase in Alloy 1 is the variant of Al_2Cu, which forms as thin hexagonal plates on the matrix {111} planes [*8*].

The nominal composition in weight % of Alloy 2 is aluminum-3.5 copper-0.96 lithium-0.4 magnesium-0.42 silver-0.12 zirconium-0.3 manganese. The alloy is recrystallized but exhibits a strong {011}<100>, GOSS, recrystallization texture, and grains that are elongated in the rolling direction; the aspect ratio of the grains is about 8:1 [*7*]. The primary strengthening phase in Alloy 2 is T_1, which has a composition of Al_2CuLi and forms as thin, hexagonal plates on the matrix {111} planes [*9*].

Alloy 3 is composed of aluminum-3.4 copper-0.8 lithium-0.4 magnesium-0.5 silver-0.14 zirconium. The alloy is mostly unrecrystallized, with a strong deformation texture dominated by brass, {011}<211>, and S, {123}<634>, components, with some R, {124}<211>, recrystallization components. The grains are highly elongated in the rolling direction. As in Alloy 2, the primary strengthening phase is T_1 [*10*]. Electron backscatter channeling micro-pole figure data indicate that the mean distance between high angle boundaries in the S (thickness) direction of the Alloy 3 sheet is 7 to 8 μm. In the L (rolling) direction, the mean distance between high angle boundaries is greater than 200 μm.

All three alloys were provided as sheet product as 2.3 mm thick in the T8 (stretched and artificially aged to peak strength) condition. The precipitation aging temperatures were 175°C for Alloy 1 and 160°C for Alloys 2 and 3.

Experimental Procedures

Elevated Temperature Exposure

The test alloys were exposed in air-circulating ovens for times ranging from 100 to 9000 h depending on the alloy and exposure temperature. Exposure temperatures were 93, 107, and 135°C (Alloy 3 was not exposed at 93°C). Temperature control in the ovens was ±2.8°C.

Hardness Testing

Rockwell A scale hardness was determined for all of the alloys as a function of exposure time at elevated temperature. The average of five tests is reported for each condition.

Fracture Testing

For each exposure condition, duplicate (triplicate for some Alloy 3 exposure conditions) *R*-curves were produced by the *J*-integral method according to ASTM Test Method for Determining *J-R* Curves (E 1152-87). The unloading compliance method was used for physical crack length measurement. *J-R* curves were converted to *K-R* curves via the following equation [*12*]:

$$K = \sqrt{J \times E} \tag{1}$$

Specimens were compact tension type with $W = 50.8$ mm. The load-line displacement rate was 0.004 mm/s, and unloads were performed after each 0.04 mm of displacement. Starting a/W was 0.6. In the results section, total *R*-curves will not normally be presented; instead, the *R*-curve values at physical crack extensions of 0.1 and 2.0 mm will be used to represent, respectively, the initiation toughness and the tearing resistance of the material. The definitions of the initiation toughness and tearing resistance are illustrated in Fig. 1.

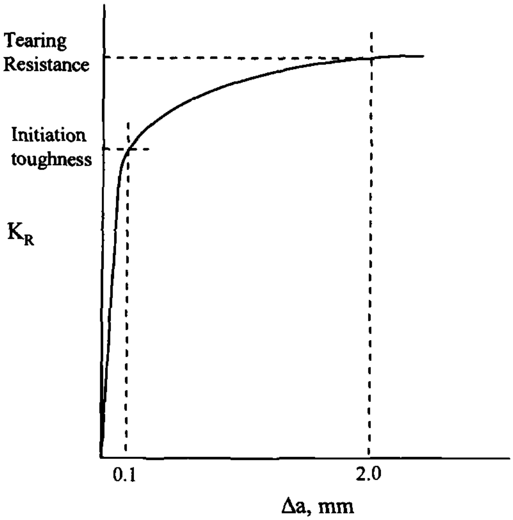

FIG. 1—*Schematic* R-*curve illustrating initiation toughness determined at* Δa = *0.1 mm and tearing resistance determined at* Δa = *2.0 mm.*

Fractography

Fractography was performed in a scanning electron microscope in order to qualitatively assess changes in fracture mode and path. Quantitative analysis of area fraction of intergranular fracture was determined for selected conditions by manual point counting on fractographs taken at ×500 magnification. The percent of intergranular fracture was determined at a physical crack extension of 2 mm and, in some cases, at the initiation of stable tearing. For each determination, a minimum of four views were analyzed, giving a minimum area of analysis of 164 000 μm^2. The grid used for the analysis had an equivalent spacing of 10 μm between intersections.

Results

Hardness

The results of the hardness tests are presented in Figs. 2*a-c*. Alloys 1 and 2 exhibit monotonically increasing hardness with increasing exposure time at 93 and 107°C. Exposure at 135°C causes decreasing hardness in Alloy 1 and increasing followed by decreasing hardness in Alloy 2. After 3000 h at 135°C, both alloys have lower hardness than in the T8 condition. Alloy 3 exhibits an increase in hardness due to exposure at 107°C for times up to 7000 h. After 7000 h of exposure, the hardness decreases but remains above the T8 hardness. Alloy 3 hardness resulting from exposure at 135°C peaks at 1000 h of exposure, and by 7000 h of exposure the hardness is below the T8 level. While it would be difficult to compare strength levels from alloy to alloy based on hardness measurements, comparison of hardness for one alloy at different conditions should be relatable to alloy strength.

Fracture Behavior

Alloy 1—Alloy 1 was tested in the T8 condition and after exposure at 93, 107, and 135°C for 1000 and 3000 h. Initiation toughness as a function of exposure time and temperature is

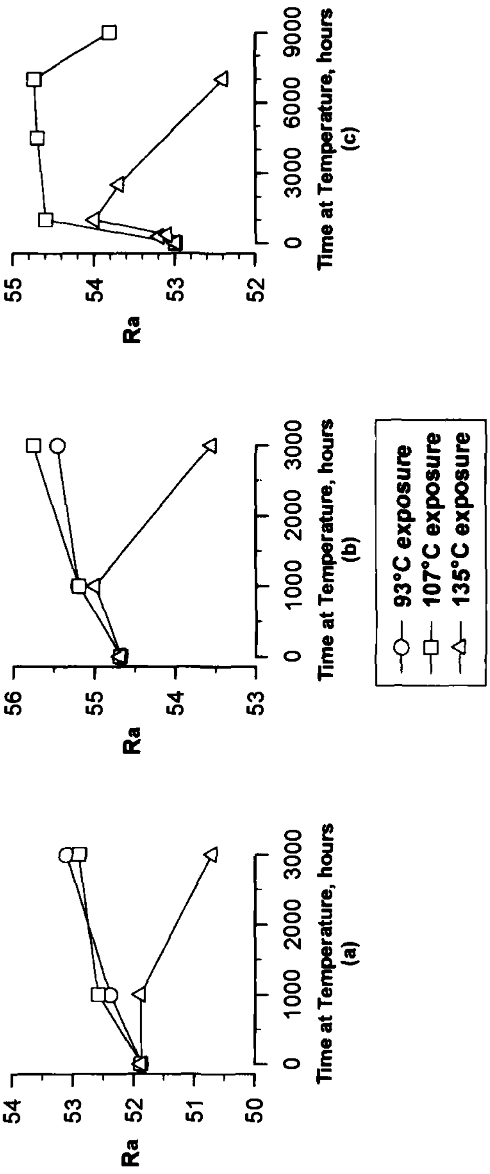

FIG. 2—*Rockwell "A" scale hardness of the test alloys as functions of exposure time and temperature:* (a) *Alloy 1,* (b) *Alloy 2,* (c) *Alloy 3.*

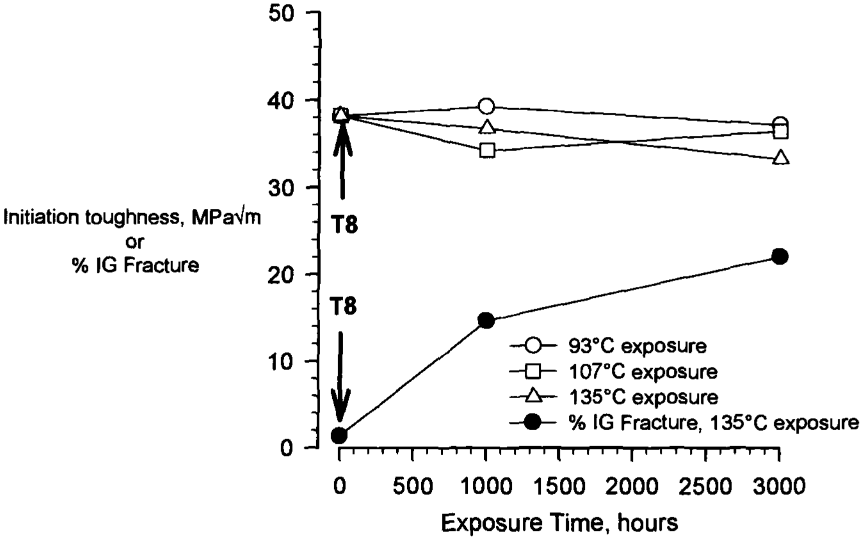

FIG. 3—*Initiation fracture toughness and % IG fracture at* Δa *= 0.1 mm as functions of exposure time and temperature: Alloy 1 in the L-T orientation.*

shown in Fig. 3. The range of initiation toughness observed is small, but a trend of decreasing toughness with increased exposure time may be observed in the data for exposure at 135°C. The percentage of intergranular (% IG) fracture at crack initiation in the T8 condition and after 1000 and 3000 h of exposure at 135°C is also plotted in Fig. 3 (closed circles). The trend in % IG fracture supports the observed trend in initiation toughness.

The tearing resistance (TR) and % IG fracture of Alloy 1 at Δa = 2 mm are plotted in Fig. 4 as functions of exposure time and temperature. The fracture behavior due to exposure at all

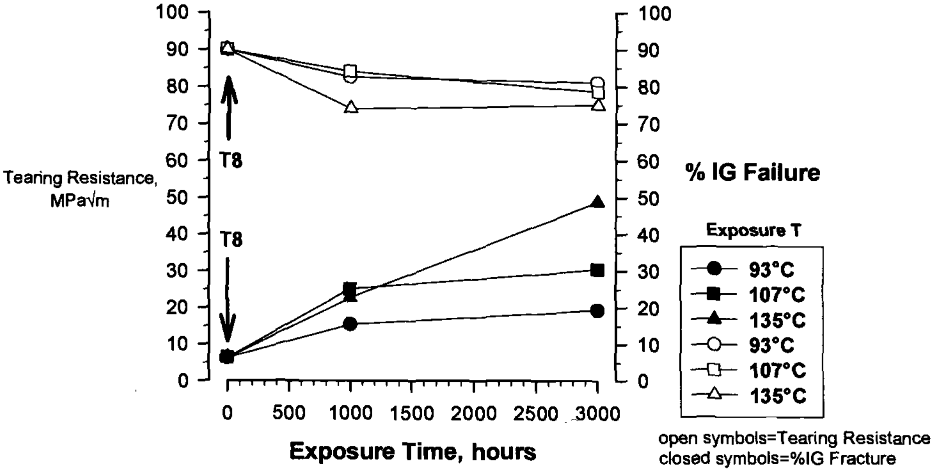

FIG. 4—*Tearing resistance and % IG fracture at* Δa *= 2.0 mm as functions of exposure time and temperature: Alloy 1 in the L-T orientation.*

three temperatures is characterized by a sharp drop between the T8 condition and 1000 h of exposure followed by a smaller decline or property stabilization between 1000 and 3000 h of exposure. Reductions are similar for 93 and 107°C exposures and larger for 135°C exposures. The 93 and 107°C fracture mode data correlate well with the TR data but the correlation with the 135°C exposure data is not as good. A large increase in area fraction of IG failure between 1000 and 3000 h of exposure at 135°C does not correspond to a large decrease in TR, indicating that other factors (possibly related to the observed reduction in hardness) are involved. Comparison of Figs. 3 and 4 indicates that 135°C exposure causes a greater reduction in tearing resistance than in initiation toughness.

Figures 5*a-d* are representative micrographs of initiation and stable tearing regions ($\Delta a = 2$ mm) of Alloy 1 fracture surfaces in the T8 condition and after 3000 h of exposure at 135°C. The increase in intergranular fracture after exposure is readily evident in these micrographs. Microvoids in the transgranular region are nucleated primarily at large constituent particles, which may have diameters greater than 1 μm. Intergranular fracture facets are dimpled as well, but the dimples are shallower than those that occur in transgranular regions and the nucleating particles; when they are observed, are submicron in size.

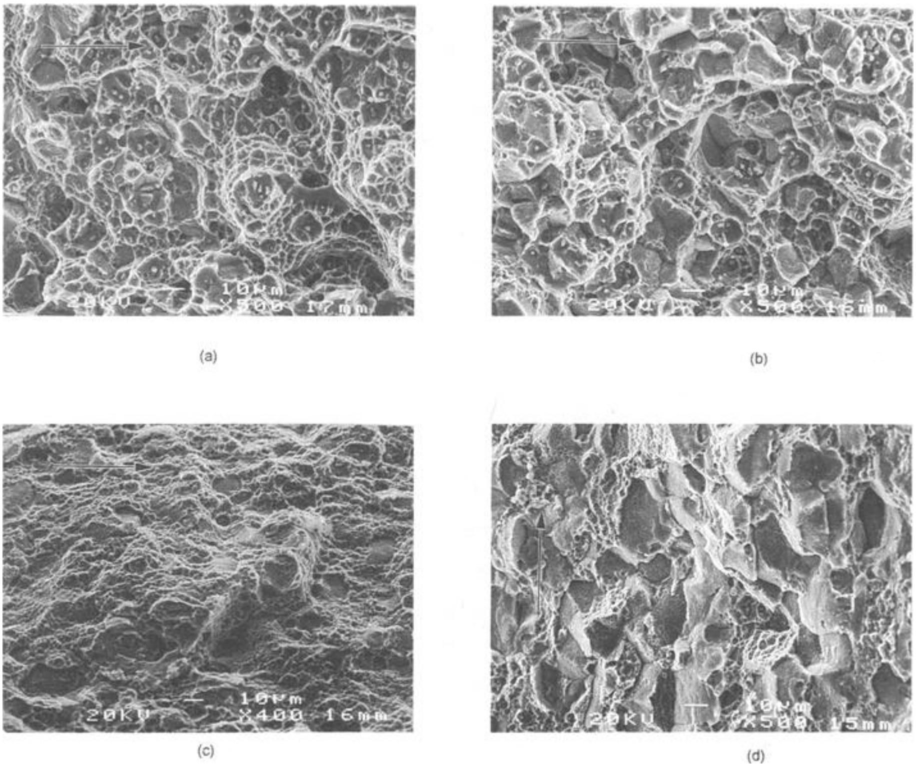

FIG. 5—*Representative Alloy 1 fractographs from L-T specimens. Arrows indicate macroscopic crack growth directions:* (a) *T8 condition in the initiation region;* (b) *T8 + 3000 h at 135°C condition in the initiation region;* (c) *T8 condition at* Δa *= 2 mm;* (d) *T8 + 3000 h at 135°C condition at* Δa *= 2 mm.*

Alloy 2—Alloy 2 was tested in the T8 condition and after exposure at 93, 107, and 135°C for 1000 and 3000 h (the same conditions as Alloy 1). In addition to L-T data, fracture toughness data in the T-L direction were obtained. The fracture behavior of Alloy 2 is well behaved in that it generally follows expected trends of decreasing initiation toughness and TR with increasing severity of exposure. All of the Alloy 2 *R*-curve data are summarized in Figs. 6*a-d*. T-L initiation toughness (Fig. 6*a*) degrades monotonically with increasing exposure time and temperature. L-T initiation toughness (Fig. 6*b*) shows similar trends with the exception of the 93°C, 3000-h data point. If that point is disregarded, severity of exposure again correlates with reduction in toughness. Alloy 2 T-L and L-T tearing resistance as functions of exposure time and temperature are plotted in Figs. 6*c* and 6*d*, respectively. The T8 TR is 20% lower in the T-L orientation than in the L-T, but the two orientations display similar trends with respect to elevated temperature exposure. In both cases, degradation after 93°C exposure is mild, degradation is severe after 135°C exposure, and intermediate after 107°C exposure.

The % IG fracture in Alloy 2 was measured for the T8 condition and after exposure at 135°C for 1000 and 3000 h. Measurements were made at $\Delta a = 2$ mm for the T-L and L-T orientations. Figure 7 is a plot of the $\Delta a = 2$ mm tearing resistance plotted as a function of the % IG fracture for both the T-L and L-T orientations. An excellent correlation is obtained between tearing resistance and % IG fracture. It is interesting to note that the % IG fracture in the T8 condition is relatively high, suggesting that the level of grain boundary precipitation is high in the T8 condition. Figures 8*a* and 8*b* are representative micrographs of Alloy 2 fracture surfaces at T8 and after exposure at 135°C for 3000 h. As in Alloy 1, the increase in area fraction of IG failure is readily observed by comparison of the two micrographs.

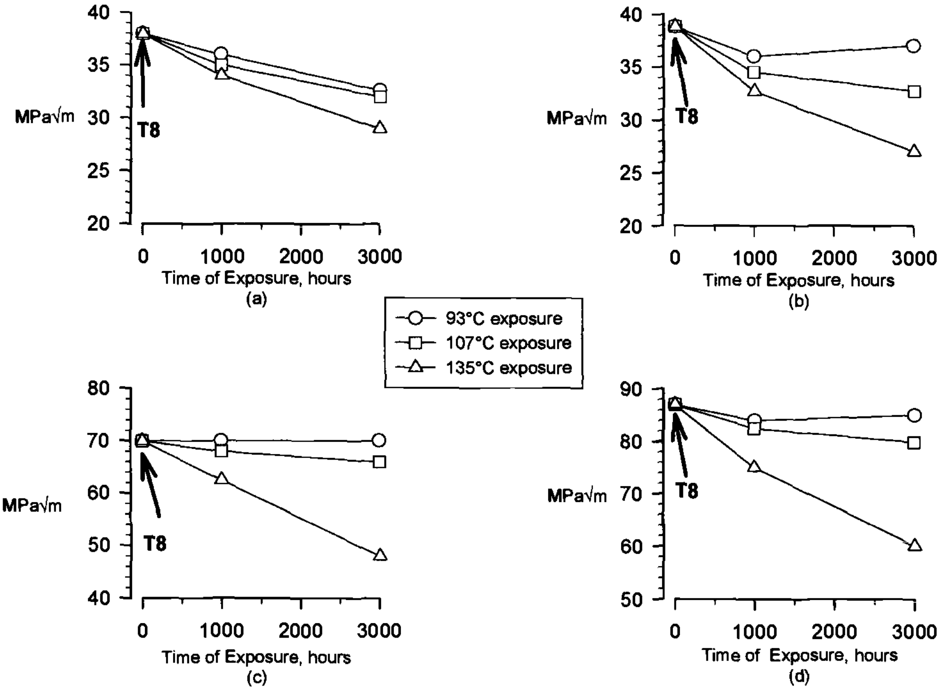

FIG. 6—*Alloy 2 fracture resistance:* (a) *T-L orientation,* $\Delta a = 0.1$ *mm,* (b) *L-T orientation,* $\Delta a = 0.1$ *mm,* (c) *T-L orientation,* $\Delta a = 2.0$ *mm,* (d) *L-T orientation,* $\Delta a = 2.0$ *mm.*

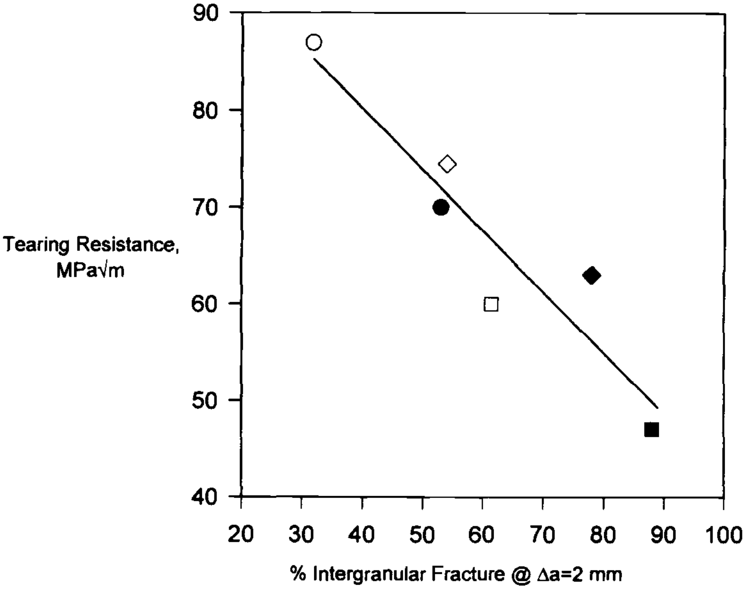

FIG. 7—*The effect of fracture path on tearing resistance: Alloy 2 exposed at 135°C. Open symbols, L-T orientation; closed symbols, T-L orientation; circles, T8; diamonds, 1000-h exposure; squares, 3000-h exposure.*

Alloy 3—Depending on the conditions of elevated temperature exposure, Alloy 3 exhibited three distinctly different types of *R*-curve. These three types of *R*-curve are illustrated in Fig. 9. The first type (open circles) is characterized by stable crack growth at toughness levels similar to or slightly higher than Alloys 1 and 2; this type of *R*-curve is representative of the behavior of T8 material. The second type of *R*-curve (closed circles) is characterized by initial crack extension (up to about 0.5 mm) similar to that in T8 material followed by unstable crack growth or pop-in at a low, constant, stress intensity level. The initial pop-in event typically results in crack extension of greater than 2 mm. The third type of *R*-curve behavior observed (open squares) is stable tearing at toughness levels below that observed for T8 material. This type of behavior is typical of material that has been exposed at 135°C.

The fracture behavior of Alloy 3 as a function of elevated temperature exposure is summarized in Figs. 10*a* and 10*b*. Exposure at 107°C results in complex *R*-curve behavior (Fig. 10*a*). Initiation toughness remains nearly constant between 0 and 9000 h of exposure. Between 1000 and 7000 h of exposure the *R*-curves are of the pop-in type, and the Δa = 2 mm TR goes through an apparent minimum at 4500 h of exposure (the TR for pop-in type *R* curves is assumed equal to the stress intensity at the pop-in). After 9000 h of exposure, the behavior is similar to the T8 condition. Exposure of Alloy 3 at 135°C results in monotonic reductions in initiation toughness and Δa = 2 mm TR with increasing exposure time (Fig. 10*b*). The *R*-curves are of the stable tearing type at reduced toughness level.

Each type of *R*-curve behavior is associated with a characteristic fracture morphology (shown in Figs. 11*a*-*c*). T8 material fractures primarily by transgranular microvoid coalescence (TG MVC) with some IG fracture (Fig. 11*a*); material exposed at 107°C for 9000 h exhibits fracture surface characteristics similar to the T8 material. Pop-in fractures are characterized by inter-

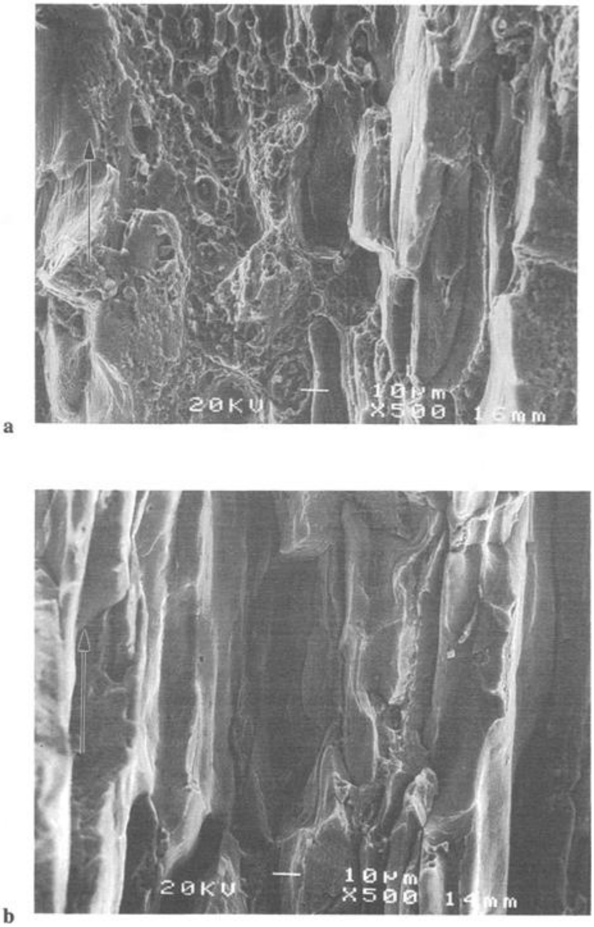

FIG. 8—*Representative Alloy 2 fractographs: L-T specimens at* Δa *= 2 mm. Arrows indicate macroscopic crack growth direction:* (a) *T8 condition;* (b) *T8 + 3000 h at 135°C condition.*

granular and inter-subgranular failure, which exhibits extremely shallow dimpling on boundary facets. In some cases, dimples are not resolved (Fig. 11*b*). Stable tearing at low toughness levels also results in IG and inter-subgranular fracture, but grain boundary facet dimpling is more pronounced that in the pop-in failures and the failure mode could be termed "ductile intergranular" (Fig. 11*c*).

Figures 12*a* and 12*b* are, respectively, a low magnification SEM micrograph representative of the slant fracture region of Alloy 3 fracture surfaces from material that has been exposed at elevated temperature (the differences between the pop-in and low toughness stable tearing fracture surfaces mentioned in the previous paragraph are evident only at higher magnification) and an optical micrograph of a metallographic section through a fracture surface with the crack growth direction into the plane of the picture. As the two figures show, the slant fracture regions are made up of a series of steps formed by boundary fractures. The components of the fracture

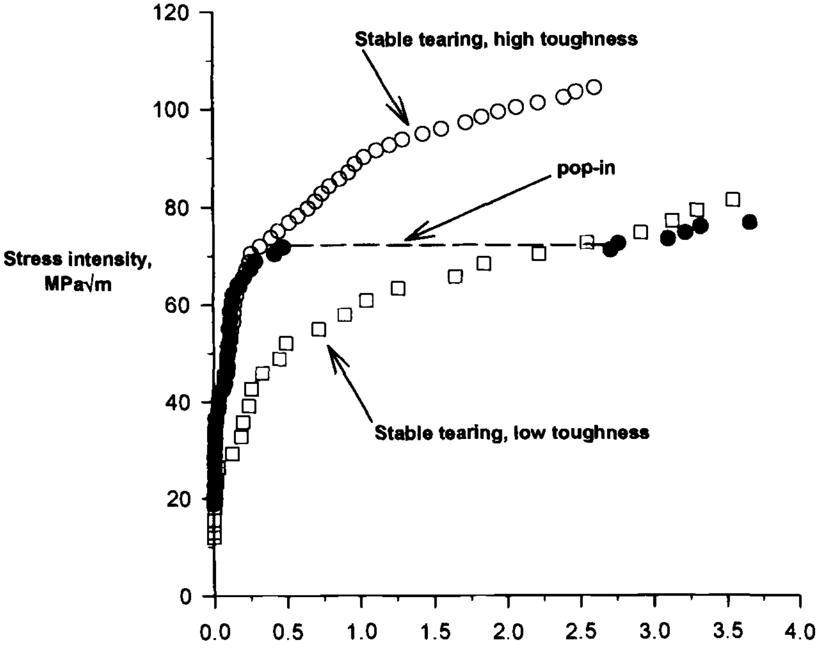

FIG. 9—*Alloy 3* R-*curve types.*

surface that are parallel to the loading direction may be thought of as the "risers" of the steps, while the horizontal components (perpendicular to the loading direction) may be considered the "treads" of the steps. The width of the "treads" was measured from SEM micrographs and found to be 3.5 μm on average.

As reported in the "Materials" section of this paper, the distance between high angle boundaries in the S direction (perpendicular to the "risers," parallel to the "treads") is approximately 7 to 8 μm, and the distance between boundaries of any type is approximately 3.5 μm. The distance between high angle boundaries in the L direction (parallel to the "risers," perpendicular to the "treads") is greater than 200 μm. This suggests that the "risers" of the steps that comprise the fracture surface may be either high or low angle boundaries, while the treads are almost exclusively low angle boundaries. Recent TEM studies of similar alloys indicate that even very low angle boundaries (<2°) may be heavily decorated with precipitates, perhaps resulting in low-energy fracture paths [5].

Discussion

Ductile Boundary Failure

The observed fracture behavior of Alloys 1, 2, and 3 as a function of elevated temperature exposure may be divided into two types of response. The first type is that exhibited by Alloys 1 and 2 at all exposure temperatures and by Alloy 3 due to exposure at 135°C. This first type

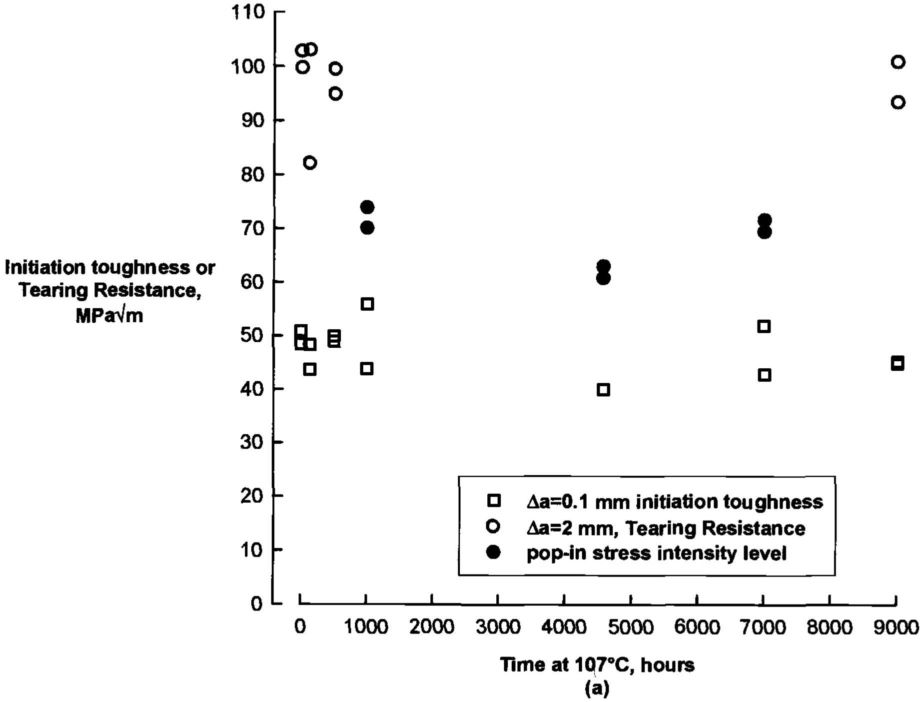

FIG. 10—*The effect of elevated temperature exposure on the fracture behavior of Alloy 3:* (a) *107°C exposure,* (b) *135°C exposure.*

of fracture may be viewed as a competition between TG MVC due to void nucleation at large constituent particles and ductile grain boundary failure.

The size and hence the ability of the large constituent particles to nucleate voids are relatively insensitive to aging at the exposure temperatures used in this study [*13*]. Changes in void nucleation at incoherent, second-phase particles of constant size are a function of the ability of the surrounding matrix to accommodate strains at the particle interfaces. The ability of the grain boundary particles to nucleate voids will also be primarily a function of their size and spacing, which *are* expected to change as a function of the elevated temperature exposures used in this study [*14,15*].

Fractography suggests that the primary mechanisms of fracture toughness degradation in these aluminum alloys are related to changes in the grain boundaries that occur during long-term elevated temperature exposure. At exposure temperatures below the aging temperature, the solid solution initially developed during the solution heat treatment and quench will continue to be supersaturated. Additional precipitation will result if sufficient thermal energy is available for diffusion. Boundary diffusion is fast compared to bulk diffusion at the temperatures of interest, and grain boundary particles may grow rapidly until solute in the grain boundary region is depleted (grain boundary diffusion rates may be as much as six orders of magnitude higher than volume diffusion rates at the temperatures of interest) [*16*]. The coupled increases in the % IG fracture and decreased toughness measured in Alloys 1 and 2 as a result of elevated temperature exposure are in accord with the above observations as is the observation of dimpled IG fracture and reduced toughness in Alloy 3 exposed at 135°C.

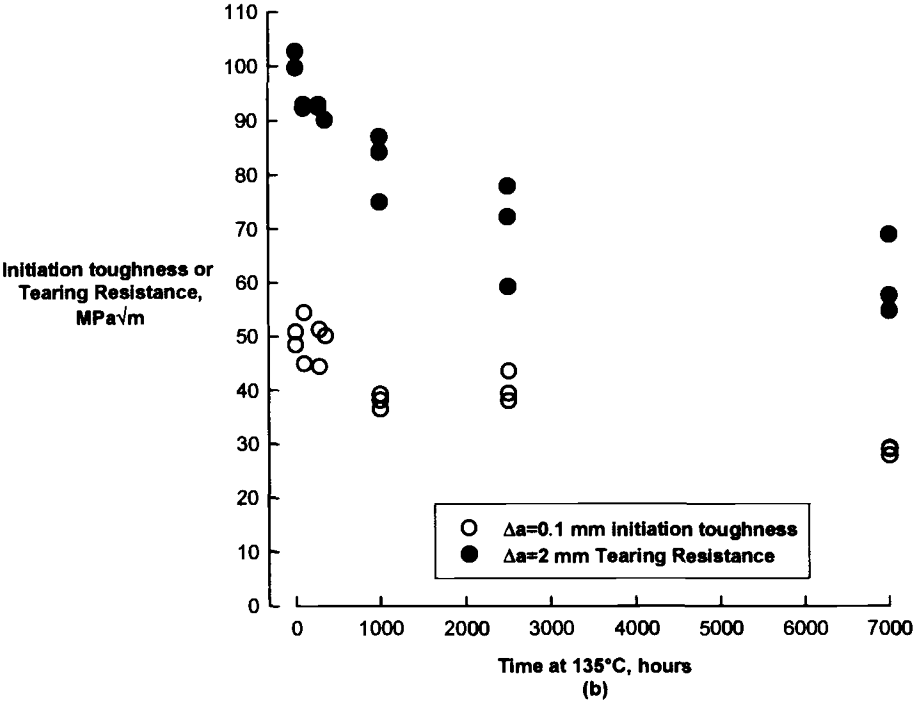

FIG. 10—*Continued*

Brittle Boundary Failure

The overall fracture behavior of Alloy 3 as a function of elevated temperature exposure appears to be the result of two different mechanisms. As stated above, exposure at 135°C results in ductile grain boundary fracture similar to the behavior of Alloys 1 and 2. Degradation in both the initiation toughness and the tearing resistance is observed as would be expected if

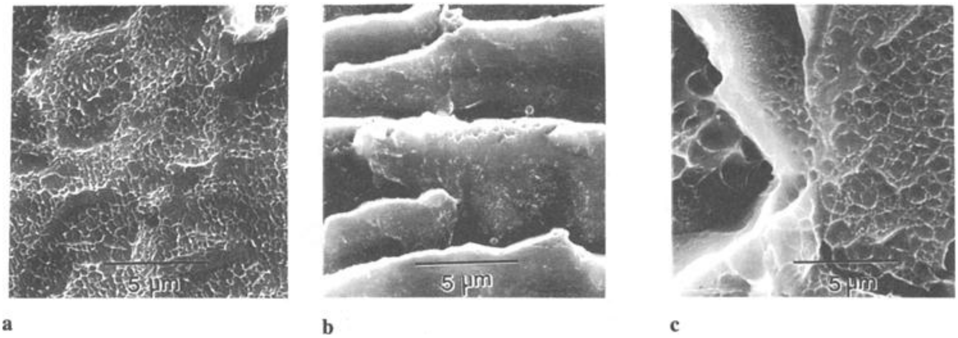

FIG. 11—*Representative Alloy 3 fractographs from L-T specimens:* (a) *T8 condition, high toughness, stable tearing* R*-curve,* (b) *T8 + 4500 h at 107°C condition, pop-in type* R*-curve, and* (c) *T8 + 7000 h at 135°C, low toughness, stable tearing type* R*-curve. In all cases, the macroscopic crack growth direction is horizontal.*

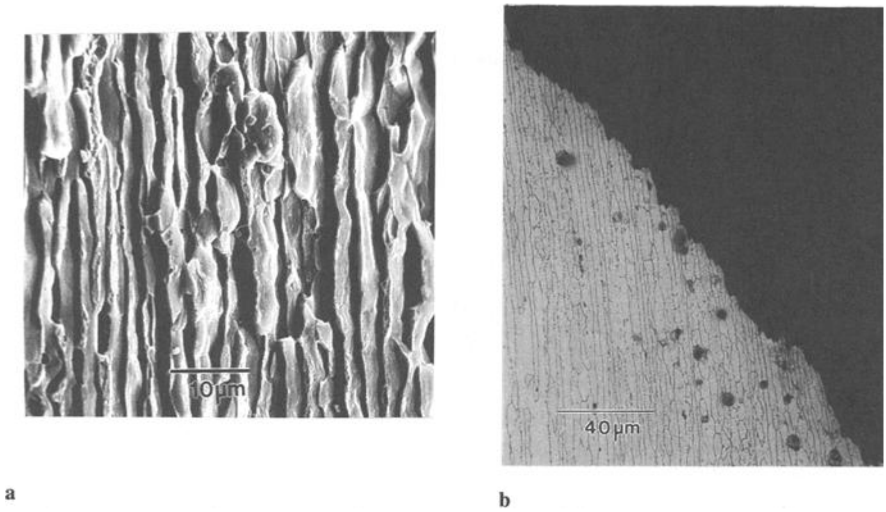

FIG. 12—*Alloy 3 slant region fracture morphology:* (a) *scanning electron micrograph looking down onto the surface of an L-T specimen exhibiting intergranular and inter-subgranular fracture. Crack growth direction is vertical, S direction is horizontal;* (b) *optical metallographic section through Alloy 3 slant fracture region. Crack growth direction is into the plane of the picture, L direction is vertical, and S direction is horizontal.*

boundary precipitates are growing larger with increasing time of exposure. Exposure at 107°C results in pop-in behavior at low tearing resistance followed by recovery of T8 behavior and fracture mode after 9000 h of exposure. In addition, initiation toughness remains almost unchanged for all exposure times at 107°C, and *R*-curves up to the point of pop-in are similar to T8 *R*-curves. The boundary failure observed in Alloy 3 after exposure at 107°C is more brittle than that observed in any of the alloys after any of the other exposures. Whether the brittle boundary facets are truly smooth or are covered with unresolved dimples is not presently known. What is certain about the pop-in behavior and the brittle boundary fracture mode is that it occurs primarily along low angle boundaries.

Nucleation of voids at grain boundary particles is controlled by a critical *strain*, which will decrease with increasing particle size at constant strength (increased alloy strength will reduce the critical strain for void nucleation). Particle size on grain and sub-grain boundaries increases with increasing time at 135°C, resulting in crack initiation and stable tearing at progressively lower toughness levels and ductile/dimpled boundary fracture as observed in the SEM micrographs. Exposure at 107°C, on the other hand, results in very smooth boundary fracture and unstable pop-in crack growth similar to cleavage phenomena that are critical *stress* controlled [*17*]. A candidate mechanism for production of this type of failure is segregation of an embrittling element to boundaries [*18*]. Lynch and Byrnes performed an activation energy study of embrittlement of Alloy 8090 and have proposed that lithium may serve the role of boundary segregant and embrittler in Al-Li-X-X alloys [*19*]. The elevated temperature exposures that produce the highest hardness in Alloy 3 are also the exposures that result in pop-in fracture behavior. It may be that the pop-in behavior can occur only when the yield strength is high enough for a critical stress to be achieved across a sufficient number of subgrain boundaries. When the hardness of Alloy 3 is observed to decrease after 9000 h of exposure at 107°C, the pop-in behavior is also eliminated, lending credence to the explanation proposed. Combination of the segregated lithium with copper and aluminum to form grain boundary T_1 precipitates at long times may also account for the recovery of T8 toughness levels after 9000 h of exposure.

An alternative explanation for the occurrence of the brittle boundary fracture in Alloy 3 follows. The ease of grain or subgrain boundary dimpled rupture is dependent on the size of grain boundary particles, the interparticle distance, and the area fraction of the boundary that is covered by the particles [*17,20*]. One might suppose that growth of existing particles would be faster at 135°C than at 107°C, while nucleation of new particles would be favored by the greater supersaturation achieved at 107°C. Hence, 107°C exposure would result in grain or subgrain boundaries that were populated by a greater number density of smaller particles relative to exposure at 135°C. In addition, the volume of precipitate may be lower after 107°C exposure, resulting in a narrower precipitate free zone (PFZ). It has been suggested that a narrow PFZ contributes to lower grain boundary strain to fracture and more rapid work hardening of the PFZ relative to wider PFZs [*21,22*]. The narrow, rapidly hardening PFZ and a strong matrix would result in high normal stresses that could cause decohesion of particle matrix interfaces at low strains. The small spacing between void nucleating particles would cause those voids to interact after very little growth [*21*] and could result in the type of fracture observed in Alloy 3 after 107°C exposures, which result in increased strength relative to the T8 condition (those between 1000 and 7000 h). The reduction in strength observed after 9000 h of exposure could prevent grain boundary stresses from rising to a level capable of causing interface decohesion (void nucleation) at the small grain boundary particles. So, the dominant fracture mechanism after 9000 h of exposure would revert to the MVC observed in the T8 material.

An explanation for the failure to observe smooth grain boundary facets in Alloy 2 is also required. Alloy 2 exhibits similar strength and composition as Alloy 3; however, its grain structure is significantly different. Recall that a large fraction of the grain boundary failures in Alloy 3 are subgrain boundary failures. Precipitates growing on subgrains in alloys similar to Alloy 3 [*5*] generally retain a higher aspect ratio than do those on high angle boundaries, which tend to assume a blocky morphology, and they tend to grow fastest in orientations that are nearly parallel to the boundary. This difference in aspect ratio and preferred orientation may result in greater areal coverage of subgrain boundaries versus grain boundaries for a given volume of boundary precipitate. In addition, the combined grain boundary and subgrain boundary area in Alloy 3 is much greater than that in Alloy 2 which, being recrystallized, has no subgrains. In Alloy 3 a continuous, fracture path along boundaries will be much more accessible that in Alloy 2: this alone could explain the absence of pop-in behavior in Alloy 2.

Summary

Except for the case of Alloy 3 exposed at 107°C, reductions in fracture toughness associated with elevated temperature exposure of precipitation-hardened alloys in this study correlate well with an increase in ductile intergranular failure. Toughness reductions and % IG fracture generally scale with the severity of elevated temperature exposures. It is proposed that the observed increases in the percentage of ductile IG fracture are a result of increased boundary precipitation with increased severity of elevated temperature exposure. The increased boundary precipitation may be occurring on high angle boundaries (all alloys) or low angle boundaries (Alloy 3).

The pop-in behavior observed in Alloy 3 occurs only after elevated temperature exposures, which produce the highest observed hardness levels in the alloy. The fracture appearance associated with the pop-in is brittle intergranular, and the *R*-curve behavior suggests a stress-controlled fracture mode [*17*]. The above observations indicate that some embrittlement phenomenon could be controlling fracture at the highest strength levels. Segregation of lithium has been reported to be energetically feasible in the embrittlement of Alloy 8090 and is a possible explanation for the observed behavior in Alloy 3 [*19*]; however, the possibility that finely dispersed precipitates on Alloy 3 boundaries after 107°C exposure are responsible for the pop-in behavior cannot be dismissed.

Based on this study and previous work on precipitation-hardened aluminum alloys intended for elevated temperature service [*6*], it is apparent that screening methods for microstructural stability that are based primarily on consideration of retention of strength are inadequate. Hardness (this study) and strength [*6*] may rise or remain steady with elevated temperature exposure; hence, no indication of material degradation is received. Changes in grain boundary character may become evident only in the severe stress state developed at a crack tip, as in a fracture test. In all cases, evaluation via mechanical testing should be coupled with identification of changes in fracture mechanisms via electron microscopy.

Acknowledgments

This work was performed under NASA Contract No. NAS1-19708, Task No. MM-2, D. M. Royster, Contract Monitor. The authors would also like to thank S. Hales for performing the texture determinations.

References

[*1*] Polmear, I. J. and Chester, R. J., *Scripta Metallurgica* Vol. 23, 1989, pp. 1213–1218.
[*2*] Polmear, I. J., *Transactions of the Metallurgical Society of AIME*, Vol. 230, October 1964, pp. 1331–1339.
[*3*] Vietz, J. T. and Polmear, I. J., *Journal of the Institute of Metals*, Vol. 94, 1966, pp. 410–419.
[*4*] Sen, N. and West, D. R. F., *Journal of the Institute of Metals*, Vol. 97, 1969, pp. 87–92.
[*5*] Mou, Y., Howe, J. M., and Starke, E. A., Jr., *Metallurgical and Materials Transactions A*, Vol. 26A, June 1995, pp. 1591–1595.
[*6*] Reynolds, A. P. and Royster, D. M., *Scripta Metallurgica et Materiala*, Vol. 30, 1994, pp. 1485–1490.
[*7*] Hales, S. J., unpublished research.
[*8*] Muddle, B. C. and Polmear, I. J., *Acta Metallurgica*, Vol. 37, No. 3, 1989, pp. 777–789.
[*9*] Huang, J. C. and Ardell, A. J., *Materials Science and Technology*, March 1987, Vol. 3, pp. 176–188.
[*10*] Starke, Jr., E. A., NASA Contractor Report 4645, Grant No. NAG1-745, February 1995.
[*11*] Randle, V., *Microtexture Determination and its Applications*, The Institute of Materials, London, UK, 1992.
[*12*] Anderson, T. L., *Fracture Mechanics: Fundamentals and Applications*, CRC Press, Boston, MA, 1991.
[*13*] *Aluminum: Properties and Physical Metallurg*, J. E. Hatch, Ed., ASM, Metals Park, OH, 1984.
[*14*] Garrett, G. G. and Knott, J. F., *Metallurgical Transactions A*, Vol. 9, September 1978, pp. 1187–1201.
[*15*] Becker, R. et al., *Acta Metallurgica*, Vol. 37, No. 1, 1989, pp. 99–120.
[*16*] *Physical Metallurgy Principles*, 2nd ed., Reed-Hill, R. E., PWS Publishers, Boston, MA, 1973.
[*17*] Ritchie, R. O. and Thompson, A. W., *Metallurgical Transactions A*, Vol. 16a, February 1985, pp. 233–248.
[*18*] Wang, J. S., *Scripta Metallurgica*, Vol. 25, 1991, pp. 1339–1344.
[*19*] Lynch, S. P. and Byrnes, R. T., *Proceedings*, Fourth International Conference on Aluminum Alloys, Vol. 2, 1994, pp. 444–451.
[*20*] Vasudevan, A. K. and Doherty, R. D., *Acta Metallurgica*, Vol. 35, No. 6, 1987, pp. 1193–1219.
[*21*] Kawabata, T. and Izumi, O., *Acta Metallurgica*, Vol. 24, 1976, p. 817.
[*22*] Abe, M., Asano, K., and Fujiwara, A., *Metallurgical Transactions A*, Vol. 4, June 1973, pp. 1499–1505.

Fan Yang,[1] *Ashok Saxena*,[1] *and Thomas L. Starr*[1]

Oxidation and Mechanical Damage in a Unidirectional SiC/Si_3N_4 Composite at Elevated Temperature

---

REFERENCE: Yang, F., Saxena, A., and Starr, T. L., "**Oxidation and Mechanical Damage in a Unidirectional SiC/Si_3N_4 Composite at Elevated Temperature,**" *Elevated Temperature Effects on Fatigue and Fracture, ASTM STP 1297*, R. S. Piascik, R. P. Gangloff, and A. Saxena, Eds., American Society for Testing and Materials, 1997, pp. 206–224.

ABSTRACT: The results of a study on the high-temperature damage mechanisms in a unidirectional Nicalon fiber-reinforced reaction-bonded silicon nitride (RBSN) composite are presented in this paper. The microstructure of the as-manufactured and tested specimens were characterized using a variety of techniques including: X-ray diffraction; optical, scanning, and transmission microscopy; and dilatometry. Single-edge notch specimens under three-point bend loading were tested under a constant displacement-rate condition as well as under a sustained loading condition at 1000°C in air. The load-line displacement was used as the in situ indicator of damage accumulation. The fracture surface and the damage zone around the main crack were characterized in the fractured specimens to investigate the high-temperature fracture mechanisms. Under constant displacement rate, the composite showed extensive nonlinear load versus displacement behavior, indicating that the presence of the fiber has indeed toughened the composite. Cracks propagated nominally along the notch plane, though some delaminations were also observed. The substantial bulk oxidation occurred even at test temperatures as low as 800°C and resulted in significant changes in the dimension of the composite specimens. The fiber pullout, fracture surface morphology, and delamination were all strongly influenced by the high-temperature oxidation.

KEYWORDS: ceramic matrix composite, reaction-bonded silicon nitride, Nicalon fiber, oxidation, damage, creep, cracks

The motivation to increase the thermal efficiency of heat engines has stimulated renewed interest in the use of ceramic components. Unfortunately, monolithic ceramics are extremely brittle. The need to improve their fracture resistance, hence the reliability of ceramic components, has pushed the research on ceramic matrix composites (CMCs) to the forefront of materials research and development [*1*].

Both silicon nitride and silicon carbide possess outstanding resistance to thermal shock, creep, and corrosion at elevated temperatures. Therefore, silicon-carbide-reinforced silicon nitride composites are considered as promising candidate materials for high-temperature components. However, prior to the engineering application, the fracture behavior of the composites must be thoroughly understood. On the other hand, for non-oxide ceramics, attention must be paid to the possible chemical degradation at high temperatures in an oxidizing atmosphere. Most of the research so far on silicon-carbide-reinforced silicon nitride composites has concentrated separately on either the mechanical behavior at room temperature or the bald oxidation

---

[1] Ph.D. candidate, professor and chairman, and principal research scientist, respectively, School of Materials Science and Engineering, Georgia Institute of Technology, Atlanta, GA 30332-0245.

effects of the materials at elevated temperatures [*2–4*]. Relatively little work has been devoted to correlate the crack growth and fracture behavior of the composites with long-term oxidation at high temperatures [*5,6*].

The defects in the as-manufactured composite have a significant influence on both the chemical and mechanical behavior of the composite since they can serve as the oxygen passages and also as fracture initiation sites during high-temperature loading.

Since this composite is designed for high-temperature applications, microstructural and dimensional stability in the service environment is a critical requirement. The oxidation throughout the bulk material will alter not only the material properties but also the component dimensions. Even local oxidation in regions containing cracks will have considerable influence on the fracture behavior. This therefore provides the impetus for the present work.

Materials and Experimental Procedure

Test Materials

The continuous Nicalon fiber-reinforced RBSN composite used in this research is manufactured using the reaction sintering technique [*7*]. The ceramic grade Nicalon fiber has a diameter of approximately 15 μm and consists of a Si-C-O compound [*1*]. Filament winding is used to fabricate the green composite, which yields a relatively homogeneous impregnation of the silicon powder into the gaps between fibers. In this process, first, the fiber tow is impregnated with a slurry of attritor-milled 0.2 to 0.5-μm-diameter silicon powder in ethanol with the addition of a fugitive binder and a dispersant. Then, the fiber tow is wound upon a mandrel with a tow spacing of 0.5 mm per turn to form a unidirectional fiber tape. The number of wound fiber tow plies is determined by the required composite plate thickness. A typical nitriding step consists of heating the dried and dimensionally constrained green composite plates in vacuum to 900°C, followed by filling the furnace with a gas mixture of 95% nitrogen and 5% hydrogen. The temperature is then ramped to 1200°C. During the reaction sintering process, the pressure in the furnace is maintained at the ambient level by adding nitrogen as it is consumed by the reaction. After holding at the maximum temperature for up to 3 h, samples are cooled and removed from the furnace. Examination of the cross section of the composite showed that the silicon powder penetrates into the fiber tows satisfactorily because minimal fiber touching was observed. Since the fiber tow was wound onto the mandrel layer by layer, the composite has an alternate fiber-rich and matrix-rich layer structure. The thickness of the matrix-rich layers is controlled by the packing of the silicon powder into the fiber tows during the green composite manufacturing process.

For comparison, pure RBSN was also fabricated with the same sintering process starting from the same raw silicon slurry. Microstructural characterization was performed on this pure RBSN. Since the microstructure of pure RBSN was very different from the microstructure of RBSN in the composite matrix, no further mechanical testing was conducted on this pure RBSN. It was felt that no meaningful comparisons between properties could be made between pure RBSN and the RBSN in the composite matrix. There are some free fibers at the incompletely densified composite plate edges. Loose fibers were split from these composite edges to investigate the damage on the fiber caused during the whole composite manufacturing process.

Microstructural Characterization

The polished cross sections of the as-received material and the material tested at 1000°C, as well as the pure RBSN, were examined with the optical microscope. The porosity associated with the large pores was measured using the point counting method on the video screen attached to the optical microscope to determine the area fraction [8,9]. For continuous fiber composites, the area fraction of fibers is also equal to the volume fraction of fibers. Surfaces of the fibers subjected to different processes were examined using SEM. Finely polished composite samples were exposed to hydrofluoric acid for 5 min, which is expected to selectively etch out the silicon dioxide. Thereafter, the silica-rich regions could be identified under the microscope as evidence of oxidation.

The samples of the composite and the composite constituents as shown in Table 1 were examined using an X-ray diffraction (XRD) pattern to investigate the composition and microstructural changes caused by reaction sintering and 1000°C exposure in air. The machine parameters for X-ray generation and collection were maintained the same for collecting the XRD data for all the samples. Therefore, the relative peak intensities in the spectra have certain quantitative comparability. Since XRD can only obtain data averaged over a relatively large region, composite samples were also examined under a transmission electron microscope (TEM) and the attached energy dispersive X-ray spectrometer (EDS) to determine the local crystal structures and compositions.

The dimensional changes of the composite at different temperatures were studied using a computer-controlled double push rod dilatometer [10]. Rectangular bars were prepared with their length oriented in the directions perpendicular and parallel to the reinforcing fibers to measure the transverse and longitudinal thermal expansions of the composite as temperature changed. The constant temperature dilatometry measurement was conducted at 600, 700, 800, 900, and 1000°C with a hold time of 10 h at each temperature. The heating rate of the dilatometer furnace between each temperature stage was chosen as 3°C/min to allow uniform temperature throughout the sample.

Mechanical Tests

Single-edge-notched bend (SENB) bars were machined from the as-manufactured composite plates. These specimens were used to perform the high-temperature fracture tests. The specimen geometry and loading configuration are illustrated in Fig. 1. The ratio of the initial crack length, a_0 to the width, W, is 0.3 to permit sufficient remaining ligament for studying the crack propagation behavior. The three-point bend geometry also assists in maintaining the crack growth along the notch plane since the maximum stress occurs only on this plane. Due to the brittleness of ceramic materials, fatigue precracking is difficult and also not deemed necessary because the microcracks produced during the specimen machining can serve the same purpose as the precrack [11]. The conventional crack monitoring techniques, such as compliance measurement, are not directly applicable to this material at elevated temperature due to nonlinearities associated with creep [12]. Further, the presence of the fiber makes the definition of a crack length somewhat ambiguous due to phenomena such as fiber bridging and asynchronous break-

TABLE 1—*The sample conditions for XRD analysis.*

Number	Material	1000°C Exposure Time, h	Sample State
A	As-received Nicalon fiber	. . .	Powder
B	Fiber split from composite	. . .	Powder
C	Pure RBSN matrix	. . .	Solid surface
D	As-manufactured composite	. . .	Solid surface
E	Composite	20	Solid surface
F	Composite	135	Solid surface
G	Composite	520	Solid surface

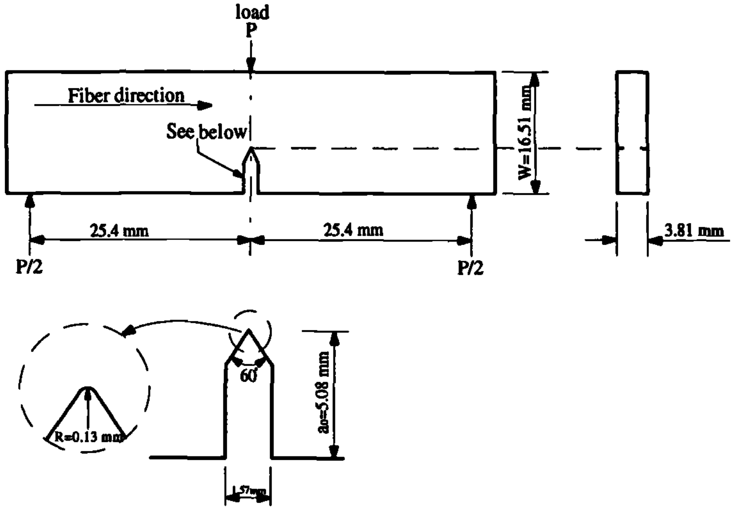

FIG. 1—*The specimen configuration and the loading mode.*

age of the fiber and the matrix. Some success has been achieved in correlating electrical resistance to damage development at room temperature but not at high temperatures. The in situ damage development at elevated temperatures can only be measured qualitatively by monitoring the load-line displacement.

Three-point bend tests were performed at 1000°C in air. A special loading fixture was designed to perform the bend test in a tensile loading frame. One specimen was tested with monotonic loading at a constant load-point displacement rate of 50 μm/min while continuously monitoring load and load-line displacement. Two specimens were tested under dead-weight loading in a creep test frame at load levels of 175 and 215 N and held at 1000°C for 115 and 500 h, respectively. Prior to loading, all specimens were soaked at 1000°C for 20 h to stabilize the temperature in the furnace.

Results and Discussion

Microstructural Characterization

Figure 2 shows the optical micrographs of the pure RBSN and the as-manufactured composite. It can be seen that the pores in the RBSN have a uniform spatial distribution and are smaller in size compared to the pores in the composite, which are irregular in shape and vary in size. The majority of the large pores in the composite are concentrated in the fiber-rich regions. Such pores can potentially decrease the fracture strength and oxidation resistance of the composite by serving as fracture initiation sites and also passages for oxygen. The measured porosities for the pure RBSN and the composite were 6 and 16 vol%, respectively. When microscale porosity is also included [*11,13*], the total porosity in the composite is estimated to be in the range of 35 to 40 vol%. Thus, the 16% porosity mentioned above applies only to the large pores. The fiber fraction of the composite is also measured using the point-counting technique to be approximately 15 vol%.

Figure 3 shows SEM micrographs of an as-received fiber, fibers exposed to 1000 and 1200°C (the test temperature and the peak manufacturing temperature, respectively) in air for 2 h, and a free fiber removed from the loose plate edge of the as-manufactured composite. The as-

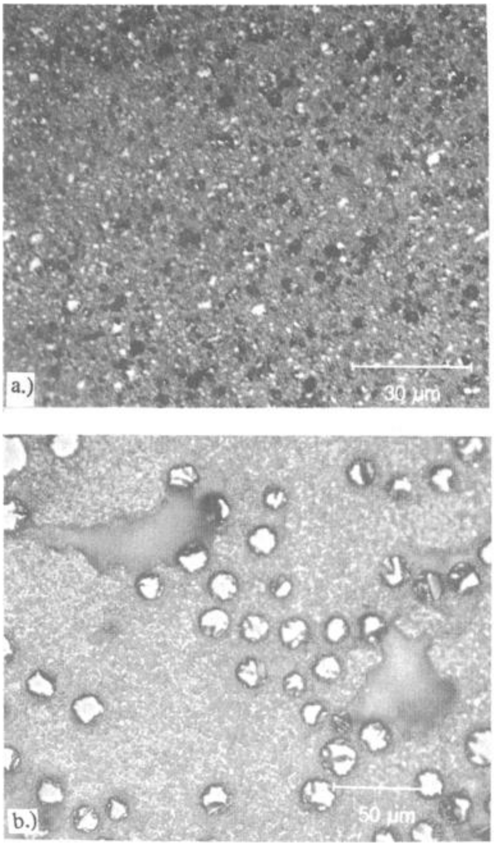

FIG. 2—*The micrographs of the as-polished cross sections:* (a) *RBSN;* (b) *as-received composite.*

received fiber has a smooth surface, and no visible damage is detected in the fiber exposed to 1000°C. Some superficial reaction spots are evident on the otherwise smooth surface (Fig. 3*c*) of the fiber exposed to 1200°C. By comparison, the loose fiber extracted from the composite edge appears to have damage spots that run deeper into the fiber (Fig. 3*d*). This indicates that heating in air is less aggressive for the fiber than the reaction sintering process, in which a combination of nitrogen and hydrogen was used along with the silicon powder and the accompanying impurities. There are numerous low-density whisker mats around the fiber split from the composite. Since the formation of α-Si_3N_4 in the form of whisker mats [*13*] is favored at reaction temperatures below the silicon melting point, whisker mats that stick to fibers in the composite are assumed to be a reaction sintering product of α-Si_3N_4.

XRD Data—Figure 4 is the XRD patterns obtained from various samples as listed in Table 1. Pattern A, obtained from the initial Nicalon fiber powder, demonstrates that the as-received fiber consists of ultra-fine β-silicon carbide, consistent with the manufacturer's report [*14*], which noted that the Nicalon fiber is homogeneously composed of ultra-fine β-SiC crystals

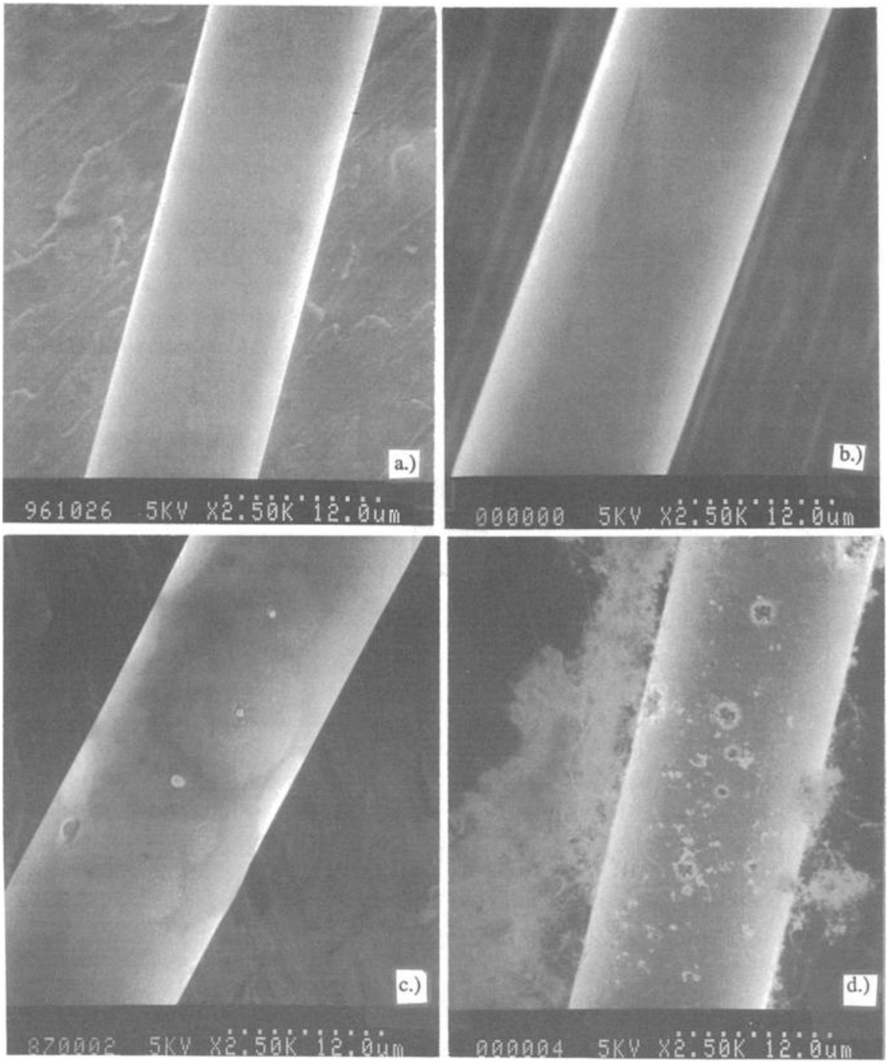

FIG. 3—*The SEM photos of the different fiber:* (a) *as-received;* (b) *fired at 1000°C in air for 2 h;* (c) *fired at 1200°C in air for 2 h;* (d) *split from failed composite.*

with excess carbon and 9 to 11% oxygen. Pattern B from the ground powder of the loose fibers extracted from the composite edges shows α-Si_3N_4 peaks and β-SiC humps. The β-SiC humps indicate that the reaction sintering process does not induce grain growth in the fiber. The TEM diffraction pattern inside the fiber showed a ring pattern resulting from the ultra-fine crystal grains, while the diffraction from the matrix region in the composite showed clear diffraction spots. In addition, the local EDS spectrum obtained from inside of the fiber in the composite also confirmed that the fiber has a uniform Si-C-O composition [*15*]. The α-Si_3N_4 peaks observed in the XRD pattern of the powdered fibers split from the composite are attributed to the loose reaction sintering product of whisker mats stuck on the fiber surface.

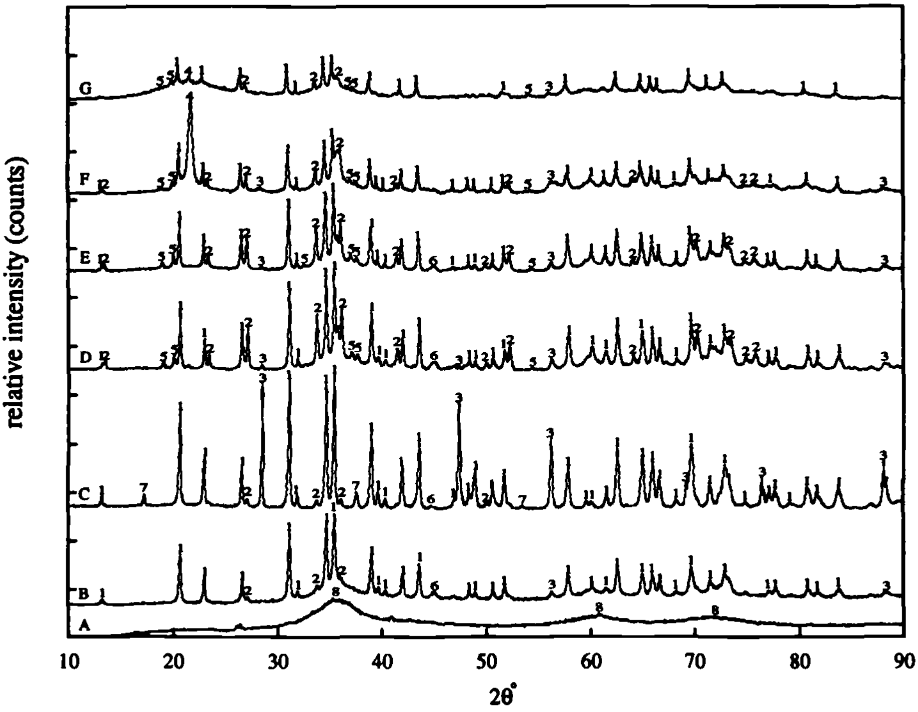

FIG. 4—*The XRD spectra of samples listed in Table 1. Note: 1 = α-Si_3N_4; 2 = β-Si_3N_4; 3 = silicon; 4 = crystobalite (SiO_2); 5 = Si_2ON_2; 6 = $C_{0.17}Fe_{0.81}Si_{0.02}$; 7 = Ferrous disilicide ($FeSi_2$); 8 = β-SiC.*

The XRD pattern, labelled C, from the pure RBSN has much more residual elemental silicon than the composite samples. This indicates that the high porosity and coarse pores in the composite matrix may be helpful during nitriding of silicon in the reaction sintering process since these open pores assist the nitrogen in infiltrating into the whole green composite plate. The ferrous disilicide ($FeSi_2$) is exclusively found in the pure RBSN sample. Carbon, iron, and silicon compound ($C_{0.17}Fe_{0.18}Si_{0.02}$) has stronger peaks in the powder sample of the fiber extracted from the composite and also in samples from other composites but was not observed in the RBSN sample. This implies that, during the sintering process, the iron—a trace contaminant generated during attritor milling—reacts with the excess carbon in the fiber and the silicon to form the compound, which concentrates in the fiber-rich regions of the composite, perhaps at the fiber/matrix interface. It is also possible that at high temperatures in the reducing nitrogen atmosphere SiO may escape from the fiber surfaces and form silicon oxynitride or even silicon nitride [*1,13*]. These two reactions occurring during the reaction sintering process may explain the damage spots seen in Fig. 3*d* on the surface of the fiber removed from the as-manufactured composite edge.

The XRD Pattern D of the as-manufactured composite shows that the composite contains mainly silicon nitride and traces of residual silicon, silicon oxynitride (Si_2ON_2), and the carbon, iron, and silicon compound. These observations are consistent with the observed composition of the fiber that was extracted from the composite, as demonstrated in Pattern B. The matrix contributes silicon nitride and residual silicon in addition to the peaks corresponding to the composition of the interface and the fiber.

Comparing the XRD pattern labelled from D to G in Fig. 4, it is evident that the composite oxidized at 1000°C by a reaction between Si_3N_4 and oxygen to form silicon dioxide. As the exposure time increases, the amount of silica increases dramatically, while no silica was detected in the as-manufactured composite. The relative intensities of silica humps or the crystobalite peaks from Sample E to Sample G increase greatly, and the corresponding intensities of Si_3N_4 peaks decrease sharply. At 1000°C, glassy silica has a tendency to crystallize into crystobalite [*16*]. However, at this temperature the transformation needs to overcome a relatively high nucleation energy barrier. Therefore, whether the transformation can take place is determined by the availability of proper crystal nucleation sites in the material. Even subtle material condition change, such as a residual finger print on the original sample surface, can alter the transformation. Accordingly, it is easy to understand why Sample G, which was exposed to 1000°C for 520 h, has much less crystobalite than Sample F, which was exposed to the same temperature for 135 h. However, it is clear that the oxide content in Sample G is more than in Sample F as indicated by the decreasing relative Si_3N_4 peak intensities. Even though only one pattern is presented for each sample in Fig. 4, scanning at different sample depths of the same composite specimen yielded similar patterns.

Optical Microscope and SEM Analysis—Figure 5 shows optical micrographs of the polished cross sections of the composite in the as-manufactured condition and after exposure to 1000°C in air for 520 h. It shows that the matrix in the high-temperature exposed composite is flatter and has higher reflectivity. This may be due to the fact that newly produced high-volume silica sealed some matrix pores. Figure 6 shows the same sections but etched in hydrofluoric acid for 5 min. It appears that the hydrofluoric acid did not attack the as-manufactured composite because its appearance is the same as before etching. On the other hand, the etchant severely attacked the regions surrounding the fibers in the composite exposed to 1000°C in air for 520 h. The large voids produced by the etchant in the matrix regions surrounding the fibers were visible even more clearly under SEM at high magnification. Because hydrofluoric acid selectively attacks silicon dioxide, it can be concluded that the etched regions are where the silicon dioxide formed during high-temperature exposure.

Silicon nitride is thermodynamically unstable in comparison with the oxide in air at high temperatures [*1,17*]. However, the oxidation rate of the nitride depends strongly on the porosity and impurities in the original silicon nitride and the environmental conditions. The pure dense silicon nitride can resist oxidation up to 1500°C [*18*]. Nevertheless, a silicon nitride specimen with low-density, coarse open pores and high impurity content such as the RBSN in the composite matrix will oxidize at a much lower temperature. Because the densities of glassy silica and crystobalite are 2.2 and 2.7 g/cm^3, respectively, and the density of Si_3N_4 is 3.2 g/cm^3, the oxidation of Si_3N_4 will result in a more than 50% volume increase. In the case of porous RBSN, as long as the pore radii are mainly below 0.04 to 0.05 μm, the surface pores will be effectively sealed by the initial oxidation products. This stops further supply of oxygen to the inner material [*17*]. It has been shown that silicon nitride specimens with large thickness and containing only small pores do not show detectable oxidation in the interior up to temperatures as high as 1300°C [*17*].

As discussed previously, the matrix in the composite has high porosity consisting of coarse open pores. Thus, oxygen can easily penetrate into the inner material, and the oxidation can begin on the surface and the interior of the sample simultaneously. Since the open pores are too big to be effectively sealed by the oxidation products, the whole specimen will be oxidized rapidly. In addition to the coarse open pores in the matrix, the loose whisker mat layer around each fiber, as shown in Fig. 3, also forms a cylindrical open passage for oxidation. The hydrofluoric acid-etched sample of the high-temperature exposed composite shown in Fig. 6 proves that the regions around fibers are oxidized more severely than the surrounding dense matrix

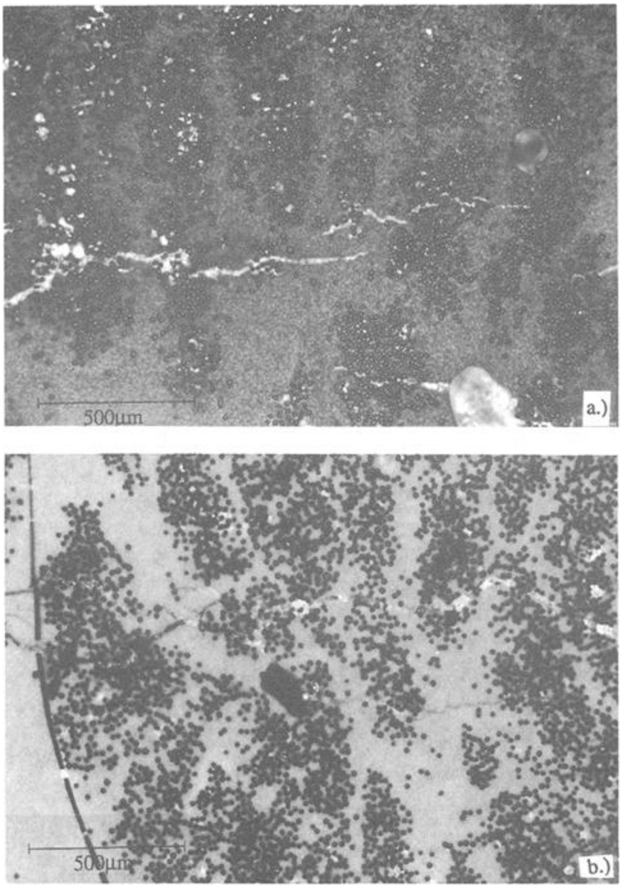

FIG. 5—*The as-polished composite surface:* (a) *in the as-manufactured condition;* (b) *after exposed to 1000°C for 520 h.*

regions. The identical XRD patterns obtained at different sample depths of the same high-temperature exposed specimen verify that the oxidation took place throughout the whole sample thickness during the high-temperature exposure.

The oxidation proceeds into grains through the grain boundary after the surfaces are oxidized and results in the destruction of the crystalline nature of the boundaries [*17*]. The grain-boundary glassy phase that forms will facilitate the relative grain movement, which enhances creep deformation. However, the crystallization of the silica in the boundary phase will compensate for some of the creep-enhancing effect of the glassy phase because the crystalline phase is expected to have a higher thermal activation barrier for viscous processes such as creep in the boundary layer. The unpredictability of the transformation from silica to crystobalite at 1000°C makes predicting the creep behavior of the composite even more complicated.

Thermodynamically, SiC is also unstable in air at high temperatures. However, the photomicrograph in Fig. 3 shows that the oxidation does not attack the fibers in the composite

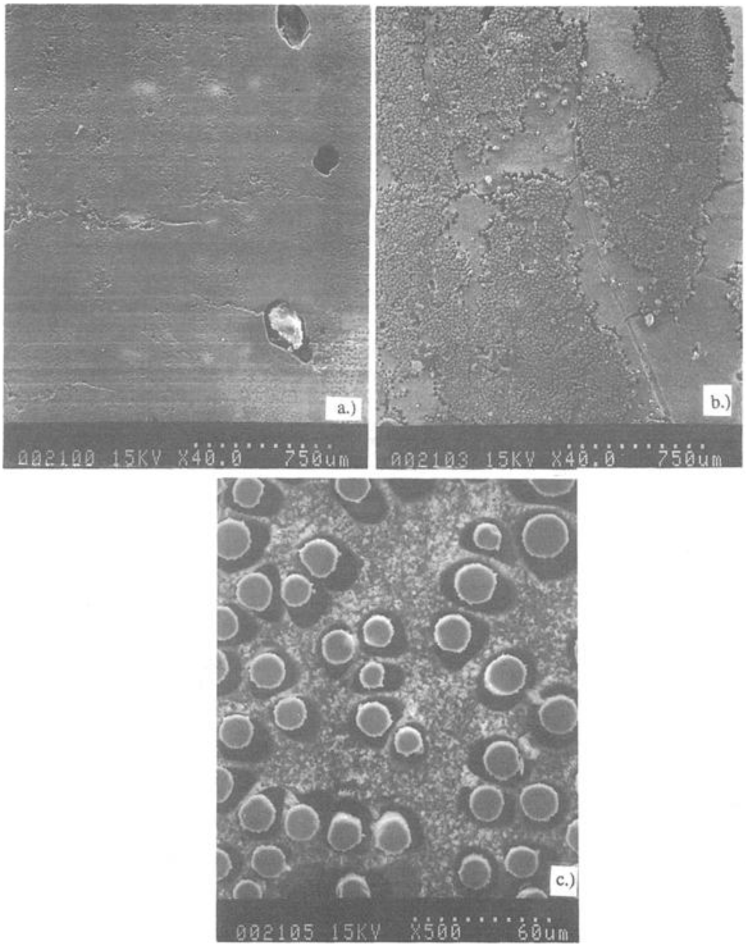

FIG. 6—*The polished and etched (in HF for 5 min) surfaces of the composite:* (a) *in the as-manufactured condition;* (b, c) *after exposed to 1000°C for 520 h.*

significantly during the 1000°C exposure. The oxidation resistance of the fibers may be a result of its finer pore size and a higher density compared with the matrix. On the other hand, the silica surrounding the fiber formed by the oxidation of the loose Si_3N_4 whisker mat may also have served as a sealing layer, thus stopping the oxygen from diffusing into the fiber.

Figure 7 shows the expansion of the composite as a function of time at various temperatures in both transverse and longitudinal directions. These results clearly demonstrate that for temperatures equal to or higher than 800°C, the specimens were expanding even when the temperature was held constant. Since the oxidation of either Si_3N_4 or SiC will result in volume expansion, the expansion confirms that the oxidation occurs in the composite in air at a temperature as low as 800°C. It is also evident from Fig. 7 that the dimensional change caused by the oxidation is larger in the transverse direction than in the longitudinal direction. This verifies

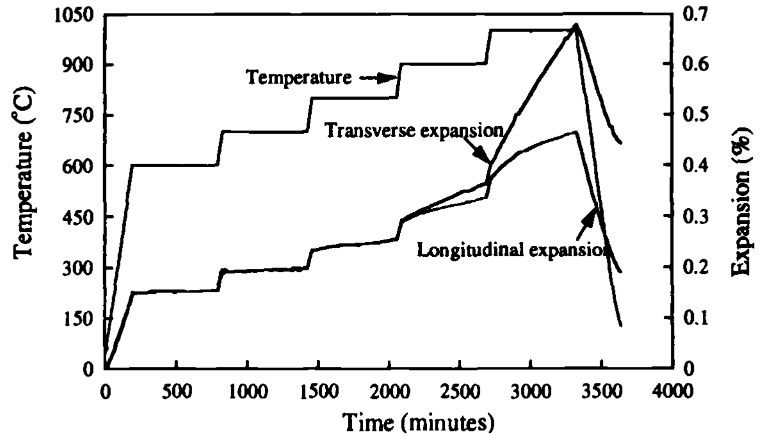

FIG. 7—*The expansion of the composite at different temperatures.*

further that the fiber was less oxidized than the matrix since the less oxidized fibers will constrain the longitudinal expansion of the composite while the constraint is significantly smaller in the lateral direction.

Fracture and Crack Growth Tests

Figure 8 is the load versus load-line displacement plot of the test conducted on the composite under displacement-controlled monotonic loading conditions. Several sharp load drops were observed throughout the plot. These sudden load drops were caused by unstable crack propagation. Since the fiber is the toughening element, the sudden load drops may have been caused by fracture of the fiber tows at the crack tip, by sudden debonding of the fiber tows from the matrix, or by sudden crack propagation in the composite between two strong fiber-rich regions. However, throughout the test, the composite held reasonable strength value and did not fail catastrophically. In fact, subsequent to each load drop, an increased load was necessary to

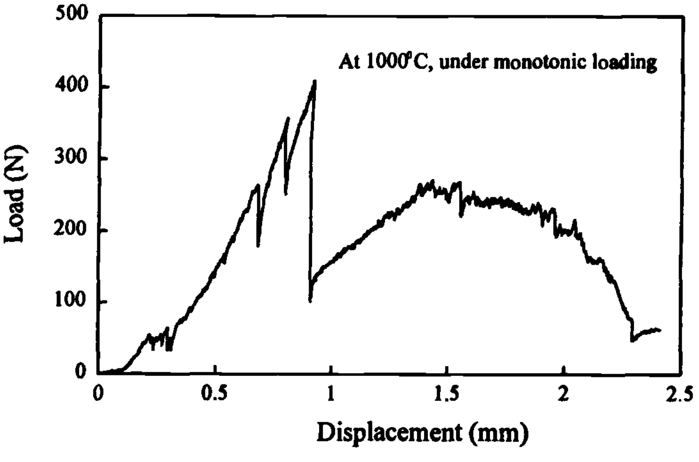

FIG. 8—*The load versus load-line displacement for the monotonic loading test.*

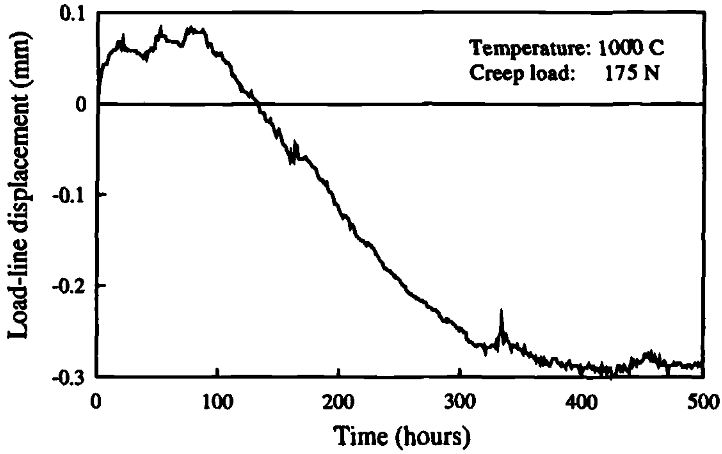

FIG. 9—*Load-point displacement versus time plot of the creep test.*

continue further deformation such as observed for ductile materials which show a rising *R*-curve type behavior. This indicates that the presence of the reinforcing fibers has toughened the ceramic matrix.

Figure 9 is the plot of load-point displacement versus test time during a sustained load test at a load of 175 N and a temperature of 1000°C. The initial time and zero displacement are defined as the point immediately after the test load was applied to the specimen following heating and soaking. Thus, the elastic deformation caused by loading and the thermal expansion during heating and soaking periods (20 h) are eliminated in this plot. Except during the initial period, the displacement during the sustained load tests gradually decreased. Such behavior can only be caused by a change in specimen dimension due to oxidation, which apparently dominated the displacement measurement. Figure 10 shows the relationship between the post-

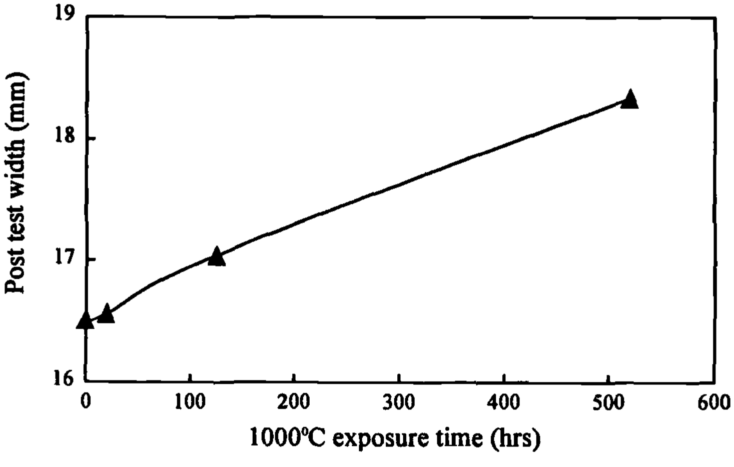

FIG. 10—*Post-test specimen width versus 1000°C exposure time.*

test specimen width as a function of exposure time at 1000°C, showing a continuous increase with time and confirming the above postulate. This result plus the dilatometer measurement in Fig. 7 imply that under the test conditions the oxidation rate follows a linear kinetic law [*19*].

From Fig. 9 it appears that the composite has a high initial inelastic, time-dependent deformation rate. This may be due to the fiber/matrix interfacial glassy silica layer that formed during the heating and the soaking period from the oxidation of the loose Si_3N_4 whisker mats. The silica layer will aid the fiber/matrix sliding, and it is possible that during the initial period of the test, the displacement caused by sliding processes dominated the expansion produced by oxidation. However, as time progresses the dimensional changes due to oxidation overwhelm the effects due to deformation. The displacement versus time plot also shows that a state of nearly constant displacement is reached after 400 h. There are two possible explanations for the constant displacement stage. The first is that the oxidation reaction slowed down as the available Si_3N_4 was consumed or the oxygen paths were increasingly blocked by the oxide. The second explanation is that as the silica amount increases in the whole specimen, providing more opportunity for the fiber/matrix interface and the grain boundary to slip and thus enhancing the creep rate, which will tend to contribute positively to the displacement. Simultaneously, the displacement rate may also have increased due to damage accumulation and the resultant stiffness reduction of the composite. More tests are needed to determine which one is the controlling factor. Fracture in these specimens occurred when the specimen was cooled down to about 800°C after completion of the 1000°C exposure.

Fracture Mechanisms

Figure 11 shows the crack profiles of the three fractured specimens. All the cracks appear to be propagating nominally along the notch plane. Delamination along the fiber direction is observed in all three specimens, but the extent of delamination seems to decrease with an increase in high-temperature exposure time.

Figure 12 shows the appearance of the pulled-out fibers from the three fractured specimens. Substantial loose whisker material remained attached to the fiber pulled out from the 20-h exposed specimen and only some particles adhere on the smooth fiber surface. There is a thick layer of loose material surrounding the fiber pulled out from the 120-h exposed specimen. The fiber from the 500-h tested specimen has a dense and clean layer at the surface that is most likely the silica layer from the interface oxidation. The fiber pull-out length over the whole crack plane was examined. The longest pulled-out fiber length for each fractured specimen was measured using SEM. It shows that this length decreases as the high-temperature exposure time increases. The measured longest pulled-out fibers are 360, 170, and 75 μm for specimens subjected to 1000°C for 20, 135, and 520 h, respectively. These observations clearly display the increase in the bonding between the fiber and the matrix with increasing 1000°C exposure time.

The XRD Pattern E in Fig. 4 shows that for 20-h exposure at 1000°C, oxidation has not attacked the composite substantially. The pulled-out fiber in Fig. 12*a* shows that after this short time exposure, loose whiskers that formed during the composite manufacture remained on the fiber surface. The loose whisker layer, along with the possible glassy silica in the interface regions that formed during the heating and soaking period, may assist the relative sliding between the fiber and the matrix as argued before. As the exposure time increased, more loose Si_3N_4 whiskers at the interface were converted into dense and high-volume oxide. The fiber/matrix interface was strengthened by the oxide. When this new interface is stronger than the surrounding matrix, some loose matrix material will be pulled out with the fiber from the composite as seen in Fig. 12*b*. On the other hand, if the oxidation produces a uniform glassy silica layer which has low viscosity at high temperature, around the fiber, the pulled-out fibers

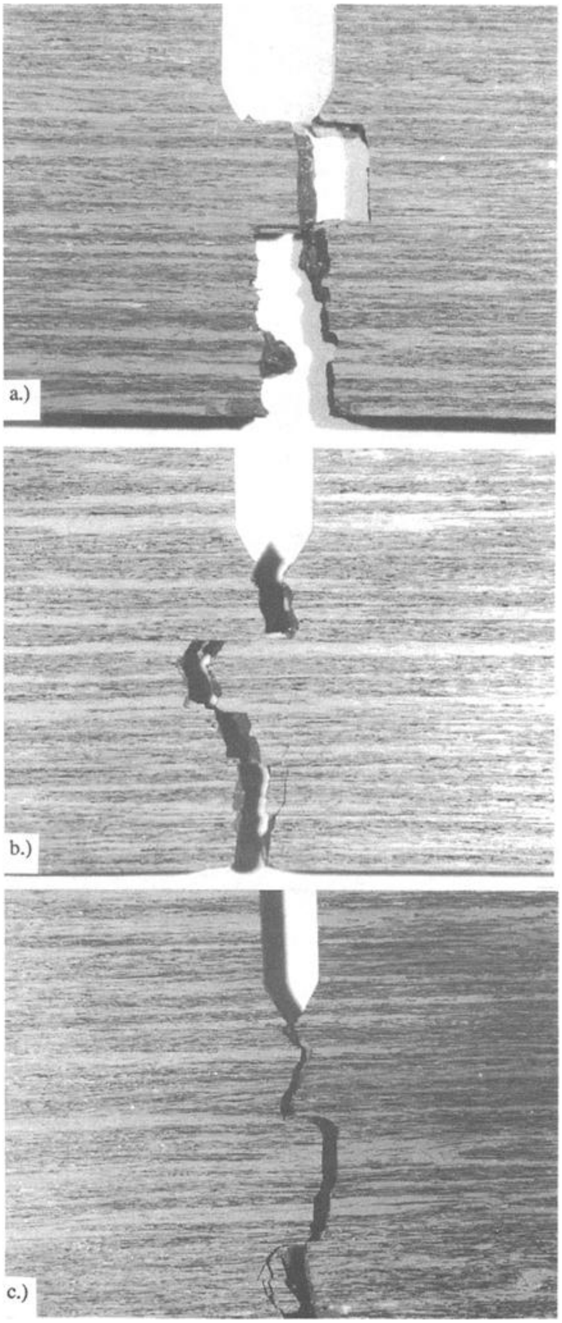

FIG. 11—*The fractured specimens tested under different conditions:* (a) *monotonic loading;* (b) *215 N, 115 h;* (c) *175 N, 500 h.*

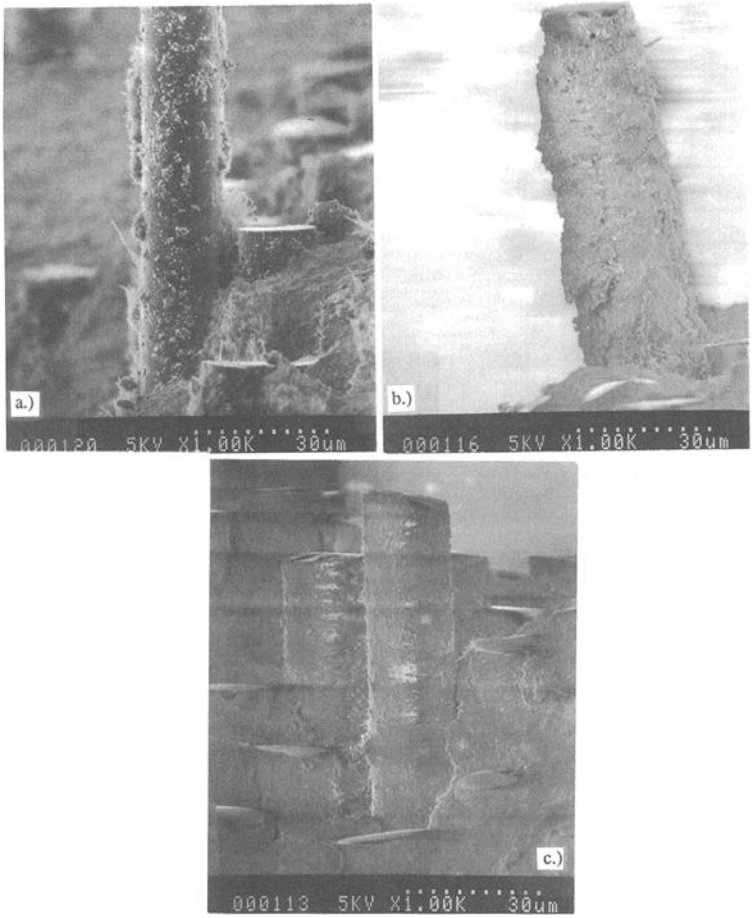

FIG. 12—*The pulled-out fibers from the composite specimens shown in Fig. 11.*

will have a clean surface, as in the case of the third fiber in Fig. 12*c*. The above arguments are only rational after-the-fact explanations. From these results, it is not possible to make any predictions on the nature of the interface unless a better understanding of the kinetics of the formation of crystalline silicon dioxide is available.

Figure 13 shows the fracture surfaces of the three tested specimens close to the notch tip. The fracture surface becomes flatter as the exposure time increases. No obvious steps of different height can be observed on the fracture surface of the specimen that was tested under a sustained load for 500 h, while such steps were observed around some fibers on the other two fracture surfaces. In Fig. 13*a*, from the specimen exposed to temperature for 20 h, the fiber fracture is flat. However, the matrix surrounding the fiber was uneven. Thus, the overall roughness was higher in this specimen than for the other two cases. This is another indication that oxidation has altered the interface behavior. When the interfacial strength is low, as the crack approaches the fiber, debonding will deflect the crack [*20*]. The crack has to restart when it passes a fiber to be able to propagate further. This will produce an uneven

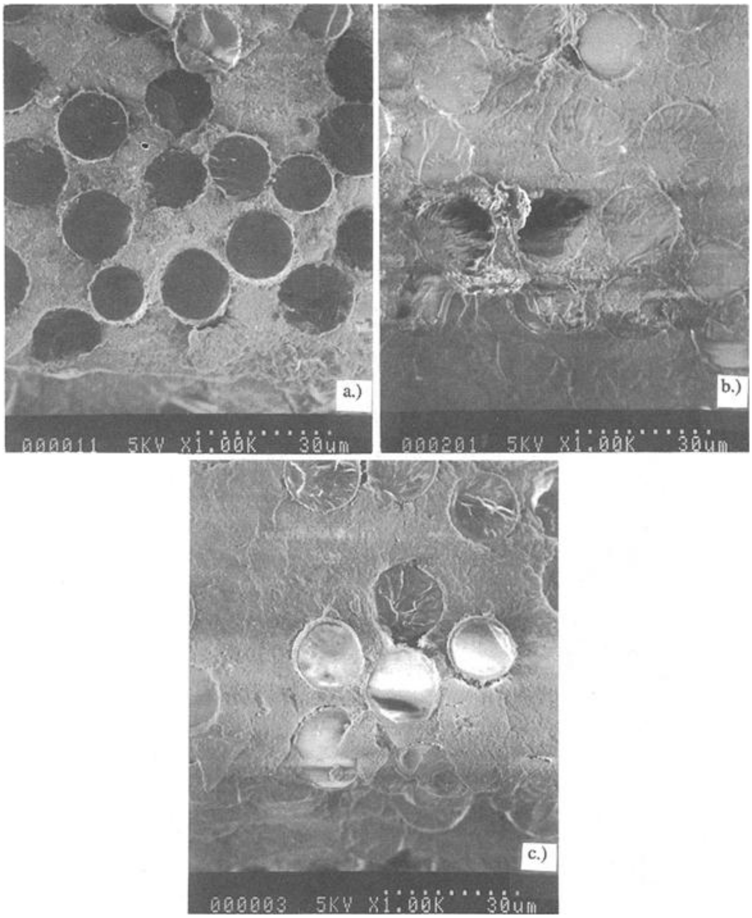

FIG. 13—*The fracture surfaces of the specimens shown in Fig. 11.*

fracture surface. In contrast, when the interface is strong, such as after longer exposure periods, the crack will cut through the fiber directly and produce a flatter fracture surface. The strengthening of the interface will decrease the composite toughness since the crack can cut through the fiber directly.

Figure 14 shows the polished longitudinal sections of the fractured specimens close to the crack plane. The photomicrographs reveal that delamination occurs primarily in the fiber-rich region where the matrix was not well consolidated and defects are present. Some transverse matrix cracking around the main crack plane is also evident on the specimen, which was tested under monotonic loading. These transverse matrix cracks occurred in the region halfway between the notch tip and the back edge of the specimen and appear to have grown just in the matrix region bounded by fiber tows. The transverse matrix cracks are bridged or stopped by the fibers in their paths of propagation. The formation of these transverse cracks must be time and stress state dependent since no such transverse matrix cracks are found in the two specimens tested under sustained load. The formation of these transverse matrix cracks can be explained

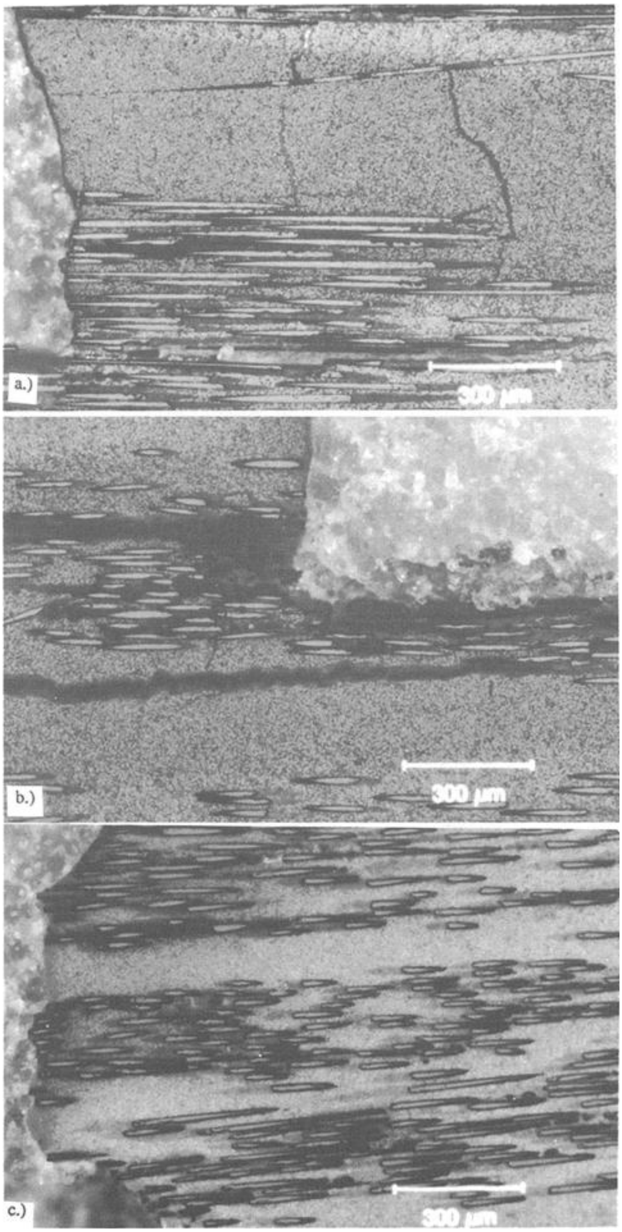

FIG. 14—*The longitudinal sections of fractured specimens shown in Fig. 11.*

using the shear-lag model [*21,22*], which states that the applied stress in the matrix is transferred to the fiber by means of the interfacial shear stress and if the fiber is strong enough multiple transverse cracks will occur in the matrix. The formation and propagation of such secondary cracks will consume extra energy and will thus effect material toughening.

More testing at different temperatures is necessary to fully characterize the mechanical damage in these composite systems in the absence of environmental effects. In the future, more tests are planned at 1000°C and below 800°C to further understand the changes in microstructure due to thermal effects and to provide further insight into the complex damage mechanisms during the simultaneous presence of oxidation and creep.

Summary and Conclusions

The high-temperature fracture behavior of the unidirectional Nicalon fiber-reinforced RBSN composite was studied. The microstructure of the as-received and post-high-temperature exposed materials was extensively characterized. Three-point bend tests were performed on the SENB specimens of this composite at 1000°C in air to determine the fracture mechanisms under these conditions. The oxidation of the composite and its effects on the fracture behavior at elevated temperatures were discussed.

The composite was found to have high porosity and many coarse open pores, especially in the fiber-rich regions. A loose whisker layer of Si_3N_4 at the fiber/matrix interface was also observed in the composite. This structure makes the composite sensitive to oxidation, which was observed at a temperature as low as 800°C. Severe oxidation attacked the matrix material at 1000°C in air, while the reinforcing fiber remained almost unattacked. The oxidation caused the composite to expand substantially in the transverse direction. By comparison, the expansion in the fiber direction was smaller due to the constraint imposed by the fibers.

The oxidation changed the matrix properties and the interface structure in the composite. XRD studies showed that as the 1000°C exposure time increased, the oxidation increased greatly. At 1000°C, the oxidation of the composite increased linearly with time and the products included glassy silica as well as crystobalite. It was not possible to predict under what conditions crystobalite forms at 1000°C; it is thus difficult to predict the influence of oxidation on the fracture mechanisms at this temperature because the formation of crystobalite or glassy silica have very different influences on the strength of the fiber/matrix interface.

Under three-point bend loading, despite some delamination and secondary matrix transverse cracking, the crack initiated and propagated nominally along the notch plane in the direction perpendicular to the principal stress direction, i.e., the Mode I cracking direction. However, some weak fiber/matrix interfacial regions in the composite deflected the crack in the transverse direction, causing delamination. This crack deflection temporarily stopped the major crack propagation and contributed to the crack growth resistance of the composite.

Acknowledgments

The authors wish to acknowledge partial support of NSF Grant MSS-9202932 from the Engineering Directorate for this study. The composite materials were fabricated with the support of the U.S. Department of Energy, Fossil Energy Advanced Research and Technology Development Materials Program. The assistance of R. C. Brown in mechanical testing, R. F. Speyer in dilatometry measurements, and S. R. Stock in X-ray measurements is also gratefully acknowledged. All are associated with the School of Materials Science and Engineering at the Georgia Institute of Technology.

References

[1] Mazdiyasni, K. S., *Fiber Reinforced Ceramic Composites, Materials, Processing and Technology*, Noyes Publications, Park Ridge, NJ, 1990.

[2] Starr, T. L. and Mohr, D. L., "GT-1 Development of Advanced Fiber Reinforced Ceramics," GTRI report, Materials Science and Technology Laboratory, Georgia Tech Research Institute, Atlanta, 1993.

[3] Mah, T., Hecht, N. L., McCullum, D. E., et al., "Thermal Stability of SiC Fibers (Nicalon ®)," *Journal of Materials Science*, Vol. 19, 1984, p. 1191.

[4] Wilcox, W. R., *Preparation and Properties of Solid State Materials*, Vol. 7, Marcel Dekker, Inc., New York, 1982.

[5] Henager, C. H., Jr. and Jones, R. H., "The Effects of an Aggressive Environment on the Subcritical Crack Growth of a Continuous-Fiber Ceramic Composite," *Ceramic Engineering and Science Proceedings*, Vol. 13, 1992.

[6] Bhatt, R. T., "Oxidation Effects on the Mechanical Properties of A SiC-Fiber-Reinforced Reaction-Bonded Si_3N_4 Matrix Composite," *Journal of American Ceramic Society*, Vol. 75, 1992, p. 406.

[7] Starr, T. L., Mohr, D. L., and Hanigofsky, J. A., "Development of Silicon Nitride Composites with Continuous Reinforcement," *Proceedings*, Seventh Annual Conference on Fossil Energy Materials, Oak Ridge, TN, May 1993, p. 79.

[8] ASTM Standard E 562-89, Practice for Determining Volume Fraction by Systematic Manual Point Count, *Annual Book of ASTM Standards*, Vol. 03.01.

[9] Underwood, E. E., *Quantitative Stereology*, Addison-Wesley Publishing Co., Reading, MA, 1970.

[10] Speyer, R. F., *Thermal Analysis of Materials*, Marcel Dekker, Inc., New York, 1994.

[11] Richerson, D. W., *Modern Ceramic Engineering—Properties, Processing, and Use in Design*, Marcel Dekker, Inc., New York, 1982.

[12] Ogawa, T. and Suresh, S., "Surface Film Technique for Crack Length Measurement in Nonconductive Brittle Materials: Calibration and Evaluation," *Engineering Fracture Mechanics*, Vol. 39, No. 4, 1991, p. 629.

[13] Moulson, A. J., "Reaction-Bonded Silicon Nitride: Its Formation and Properties," *Journal of Materials Science*, Vol. 14, 1979, p. 1017.

[14] Dow Corning, Information about NICALON™ Ceramic Fiber, Dow Corning Corporation, Midland, MI 48686-0994.

[15] Yang, F., unpublished results, Georgia Institute of Technology, Atlanta, GA.

[16] Kingery, W. D., Bowen, H. K., and Uhlman, D. R., *Introduction to Ceramics*, John Wiley & Sons, New York, 1976.

[17] Grathwhol, G. and Thümmler, F., "Creep of Reaction-Bonded Silicon Nitride," *Journal of Materials Science*, Vol. 13, 1978, p. 1177.

[18] Chesters, J. H., *Refractories, Production and Properties*, 2nd ed., The Metals Society, London, 1983.

[19] Jones, D. A., *Principles and Prevention of Corrosion*, MacMillan Publishing Company, New York, 1992.

[20] Harris, B., "Micromechanisms of Crack Extension in Composites," *Metal Science*, August-September 1980, p. 351.

[21] Dicarlo, J. A., "Fibers for Structurally Reliable Metal and Ceramic Composites," *Journal of Metals*, Vol. 37, June 1985, p. 44.

[22] Aveston, J., Cooper, G. A., and Kelly, A., *Single and Multiple Fracture, The Properties of Fiber Composites*, IPC Science & Technology Press, Guildford, England, 1971, p. 15.

ISBN 0-8031-2413-9